UNIVERSITY OF SOUTHAMPTON

FACULTY OF ENGINEERING, SCIENCE AND MATHEMATICS

INSTITUTE OF SOUND AND VIBRATION RESEARCH

Decentralised velocity feedback control of structures

by

Wouter Peter Engels

A thesis submitted for the degree of

Doctor of Philosophy

March 2006

UNIVERSITY OF SOUTHAMPTON

ABSTRACT

FACULTY OF ENGINEERING, SCIENCE AND MATHEMATICS
INSTITUTE OF SOUND AND VIBRATION RESEARCH

Doctor of Philosophy

DECENTRALISED VELOCITY FEEDBACK CONTROL OF STRUCTURES

by Wouter Peter Engels

Structural vibrations can cause fatigue of the structure, high sound levels and loss of positioning accuracy. Active control of broadband structural vibrations often requires multiple control locations and often uses a centralised controller that calculates the appropriate responses from the signals of all the sensors. The disadvantages of centralised control are that a lot of wiring is required and that instability can occur if one of the components fails. This thesis investigates algorithms that allow the tuning of multiple, single loop feedback controllers in a decentralised arrangement that reduces the global vibration of the structure. Ideally, this controller should be tuned on the basis of the local properties of the structure and, when applied at multiple locations to the same structure, achieve performance comparable to a centralised controller.

Constant gain velocity feedback is a decentralised control strategy known to be effective at controlling vibrations and requires only the feedback gain to be set appropriately. Because there are no analytical solutions for the optimal feedback gain, approximations of the gain were considered. For a beam, approximations on the basis of a few modes performed almost as well as a centralised, dynamic controller but the gains could not be set consistently on the basis of the mobility in a multi-channel set-up. On a plate, setting the gain to match the impedance of an infinite plate performed well and it is shown that this gain can be calculated from the local mobility in both single- and multi-channel set-up. Tuning the gain to maximise power absorption performed well, but may be difficult to realise in the multi-channel set-up and can be sensitive to the spectrum of the excitation.

On the basis of a carefully selected model of sound radiation, controllers were also designed to minimise sound radiation. Decentralised velocity feedback control were found to perform almost as well as LQG control. Strategies that minimised the vibration performed less well at controlling radiated noise, but still provided useful performance.

Contents

List of Figures

List of Tables

List of Notations

Roman symbols

a_n	Modal displacement of mode n [m]
c	Arbitrary constant [-]
c_0	Velocity of sound waves in air [m/s]
e	The number e, being 2.7182818
f	Frequency [Hz]
$f(t)$	Point force as a function of time [N]
$f_{mn}(t)$	Excitation of a single mode as a function of time [N]
g	Control gain [-]
h	Height of the structure [m]
j	Square root of -1
k	Wavenumber in air [1/m]
k_n	Flexural wavenumber of a specific mode n [1/m]
l_x	Length in x-direction [m]
l_y	Length in y-direction [m]
$p(x,t)$	Pressure distribution [N/m] or [N/m^2]
$m(t)$	Moment as a function of time [Nm]
r	Control effort weighting factor [-]
r	Distance between two points [m]
t	Time [s]
$w(x,t)$	Transverse displacement of the structure as a function of location and time [m]
x	Coordinate of a location on the structure [m]
y	Coordinate of a location on the structure [m]
E	Elasticity modulus [Pa]
$E_{ke}(t)$	Kinetic energy as a function of time [J]

$H(j\omega)$	Transfer function [-]
I	Cross-sectional area of moment of inertia [m^4]
I	Acoustic intensity [W]
J	Cost-function [-]
L	Length [m]
M	Mass of the structure [kg]
N	Number of modes
N_n	Normalised integral of squared modeshape of mode n [-]
P	Power [W]
P_{abs}	Power, absorbed by the structure [W]
S	Cross-sectional area [m^2]
S_u	Surface area [m^2]
Z	Impedance [Ns/m]
$\mathbf{a}_s$	Vector of modal displacement of the structural modes [m]
$\mathbf{f}_d$	Vector of disturbance forces [N]
$\mathbf{f}_c$	Vector of control forces [N]
$\mathbf{x}$	Vector of state variables [-]
$\mathbf{D}_s$	Matrix with the modal damping factors on its diagonal [rad/s]
$\mathbf{E}_{\mathbf{ff}^T}$	Correlations in time between the disturbing forces [N^2]
$\mathbf{G}(j\omega)$	Control gain matrix [-]
$\mathbf{I}$	Identity matrix [-]
$\mathbf{K}$	Solution to a Lyapunov equation [-]
$\mathbf{K}_s$	Matrix with the squared modal resonance frequencies on its diagonal [rad^2/s^2]
$\mathbf{L}$	Solution to a Lyapunov equation [-]
$\mathbf{N}$	Matrix with the elements N_n on its diagonal [-]
$\mathbf{P}_w$	Matrix describing the expected modal excitation of the system, under white noise excitation [-]
$\mathbf{P}_r$	Matrix describing the expected modal excitation of the system, under red noise excitation [-]
$\mathbf{Y}$	Mobility matrix [m/Ns]

Greek symbols

$\alpha(x,t)$	Rotational displacement of the structure as a function of location and time [rad]
γ	Amplitude coefficient [-]
$\delta(x)$	Dirac delta function [-]
ζ	Relative damping [-]
ν	Poisson ratio [-]
ρ	Density [kg/m^3]
ρ_0	Density of air [kg/m^3]
$\psi_n(x)$	Amplitude of mode shape n at position x [-]
ω	Frequency [rad/s]
ω_n	Resonance frequency of mode n [rad/s]
π	The number π, being 3.1415927
$\mathbf{\Phi}(t)$	Fundamental state transition matrix [-]
$\mathbf{\Phi}(j\omega)$	Fourier transform of the fundamental state transition matrix [-]
$\mathbf{\Phi}_\omega$	Shorter notation for the above.

Mathematical operators

E	Expectation over time
trace	Trace, sum of on-diagonal elements of a matrix
$\mathbb{F}$	Fourier transform
$\mathbb{I}$	Imaginary part
$\mathbb{R}$	Real part
∂	Partial derivative
∇	Jacobian matrix
$\dot{}$	Derivative with respect to time
$\ddot{}$	Second derivative with respect to time
x^*	Complex conjugate of x
$\mathbf{X}^H$	Hermitian or complex conjugate transpose of a matrix $\mathbf{X}$
$\mathbf{X}^T$	Transpose of a matrix $\mathbf{X}$
$x * y$	Convolution of x and y

Acknowledgements

After three years, this thesis is now finished. It would not have been possible, but for the support and help of many people and I will take this opportunity to thank them. First of all, my thanks go to Dr Steve Elliott, who offered me the chance to do a PhD and then supported me with excellent supervision and encouragement.

Secondly, I need to thank the rest of the staff and PhD students at the Signal Processing and Control Group. Through them I have learned much, both in and beyond my own little area of research. In particular, I would like to thank Dr Olie Baumann. The discussions we had about the ins and outs of modelling and calculating the optimal feedback gains were very enlightening for me. I would also like to thank by name Dr Paolo Gardonio and Joyce Shotter. Outside my own group, I need to thank Dr Mike Brennan and Dr Rufus Fraanje for useful comments on my research. I also gratefully acknowledge the financial support of the Engineering and Physical Sciences Research Council.

I thank my friends and family. Thanks to my friends both in the Netherlands and the United Kingdom, these last few years have been great. Special thanks go to everyone from the Hillwalking Club, without whom I would never have spent so much top quality time in various pubs around the country and Southampton. To my parents and my brother and sister, your support, advice and encouragement have meant so much to me. I dedicate this thesis to you.

Finally, Sabine, I can not possibly thank you enough and I am very happy that you are there for me.

Chapter 1

Introduction to active vibration control

1.1 Introduction

Vibrations in structures can be the cause of several problems, such as fatigue, high pressure sound fields in the vicinity of the structure and a loss of positioning accuracy of instruments attached to the structure. A reduction of these vibrations can be achieved in different ways. One way is to apply passive elements, such as extra mass, stiffness or dampers. These passive methods are not always practical or economical. Another option is to use active control. An active controller generally consists of three elements: a sensor, an actuator and an element that sets the output of the actuators on the basis of the measurements obtained with the sensors. It is the design of this element, the control algorithm, that this thesis is most concerned with. This chapter will first examine briefly the field of active vibration control and its different applications. In the course of this examination, the focus of this thesis will be explained and narrowed down to a set of objectives, which are formulated in section 1.3. Section 1.4 outlines the structure of this thesis and points out its main contributions.

1.2 A brief history of active control of vibrations

Active feedback control of structural vibrations was suggested by Olson (1956), though practical implementation was not achieved for almost another decade. Rockwell and Lawther (1964) investigated the damping of a beam on two rubber mounts, using an accelerometer and a force actuator attached at the same point on the structure to apply local velocity feedback. An electrical integrator was used to change the signal of the accelerometer into a signal proportional to the velocity. By applying a force opposite to the velocity, power can be extracted from the structure and the damping is increased. This paper was closely followed by two papers, Knyazev and Tartakovskii (1965, 1967), which describe implementations on a beam and on a plate, respectively.

Since these beginnings, the active control of vibrations has progressed beyond the laboratory and is now found in many different applications, such as cable-stayed bridges, tall buildings, space structures, high-accuracy machining, telescopes, satellites and aircraft. The applications can roughly be divided in three types: active vibration isolation, active vibration control and active structural acoustic control.

Active vibration isolation is concerned with preventing the transmission of vibration present in one part of the structure, the base, to another, connected part, the target. This is illustrated in figure 1.1(a). Active vibration control is aimed at reducing the overall vibrations of a distributed structure (figure 1.1(b)), while active structural acoustic control is aimed specifically at controlling the vibration of the structure in such a way that the sound radiated from the structure is reduced (figure 1.1(c)). A large amount of literature is available on each of these topics, some of which will be highlighted here. The focus of this thesis is mostly on active vibration control, though some research into active structural acoustic control has also been done. For further general reading on active control of vibrations, the reader is referred to Fuller et al. (1996) or Preumont (2002) and for modern control strategies to Skogestad and Postlethwaite (1996).

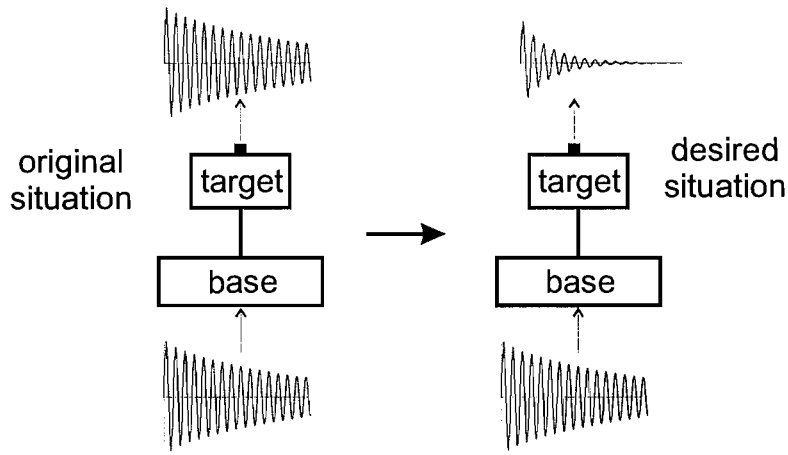

(a) Active vibration isolation

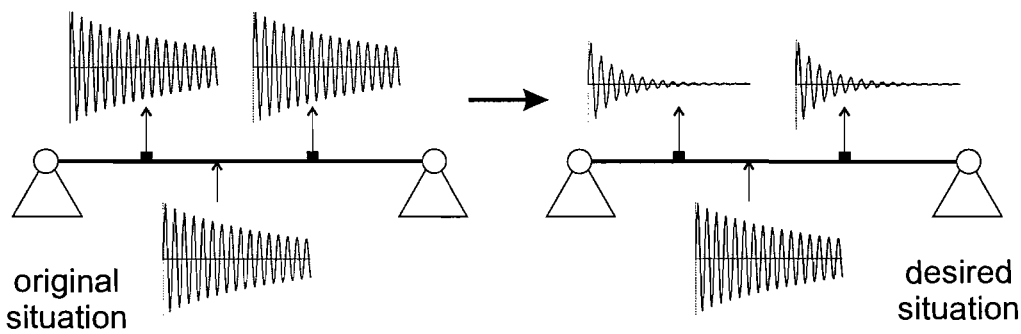

(b) Active vibration control

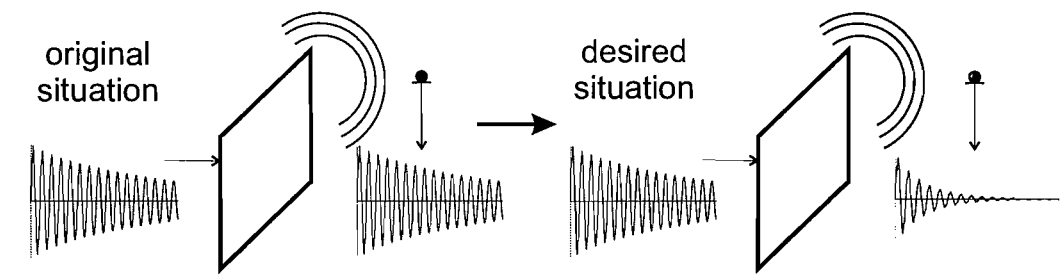

(c) Active structural acoustic control

Figure 1.1: Different goals of active control of vibrations.

1.2.1 Active vibration isolation

Active vibration isolation is concerned with preventing one part of the structure receiving vibrations present in another, connected part of the structure. Typical examples are the isolation of a sensitive piece of equipment in a satellite or aircraft and the mounting of an engine on a boat or helicopter. The best way to isolate one piece of equipment from vibrations would obviously be to physically sever the connection between the two, but that is not always possible. After all, the piece of equipment on the satellite must be connected to the rest of the satellite for it to be brought into orbit and to follow the pointing of the satellite. Similarly, the engine of a boat must follow the general pitch and jaw of a boat if it is to work properly. This is the usual trade-off in active vibration isolation, the tracking of the low-frequency base-motion versus the isolation of high or specific frequency vibrations.

Two set-ups are common in vibration isolation. One is an active mount, where the control system is part of the mount connecting the piece of equipment to be isolated and the vibrating structure. The other is the attachment of an inertial actuator to the equipment. The active mount or inertial actuators collocated with the mount can reduce, to a certain degree, the disturbing forces that act on the target equipment. Thus they can prevent vibration energy entering the equipment. The mounts are usually a hybrid of a completely passive part on which a control system is superimposed (e.g. Sutton et al. (1997), Kim et al. (2001), Preumont et al. (2002), Kim et al. (2004)). This allows for failure of the control system, with reduced performance rather than no performance or without damaging the isolated structure. The main advantage of inertial actuators is that they can be installed directly on the equipment to be isolated, which requires very few structural changes (Benassi et al. (2004)).

As an alternative to completely active control systems, a semi-passive control system can be used (e.g. Singh et al. (2004)). This can be either a system that converts vibration energy into electrical energy and dissipates it using resistors, or a system in which forces are generated by a passive structure but the characteristics of this passive element can be changed electronically. A good example of such as a system is a magneto-rheological damper (Dyke et al. (1996)). By creating a magnetic field at specific points in the flow-canal of damper, the apparent viscosity of the fluid can be changed and thus also the resulting force.

1.2.2 Active vibration control (AVC)

Active vibration control focuses on the control of vibrations over the entire structure. These structures usually consist of beam-, truss- and plate-like elements. Particularly if the structure is lightly damped and high accuracy is required, vibrations can cause a problem. Space structures are a good example of that kind of structure (Balas (1982)).The control strategies applied to cancel vibrations are dependent on the excitation. Two types of excitation that are usually examined are tonal excitations and broadband excitations. One aspect that will not be examined in great detail in this thesis, though it can be important in the actual implementation of the controllers, is where to place sensors and actuators on the structure such that maximum control results are obtained (e.g. Hiramoto et al. (2000)).

1.2.2.1 Tonal excitation, passive control

If the excitation is mainly tonal, control strategies can also focus on that particular tone. The controller is free to set the phase and amplitude of the response at that particular frequency. Dayou and Brennan (2001, 2003) showed, both in theory and in practice, that a vibration neutraliser can be used as effectively as active strategies for this purpose, provided that the frequency of interest is not too low. The vibration neutraliser is a passive device consisting of a spring, mass and damper and can be mounted onto the structure. One of the main limitations of neutralisers is that the setting of the stiffness, mass and damping is optimal for a particular frequency, thus if the frequency of the excitation changes, the control is no longer as effective or can even amplify the vibration. The solution to such a problem is to use a semi-passive strategy in which, for instance, the stiffness of the neutraliser can be actively adjusted (Brennan (1997)). This allows the neutraliser to be adaptable to some extent. Despite the effectiveness of the vibration neutralisers, active control can still be preferable due to its greater adaptability and better performance at low frequencies.

Tuned vibration neutralisers can also be constructed using devices made of piezoelectric ceramics (e.g. Jalili and Knowles (2004)). Piezoceramic patches can also be used for narrow band control in a semi-active solution (dell'Isola et al. (2003), and Niederberger et al. (2004)).

1.2.2.2 Tonal excitation, active control

The active control of tonal excitations has partly been focused on the tuning of the control strategies using power based methods (Redman-White et al. (1987), Guicking et al. (1989)). The maximisation of power absorption by the controller is particularly interesting as it requires no prior identification of the structure.

Brennan et al. (1995) compared three control strategies to control single frequency bending vibrations on an infinite and finite beam: the minimisation of the kinetic energy of the beam, the minimisation of the total power input into the beam by both the excitation and the controller and the maximisation of power extraction by the controller. It was shown that minimising kinetic energy and total energy input into the beam is possible, but that maximisation of power absorption by the control force, though effective on the infinite structure, was not effective for the finite structure and can increase the vibration of the structure considerably for tonal excitations. This is because the control force allows the excitation to increase its power input. Similar results were obtained in the maximisation of power absorption in the active control of sound fields (Elliott et al. (1991)) and on a plate structure controlled with piezo-patches (Bardou et al. (1997)). These results can be seen as a warning against using power absorption maximisation in a situation where the control force can influence the power input by the excitation. Hirami (1997b) examined the power absorption after control but before the reflection of the control signal returns to the control point and it was found to be effective when studied on a string.

The applications mentioned so far are applied for single frequencies. In these cases, the tone can serve as a reference signal and the control system can also be seen as feedforward control. Broadband excitations for which reference signals are available can also be controlled using feedforward algorithms (Vipperman et al. (1993)). If the reference signal is not available for the broadband excitation, feedforward control can not be used and feedback control must be used instead. This is examined next.

1.2.2.3 Broadband excitation

Though control of tonal excitations can be implemented effectively with passive, tuned vibration neutralisers, they are not as effective for broadband vibration control

over the entire structure, due to the resonances they introduce themselves. They can be fairly effective at reducing the vibration at specific locations on a structure though (Jacquot (2000, 2001)).

A recent development that uses both passive and active control is the heterogeneous blanket (Fuller et al. (2004)) which consists of many, randomly placed and more or less randomly tuned vibration neutralisers embedded in a foam. In its passive configuration, it was found to give good broadband reductions, while its active configuration provided additional reductions at low frequencies.

Active controllers of random vibrations in plates and beams almost always use multiple control locations. The control strategies themselves vary widely in complexity, from completely decentralised, constant gain control loops (e.g. Variyart et al. (2002)) to dynamic, multi-input multi-output controllers using all sensors and actuators (e.g. Trindade et al. (2001), Rizet et al. (2000), Singh et al. (2003)). Both these strategies have their own difficulty. In the case of the constant gain decentralised units the difficulty lies in using local measurements to choose the correct gain, because it can not 'see' the global response of the structure, see for instance, Gardonio and Elliott (2004b). For dynamic centralised controllers, one important difficulty is the robustness of the system to structural changes, such as the addition of a mass or changing resonance frequencies. Several authors focus on the robustness of these controllers using a variety of dynamic control strategies (e.g. Sadri et al. (1999), Wang and Huang (2002), Fraanje et al. (2004)), including neural networks (Smyser and Chandrashekhara (1997)).

One way of overcoming stability and spillover issues and increase robustness is to use modal sensors and actuators. These are piezoelectric sensors and actuators that are preshaped to correspond to a particular modeshape of the structure. They can typically excite and perceive only that particular mode, which makes it very robust in terms of spillover and high control gains could be applied. However, many such sensors and actuators are needed if one wishes to control many modes. A solution to that problem would be to use a high density of smaller sensors and actuators and combine the signals of the sensors and actuators according to the modeshapes using a centralised controller (Preumont et al. (2003)). This results in a fixed matrix to estimated the modal velocities from a large amount of sensors.

However, recent investigations have started to question the usefulness of completely centralised controllers for broadband applications and have shown that if the problem is spatially invariant, that is, neither the structure, excitation nor cost function change as a function of the position on the structure, a controller using only local and information from the nearest neighbours could be as effective as centralised control (Bamieh et al. (2002)). This leads us back to the problem of tuning the gain of such a decentralised loop. Hirami (1997a) examined the use of his maximum power absorption strategy within a reverberation time, in a broadband application, but found that the strategy did not converge. Interestingly, it has been observed that if the excitation is white noise, the controller can not influence the power input since the disturbance will be uncorrelated with the response by the controller (Nelson (1996)). As the power input is constant, maximising power absorption by the controller must be equal to minimising the total power input by the controller and the excitation. Minimising the total power input was the strategy that worked very well on the finite structure for single tone excitations, examined by Brennan et al. (1995). The tuning of such a decentralised controller will be the focus of this thesis.

1.2.3 Active structural acoustic control (ASAC)

Acoustic radiation from structures is one of the main reasons for applying a vibration reducing control strategy. Though the direct control of the sound field using speakers and microphones is also possible and is commercially applied, the control of the structural vibration to prevent the acoustic radiation in the first place has become more and more accepted. Many of the methods are similar to active vibration control except that the cost criterion to be minimised by the controller is changed from 'kinetic energy' to 'radiated sound power'. This means that similar problems observed for AVC occur with the implementation of the controller combined, however, with the additional problem of modeling the radiated sound power.

It can be shown that controllers specifically designed for minimising acoustic radiation provide better control, than just controlling kinetic energy (Clark Smith and Clark (1998)). Though the spatial invariance is now no longer valid, as the radiation modes add a spatial characteristic to the cost function, it has been shown that appropriately tuned decentralised constant gain controllers can still effectively control

sound radiation (Elliott et al. (2002)). A direct comparison of the performance of a decentralised, constant gain controller and a dynamic controller seems to be lacking from current literature and is one of the areas studies in this thesis.

Observing that for low frequencies the sound radiation is dominated by the modes with net volume displacement (Wallace (1972b)), controlling the net volume displacement has been examined as a possible simplified way of controlling the sound radiation (Johnson and Elliott (1995)). Equivalent to the shaped modal sensors of AVC, preshaped sensors (Rex and Elliott (1992)) and arrays of sensors of sensors (Sors and Elliott (2002)) have been used to control sound power. They are effective as long as the frequency range to be controlled is below the frequency at which the wavelength in the structure and in air become similar.

1.3 Aims and objectives

For the effective control of the global vibrations of a distributed structure, it is common practice to use multiple sensors and actuators. There are many methods available for constructing multichannel control algorithms that reduce the vibrations of structures. Most of these methods rely for tuning and/or control a central control unit that processes the information gathered at all the sensor locations. This allows the controller to use the actuators as effectively as possible. However, there are several disadvantages to this approach. One is the amount of wiring that is required to connect all the sensors and actuators. It adds weight, expense and a chance of physical failure. On the controller side, the centralised controllers may be sensitive to failure of one of the sensors or actuators. Thus, if one unit fails, the entire system may fail.

Multiple units consisting of a single loop of one sensor, one actuator and a control algorithm, that work independently may be preferable to a centralised system. They would not need as much wiring and, because of their independence, should be less sensitive to failure of one of the units. However, the control algorithm for each of these units still needs to be determined. At each control location only a limited amount of information is available. If the control algorithm can be set on the basis of information that is available, that would increase the versatility and might allow

the tracking of changes in the system. This thesis is concerned with the selection and performance of a control algorithm for such modular control systems, and the following, specific aim can be formulated:

> *To investigate algorithms that allow the design of a single loop feedback controller that is capable of reducing the global vibration of the structure. Ideally, this controller should be tuned on the basis of the local properties of the structure and, when applied at multiple locations to the same structure, achieve performance comparable to a centralised controller.*

To achieve this aim, the research needs to be broken down into several smaller objectives. These are:

- the selection and description of a model structure, cost function and disturbance parameters.
- the selection and optimisation of a control algorithm.
- to investigate how the optimal controller or approximations to the optimal controller perform in comparison to centralised controllers in terms of AVC and ASAC.
- relating the optimal controller or an approximation to the structure's local properties.

The way in which these objectives are presented in this thesis is described in section 1.4.

1.4 Contribution and structure of this thesis

The main body of this thesis is structured in 5 chapters. Chapter 2 will discuss the first objective mentioned in section 1.3: It sets out the model structure and the cost function. It is shown that the type of disturbance is important for the minimisation of the cost function.

Chapter 3 will discuss the selection and optimisation of a control algorithm for a *single-channel system.* Theoretically optimal controllers are derived, but it is shown that these are non-causal and can only be used as a feedforward contoller if infinite

advance time-information is available, or as a tonal control strategy. To keep the analysis of the controller as simple as possible, constant velocity feedback control is then selected. The feedback gain can be optimised, but doing so does not give a clear relationship between the local properties of the beam and the optimal feedback gain. Therefore, approximations to the optimal feedback gain are derived on the basis of simplified models. The performance of these approximations is compared to that of the optimised feedback controller on both a beam and a plate.

Chapter 4 analyses the performance of the approximated and optimal feedback gains in a *multi-channel set-up*. The difference in performance between optimal centralised and decentralised feedback gains is analysed for different amounts of control effort and for different control locations.

Chapter 5 examined the sound radiation from the structure. It compares the performance of an LQG controller, a centralised constant gain, velocity feedback controller and a decentralised controller when controlling the sound radiation. The performance of a controller minimising kinetic energy is compared with controllers that minimise the sound radiation.

Chapter 6 analyses how the controller can be tuned from the local mobility or power absorption in a single- and multi-channel control situation. It also examines whether it is possible to tune the controller in a practical set-up, using measurements, rather than simulations.

The main contributions of this thesis are:

- New methods for the approximating optimal velocity feedback gains minimising the kinetic energy of a modal structure and the comparison of these methods in terms of performance in AVC (chapters 3 and 4).
- A comparison of performance of centralised dynamic control and centralised and decentralised, constant gain velocity feedback control, both in terms of AVC and ASAC (chapter 4 and 5).
- A comparison of two different ways of modeling the sound radiation of a plate in an infinite baffle for ASAC (chapter 5).
- A practical method of deriving the impedance of an infinite plate from the local dynamic response (chapter 6).

Chapter 2

Model formulation and cost function

This chapter introduces the models that are used in this thesis to describe the vibration of various structures. It discusses the modal formulation of a simply supported beam, a simply supported plate and a plate of which two opposite ends are free and two are clamped. It is also shown how to calculate the kinetic energy of these structures. The kinetic energy of the structure is the cost function that is used in most of this thesis.

The beam model is used in chapters 3 and 4 to study the effects of various control strategies. The simply supported plate is then used as a well-defined, but more complex system than the beam to examine whether results for the beam still hold on a more complex structure. Finally, the clamped-free-clamped-free plate is used as a model for the test structure used to verify findings in practice as well as simulations. The test structure is the same as used by Serrand (1998) and Benassi (2004).

A detailed derivation of the dynamic, modal beam model is contained in appendix A.

Figure 2.1: A simply supported beam.

2.1 Modeling of vibration response of thin plates and beams

The modal analysis of beam and plates is based on the differential equations governing the motion of an infinitesimal portion of the plate or beam. The approach described here is used, amongst others, in Meirovitch (1986) and Fuller et al. (1996). The modeshapes and how they are scaled are particularly important (equations 2.3, 2.10 and 2.16). The choice of the scaling of the modeshapes also has consequences for the calculation of the kinetic energy of the structure (equations 2.7, 2.14 and 2.24).

2.1.1 Simply supported beam

A simply supported beam is a beam that is supported at its ends on hinges, allowing free rotation, but no displacement. This is illustrated in figure 2.1.

The detailed derivation of the beam motion is included in appendix A, in which it is shown that the motion of the beam is governed by the Euler-Bernouilli thin beam equation:

$$\frac{\partial^2}{\partial x^2} EI \frac{\partial^2 w(x,t)}{\partial x^2} + \rho S \frac{\partial^2 w(x,t)}{\partial t^2} = p(x,t) \tag{2.1}$$

Where EI is the bending stiffness of the beam, $w(x,t)$ the transverse deflection, ρ the density and S the cross-sectional area. $p(x,t)$ is an external pressure distribution acting on the beam. EI is assumed constant along the beam.

For a simply supported beam, the boundary conditions are such that there are no deflections or bending moments at the beginning ($x = 0$) and the end of the beam ($x = L$):

$$w(0,t) = 0 \qquad EI\frac{\partial^2 w(0,t)}{\partial x^2} = 0$$
$$w(L,t) = 0 \qquad EI\frac{\partial^2 w(L,t)}{\partial x^2} = 0$$

The solution to equation 2.1 is a sum of the motions of the modes of the beam:

$$w(x,t) = \sum_{n=1}^{\infty} a_n(t)\psi_n(x) \tag{2.2}$$

where $\psi_n(x)$ are the modeshapes of the simply supported beam, which satisfy the boundary conditions. They can be scaled arbitrarily and are chosen to be:

$$\psi_n(x) = \sin(k_n x) \tag{2.3}$$

where $k_n = \frac{n\pi}{L}$ and n is an integer. $a_n(t)$ in equation 2.2 are the modal displacements of the individual modeshapes at any point in time.

Assuming the external pressure distribution $p(x,t)$ in equation 2.1 is a point force, $f(t)\delta(x - x_f)$, at a point x_f along the beam, allows the formulation of the transfer function from the force to the modal displacement in terms of the Laplace variables or frequency. In terms of frequency, the transfer function is:

$$H_n(j\omega) = \frac{a_n(j\omega)}{f(j\omega)} = \frac{2}{\rho SL}\frac{\psi_n(x_f)}{(\omega_n^2 + 2j\omega\zeta\omega_n - \omega^2)} \tag{2.4}$$

where a small amount of damping is included, through the damping factor ζ and ω_n is the natural frequency of the modeshape:

$$\omega_n(x) = \left(\frac{n\pi}{L}\right)^2 \sqrt{\frac{EI}{\rho S}} \tag{2.5}$$

The transfer function can also be written in a state space formulation:

$$\begin{pmatrix} \dot{a}_n \\ \ddot{a}_n \end{pmatrix} = \begin{bmatrix} 0 & 1 \\ -\omega_n^2 & -2\zeta\omega_n \end{bmatrix} \begin{pmatrix} a_n \\ \dot{a}_n \end{pmatrix} + \frac{2}{\rho SL}\begin{bmatrix} 0 \\ \psi_n(x_f) \end{bmatrix} f(t) \tag{2.6}$$

Table 2.1 lists the variables used in the simulations of the beam. Figure 2.2(a) shows the velocity response at a location $0.6L$ along the beam to a force located at that same point. Figure 2.2(b) shows the velocity response at a location $0.24L$ along the beam for a force at a location $0.6L$ along the beam.

The kinetic energy of the beam can be calculated by integrating the kinetic energy

$EI = 1$	[Nm^2]	$\rho S = 1$	[kg/m]
$\zeta = 0.01$	[-]	$L = 1$	[m]

Table 2.1: Variables of the plate used in the simulations.

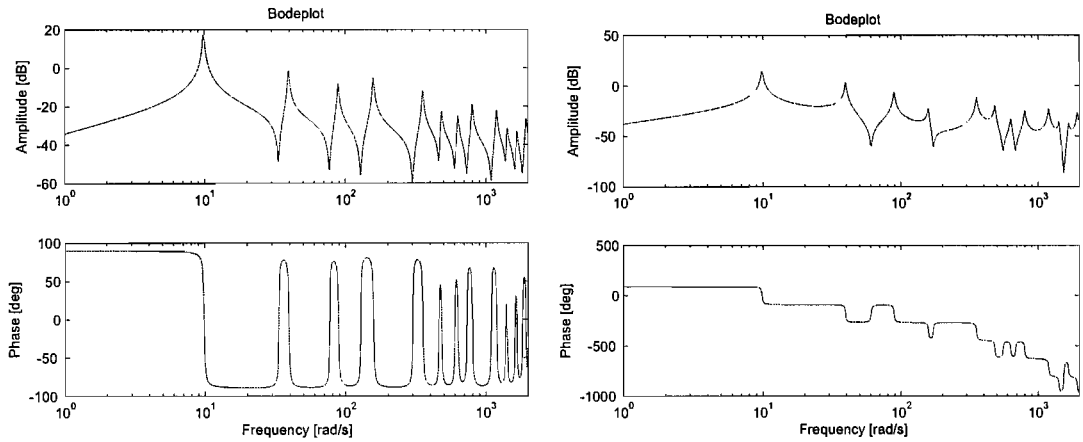

(a) Response at $x = 0.6L$ (b) Response at $x = 0.24L$

Figure 2.2: Velocity response of the beam as a function of frequency, at different locations along the beam to a unit force located at $0.6L$ of the length of the beam.

of infinitesimal elements along the beam:

$$\begin{aligned} E_{ke}(t) &= \int_{x=0}^{L} \frac{1}{2}\rho S \dot{w}(x,t)\dot{w}^*(x,t)dx \\ &= \frac{1}{2}\rho S \int_{x=0}^{L} \left(\sum_{n=1}^{\infty} \dot{a}_n(t)\psi_n(x)\right)\left(\sum_{m=1}^{\infty} \dot{a}_m(t)\psi_m(x)\right)^* dx \\ &= \frac{1}{2}\rho S \sum_{n=1}^{\infty}\sum_{m=1}^{\infty} \dot{a}_n(t)\dot{a}_m^*(t) \int_{x=0}^{L} \psi_n(x)\psi_m(x)dx \\ &= \frac{\rho S L}{4} \sum_{n=1}^{\infty} |\dot{a}_n(t)|^2 \end{aligned} \tag{2.7}$$

The fact that the modes are orthogonal has been used here to show that the kinetic energy is equal to a sum of the squared velocities of the separate modes.

2.1.2 Simply supported plate

The modeling of a simply supported plate follows much the same lines as the modeling of the simply supported beam discussed in section 2.1.1. Like the simply

supported beam, the edges of the simply supported plate allow free rotation, but no displacement. This model can also be found in Fuller et al. (1996). The plate is assumed to be uniform over its surface (isotropic). The differential equation that needs to be satisfied for this plate then is:

$$EI\left(\frac{\partial^4 w}{\partial x^4} + 2\frac{\partial^4 w}{\partial x^2 \partial y^2} + \frac{\partial^4 w}{\partial y^4}\right) + \rho h \frac{\partial^2 w}{\partial t^2} = p(x, y, t) \tag{2.8}$$

where EI is the bending stiffness of the plate this time. h is the thickness of the plate and $p(x, y, t)$ a pressure acting on a point of the plate. Strictly speaking, the Poisson ratio, ν,should also be included by in equation 2.8. However, it can also be included in the term $I = h^3/12(1 - \nu^2)$. As this affects only the value of the I, the Poisson ratio was set to 0 for the analysis of the simply supported plate. The boundary conditions of the differential equation 2.8 are that the displacements and the moments are equal to zero along the edges of the plate:

$$\begin{array}{ll} w(0, y, t) = 0 & w(x, 0, t) = 0 \\ w(l_x, y, t) = 0 & w(x, l_y, t) = 0 \\ \frac{\partial^2 w(0,y,t)}{\partial x^2} = 0 & \frac{\partial^2 w(x,0,t)}{\partial y^2} = 0 \\ \frac{\partial^2 w(l_x,y,t)}{\partial x^2} = 0 & \frac{\partial^2 w(x,l_y,t)}{\partial y^2} = 0 \end{array}$$

The general solution again takes the form of a sum of the modal displacements, but now with two modal indices:

$$w(x, y, t) = \sum_{m=1}^{\infty} \sum_{n=1}^{\infty} a_{mn}(t) \psi_{mn}(x, y) \tag{2.9}$$

where $\psi_{mn}(x, y)$ is a sinusoidal modeshape that satisfies both the boundary conditions and the homogeneous form of differential equation 2.8:

$$\psi_{mn}(x, y) = \sin(k_m x) \sin(k_n y) \tag{2.10}$$

where k_m and k_n are the wavenumbers in x and y direction:

$$\begin{aligned} k_m &= m\pi/l_x \\ k_n &= n\pi/l_y \end{aligned}$$

l_x and l_y being the length of the plate in x and y direction respectively. The modes each have a natural resonance frequency, given by:

$$\omega_{mn} = \sqrt{\left(\frac{EI}{\rho h}\right)} \left(\left(\frac{m\pi}{l_x}\right)^2 + \left(\frac{n\pi}{l_y}\right)^2\right) \tag{2.11}$$

$E = 7 \cdot 10^{10}$	[Pa]	$\rho = 2720$	[kg/m^3]
$\zeta = 0.01$	[-]	$h = 0.001$	[m]
$l_x = 0.247$	[m]	$l_y = 0.278$	[m]

Table 2.2: Variables of the simply supported plate used in the simulations.

The transfer function $H(j\omega)$ from a point force at some point, (x_f, y_f), on the plate to the modal amplitude a_{mn} can now be calculated to be:

$$H_{mn}(j\omega) = \frac{4}{\rho h l_x l_y} \frac{\psi_{mn}(x_f, y_f)}{\omega_{mn}^2 + 2j\zeta\omega\omega_{mn} - \omega^2} \tag{2.12}$$

or in state space form:

$$\begin{pmatrix} \dot{a}_{mn} \\ \ddot{a}_{mn} \end{pmatrix} = \begin{bmatrix} 0 & 1 \\ -\omega_{mn}^2 & -2\zeta\omega_{mn} \end{bmatrix} \begin{pmatrix} a_{mn} \\ \dot{a}_{mn} \end{pmatrix} + \frac{4}{\rho h l_x l_y} \begin{pmatrix} 0 \\ \psi_{mn}(x_f, y_f) \end{pmatrix} f(t) \tag{2.13}$$

Note that the factor $2/\rho SL$ from from equations 2.4 and 2.6 has become a factor $4/\rho h l_x l_y$ in equations 2.12 and 2.13. This is because the integral of the squared modeshapes over the surface of the plate is $1/4 l_x l_y$ for the plate, in comparison to $1/2L$ for the beam.

The variables used in the simulations for the simply supported plate are listed in table 2.2. Figures 2.3(a) and 2.3(b) shows the velocity response observed at, respectively, $(0.24 l_x, 0.6 l_y)$ and $(0.33 l_x, 0.37 l_y)$ due to a force at a location $(0.24 l_x, 0.6 l_y)$ on the plate. It is important to note that the modal density of the plate (the number modes per frequency) increases with frequency, whereas it decreased for the beam.

In a similar way to the beam, the kinetic energy of the simply supported plate can be calculated as a sum of the squared modal velocities:

$$E_{ke}(t) = \frac{\rho h l_x l_y}{8} \sum_{m=1}^{\infty} \sum_{n=1}^{\infty} |\dot{a}_{mn}(t)|^2 \tag{2.14}$$

Again, because of the integral of the modeshapes over the surface of the plate, the factor $\frac{\rho SL}{4}$ has changed to $\frac{\rho h l_x l_y}{8}$.

2.1.3 Clamped-free-clamped-free plate

The differential equation describing an infinitesimal element of the clamped-free-clamped-free (CFCF) plate is the same as for the simply supported plate (equation

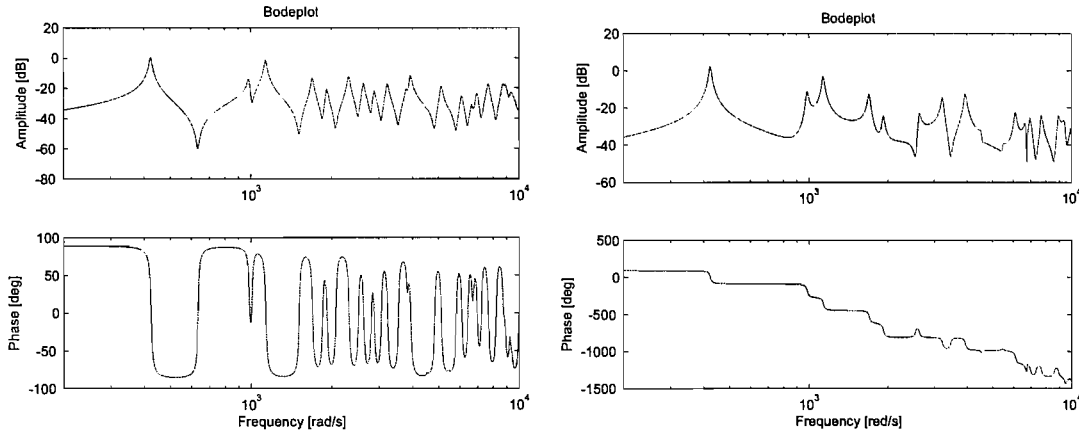

(a) Response at $(x, y) = (0.24l_x, 0.6l_y)$ (b) Response at $(x, y) = (0.33l_x, 0.37l_y)$

Figure 2.3: Velocity response of the simply supported plate as a function of frequency, at different locations on the plate to a unit force located at $(x, y) = (0.24l_x, 0.6l_y)$.

2.8). The boundary conditions, however, are different. For this particular case, the conditions are that the plate is clamped at the edges $x = 0$ and $x = l_x$ and free along $y = 0$ and $y = l_y$. Clamped edges means that rotation and displacement are not allowed, while free edges mean that there are no forces or moments acting on the edges of the plate:

$$\begin{aligned} w(0,y,t) &= 0 & \frac{\partial^2 w(x,0,t)}{\partial x \partial y} &= 0 \\ w(l_x,y,t) &= 0 & \frac{\partial^2 w(x,l_y,t)}{\partial x \partial y} &= 0 \\ \frac{\partial w(0,y,t)}{\partial x} &= 0 & \frac{\partial^3 w(x,0,t)}{\partial y^3} &= 0 \\ \frac{\partial w(l_x,y,t)}{\partial x} &= 0 & \frac{\partial^3 w(x,l_y,t)}{\partial y^3} &= 0 \end{aligned}$$

Unfortunately no analytical solution to equation 2.8 exists for $w(x, y, t)$ for these boundary conditions. An approximation is possible though. Serrand (1998) uses an approximate modal solution also used in Leissa (1969). The same solution is used here as well. The solution is based on an assumed-modes method, where the modeshapes are assumed to have a certain shape and then the modeling of the dynamics follows from that assumption. In this case, the displacement at a particular point is assumed to be:

$$w(x,y,t) = \sum_{m=1}^{\infty} \sum_{n=1}^{\infty} \psi_{mn}(x,y) a_{mn}(t) \tag{2.15}$$

where $\psi_{mn}(x,y)$ is the modeshape associated with the mnth mode, while $a_{mn}(t)$ is the modal amplitude of that particular mode. Following Leissa (1969), the modeshapes are written as:

$$\psi_{mn}(x,y) = \psi_m(x)\psi_n(y) \tag{2.16}$$

with

$$\psi_m(x) = \begin{cases} \cos\gamma_1\left(\frac{x}{l_x}-\frac{1}{2}\right) + \frac{\sin(\gamma_1/2)}{\sinh(\gamma_1/2)}\cosh\gamma_1\left(\frac{x}{l_x}-\frac{1}{2}\right) & \text{for } m = 2,4,6,\ldots \\ \sin\gamma_2\left(\frac{x}{l_x}-\frac{1}{2}\right) - \frac{\sin(\gamma_2/2)}{\sinh(\gamma_2/2)}\sinh\gamma_2\left(\frac{x}{l_x}-\frac{1}{2}\right) & \text{for } m = 3,5,7,\ldots \end{cases} \tag{2.17}$$

$$\psi_n(y) = \begin{cases} 1 & \text{for } n = 0 \\ 1-\frac{2y}{l_y} & \text{for } n = 1 \\ \cos\gamma_1\left(\frac{y}{l_y}-\frac{1}{2}\right) - \frac{\sin(\gamma_1/2)}{\sinh(\gamma_1/2)}\cosh\gamma_1\left(\frac{y}{l_y}-\frac{1}{2}\right) & \text{for } n = 2,4,6,\ldots \\ \sin\gamma_2\left(\frac{x}{l_x}-\frac{1}{2}\right) + \frac{\sin(\gamma_2/2)}{\sinh(\gamma_2/2)}\sinh\gamma_2\left(\frac{y}{l_y}-\frac{1}{2}\right) & \text{for } n = 3,5,7,\ldots \end{cases} \tag{2.18}$$

where γ_1 and γ_2 are the solutions of

$$\tan(\gamma_1/2) + \tanh(\gamma_1/2) = 0 \tag{2.19}$$

$$\tan(\gamma_2/2) - \tanh(\gamma_2/2) = 0 \tag{2.20}$$

These solutions are approximations and do not quite satisfy the boundary conditions correctly, nor are these modeshapes orthogonal. Orthogonality of the modeshapes would mean that $\int\int \psi_{kl}(x,y)\psi_{mn}(x,y)\mathrm{d}x\mathrm{d}y$ would be equal to 0 unless $mn = kl$. For the chosen modeshapes this integral is also nonzero if $kl \neq mn$. However, the values of these integrals are small compared to the value of the integral for $mn = kl$ and will thus be neglected. The integral of $\psi_{mn}(x,y)^2$ is dependent on the modeshape, and is expressed here as $N_{mn}l_xl_y$. The factors N_{mn} are rather complicated functions and have been evaluated numerically rather than analytically.

Leissa (1969) gives the corresponding natural resonance frequencies as:

$$\omega_{mn}^2 = \frac{\pi^4}{\rho}\frac{1}{1-\nu^2}\frac{h^3}{12}E\left[\frac{G_x^4}{l_x^4} + \frac{G_y^4}{l_y^4} + 2\frac{1}{l_x^2l_y^2}\left(\nu H_xH_y + (1-\nu)J_xJ_y\right)\right] \tag{2.21}$$

where G_x, G_y, H_x, H_y, J_x and J_y can be found in table 2.3. On the basis of these resonance frequencies, the transfer function from a force at a particular point on the plate to a modal amplitude can be formulated:

$$H_{mn}(j\omega) = \frac{1}{\rho h l_x l_y N_{mn}}\frac{\psi_{mn}(x_f,y_f)}{\omega_{mn}^2 + 2\zeta\omega_{mn}j\omega - \omega^2} \tag{2.22}$$

	G_x	H_x	J_x
for $m = 2$	1.506	1.248	1.248
for $m = 3, 4, 5, \ldots$	$m - \frac{1}{2}$	$(m-\frac{1}{2})^2 \left[1 - \frac{2}{(m-\frac{1}{2})\pi}\right]$	$(m-\frac{1}{2})^2 \left[1 - \frac{2}{(m-\frac{1}{2})\pi}\right]$
	G_y	H_y	J_y
for $n = 0$	0	0	0
for $n = 1$	0	0	$12\pi^2$
for $n = 2$	1.506	1.248	5.017
for $n = 3, 4, 5, \ldots$	$n - \frac{1}{2}$	$(n-\frac{1}{2})^2 \left[1 - \frac{2}{(n-\frac{1}{2})\pi}\right]$	$(n-\frac{1}{2})^2 \left[1 + \frac{6}{(n-\frac{1}{2})\pi}\right]$

Table 2.3: Factors for the calculation of the resonance frequencies for the CFCF plate.

$E = 2.06 \cdot 10^{11}$	[Pa]	$\rho = 7800$	[kg/m^3]
$\zeta = 0.01$	[-]	$h = 0.0019$	[m]
$l_x = 0.5$	[m]	$l_y = 0.7$	[m]
$\nu = 0.3$	[-]		

Table 2.4: Variables of the CFCF-plate used in the simulations.

or in state space form:

$$\begin{pmatrix} \dot{a}_{mn} \\ \ddot{a}_{mn} \end{pmatrix} = \begin{bmatrix} 0 & 1 \\ -\omega_{mn}^2 & -2\zeta\omega_{mn} \end{bmatrix} \begin{pmatrix} a_{mn} \\ \dot{a}_{mn} \end{pmatrix} + \frac{1}{\rho h l_x l_y} \begin{pmatrix} 0 \\ \psi_{mn}(x_f, y_f)/N_{mn} \end{pmatrix} F(t) \quad (2.23)$$

It is clear from equation 2.21 that the Poisson ratio plays a bigger role than in the simply supported plate. It has therefore been included in the modeling of the CFCF-plate. The variables used in the simulations for the CFCF-plate are listed in table 2.4. Figures 2.4(a) and 2.4(b) show the velocity response observed at, respectively, $(0.24l_x, 0.6l_y)$ and $(0.33l_x, 0.37l_y)$ due to a force at a location $(0.24l_x, 0.6l_y)$ on the plate. The kinetic energy of the CFCF-plate can be calculated as:

$$J_{ke} = \frac{1}{2}\rho h l_x l_y \sum_{m=1}^{\infty}\sum_{n=1}^{\infty} N_{mn} |\dot{a}_{mn}|^2 \quad (2.24)$$

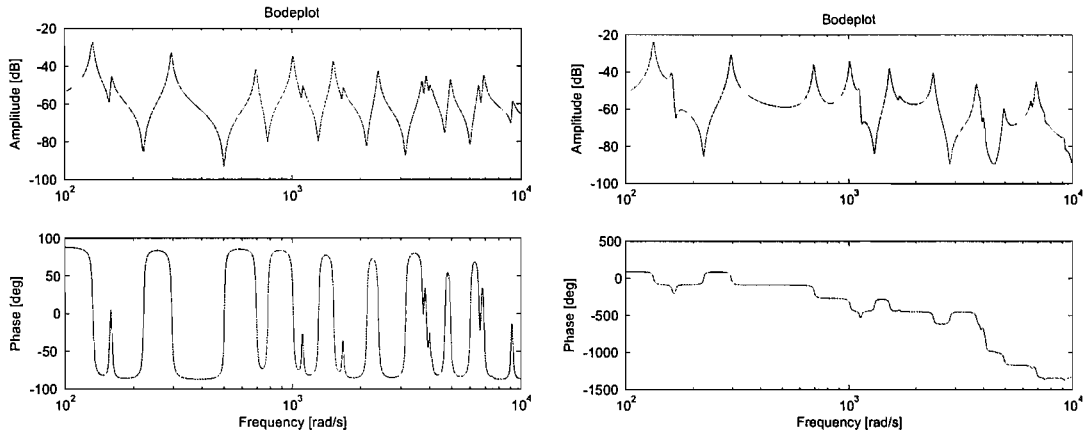

(a) Response at $(x, y) = (0.24l_x, 0.6l_y)$ (b) Response at $(x, y) = (0.33l_x, 0.37l_y)$

Figure 2.4: Velocity response of the CFCF-plate as a function of frequency, at different locations on the plate to a unit force located at $(x, y) = (0.24l_x, 0.6l_y)$.

2.2 Cost function

As mentioned in the introduction of this chapter, the kinetic energy of the structure is the cost function that is minimised in most of the thesis. The previous sections showed that the kinetic energy is a weighted sum of the squared modal velocities for each model. Another quadratic cost function is the sound radiation. This section shows how quadratic cost functions like the kinetic energy can be calculated for these models.

The analysis will assume that only a limited number, N, of modes is taken into account. This allows equations 2.6, 2.13 and 2.23 to be written in a general matrix notation:

$$\begin{pmatrix} \dot{\mathbf{a}}_s \\ \ddot{\mathbf{a}}_s \end{pmatrix} = \begin{bmatrix} 0 & \mathbf{I} \\ -\mathbf{K}_s & -\mathbf{D}_s \end{bmatrix} \begin{pmatrix} \mathbf{a}_s \\ \dot{\mathbf{a}}_s \end{pmatrix} + \frac{1}{M} \begin{pmatrix} 0 \\ \mathbf{N}^{-1}\mathbf{\Psi} \end{pmatrix} \mathbf{f}(t) \tag{2.25}$$

Here $\mathbf{a}_s$ and $\dot{\mathbf{a}}_s$ are respectively, vectors of the modal amplitudes and modal velocities. M is the total mass of the structure, and $\mathbf{N}$ is a diagonal matrix consisting of the integral of the squared modeshapes over the structure. For the simply supported beam and plate these values are equal for all modes and are $1/2$ and $1/4$ respectively. For the CFCF plate, these terms depend on the particular modeshape. The matrix $\mathbf{K}_s$ is a matrix with the squared natural frequencies, ω_{mn}^2, on its diagonal and empty otherwise. The matrix $\mathbf{D}_s$ is also a diagonal matrix, but with the damping terms

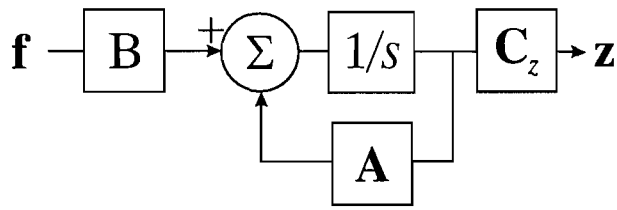

Figure 2.5: Block diagram of the model.

$2\zeta\omega_{mn}$ on its diagonal. Equation 2.25 can also be rewritten as:

$$\dot{\mathbf{x}} = \mathbf{A}\mathbf{x} + \mathbf{B}\mathbf{f}(t) \tag{2.26}$$

$$\mathbf{z} = \mathbf{C}_z\mathbf{x} \tag{2.27}$$

This is depicted as in a block diagram in figure 2.5. The elements of $\mathbf{x}$, consisting of the modal amplitudes and velocities are the *states* of the system. The vector $\mathbf{z}$ consists of the elements, which, when squared, weighted and summed give the appropriate quadratic cost function:

$$J = \mathbf{z}^H\mathbf{Q}_z\mathbf{z} \tag{2.28}$$

where $\mathbf{Q}_z$ is a diagonal matrix consisting of the appropriate weighting terms for each element of $\mathbf{z}$. If $\mathbf{C}_z$ and $\mathbf{Q}_z$ are both static matrices, then combining equations 2.28 and 2.27 results in:

$$J = \mathbf{x}^H\mathbf{C}_z^H\mathbf{Q}_z\mathbf{C}_z\mathbf{x} = \mathbf{x}^H\mathbf{Q}\mathbf{x} \tag{2.29}$$

This cost function can be evaluated both in the frequency and the time domain, which allows the calculated cost values to be verified. The frequency domain calculation also allows the numerical evaluation of cost functions for which the matrix $\mathbf{Q}$ varies with frequency, such as sound radiation.

2.2.1 Time domain approach

If the forces, $\mathbf{f}(t)$ are random, time varying signals that do not diminish in time, then the cost function, equation 2.29, should be changed to an expectation. Otherwise an integral over all time will result in an infinite cost. Thus:

$$J = \mathrm{E}\left[\mathbf{x}^T(t)\mathbf{Q}\mathbf{x}(t)\right] = \mathrm{trace}\left(\mathbf{Q}\mathrm{E}\left[\mathbf{x}(t)\mathbf{x}^T(t)\right]\right) \tag{2.30}$$

Where E denotes expectation. The states $\mathbf{x}$ can be calculated as a convolution of impulse response of the system and the time varying signal $\mathbf{f}(t)$:

$$\mathbf{x}(t) = \mathbf{\Phi}(t) * \mathbf{B}\mathbf{f}(t) \tag{2.31}$$

The matrix $\mathbf{\Phi}(t)$ is known as the *fundamental state transition matrix* and is defined as:

$$\mathbf{\Phi}(t) = \begin{cases} \mathrm{e}^{\mathbf{A}t} & \text{for} \quad t \geq 0 \\ 0 & \text{for} \quad t < 0 \end{cases} \tag{2.32}$$

Combining equations 2.31 and 2.32 with equation 2.30 results in:

$$\begin{aligned} J &= \text{trace}\left(\mathbf{Q}\mathrm{E}\left[\mathbf{x}(t)\mathbf{x}^T(t)\right]\right) \\ &= \text{trace}\left(\mathbf{Q}\mathrm{E}\left[\mathbf{\Phi}(t) * \mathbf{B}\mathbf{f}(t)\left(\mathbf{\Phi}(t) * \mathbf{B}\mathbf{f}(t)\right)^T\right]\right) \\ &= \text{trace}\left(\mathbf{Q}\mathrm{E}\left[\int_{-\infty}^{\infty} \mathbf{\Phi}(\sigma_1)\mathbf{B}\mathbf{f}(t-\sigma_1)\mathrm{d}\sigma_1 \int_{-\infty}^{\infty} \mathbf{f}^T(t-\sigma_2)\mathbf{B}^T\mathbf{\Phi}^T(\sigma_2)\mathrm{d}\sigma_2\right]\right) \\ &= \text{trace}\left(\mathbf{Q}\int_{-\infty}^{\infty}\int_{-\infty}^{\infty} \mathbf{\Phi}(\sigma_1)\mathbf{B}\mathrm{E}\left[\mathbf{f}(t-\sigma_1)\mathbf{f}^T(t-\sigma_2)\right]\mathbf{B}^T\mathbf{\Phi}^T(\sigma_2)\mathrm{d}\sigma_1\mathrm{d}\sigma_2\right) \end{aligned} \tag{2.33}$$

$\mathrm{E}\left[\mathbf{f}(t-\sigma_1)\mathbf{f}^T(t-\sigma_2)\right]$ contains the correlations in time between the disturbing forces. If these forces are mutually uncorrelated, the matrix is diagonal. If the signals are uncorrelated in time, i.e. for white noise excitation, the matrix is only non-zero if $\sigma_1 = \sigma_2$, in which case, the expectation is a constant matrix, $\mathbf{E}_{\mathbf{f}\mathbf{f}^T}$, multiplied by a delta function, $\delta(\sigma_1 - \sigma_2)$ and equation 2.33 simplifies considerably:

$$J = \text{trace}\left(\mathbf{Q}\int_0^{\infty} \mathbf{\Phi}(\sigma)\mathbf{B}\mathbf{E}_{\mathbf{f}\mathbf{f}^T}\mathbf{B}^T\mathbf{\Phi}^T(\sigma)\mathrm{d}\sigma\right) \tag{2.34}$$

Or:

$$J = \text{trace}\left(\int_0^{\infty} \mathbf{\Phi}^T(\sigma)\mathbf{Q}\mathbf{\Phi}(\sigma)\mathrm{d}\sigma\mathbf{B}\mathbf{E}_{\mathbf{f}\mathbf{f}^T}\mathbf{B}^T\right) \tag{2.35}$$

If the system defined in equation 2.26 is asymptotically stable and the matrix $\mathbf{Q}$ is positive semi-definite, the cost is equal to (Kalman and Bertram (1960)):

$$J = \text{trace}\left(\mathbf{K}\mathbf{B}\mathbf{E}_{\mathbf{f}\mathbf{f}^T}\mathbf{B}^T\right) \tag{2.36}$$

with $\mathbf{K}$ the positive definite solution of the Lyapunov equation:

$$\mathbf{K}\mathbf{A} + \mathbf{A}^T\mathbf{K} + \mathbf{Q} = \mathbf{0} \tag{2.37}$$

It is interesting to note that equation 2.35 is similar to what the cost function would be, if an initial value problem had been considered:

$$\begin{aligned} J &= \int_0^\infty \mathbf{x}_0^T \mathbf{\Phi}^T(t)\mathbf{Q}\mathbf{\Phi}(t)\mathbf{x}_0 \mathrm{d}t \\ &= \mathrm{trace}\left(\int_0^\infty \mathbf{\Phi}^T(t)\mathbf{Q}\mathbf{\Phi}(t)\mathrm{d}t\mathbf{x}_0\mathbf{x}_0^T\right) \end{aligned} \tag{2.38}$$

2.2.2 Frequency domain approach

For the frequency domain calculation, equation 2.35 is used as a starting point:

$$\begin{aligned} J &= \mathrm{trace}\left(\int_{-\infty}^\infty \mathbf{\Phi}^T(\sigma)\mathbf{Q}\mathbf{\Phi}(\sigma)\mathrm{d}\sigma\mathbf{B}\mathbf{E}_{\mathrm{ff}^T}\mathbf{B}^T\right) \\ &= \frac{1}{4\pi^2}\mathrm{trace}\left(\int_{-\infty}^\infty\int_{-\infty}^\infty \mathbf{\Phi}^H(j\omega_1)\mathrm{e}^{-j\omega_1\sigma}\mathrm{d}\omega_1\mathbf{Q}\int_{-\infty}^\infty \mathbf{\Phi}(j\omega_2)\mathrm{e}^{j\omega_2\sigma}\mathrm{d}\omega_2\mathrm{d}\sigma\mathbf{B}\mathbf{E}_{\mathrm{ff}^T}\mathbf{B}^T\right) \\ &= \frac{1}{2\pi}\mathrm{trace}\left(\int_{-\infty}^\infty\int_{-\infty}^\infty \mathbf{\Phi}^H(j\omega_1)\mathbf{Q}\mathbf{\Phi}(j\omega_2)\delta(\omega_2-\omega_1)\mathrm{d}\omega_2\mathrm{d}\omega_1\mathbf{B}\mathbf{E}_{\mathrm{ff}^T}\mathbf{B}^T\right) \\ &= \frac{1}{2\pi}\mathrm{trace}\left(\int_{-\infty}^\infty \mathbf{\Phi}^H(j\omega)\mathbf{Q}\mathbf{\Phi}(j\omega)\mathrm{d}\omega\mathbf{B}\mathbf{E}_{\mathrm{ff}^T}\mathbf{B}^T\right) \end{aligned} \tag{2.39}$$

Where $\mathbf{\Phi}(j\omega)$ is the Fourier transform of $\mathbf{\Phi}(t)$ and can be calculated as:

$$\begin{aligned} \mathbf{\Phi}(j\omega) &= \mathbb{F}\left(\mathbf{\Phi}(t)\right) = \int_0^\infty \mathrm{e}^{\mathbf{A}t}\mathrm{e}^{-j\omega t}\mathrm{d}t \\ &= \int_0^\infty \mathrm{e}^{(\mathbf{A}-j\omega\mathbf{I})t}\mathrm{d}t = (j\omega\mathbf{I}-\mathbf{A})^{-1} \end{aligned} \tag{2.40}$$

That the integral over the time domain of a product of two time signals, is equal to the integral over the frequency domain of the product of the Fourier transforms of the two time signals, is generally known as Plancherel's theorem. If a squared signal is considered, i.e. the product of a time signal with itself, this property is usually referred to as Parseval's theorem.

The argument of the integral in equation 2.39 can also be examined. It is the power spectral density of the cost. Figure 2.6 shows the spectral density of the kinetic energy of the simply supported plate, for a white noise point force acting at two different locations. $\mathbf{E}_{\mathrm{ff}^T}$ has been chosen equal to 1.

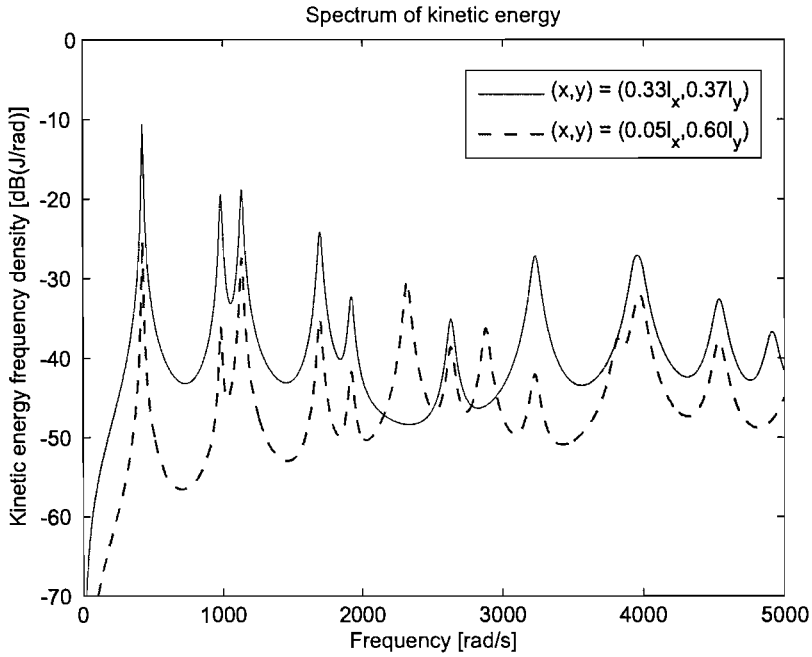

Figure 2.6: Spectrum of kinetic energy of the simply supported plate for white noise excitation at two different locations.

2.3 Effect of disturbance location

It can be seen from the simulation results in figure 2.6 that the location of the excitation influences the value of the cost function. In this analysis, the influence of the location of the excitation is an undesirable complication. It is therefore appropriate to assume an excitation where each point is excited in a similar fashion. A spatially random pressure field would satisfy this criterion and it can be shown that this is equivalent to assuming that the modes of the structure are excited equally, but in an uncorrelated fashion. This can be proved by analysing the correlation between the excitation of the diffferent modes:

Equations 2.4, 2.12 and 2.22 describe how the modes of the different models are excited by point forces. Consider now the excitation of a single mode mn of the simply supported plate, by a pressure field, $p(x, y)$. This excitation is denoted as $f_{mn}(t)$ and is calculated through:

$$f_{mn}(t) = \int_0^{l_y} \int_0^{l_x} \psi_{mn}(x, y) p(x, y, t) \mathrm{d}x \mathrm{d}y \tag{2.41}$$

The correlation between a mode kl and mode mn then is:

$$\begin{aligned} \mathrm{E}\left[f_{kl}f_{mn}\right] &= \mathrm{E}\left[\int_0^{l_y}\int_0^{l_x}\psi_{kl}(x_1,y_1)p(x_1,y_1,t)\mathrm{d}x_1\mathrm{d}y_1 \right. \\ &\quad \left. \int_0^{l_y}\int_0^{l_x}\psi_{mn}(x_2,y_2)p(x_2,y_2,t)\mathrm{d}x_2\mathrm{d}y_2\right] \\ &= \int_0^{l_y}\int_0^{l_x}\int_0^{l_y}\int_0^{l_x}\psi_{kl}(x_1,y_1)\psi_{mn}(x_2,y_2) \\ &\quad \mathrm{E}\left[p(x_1,y_1,t)p(x_2,y_2,t)\right]\mathrm{d}x_1\mathrm{d}y_1\mathrm{d}x_2\mathrm{d}y_2 \end{aligned} \tag{2.42}$$

For a spatially random pressure field, there is no correlation between the pressures at two different locations. This means that $\mathrm{E}\left[p(x_1,y_1,t)p(x_2,y_2,t)\right]$ is equal to $\delta(x_1-x_2)\delta(y_1-y_2)\mathrm{E}\left[p(x_1,y_1,t)^2\right]$. It is furthermore assumed that $\mathrm{E}\left[p(x,y,t)^2\right]$ is constant for different (x,y). Equation 2.42 can then be rewritten as:

$$\begin{aligned} \mathrm{E}\left[f_{kl}f_{mn}\right] &= \int_0^{l_y}\int_0^{l_x}\psi_{kl}(x,y)\psi_{mn}(x,y)\mathrm{E}\left[p(x,y,t)^2\right]\mathrm{d}x\mathrm{d}y \\ &= \int_0^{l_y}\int_0^{l_x}\psi_{kl}(x,y)\psi_{mn}(x,y)\mathrm{d}x\mathrm{d}y\mathrm{E}\left[p(x,y,t)^2\right] \end{aligned} \tag{2.43}$$

For the assumed, orthogonal modeshapes, the integral $\int_0^{l_y}\int_0^{l_x}\psi_{kl}(x,y)\psi_{mn}(x,y)\mathrm{d}x\mathrm{d}y$ is non-zero only if $kl=mn$, when it is equal to S_uN_{mn}, where S_u is the surface area of the object. The corresponding matrix $\mathbf{B}_m$ for the modal forces is equal to:

$$\mathbf{B}_m = \frac{1}{M}\begin{pmatrix} 0 \\ \mathbf{N}^{-1} \end{pmatrix} \tag{2.44}$$

If the pressure field is assumed to have a white spectrum in time, as well as space, then equations 2.43 and 2.35 can be combined:

$$J = \mathrm{trace}\left(\int_0^{\infty}\mathbf{\Phi}^T(\sigma)\mathbf{Q}\mathbf{\Phi}(\sigma)\mathrm{d}\sigma\mathbf{P}_w\right) \tag{2.45}$$

with

$$\mathbf{P}_w = \frac{1}{M^2}S_u\begin{bmatrix} 0 & 0 \\ 0 & \mathbf{N}^{-1} \end{bmatrix}\mathrm{E}\left[p(x,y,t)^2\right] \tag{2.46}$$

For the beam, $S_u = L$ and $\mathrm{E}\left[p(x,y,t)^2\right]$ has been chosen equal to $2/L$. For the simply supported plate, $S_u = l_xl_y$ and the expectation $\mathrm{E}\left[p(x,y,t)^2)\right]$ was chosen to be equal to $4/l_xl_y$ $[N^2/m^4]$. For the CFCF plate, $S_u = l_xl_y$ and $\mathrm{E}\left[p(x,y,t)^2)\right]$ has been chosen equal to $1/l_xl_y$ instead.

Figure 2.7 shows the spectrum of the kinetic energy of the simply supported plate, excited by a randomly distributed, white noise excitation.

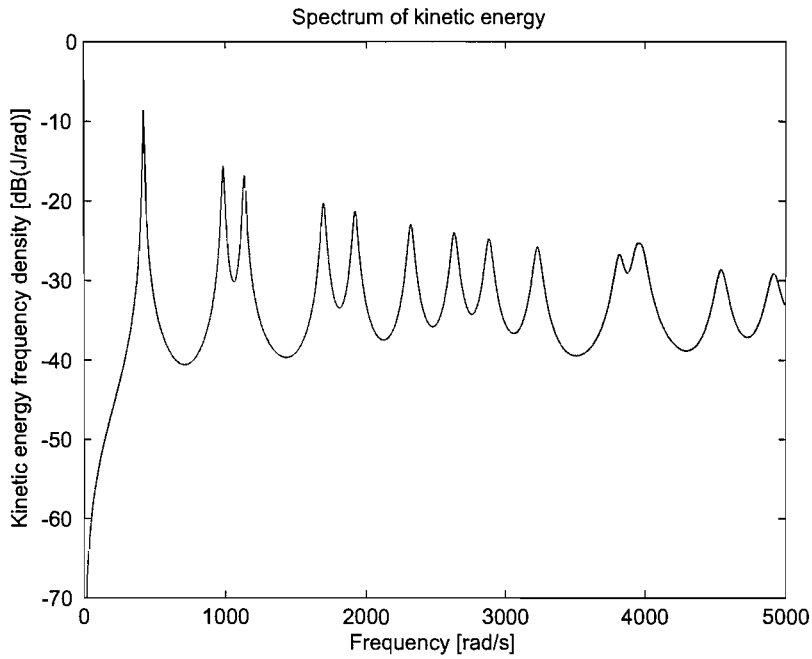

Figure 2.7: Spectrum of kinetic energy of the simply supported plate for a randomly distributed white noise excitation.

If the excitation has a non-white spectrum, but is still a random signal, it can be approximated by assuming that the excitation is a white signal filtered through a frequency shaping filter. The states of this filter should than be included in the model dynamics. However, for 'red' noise (time-integrated white noise) excitation on a structure where velocity sensors are used and the cost function is derived from the modal velocities, it can be shown that the shaping of the white noise can also be done without adding extra states. The way in which this can be achieved is shown in figures 2.8(a) to 2.8(c).

Mathematically, this is equivalent to using the following matrix instead of $\mathbf{P}_w$ to calculate the cost:

$$\mathbf{P}_r = \frac{1}{M^2} S_u \begin{bmatrix} \mathbf{K}_s^{-T}\mathbf{N}^{-1}\mathbf{K}_s^{-1}\mathrm{E}\left[\mathbf{f}_w\mathbf{f}_w^T\right] & \mathbf{0} \\ \mathbf{0} & \mathbf{0} \end{bmatrix} \tag{2.47}$$

where $\mathbf{K}_s$ is the part of the matrix in equation 2.25 and should not be confused with the solution of Lyapunov equation 2.37. Note that, though the integrated white noise signal will tend to infinity at low frequencies, the response of the system in terms of modal velocity tends to 0. In section 2.2.1 it was shown that the cost function can be evaluated using a solution of Lyapunov equation 2.37 as long as the

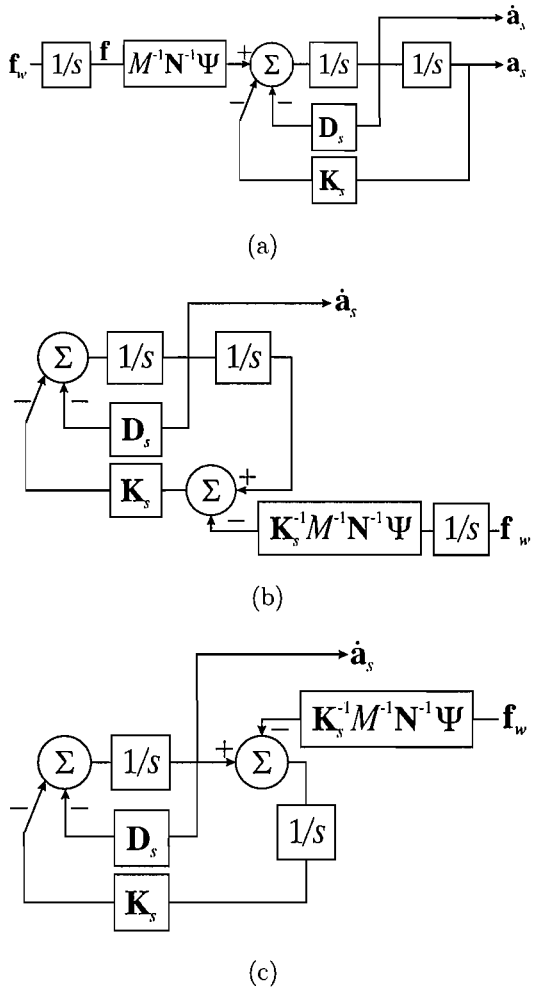

Figure 2.8: Equivalent ways of modeling red noise acting on the system.

system is asymptotically stable. Using this Lyapunov equation, it is found that the cost function remains bounded for a red noise excitation.

2.4 Effects of number of modes on the model and frequency range of interest

The number of modes taken into account increases the computational load in any optimisation process. Thus the number of modes must be limited. However, the number of modes included in the model must be sufficient to allow a realistic modeling of the beam, such that spillover through the controller to the unmodelled modes

is limited.

The rate of change in time and space for a white, randomly distributed pressure field would be infinite. This is not physically realisable. A limit on the maximum rate of change limits the frequency range of the model's excitation.

This section examines how the number of modes in the model and the number of modes that are excited influence the calculation of the kinetic energy and the power in- and output of the plate. The relations between frequency range, kinetic energy and power is also examined.

2.4.1 Calculation of power input

The expectation of the power supplied to the modes by a spatially random excitation is the product of the modal velocity and the force acting on the mode and can be written as:

$$\begin{aligned} \mathrm{E}\left[P_{sup}\right] &= \mathrm{E}\left[\sum \dot{a}_{mn}(t) f_{mn}(t)\right] \\ &= \mathrm{E}\left[\dot{\mathbf{a}}(t)^T \mathbf{f}(t)\right] \end{aligned} \tag{2.48}$$

The modal velocities are the convolution of the impulse response of the modes of the system, $\mathbf{\Phi}(t)$, and the disturbance forces on the modes, $\mathbf{f}(t)$:

$$\mathrm{E}\left[P_{sup}\right] = \mathrm{E}\left[\left(\mathbf{f}^T(t) * \mathbf{B}_m^T \mathbf{\Phi}^T(t) \mathbf{C}_m^T\right) \mathbf{f}(t)\right] \tag{2.49}$$

where the matrix $\mathbf{C}_m$ selects the modal velocities from the state vector according to:

$$\dot{\mathbf{a}} = \mathbf{C}_m \mathbf{x} \tag{2.50}$$

In the frequency domain equation 2.49 is equal to:

$$\begin{aligned} \mathrm{E}\left[P_{sup}\right] &= 2\frac{1}{2\pi}\mathrm{E}\left[\mathbb{R}\left(\int_0^\infty (\mathbf{f}(j\omega)^H \mathbf{B}_m^T \mathbf{\Phi}^H(j\omega)) \mathbf{C}_m^T \mathbf{f}(j\omega) \mathrm{d}\omega\right)\right] \\ &= 2\frac{1}{2\pi}\mathbb{R}\left(\mathrm{trace}\left(\int_0^\infty \mathbf{B}_m^T \mathbf{\Phi}^H(j\omega) \mathbf{C}_m^T \mathrm{E}\left[\mathbf{f}(j\omega)\mathbf{f}^H(j\omega)\right] \mathrm{d}\omega\right)\right) \end{aligned} \tag{2.51}$$

Where $\mathbb{R}$ denotes a function taking the real part of the complex variables of its arguments. If the forces are white in their spectrum, it has already been seen that

this is equal to:

$$\mathrm{E}\left[P_{sup}\right] = 2\frac{1}{2\pi}\mathrm{trace}\left(\mathbb{R}\left(\int_0^\infty \mathbf{B}_m^T \mathbf{\Phi}^H(j\omega)\mathbf{C}_m^T \mathbf{P}_w \mathrm{d}\omega\right)\right) \tag{2.52}$$

Solving this equation requires an integration over all frequencies.

One can also see that, in a steady state situation, the power input must be equal to the total power lost. If no power is absorbed in a controller, power lost to structural damping in the modes must equal the power input into the system. Power loss can be calculated by multiplying the modal velocities with the modal damping forces. The modal damping force is equal to the modal velocity, multiplied by the modal damping forces, $\mathbf{f}_{sd}$. The modal damping forces are related to the the modal velocities as:

$$\mathbf{f}_{sd} = M\mathbf{N}\mathbf{D}_s\dot{\mathbf{a}}_s \tag{2.53}$$

where $\mathbf{D}$ is the same matrix as in equation 2.25. For the power absorbed in the structure we can then write:

$$\begin{aligned} \mathrm{E}\left[P_{abs}\right] &= \mathrm{E}\left[\dot{\mathbf{a}}_s^T(t)\mathbf{f}_{sd}(t)\right] \\ &= \mathrm{E}\left[\dot{\mathbf{a}}_s^T(t)M\mathbf{N}\mathbf{D}_s\dot{\mathbf{a}}_s\right] \end{aligned} \tag{2.54}$$

The modal velocities can be calculated with the convolution of the impulse-response of the states and the excitation forces:

$$\begin{aligned} \mathrm{E}\left[P_{abs}\right] &= \left[\dot{\mathbf{a}}_s^T(t)M\mathbf{N}\mathbf{D}_s\dot{\mathbf{a}}_s\right] \\ &= M\mathrm{E}\left[\int_0^\infty \mathbf{f}^T(\sigma_1)\mathbf{B}_m^T\mathbf{\Phi}^T(t-\sigma_1)\mathbf{C}_m^T\mathrm{d}\sigma_1\mathbf{N}\mathbf{D}_s\int_0^\infty \mathbf{C}_m\mathbf{\Phi}(t-\sigma_2)\mathbf{B}_m\mathbf{f}(\sigma_2)\mathrm{d}\sigma_2\right] \\ &= M\mathrm{trace}\left[\int_0^\infty\int_0^\infty \mathbf{\Phi}^T(t-\sigma_1)\mathbf{C}_m^T\mathbf{N}\mathbf{D}_s\mathbf{C}_m\mathbf{\Phi}(t-\sigma_2)\delta(\sigma_1-\sigma_2)\mathbf{P}\mathrm{d}\sigma_1\mathrm{d}\sigma_2\right] \\ &= M\mathrm{trace}\left[\int_0^\infty \mathbf{\Phi}^T(t)\mathbf{C}_m^T\mathbf{N}\mathbf{D}_s\mathbf{C}_m\mathbf{\Phi}(t)\mathrm{d}t\mathbf{P}\right] \end{aligned} \tag{2.55}$$

This equation is similar to equation 2.35 and is thus equal to:

$$\mathrm{E}\left[P_{abs}\right] = \mathrm{trace}\left[\mathbf{K}\mathbf{P}\right] \tag{2.56}$$

with $\mathbf{K}$ the positive semi-definite solution of:

$$\mathbf{K}\mathbf{A}_c + \mathbf{A}_c^T\mathbf{K} + \mathbf{Q}_{abs\ struct} = 0 \tag{2.57}$$

where $\mathbf{Q}_{abs\ struct}$ is equal to:

$$\mathbf{Q}_{abs\ struct} = M\begin{bmatrix} 0 & 0 \\ 0 & \mathbf{N}\mathbf{D}_s \end{bmatrix} \tag{2.58}$$

f_{max}	N	$P[t]$	P[1 kHz]	P[2 kHz]	P[3 kHz]	P[4 kHz]	P[5 kHz]
1 kHz	25	25.00	24.65	*24.93*	24.95	24.96	24.96
2 kHz	35	35.00	24.73	*34.67*	34.87	34.91	34.92
3 kHz	43	43.00	24.73	34.89	42.59	42.82	42.86
4 kHz	50	50.00	24.73	34.90	42.87	49.44	49.76
5 kHz	56	56.00	24.73	*34.91*	42.89	49.67	55.35
f_{max}	N	$J[t]$	J[1 kHz]	J[2 kHz]	J[3 kHz]	J[4 kHz]	J[5 kHz]
1 kHz	25	4.067	4.030	4.032	4.032	4.032	4.032
2 kHz	35	4.095	4.030	4.059	4.060	4.060	4.060
3 kHz	43	4.108	4.030	4.059	4.072	4.073	4.073
4 kHz	50	4.117	4.030	4.059	4.073	4.080	4.081
5 kHz	56	4.122	4.030	4.059	4.073	4.081	4.086

Table 2.5: Expected total power supplied to the simply supported *beam*, $P[t]$, and the expected total kinetic energy, $J[t]$, together with the power and kinetic energy in the bandwidth up to 1 kHz to 5 kHz (P[1 kHz], P[2 kHz], etc. and J[1 kHz], J[2 kHz], etc.) for a varying number of modes N.

This method of calculation saves the rather numerically intensive process of integrating over all frequencies.

2.4.2 Results for power input and kinetic energy

Table 2.5 lists the calculated power supplied to the simply supported beam, calculated with both the time and frequency approach of calculation. The frequency integral was approximated by summing the results per frequency over limited frequency ranges. The power supplied to the beam has been calculated for different frequencies, f_{max}, up to which all modes with a resonance frequency below f_{max} have been taken into account. All modes are assumed to be excited by the random pressure field. In the same table, the appropriate expected kinetic energy has also been listed. This too has been calculated in time domain or the frequency domain.

It can be seen that the total power input, P[t], varies linearly with the number of modes, N, included in the model. However, the total kinetic energy, J[t], varies much more slowly with the number of modes. An initial amount of energy put

into the higher order modes is dissipated more quickly than in the lower order modes, because the damping coefficient ($2\zeta\omega_{mn}$) is higher for the higher order modes. The contribution of the higher order modes to the time-averaged kinetic energy is therefore smaller.

The numerical integration over a limited bandwidth results in differences in the calculated power input and kinetic energy. By reducing the frequency spacing the estimates can be improved. Comparing the power calculated over a 2 kHz frequency range and 25 modes to the power calculated over the same frequency range but with a higher number of modes, say 35 and 56, shows that adding modes to the model with a resonance frequency higher than the frequency range of interest does not improve the calcution of the power estimate much, whereas adding modes with resonance frequencies lower than the frequency range of interest is important to get a good estimate. Vice versa, one could say that the calculation of the total power input is a good approximation of the power input over a limited frequency range, if one excites only the modes in the model with a resonance frequency below the frequency range of interest.

The number of modes per frequency decreases with frequency as approximately $1/\sqrt{\omega}$. The number of modes therefore tends to infinity as f_{max} goes to infinity. For white noise inputs, the power thus also goes to infinity.

Table 2.6 lists the same quantities, but now calculated for the simply supported plate. It shows that the power input is still linearly related to the number of modes taken into account. The kinetic energy varies more than for the simply supported beam and a higher proportion of the kinetic energy is located at higher frequencies. It can also be seen that, unlike the beam, the number of modes per frequency increases with frequency and thus approaches infinity at a much higher rate.

It seems that either the frequency range of interest, or the number of excited modes must be limited, if one is to examine the power flow into the structure. For the kinetic energy the number of modes is much less critical. This makes sense, as the modes that are added are high order modes that damp out faster than the lower order modes.

If one is only examining excitation over a limited frequency range, one can also limit the number of excited modes to that frequency range, because including more

f_{max}	N	$P[t]$	P[1 kHz]	P[2 kHz]	P[3 kHz]	P[4 kHz]	P[5 kHz]
1 kHz	18	192.7	189.0	191.7	192.0	192.1	192.2
2 kHz	39	417.6	190.9	409.2	415.1	415.8	416.1
3 kHz	60	642.5	191.0	416.6	632.0	638.1	639.3
4 kHz	84	899.5	191.0	417.0	644.5	881.2	892.5
5 kHz	106	$1.135 \cdot 10^3$	191.0	417.1	645.1	889.0	$1.110 \cdot 10^3$
f_{max}	N	$J[t]$	J[1 kHz]	J[2 kHz]	J[3 kHz]	J[4 kHz]	J[5 kHz]
1 kHz	18	2.341	2.304	2.318	2.320	2.321	2.321
2 kHz	39	2.965	2.310	2.925	2.939	2.942	2.943
3 kHz	60	3.333	2.311	2.939	3.295	3.306	3.308
4 kHz	84	3.628	2.311	2.939	3.311	3.586	3.599
5 kHz	106	3.835	2.311	2.939	3.312	3.593	3.791

Table 2.6: Expected total power supplied to the simply supported *plate*, $P[t]$, and the expected total kinetic energy, $J[t]$, together with the power and kinetic energy in the bandwidth up to 1 kHz to 5 kHz (P[1 kHz], P[2 kHz], etc. and J[1 kHz], J[2 kHz], etc.) for a varying number of modes N.

modes in the model does not influence the kinetic energy or the power input in that frequency range much. The time domain method of calculating the kinetic energy can then be used as an approximation of integrating over a limited bandwidth.

In this analysis no coupling was present between the modes and adding control may result in energy being transferred between the higher or lower order modes, thus influencing the expectation of the kinetic energy. Also, when one tries to control the model with discrete control locations, one must also make sure that the system has many more degrees of freedom than control locations.

Unless mentioned otherwise, the simulations in this thesis have used the first 50 modes of the simply supported beam, the first 106 modes (all modes up to 5 kHz) of the simply supported plate, and the first 170 modes (all modes up to 3 kHz) of the CFCF plate.

2.5 Summary

This chapter showed how modal models of a simply supported beam and plate can be derived from the differential equations governing an infinitesimal part of the plate or beam and the boundary conditions at the edges of the structure. It was also noted that for the clamped-free-clamped-free plate no analytical functions are known that match the boundary conditions. An appropriate approximation of the modeshapes is used from the literature instead.

It has also been shown that the kinetic energy of the structure can be calculated in both the frequency and the time domain and that the location of the excitation can influence the spectrum of the kinetic energy. The influence of the excitation on the spectrum is considered an unwanted complication and a spatially random distributed pressure field acting on the structure is used instead. This spatially random pressure distribution is equivalent to independent excitations acting on each mode of the structure.

The power input into the structure and the kinetic energy were analysed for this excitation, when different frequency ranges are considered and different numbers of modes are taken into account. It was shown that for a driving pressure field that is completely white in both time and frequency, the power input into the structure would be infinite. If either the frequency range of the excitation or the number of modes is limited, the power input is finite. It was also shown that if one is examining only a limited frequency range, excitation of modes with a higher natural frequency than the frequency range of interest does not significantly influence the power input or the kinetic energy of the structure and can thus be excluded. Furthermore, one can then use the time-domain method of calculating the kinetic energy and power, rather than the frequency domain.

Chapter 3

Single-channel control

This chapter focuses on the design of a single-channel controller. This is because a multi-channel, decentralised controller can also be seen as a combination of a number of single-channel controllers applied to the same structure. The design of the controller is usually confined to the question: *Given the structural and performance parameters, what should the controller do to give optimal performance?* This means that to control the structure optimally, complete knowledge of the structure and the excitation would be necessary. In this section another question is therefore considered: *Can optimal control be approximated on the basis of a small number of parameters?* Chapter 6 will then consider how such parameters can be identified on the basis of the local mobility. The mobility of a particular point of the structure can be defined as the velocity response of a particular point on the structure per unit force.

Section 3.1 considers unconstrained controller design. The controllers examined there are not confined to be causal or stable. This may not be directly relevant for the design of the controller for a broadband application, but can give interesting insights into the fundamental limits of performance. It also should show what phase and gain the controller should be tuned to at a single frequency or what the controller should do if feedforward were possible. It is hoped that this will also give some insight into the relation of optimal control to the structural variables. It will examine both unconstrained feedforward and feedback control to minimise the kinetic energy of a structure.

Under a steady state excitation, there is a balance between the power that enters the system through the disturbance and the dissipation in the system itself through internal damping. The control forces may be able to increase or reduce the power input and can also absorb power themselves. Therefore, minimising the total power input by both disturbance and control forces and maximising the power absorption by the control forces only are considered as possible sub-optimal control strategies. The ideas of examining power in- and output are not new and have also been examined in literature, as discussed in sections 1.2.2.2 and 1.2.2.3. Brennan et al. (1995) compared both strategies for single frequency disturbances in a feedforward set-up on a beam. Maximising power absorption has been examined extensively for both structural and noise control, e.g. Guicking et al. (1989), Elliott et al. (1991), Clark and Cole (1995) and Hirami (1997a,b), though mostly in single frequency applications.

Section 3.2 focuses on stable feedback control strategies and mainly on constant gain, absolute velocity feedback control. As it has only a single parameter to set, i.e. the gain, it is an obvious choice to examine if it may be possible to relate the optimal, or a sub-optimal feedback gain, to locally measurable variables. The performance of the approximations is then compared to that of the optimised constant gain velocity feedback controller and to the performance of an LQG controller.

3.1 Unconstrained optimisation

The unconstrained optimisation of feedforward and feedback controllers are examined in this section. Though they may not be feasible for active control of a broadband disturbance, it sets limits on the absolute performance, and may provide some insight on the dependency on the structural characteristics.

For both feedforward and feedback control, three strategies are examined. The first minimises the total kinetic energy of the structure. The second minimises the total power input by the disturbance and control force into the structure. The third maximises the power absorption by the control force. These latter two control strategies are examined as they might be useful as approximations to minimising the kinetic energy.

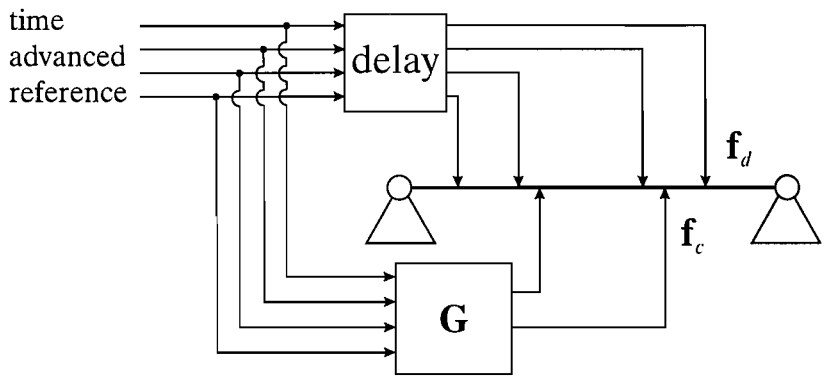

Figure 3.1: Feedforward control of the beam using a time-advanced reference signal.

3.1.1 Feedforward control

This section examines feedforward controllers. The principal of feedforward control is that the control forces, f_c, are calculated using knowledge of the disturbance forces, f_d. In the unconstrained case, this can also be advanced knowledge of what the disturbance forces will be at some later time. This is illustrated in figure 3.1.

The controller requires complete knowledge of the disturbance forces acting on the structure. For a system where disturbances do not act upon the structure at discrete points, this condition may be difficult to meet. Nevertheless the feedforward controllers can serve a reference for the design of a controller, because feedforward control gives an upper bound to the maximum possible reduction in vibration. The feedforward controller thus shows the absolute limitation of performance of the system.

To calculate the optimal control force, an optimality criterion or cost function is required. The optimal feedforward control to minimise the kinetic energy of the system is examined first.

3.1.1.1 Minimum kinetic energy

The kinetic energy (E_{ke}) can be calculated as the sum of the kinetic energy in each of the modes (equations 2.7, 2.14 and 2.24):

$$E_{ke} = \frac{1}{2} M \sum_{n=1}^{\infty} \sum_{m=1}^{\infty} N_{mn} \dot{a}_{mn}^2 \tag{3.1}$$

Where N_{mn} is the integral of the squared modeshape over the surface of the structure and M is the total mass of the structure. Since the response can be approximated with a limited number of terms, this can be written as a finite sum, or in state space notation (equation 2.29):

$$E_{ke} = \mathbf{x}^T \mathbf{Q} \mathbf{x} \tag{3.2}$$

In figure 2.5 and equation 2.26 a general state-space notation was used to describe the excitation of the model due to a set of forces $\mathbf{f}$. Assume now that some of these forces are disturbance forces, $\mathbf{f}_d$, and others are control forces, $\mathbf{f}_c$, attempting to minimise the kinetic energy, as a function of the control forces:

$$\dot{\mathbf{x}} = \mathbf{A}\mathbf{x} + \mathbf{B}_d \mathbf{f}_d(t) + \mathbf{B}_c \mathbf{f}_c(t) \tag{3.3}$$

or, using frequency domain notation:

$$\mathbf{x} = (j\omega \mathbf{I} - \mathbf{A})^{-1} \left(\mathbf{B}_d \mathbf{f}_d(j\omega) + \mathbf{B}_c \mathbf{f}_c(j\omega) \right) \tag{3.4}$$

$$= \mathbf{\Phi}_\omega(j\omega) \left(\mathbf{B}_d \mathbf{f}_d(j\omega) + \mathbf{B}_c \mathbf{f}_c(j\omega) \right) \tag{3.5}$$

Dropping $(j\omega)$ from the notation for brevity, the kinetic energy of the structure can then be calculated as:

$$\begin{aligned} E_{ke}(j\omega) &= \mathbf{x}^H \mathbf{Q} \mathbf{x} \\ &= \left[\mathbf{f}_d^H \mathbf{B}_d^T + \mathbf{f}_c^H \mathbf{B}_c^T \right] \mathbf{\Phi}_\omega^H \mathbf{Q} \mathbf{\Phi}_\omega \left[\mathbf{B}_d \mathbf{f}_d + \mathbf{B}_c \mathbf{f}_c \right] \\ &= \mathbf{f}_d^H \mathbf{B}_d^T \mathbf{\Phi}_\omega^H \mathbf{Q} \mathbf{\Phi}_\omega \mathbf{B}_d \mathbf{f}_d + 2\mathbf{f}_c^H \mathbf{B}_c^T \mathbf{\Phi}_\omega^H \mathbf{Q} \mathbf{\Phi}_\omega \mathbf{B}_d \mathbf{f}_d + \mathbf{f}_c^H \mathbf{B}_c^T \mathbf{\Phi}_\omega^H \mathbf{Q} \mathbf{\Phi}_\omega \mathbf{B}_c \mathbf{f}_c \end{aligned} \tag{3.6}$$

This function is a quadratic function in $\mathbf{f}_c$, which means that, provided $\mathbf{Q}$ is positive definite, there is a global minimum. The control force at this minimum can be found by taking the derivative of equation 3.6 with respect to the control forces and equating it to zero. This leads to a new set of equations:

$$0 = 2 \left[\mathbf{B}_c^T \mathbf{\Phi}_\omega^H \mathbf{Q} \mathbf{\Phi}_\omega \mathbf{B}_d \right] \mathbf{f}_d + 2 \left[\mathbf{B}_c^T \mathbf{\Phi}_\omega^H \mathbf{Q} \mathbf{\Phi}_\omega \mathbf{B}_c \right] \mathbf{f}_c \tag{3.7}$$

$$\Downarrow$$

$$\mathbf{f}_c(j\omega) = - \left[\mathbf{B}_c^T \mathbf{\Phi}_\omega^H \mathbf{Q} \mathbf{\Phi}_\omega \mathbf{B}_c \right]^{-1} \left[\mathbf{B}_c^T \mathbf{\Phi}_\omega^H \mathbf{Q} \mathbf{\Phi}_\omega \mathbf{B}_d \right] \mathbf{f}_d(j\omega) \tag{3.8}$$

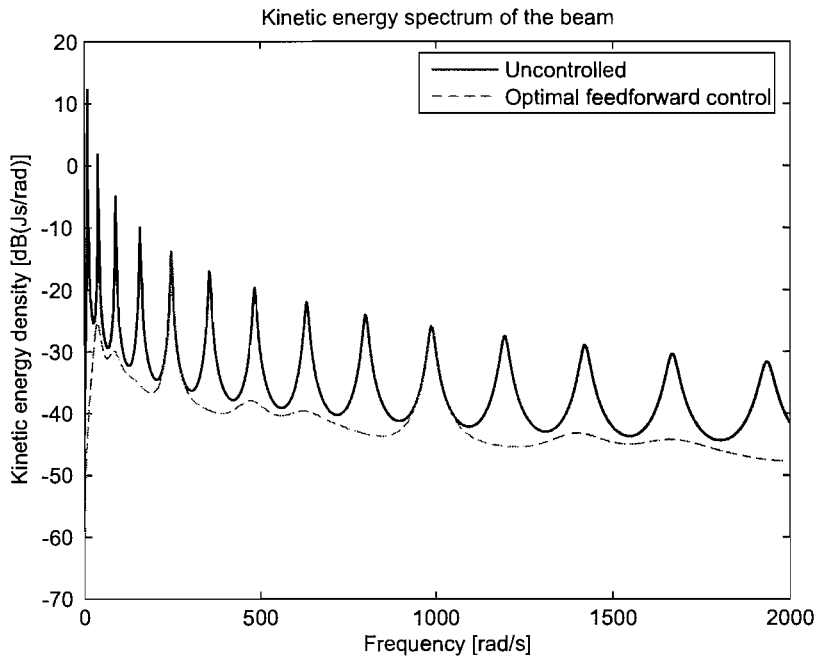

Figure 3.2: Spectrum of the kinetic energy of the beam with and without optimal feedforward control, minimising kinetic energy, excited by a randomly distributed excitation and controlled at 0.6 of the length of the beam.

This feedforward control force minimises the quadratic cost function, for a specific excitation $\mathbf{f}_d(j\omega)$. Note that due to the Hermitian transposes of the impulse responses of the modes, $\mathbf{\Phi}_\omega(j\omega)$, the time domain transformation of the control function is not causal. It would require the knowledge of what the disturbance force is going to do in the future to calculate the control force at any particular point in time. Note also that, for the inverse of $\left[\mathbf{B}_c^T\mathbf{\Phi}_\omega^H\mathbf{Q}\mathbf{\Phi}_\omega\mathbf{B}_c\right]$ to exist, the matrix must have full rank. This implies that both $\mathbf{Q}$ and $\mathbf{\Phi}_\omega$ must have a rank larger than or equal to the number of control locations. Even then, the rank of the matrix may not be sufficient if some modes can not be controlled. This implies that for the optimal solution to the cost function to be unique, both the number of states and the number of states taken into account for the cost function must be larger than the number of control locations.

The spectrum of the kinetic energy of the beam for a randomly distributed excitation, with and without this feedforward control is depicted in figure 3.2. In this case the reference signals are the waveforms of the modal forces described in section 2.3. The beam is controlled with a single point force actuator at 0.6 of the length of the beam.

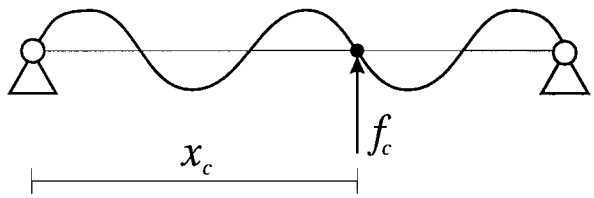

Figure 3.3: Modeshape of the beam for which the control force, f_c, has no influence on the excitation

The figure shows that optimal control reduces the energy density most at resonances. However, there are several resonance frequencies where there is no or very little reduction possible in the kinetic energy. These are frequencies where the dominant modeshapes have a node at the point where the control force is located. This means the control force has no influence on the excitation of those modes. This is illustrated in figure 3.3.

3.1.1.2 Minimum power input

An alternative to minimising the kinetic energy is minimising the total power fed into the system by the disturbance force and the control force. In the steady state situation, the power input into the system is equal to the power dissipated through internal damping. If the damping is viscous, the power dissipated is equal to the modal velocity times the damping force. As the damping force is equal to the damping constant times the modal velocity, the power dissipated in each mode is linearly related to the kinetic energy of that mode, but the constant of proportionality is different for each mode. Thus reducing the power input should also reduce the kinetic energy of the modes. The total power input depends partly on the local behaviour at the control point and therefore might have a strong relation between local behaviour and the control force. The power input to the system can be calculated as:

$$P(t) = \mathbf{f}_d^T(t)\dot{\mathbf{w}}_d(t) + \mathbf{f}_c^T(t)\dot{\mathbf{w}}_c(t) \tag{3.9}$$

Where $\dot{\mathbf{w}}_d$ and $\dot{\mathbf{w}}_c$ are the velocities of the structure at the disturbance and control location respectively. This can also be written in the frequency domain as:

$$\begin{aligned} P(j\omega) &= \mathbb{R}\left(\mathbf{f}_d^H \dot{\mathbf{w}}_d(j\omega) + \mathbf{f}_c^H \dot{\mathbf{w}}_c(j\omega)\right) \\ &= \mathbb{R}\left(\mathbf{f}_d^H \boldsymbol{\Psi}_d^T \dot{\mathbf{a}}(j\omega) + \mathbf{f}_c^H \boldsymbol{\Psi}_c^T \dot{\mathbf{a}}(j\omega)\right) \\ &= \mathbb{R}\left(\mathbf{f}_d^H \mathbf{C}_d \boldsymbol{\Phi}_\omega(j\omega)\left(\mathbf{B}_d \mathbf{f}_d + \mathbf{B}_c \mathbf{f}_c\right) + \mathbf{f}_c^H \mathbf{C}_c \boldsymbol{\Phi}_\omega(j\omega)\left(\mathbf{B}_d \mathbf{f}_d + \mathbf{B}_c \mathbf{f}_c\right)\right) \end{aligned} \tag{3.10}$$

Where $\dot{\mathbf{w}}_d$ and $\dot{\mathbf{w}}_c$ are the velocities in the frequency- domain at locations of the primary and secondary respectively. In equation 3.10 $\mathbf{C}_d \boldsymbol{\Phi}_\omega(j\omega)\mathbf{B}_d$ is the mobility matrix $\mathbf{Y}_{dd}$, which is the response of the velocity of the structure at x_d to the forces at that same point. For the control locations, a different mobility matrix, $\mathbf{Y}_{cc}$, can be derived. For the cross terms, cross mobility matrices $\mathbf{Y}_{cd}$ and $\mathbf{Y}_{dc}$ are defined. $\mathbf{Y}_{cd}$ and $\mathbf{Y}_{dc}$ are each other's transpose. Using the mobility matrices in equation 3.10 and splitting the functions in their real and imaginary parts results in:

$$P(j\omega) = \mathbb{R}\left(\mathbf{f}_d^H \mathbf{Y}_{dd} \mathbf{f}_d + \mathbf{f}_d^H \mathbf{Y}_{cd} \mathbf{f}_c + \mathbf{f}_c^H \mathbf{Y}_{dc} \mathbf{f}_d + \mathbf{f}_c^H \mathbf{Y}_{cc} \mathbf{f}_c\right) \tag{3.11}$$

$$\begin{aligned} &= \mathbb{R}\left(\mathbf{f}_d\right)^T \mathbb{R}\left(\mathbf{Y}_{dd}\right) \mathbb{R}\left(\mathbf{f}_d\right) + \mathbb{I}\left(\mathbf{f}_d\right)^T \mathbb{R}\left(\mathbf{Y}_{dd}\right) \mathbb{I}\left(\mathbf{f}_d\right) \\ &\quad + 2\mathbb{R}\left(\mathbf{f}_c\right)^T \mathbb{R}\left(\mathbf{Y}_{dc}\right) \mathbb{R}\left(\mathbf{f}_d\right) + 2\mathbb{I}\left(\mathbf{f}_c\right)^T \mathbb{R}\left(\mathbf{Y}_{dc}\right) \mathbb{I}\left(\mathbf{f}_d\right) \\ &\quad + \mathbb{R}\left(\mathbf{f}_c\right)^T \mathbb{R}\left(\mathbf{Y}_{cc}\right) \mathbb{R}\left(\mathbf{f}_c\right) + \mathbb{I}\left(\mathbf{f}_c\right)^T \mathbb{R}\left(\mathbf{Y}_{cc}\right) \mathbb{I}\left(\mathbf{f}_c\right) \end{aligned} \tag{3.12}$$

This is a quadratic equation which can be minimised in the same way as described in section 3.1.1.1 if $\mathbb{R}\left(\mathbf{Y}_{cc}\right) > 0$. For a passive system, the real part of the mobility is always larger than zero, otherwise power extraction from the system would be possible. That would imply that a power source is present in the system, which can not be the case for a passive system. The minimisation leads to the following equation for the control force:

$$\mathbf{f}_{c\,opt}(j\omega) = -\mathbb{R}\left(\mathbf{Y}_{cc}\right)^{-1} \mathbb{R}\left(\mathbf{Y}_{dc}\right) \mathbf{f}_d \tag{3.13}$$

Note that for this solution to be unique, the mobility matrix may not be rank-deficient. By using this control force, the response at each frequency can be calculated. In figure 3.4(a), the spectrum of the kinetic energy of the beam has been depicted before control and when the total power input is minimised. The results that were obtained by minimising the kinetic energy are also depicted. The excitation was again assumed to be randomly distributed and to have a white spectrum. The close-up on a small portion of the frequency-range in figure 3.4(b) shows that the kinetic energy is not reduced as much when the kinetic energy is minimised. However, the differences are minimal.

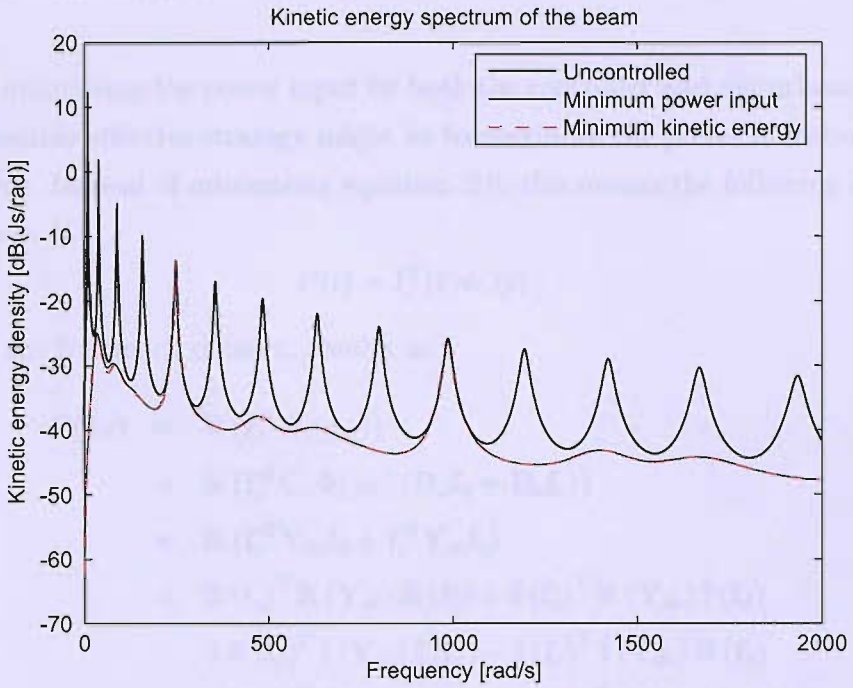

(a) Full frequency range

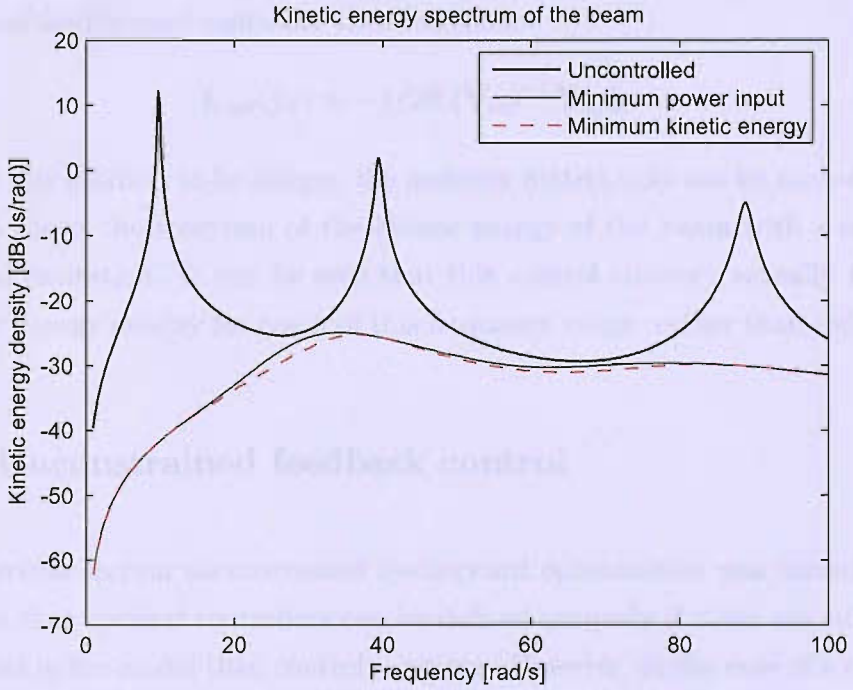

(b) Zoom

Figure 3.4: Spectrum of the kinetic energy of the beam with and without control minimising the total power input into the beam, excited by a randomly distributed excitation and controlled at 0.6 of the length of the beam.

3.1.1.3 Maximum power absorbed by controller

Instead of minimising the power input by both the controller and disturbance forces, another possible effective strategy might be to maximise the power absorbed by the control force. Instead of minimising equation 3.9, this means the following equation is minimised:

$$P(t) = \mathbf{f}_c^T(t)\dot{\mathbf{w}}_c(t) \tag{3.14}$$

Which, in the frequency domain, results in:

$$\begin{aligned} P(j\omega) &= \mathbb{R}\left(\mathbf{f}_c^H \dot{\mathbf{w}}_c(j\omega)\right) \\ &= \mathbb{R}\left(\mathbf{f}_c^H \mathbf{C}_c \mathbf{\Phi}(j\omega)\left(\mathbf{B}_d \mathbf{f}_d + \mathbf{B}_c \mathbf{f}_c\right)\right) \\ &= \mathbb{R}\left(\mathbf{f}_c^H \mathbf{Y}_{dc} \mathbf{f}_d + \mathbf{f}_c^H \mathbf{Y}_{cc} \mathbf{f}_c\right) \\ &= \mathbb{R}\left(\mathbf{f}_c\right)^T \mathbb{R}\left(\mathbf{Y}_{dc}\right) \mathbb{R}\left(\mathbf{f}_d\right) + \mathbb{I}\left(\mathbf{f}_c\right)^T \mathbb{R}\left(\mathbf{Y}_{dc}\right) \mathbb{I}\left(\mathbf{f}_d\right) \\ &\quad + \mathbb{R}\left(\mathbf{f}_c\right)^T \mathbb{I}\left(\mathbf{Y}_{dc}\right) \mathbb{I}\left(\mathbf{f}_d\right) - \mathbb{I}\left(\mathbf{f}_c\right)^T \mathbb{I}\left(\mathbf{Y}_{dc}\right) \mathbb{R}\left(\mathbf{f}_d\right) \\ &\quad + \mathbb{R}\left(\mathbf{f}_c\right)^T \mathbb{R}\left(\mathbf{Y}_{cc}\right) \mathbb{R}\left(\mathbf{f}_c\right) + \mathbb{I}\left(\mathbf{f}_c\right)^T \mathbb{R}\left(\mathbf{Y}_{cc}\right) \mathbb{I}\left(\mathbf{f}_c\right) \end{aligned} \tag{3.15}$$

The optimal feedforward controller then becomes:

$$\mathbf{f}_{c\,opt}(j\omega) = -1/2\mathbb{R}\left(\mathbf{Y}_{cc}\right)^{-1} \mathbf{Y}_{dc}^* \mathbf{f}_d \tag{3.16}$$

Again for this solution to be unique, the mobility matrix may not be rank-deficient. Figure 3.5 shows the spectrum of the kinetic energy of the beam with a randomly distributed excitation. It can be seen that this control strategy actually increases the kinetic energy density for much of this frequency range, rather than reducing it.

3.1.2 Unconstrained feedback control

In the previous section unconstrained feedforward optimisation was considered. It was shown that optimal controllers can be defined uniquely if there are sufficiently more modes in the model than control locations. However, in the case of a structure excited by a randomly distributed excitation, the disturbance forces are unlikely to be available as a reference. This section therefore explores the optimisation of feedback controllers, as illustrated in figure 3.6. The optimisation can be considered as: *Given a certain distribution of excitation at a certain frequency, what should the phase and gain of the controller be to optimise the specified cost function?* This

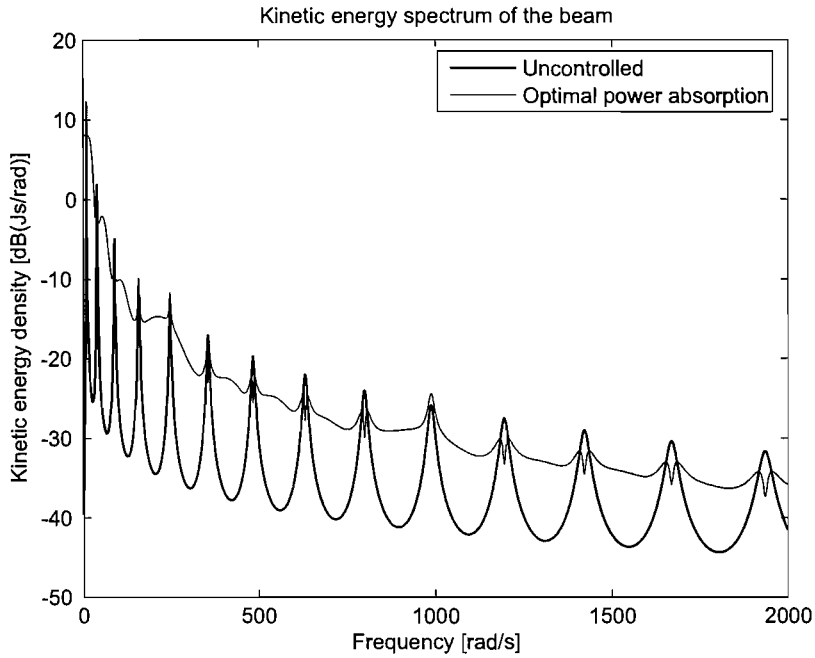

Figure 3.5: Kinetic energy of the beam with and without optimal feedforward control, maximising power absorption, excited by a randomly distributed excitation and controlled at 0.6 of the length of the beam.

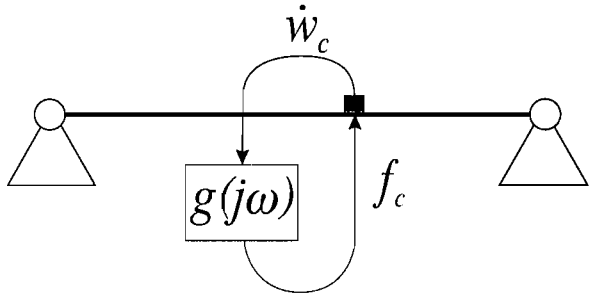

Figure 3.6: Feedback control of the beam

seems very similar to the optimisation of the feedforward controller, but force generated with the feedback controller is constrained to be proportional to the velocity measured at the control point, whereas this was not necessary for the feedforward controller. The results are therefor slightly different. The results are not expected to be feasible for a broadband excitation, but provide an intermediate step between feedforward with complete knowledge of the disturbance and causally constrained feedback control. It is hoped that the optimisation of the different feedback controllers will show a clear relation to the local dynamics.

3.1.2.1 Minimum kinetic energy

In section 3.1.1.1 the kinetic energy as a function of the disturbance and control forces was considered in equations 3.5 and equation 3.6. In a feedback situation the control signal is a function of the velocity at the control point:

$$\begin{aligned}
\mathbf{f}_c(j\omega) &= \mathbf{G}(j\omega)\dot{\mathbf{w}}_c(j\omega) \\
&= \mathbf{G}(j\omega)\mathbf{C}_c\mathbf{x}(j\omega) \\
&= \mathbf{G}(j\omega)\mathbf{C}_c\mathbf{\Phi}_\omega(j\omega)\left(\mathbf{B}_d\mathbf{f}_d(j\omega)+\mathbf{B}_c\mathbf{f}_c(j\omega)\right) \\
&= \left[\mathbf{I}-\mathbf{G}(j\omega)\mathbf{C}_c\mathbf{\Phi}_\omega(j\omega)\mathbf{B}_c\right]^{-1}\mathbf{G}(j\omega)\mathbf{C}_c\mathbf{\Phi}_\omega(j\omega)\mathbf{B}_d\mathbf{f}_d(j\omega) \\
&= \left[\mathbf{I}-\mathbf{G}(j\omega)\mathbf{Y}_{cc}\right]^{-1}\mathbf{G}(j\omega)\mathbf{Y}_{dc}\mathbf{f}_d(j\omega) \qquad (3.17)
\end{aligned}$$

Combining this with equation 3.6 and dropping $(j\omega)$-terms from the notation for brevity results in:

$$\begin{aligned}
E_{ke}(j\omega) &= \left[\mathbf{f}_d^H\mathbf{B}_d^T+\mathbf{f}_c^H\mathbf{B}_c^T\right]\mathbf{\Phi}_\omega^H\mathbf{Q}\mathbf{\Phi}_\omega\left[\mathbf{B}_d\mathbf{f}_d+\mathbf{B}_c\mathbf{f}_c\right] \\
&= \mathbf{f}_d^H\left[\mathbf{B}_d^T+\mathbf{Y}_{dc}^H\mathbf{G}^H\left[\mathbf{I}-\mathbf{G}\mathbf{Y}_{cc}\right]^{-H}\mathbf{B}_c^T\right]\mathbf{\Phi}_\omega^H\mathbf{Q}\mathbf{\Phi}_\omega \\
&\quad\cdot\left[\mathbf{B}_c\left[\mathbf{I}-\mathbf{G}\mathbf{Y}_{cc}\right]^{-1}\mathbf{G}\mathbf{Y}_{dc}+\mathbf{B}_d\right]\mathbf{f}_d \qquad (3.18)
\end{aligned}$$

Differentiating the cost function with respect to the elements of $\mathbf{G}$, and setting the derivative equal to zero results in the following equation:

$$\begin{aligned}
0 &= 2\left[\mathbf{I}-\mathbf{G}\mathbf{Y}_{cc}\right]^{-H}\mathbf{B}_c^T\mathbf{\Phi}_\omega^H\mathbf{Q}\mathbf{\Phi}_\omega\mathbf{B}_d^T\mathbf{f}_d\mathbf{f}_d^H\mathbf{Y}_{dc}^H\left[\mathbf{G}^H\left[\mathbf{I}-\mathbf{G}\mathbf{Y}_{cc}\right]^{-H}\mathbf{Y}_{cc}^H+\mathbf{I}\right] \\
&\quad+2\left[\mathbf{I}-\mathbf{G}\mathbf{Y}_{cc}\right]^{-H}\mathbf{B}_c^T\mathbf{\Phi}_\omega^H\mathbf{Q}\mathbf{\Phi}_\omega\mathbf{B}_c\left[\mathbf{I}-\mathbf{G}\mathbf{Y}_{cc}\right]^{-1}\mathbf{G}\mathbf{Y}_{dc}\mathbf{f}_d\mathbf{f}_d^H\mathbf{Y}_{dc}^H \\
&\quad\cdot\left[\mathbf{G}^H\left[\mathbf{I}-\mathbf{G}\mathbf{Y}_{cc}\right]^{-H}\mathbf{Y}_{cc}^H+\mathbf{I}\right] \qquad (3.19)
\end{aligned}$$

This equation is not a linear equation like equation 3.7. This is because equation 3.18 is not a quadratic equation in terms of $\mathbf{G}$. The consequence of this is that there may be more than one solution $\mathbf{G}$ that satisfies equation 3.19. It is found though that only one of the solutions corresponds to a minimum in the cost surface.

For brevity in notation, the following matrices are defined:

$$\begin{aligned}
\mathbf{\Xi}_1 &= \mathbf{B}_c^T\mathbf{\Phi}_\omega^H\mathbf{Q}\mathbf{\Phi}_\omega\mathbf{B}_d\mathbf{f}_d\mathbf{f}_d^H\mathbf{Y}_{dc}^H \\
\mathbf{\Xi}_2 &= \mathbf{B}_c^T\mathbf{\Phi}_\omega^H\mathbf{Q}\mathbf{\Phi}_\omega\mathbf{B}_c \\
\mathbf{\Xi}_3 &= \mathbf{Y}_{dc}\mathbf{f}_d\mathbf{f}_d^H\mathbf{Y}_{dc}^H
\end{aligned}$$

provided that the inverses of Ξ_2 and $\left[\Xi_3 - \mathbf{Y}_{cc}\Xi_2^{-1}\Xi_1\right]$ exist, the solution of equation 3.19, corresponding to a minimum in the function is given by:

$$\mathbf{G} = -\Xi_2^{-1}\Xi_1\left[\Xi_3 - \mathbf{Y}_{cc}\Xi_2^{-1}\Xi_1\right]^{-1} \tag{3.20}$$

Equation 3.20 still contains the actual disturbance forces $\mathbf{f}_d$. To obtain a defined gain that is independent on the actual force, a randomly distributed pressure excitation is assumed. As explained in section 2.3 this results in independent excitation of each of the modes. In equation 3.19, $\left[\mathbf{B}_d\mathbf{f}_d\mathbf{f}_d^H\mathbf{B}_d^T\right]$ is then changed to an expectation, $\mathbf{P}$ of the excitation of the modes. In a single-channel analysis this results in:

$$g = -\frac{\mathbf{B}_c^T\mathbf{\Phi}_\omega^H\mathbf{Q}\mathbf{\Phi}_\omega\mathbf{P}\mathbf{\Phi}_\omega^H\mathbf{B}_c}{\mathbf{B}_c^T\mathbf{\Phi}_\omega\mathbf{P}\mathbf{\Phi}_\omega^H\mathbf{B}_c\mathbf{B}_c^T\mathbf{\Phi}_\omega^H\mathbf{Q}\mathbf{\Phi}_\omega\mathbf{B}_c - Y_{cc}\mathbf{B}_c^T\mathbf{\Phi}_\omega^H\mathbf{Q}\mathbf{\Phi}_\omega\mathbf{P}\mathbf{\Phi}_\omega^H\mathbf{B}_c} \tag{3.21}$$

Figure 3.7 shows the spectrum of the kinetic energy of the beam with a white, randomly distributed excitation, with this feedback control. Results are similar to, but not quite as good as the feedforward control in equation 3.2.

3.1.2.2 Minimum power input

By combining equation 3.10 and 3.17 the power put into the system can be calculated:

$$\begin{aligned}
P(j\omega) &= \mathbb{R}\left(\mathbf{f}_d^H\mathbf{C}_d\mathbf{\Phi}_\omega\left(\mathbf{B}_d\mathbf{f}_d + \mathbf{B}_c\mathbf{f}_c\right) + \mathbf{f}_c^H\mathbf{C}_c\mathbf{\Phi}_\omega\left(\mathbf{B}_d\mathbf{f}_d + \mathbf{B}_c\mathbf{f}_c\right)\right) \\
&= \mathbb{R}\left(\mathbf{f}_d^H\mathbf{Y}_{dd}\mathbf{f}_d + \mathbf{f}_d^H\mathbf{Y}_{cd}\mathbf{f}_c + \mathbf{f}_c^H\mathbf{Y}_{dc}\mathbf{f}_d + \mathbf{f}_c^H\mathbf{Y}_{cc}\mathbf{f}_c\right) \\
&= \mathbb{R}\left(\mathbf{f}_d^H\mathbf{Y}_{dd}\mathbf{f}_d + \mathbf{f}_d^H\mathbf{Y}_{cd}\left[\mathbf{I} - \mathbf{G}\mathbf{Y}_{cc}\right]^{-1}\mathbf{G}\mathbf{Y}_{dc}\mathbf{f}_d\right. \\
&\quad + \mathbf{f}_d^H\mathbf{Y}_{dc}^H\mathbf{G}^H\left[\mathbf{I} - \mathbf{G}\mathbf{Y}_{cc}\right]^{-H}\mathbf{Y}_{dc}\mathbf{f}_d \\
&\quad \left. + \mathbf{f}_d^H\mathbf{Y}_{dc}^H\mathbf{G}^H\left[\mathbf{I} - \mathbf{G}\mathbf{Y}_{cc}\right]^{-H}\mathbf{Y}_{cc}\left[\mathbf{I} - \mathbf{G}\mathbf{Y}_{cc}\right]^{-1}\mathbf{G}\mathbf{Y}_{dc}\mathbf{f}_d\right)
\end{aligned} \tag{3.22}$$

Taking the derivative with respect to the elements of the feedback gain matrix $\mathbf{G}$ of this cost function results in:

$$\begin{aligned}
\frac{\partial P(j\omega)}{\partial \mathbf{G}^H} &= 2\left[\mathbf{I} - \mathbf{G}\mathbf{Y}_{cc}\right]^{-H}\left[\mathbb{R}(\mathbf{Y}_{dc})\mathbf{f}_d\mathbf{f}_d^H\mathbf{Y}_{dc}\right. \\
&\quad + \mathbb{R}(\mathbf{Y}_{cc})\left[\mathbf{I} - \mathbf{G}\mathbf{Y}_{cc}\right]^{-1}\mathbf{G}\mathbb{R}\left(\mathbf{Y}_{dc}\mathbf{f}_d\mathbf{f}_d^H\mathbf{Y}_{dc}^H\right)\left.\right] \\
&\quad \cdot\left[\mathbf{G}^H\left[\mathbf{I} - \mathbf{G}\mathbf{Y}_{cc}\right]^{-H}\mathbf{Y}_{cc}^H + \mathbf{I}\right] \\
&\quad + 2\left[\mathbf{I} - \mathbf{G}\mathbf{Y}_{cc}\right]^{-H}\mathbb{I}(\mathbf{Y}_{cc})\left[\mathbf{I} - \mathbf{G}\mathbf{Y}_{cc}\right]^{-1}\mathbf{G}\mathbb{I}\left(\mathbf{Y}_{dc}\mathbf{f}_d\mathbf{f}_d^H\mathbf{Y}_{dc}^H\right) \\
&\quad \cdot\left[\mathbf{G}^H\left[\mathbf{I} - \mathbf{G}\mathbf{Y}_{cc}\right]^{-H}\mathbf{Y}_{cc}^H + \mathbf{I}\right]
\end{aligned} \tag{3.23}$$

This is not easily solved, unless $\mathbb{I}\left(\mathbf{Y}_{dc}\mathbf{f}_d\mathbf{f}_d^H\mathbf{Y}_{dc}^H\right) = \mathbf{0}$, in which case the solution is given by:

$$\mathbf{G} = -\mathbb{R}(\mathbf{Y}_{cc})^{-1}\mathbb{R}(\mathbf{Y}_{dc})\mathbf{f}_d\mathbf{f}_d^H\mathbf{Y}_{dc}^H\left[\mathbb{R}\left(\mathbf{Y}_{dc}\mathbf{f}_d\mathbf{f}_d^H\mathbf{Y}_{dc}^H\right) - \mathbf{Y}_{cc}\mathbb{R}(\mathbf{Y}_{cc})^{-1}\mathbb{R}(\mathbf{Y}_{dc})\mathbf{f}_d\mathbf{f}_d^H\mathbf{Y}_{dc}^H\right]^{-1} \tag{3.24}$$

This is only true if the required inverses exist, otherwise the solution is not uniquely defined. Note that for the randomly distributed excitation, $\mathbb{I}\left(\mathbf{Y}_{dc}\mathbf{f}_d\mathbf{f}_d^H\mathbf{Y}_{dc}^H\right)$ is indeed equal to $\mathbf{0}$. In a single-channel case the solution can be simplified to:

$$G = -\frac{\mathbf{B}_c^T\mathbb{R}(\mathbf{\Phi}_\omega)\mathbf{P}\mathbf{\Phi}_\omega^H\mathbf{B}_c}{\mathbb{R}(Y_{cc})\mathbf{B}_c^T\mathbf{\Phi}_\omega\mathbf{P}\mathbf{\Phi}_\omega^H\mathbf{B}_c - Y_{cc}\mathbf{B}_c^T\mathbb{R}(\mathbf{\Phi}_\omega)\mathbf{P}\mathbf{\Phi}_\omega^H\mathbf{B}_c} \tag{3.25}$$

Figure 3.7 shows the spectrum of the kinetic energy of the beam with a randomly distributed, white noise excitation, with this type of feedback control. As with feedforward control, there is little difference with the optimal minimisation of the kinetic energy.

3.1.2.3 Maximum power absorption

By combining equation 3.15 and 3.17 a feedback control force, maximising power absorption, can be calculated:

$$\begin{aligned} P(j\omega) &= \mathbb{R}\left(\mathbf{f}_c^H\mathbf{C}_c\mathbf{\Phi}_\omega\left(\mathbf{B}_d\mathbf{f}_d + \mathbf{B}_c\mathbf{f}_c\right)\right) \\ &= \mathbb{R}\left(\mathbf{f}_c^H\mathbf{Y}_{dc}\mathbf{f}_d + \mathbf{f}_c^H\mathbf{Y}_{cc}\mathbf{f}_c\right) \\ &= \mathbb{R}\Big(\mathbf{f}_d^H\mathbf{Y}_{dc}^H\mathbf{G}^H\left[\mathbf{I} - \mathbf{G}\mathbf{Y}_{cc}\right]^{-H}\mathbf{Y}_{dc}\mathbf{f}_d \\ &\quad + \mathbf{f}_d^H\mathbf{Y}_{dc}^H\mathbf{G}^H\left[\mathbf{I} - \mathbf{G}\mathbf{Y}_{cc}\right]^{-H}\mathbf{Y}_{cc}\left[\mathbf{I} - \mathbf{G}\mathbf{Y}_{cc}\right]^{-1}\mathbf{G}\mathbf{Y}_{dc}\mathbf{f}_d\Big) \end{aligned} \tag{3.26}$$

Differentiating with respect to the feedback gain matrix gives:

$$\begin{aligned} \frac{\partial P(j\omega)}{\partial \mathbf{G}^H} &= \left[\mathbf{I} - \mathbf{G}\mathbf{Y}_{cc}\right]^{-H}\mathbf{Y}_{dc}\mathbf{f}_d\mathbf{f}_d^H\mathbf{Y}_{dc}\left[\mathbf{G}^H\left[\mathbf{I} - \mathbf{G}\mathbf{Y}_{cc}\right]^{-H}\mathbf{Y}_{cc}^H\mathbf{I}\right] \\ &\quad + 2\left[\mathbf{I} - \mathbf{G}\mathbf{Y}_{cc}\right]^{-H}\mathbb{R}(\mathbf{Y}_{cc})\left[\mathbf{I} - \mathbf{G}\mathbf{Y}_{cc}\right]^{-1}\mathbf{G}\mathbb{R}\left(\mathbf{Y}_{dc}\mathbf{f}_d\mathbf{f}_d^H\mathbf{Y}_{dc}^H\right) \\ &\quad \cdot\left[\mathbf{G}^H\left[\mathbf{I} - \mathbf{G}\mathbf{Y}_{cc}\right]^{-H}\mathbf{Y}_{cc}^H + \mathbf{I}\right] \\ &\quad + 2\left[\mathbf{I} - \mathbf{G}\mathbf{Y}_{cc}\right]^{-H}\mathbb{I}(\mathbf{Y}_{cc})\left[\mathbf{I} - \mathbf{G}\mathbf{Y}_{cc}\right]^{-1}\mathbf{G}\mathbb{I}\left(\mathbf{Y}_{dc}\mathbf{f}_d\mathbf{f}_d^H\mathbf{Y}_{dc}^H\right) \\ &\quad \cdot\left[\mathbf{G}^H\left[\mathbf{I} - \mathbf{G}\mathbf{Y}_{cc}\right]^{-H}\mathbf{Y}_{cc}^H + \mathbf{I}\right] \end{aligned} \tag{3.27}$$

Which is again difficult to solve, unless $\mathbb{I}\left(\mathbf{Y}_{dc}\mathbf{f}_d\mathbf{f}_d^H\mathbf{Y}_{dc}^H\right) = \mathbf{0}$. in which case the solution is:

$$\mathbf{G} = -\left[\mathbf{Y}_{cc}^*\right]^{-1} \tag{3.28}$$

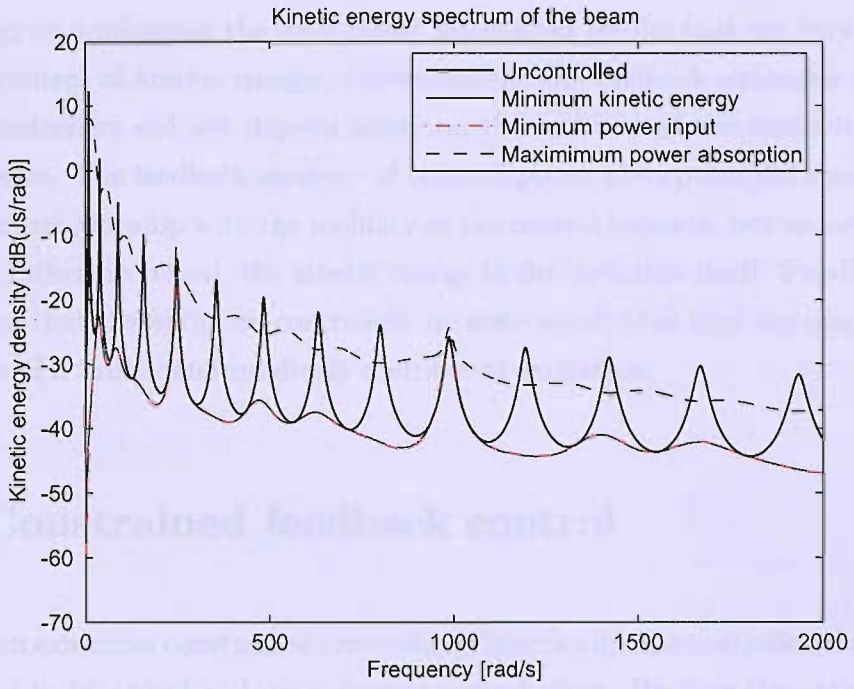

Figure 3.7: Kinetic energy of the beam with and without optimised feedback control, respectively minimising total kinetic energy (thin line), the total power input (dot-dashed line) or maximising the power absorbed by the controller (dashed line), when the beam excited by a randomly distributed excitation and controlled at 0.6 of the length of the beam.

which is the well known case of matched conjugate impedance. This control method shows a very clear relation to the local characteristics of the structure. In a single-channel system:

$$G = -1/Y_{cc}^{*} \tag{3.29}$$

Again, figure 3.7 shows the spectrum of the kinetic energy of the beam with a randomly distributed excitation, with this feedback control. As with feedforward control, maximising the power absorption leads to an overall increase in the kinetic energy.

3.1.3 Summary

It has been shown that, to obtain a unique optimal solution both the number of modes taken into account and the number of independent sources of excitation must be equal to or larger than the number of control locations. It was also seen that

the strategy of minimising the total power input gives results that are very close to optimum control of kinetic energy. Unfortunately, the feedback strategies of either of these controllers did not depend solely on the mobility of the structure at the control points. The feedback strategy of optimal power absorption did show a very clear, direct relationship with the mobility at the control location, but unfortunately increased, rather decreased, the kinetic energy in the structure itself. Finally, it can also be seen that the optimum controllers are non-causal, thus they are inapplicable in the case of a broadband randomly distributed excitation.

3.2 Constrained feedback control

This section examines constrained controllers. Specifically, the controllers have been constrained to be causal and use a limited control effort. Because the optimisation can not be done on a per frequency basis while ensuring stability, the expectation of the cost function will be minimised. Section 2.2.1 described how the expectation of a quadratic cost function can be evaluated for a general state space model. Here, it will be shown how the same techniques can be used to calculate the cost function in a feedback situation.

Doyle et al. (1989) showed a general structure for calculating an optimal dynamic feedback controller to minimise a quadratic cost function. However, Linear Quadratic Gaussian (LQG) control is used as a comparison for the constrained controller, due its simple and easy to comprehend structure. For the design of the LQG controller, the reader is referred to available literature, e.g. Stein and Athans (1987) and Skogestad and Postlethwaite (1996). LQG control uses an internal model of the system to estimate the states of the system. The inputs of the estimator consist of the measured response and the control signal. Though the strategy can perform well in this way in a single-channel system, it is not particulary suitable to use multiple SISO LQG controllers on the same structure, as the other control signals are not available to the estimators at any one point. This would then result in a worse estimation of the states of the model. Furthermore, combinations of differences in modeling might result in instability. Therefore LQG control is considered as a reference rather than as a candidate control strategy for the problem set out in this thesis.

LQG control strategies require control effort weighting as part of the design. As it is undesirable to use very high control efforts and it is desirable to compare control strategies on an even footing by making sure they use the same control effort, the inclusion of control effort weighting in the cost function is considered in section 3.2.1.

To simplify relating the variables of the controller to structural variables, a constant gain, absolute velocity feedback controller is examined in section 3.2.2.

3.2.1 Limitation of control effort

The control effort can be limited by including it in the cost function. The control effort is defined here as the sum of the squared control signals, $\mathbf{u}$. This changes the original cost function for kinetic energy, equation 2.30, to:

$$J = \mathrm{E}\left[\mathbf{x}^T(t)\mathbf{Q}\mathbf{x}(t) + \mathbf{u}^T(t)\mathbf{R}\mathbf{u}(t)\right] \tag{3.30}$$

where $\mathbf{R}$ is a diagonal weighting matrix, introduced to weigh the control effort relative to the cost criterion described by $\mathbf{Q}$. The on-diagonal elements are all chosen to be equal, to weigh the effort at different control locations equally. Other cost functions, such as minimum power input, or maximum power absorption can be similarly adapted, by adding the term $\mathrm{E}\left[\mathbf{u}^T(t)\mathbf{R}\mathbf{u}(t)\right]$ to the relevant function.

3.2.2 Absolute velocity feedback

3.2.2.1 Introduction

Constant gain, absolute velocity feedback has been examined as a control method since some of the earliest publications of active vibration control (Olson (1956), Rockwell and Lawther (1964), Knyazev and Tartakovskii (1965) and Knyazev and Tartakovskii (1967)). This is for its obvious stability advantages, as illustrated by Balas (1979), as well as good performance. Here, a constant gain, absolute velocity feedback is used in a single local control loop, as illustrated in figure 3.8(a) and a the state space diagram in figure 3.8(b). The control signal, u, is the control force f_c. $\mathbf{z}$ are the outputs whose squared, weighted and summed output is equal to the

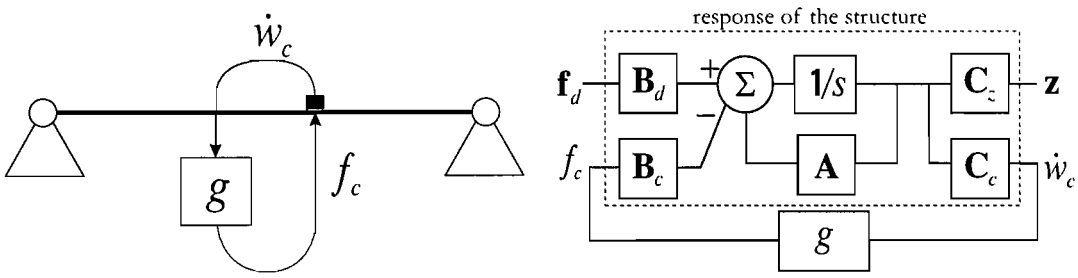

(a) On the structure (b) State space diagram

Figure 3.8: Constant gain velocity feedback control.

cost function, as defined in equation 2.28. In state space notation:

$$\begin{aligned} \dot{\mathbf{x}} &= \mathbf{A}\mathbf{x} + \mathbf{B}_d\mathbf{f}_d(t) + \mathbf{B}_c f_c(t) \\ y &= \mathbf{C}_c\mathbf{x} \\ u &= f_c = -gy; \end{aligned} \tag{3.31}$$

or:

$$\dot{\mathbf{x}} = [\mathbf{A} - \mathbf{B}_c g \mathbf{C}_c]\,\mathbf{x} + \mathbf{B}_d\mathbf{f}_d(t) \tag{3.32}$$

The cost function for kinetic energy, equation 3.30 can then be written as:

$$J_{ke} = \mathrm{E}\left[\mathbf{x}^T(t)\left[\mathbf{Q} + \mathbf{C}_c^T g^T R g \mathbf{C}_c\right]\mathbf{x}(t)\right] \tag{3.33}$$

Where R is the single-channel weighting factor associated with the control effort and $\mathbf{Q}$ is the modal weighting matrix. Using the analysis in sections 2.2 and 2.3 this can also be written as:

$$J_{ke} = \mathrm{trace}\left(\int_0^\infty \mathbf{\Phi}_c^T(\sigma)\left[\mathbf{Q} + \mathbf{C}_c^T g^T R g \mathbf{C}_c\right]\mathbf{\Phi}_c(\sigma)\mathrm{d}\sigma\mathbf{P}\right) \tag{3.34}$$

If this is compared to equation 2.45, the added term due to the control effort is clearly visible. The other difference is that the function $\mathbf{\Phi}(t)$ is replaced by $\mathbf{\Phi}_c(t)$. $\mathbf{\Phi}_c(t)$ is the fundamental transition matrix for the controlled system which is defined as equation 2.32, but the matrix $\mathbf{A}$, which described the uncontrolled system is replaced by the $\mathbf{A}_c$, which describes the dynamics of the controlled system. For this constant gain, output feedback controller, the matrix $\mathbf{A}_c$ is defined as:

$$\mathbf{A}_c = \mathbf{A} - \mathbf{B}_c g \mathbf{C}_c \tag{3.35}$$

Thus, $\mathbf{\Phi}_c(t)$ is:

$$\mathbf{\Phi}_c(t) = \mathrm{e}^{[\mathbf{A}-\mathbf{B}_c g \mathbf{C}_c]t} = \mathrm{e}^{\mathbf{A}_c t} \tag{3.36}$$

For the calculation of minimum power input and maximum power absorption, the cost functions can be written in a similar form to equation 3.34. The power input in a steady state situation is equal to the sum of power dissipated in the structure (equation 2.55) and the power absorbed by the controller (equation 3.14):

$$\begin{aligned} P_{in} &= \mathrm{E}\left[\mathbf{x}^T(t)M\begin{bmatrix} 0 & 0 \\ 0 & \mathbf{N}\mathbf{D}_s \end{bmatrix}\mathbf{x}(t) + f_c(t)^T\dot{w}_c(t)\right] \\ &= \mathrm{E}\left[\mathbf{x}^T(t)\mathbf{Q}_{abs\ struct}\mathbf{x}(t) + \mathbf{x}(t)^T\mathbf{C}_c^T g\mathbf{C}_c\mathbf{x}(t)\right] \end{aligned} \tag{3.37}$$

Including the control effort weighting results in:

$$J_{P\,in} = \mathrm{trace}\left(\int_0^\infty \mathbf{\Phi}_c^T(\sigma)\left[\mathbf{Q}_{abs\ struct} + \mathbf{C}_c^T g\mathbf{C}_c + \mathbf{C}_c^T g^T Rg\mathbf{C}_c\right]\mathbf{\Phi}_c(\sigma)\mathrm{d}\sigma\mathbf{P}\right) \tag{3.38}$$

For the maximisation of the absorbed power by controller, the cost function to maximise would become:

$$J_{P\,abs} = \mathrm{trace}\left(\int_0^\infty \mathbf{\Phi}_c^T(\sigma)\left[\mathbf{C}_c^T g\mathbf{C}_c - \mathbf{C}_c^T g^T Rg\mathbf{C}_c\right]\mathbf{\Phi}_c(\sigma)\mathrm{d}\sigma\mathbf{P}\right) \tag{3.39}$$

The control effort has been included in a negative way, because the optimisation is a maximisation rather than a minimisation.

3.2.2.2 Optimisation

Figures 3.9(a) and 3.9(b) show the kinetic energy of the beam as a function of the feedback gains. For the structural models examined, the minimum can not be practically calculated in an analytical way from the cost function, equation 3.34. Moreover, when optimising output feedback controllers, it is difficult to prove that a local minimum of the cost function is also the global minimum. This is discussed, amongst others, by Levine and Athans (1970). They used an algorithm to find a minimum of the cost function, but also noted this algorithm is not guaranteed to converge. A different algorithm is used here, which is similar to one discussed by Anderson and Moore (1971) and is essentially a gradient descent algorithm. This section describes how this algorithm is implemented for the single-channel controller.

Levine and Athans (1970) examined a general state space model:

$$\begin{aligned} \dot{\mathbf{x}}(t) &= \mathbf{A}\mathbf{x}(t) + \mathbf{B}_c\mathbf{u}(t) \\ \mathbf{y}(t) &= \mathbf{C}_c\mathbf{x}(t) \end{aligned} \tag{3.40}$$

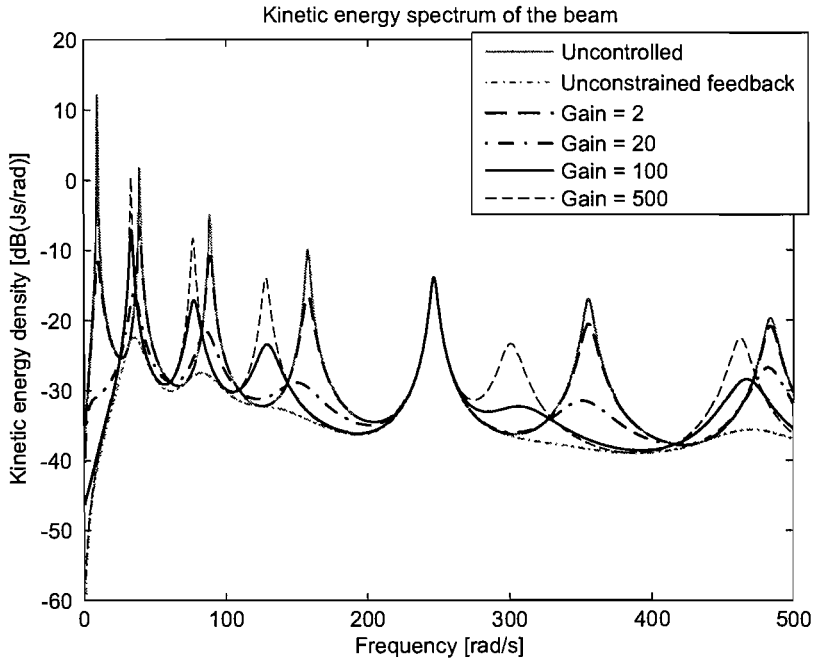

(a) Spectrum

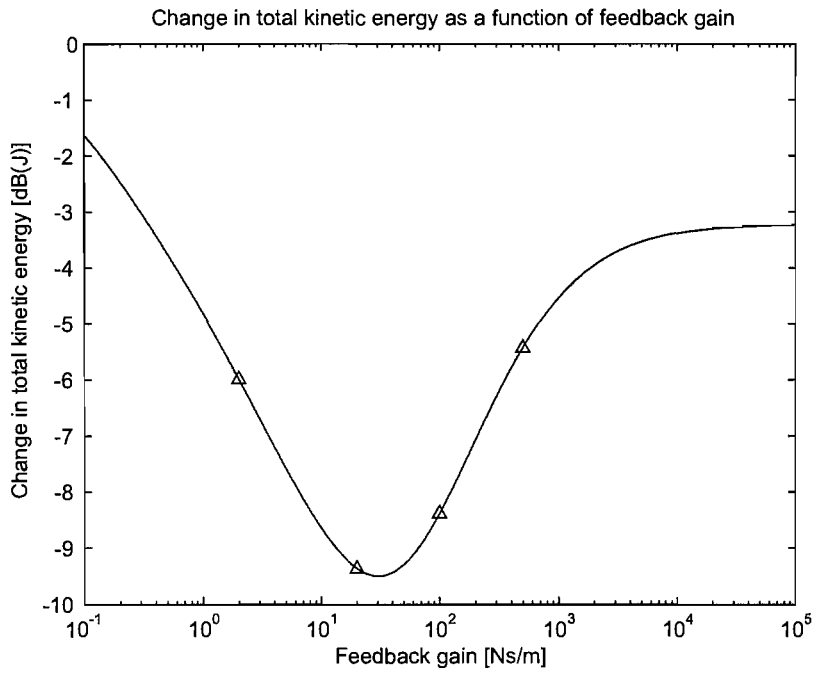

(b) Change in expectation

Figure 3.9: The change in the spectrum of and the expectation of kinetic energy of the beam under white noise excitation as a function of the constant velocity feedback gain. The beam is controlled at $x = 0.6L$.

with constant output feedback gain:

$$\mathbf{u}(t) = -\mathbf{G}\mathbf{y}(t) \tag{3.41}$$

The cost function that was used in that paper is an initial value problem:

$$\begin{aligned} J &= \mathbf{x}^T(0) \int_0^\infty \mathbf{\Phi}_c^T(t) \left[\mathbf{Q} + \mathbf{C}_c^T \mathbf{G}^T \mathbf{R} \mathbf{G} \mathbf{C}_c\right] \mathbf{\Phi}_c(t) \mathrm{d}t \, \mathbf{x}(0) \\ &= \mathrm{trace} \left(\int_0^\infty \mathbf{\Phi}_c^T(t) \left[\mathbf{Q} + \mathbf{C}_c^T \mathbf{G}^T \mathbf{R} \mathbf{G} \mathbf{C}_c\right] \mathbf{\Phi}_c(t) \mathrm{d}t \, \mathbf{x}(0)\mathbf{x}^T(0) \right) \end{aligned} \tag{3.42}$$

It can be seen that equation 3.42 is similar to equation 3.34, with $\mathbf{x}(0)\mathbf{x}^T(0)$ replaced by $\mathbf{P}$. If the system is asymptotically stable and the matrix $\left[\mathbf{Q} + \mathbf{C}_c^T \mathbf{G}^T \mathbf{R} \mathbf{G} \mathbf{C}_c\right]$ is positive semi-definite, the cost is equal to (Kalman and Bertram (1960)):

$$J_{ke} = \mathrm{trace}\,(\mathbf{K}\mathbf{P}) \tag{3.43}$$

with $\mathbf{K}$ the positive definite solution of the Lyapunov equation:

$$\mathbf{K}\left[\mathbf{A} - \mathbf{B}_c \mathbf{G} \mathbf{C}_c\right] + \left[\mathbf{A} - \mathbf{B}_c \mathbf{G} \mathbf{C}_c\right]^T \mathbf{K} + \left[\mathbf{Q} + \mathbf{C}_c^T \mathbf{G}^T \mathbf{R} \mathbf{G} \mathbf{C}_c\right] = \mathbf{0} \tag{3.44}$$

The derivative of the cost function, J_{ke}, with respect to the elements of the feedback gain matrix, $\mathbf{G}$, is equal to:

$$\frac{\partial J_{ke}}{\partial \mathbf{G}} = 2\mathbf{R}\mathbf{G}\mathbf{C}_c\mathbf{L}\mathbf{C}_c^T - 2\mathbf{B}_c^T\mathbf{K}\mathbf{L}\mathbf{C}_c^T \tag{3.45}$$

where $\mathbf{K}$ is the solution of equation 3.44 and $\mathbf{L}$ is the solution of:

$$\left[\mathbf{A} - \mathbf{B}_c \mathbf{G} \mathbf{C}_c\right] \mathbf{L} + \mathbf{L} \left[\mathbf{A} - \mathbf{B}_c \mathbf{G} \mathbf{C}_c\right]^T + \mathbf{P} = \mathbf{0} \tag{3.46}$$

Because the matrices $\mathbf{K}$ and $\mathbf{L}$ in equation 3.45 also depend on the matrix of feedback gains $\mathbf{G}$, the optimal feedback gains can, generally, not be directly established and a convergent algorithm must be used.

Using the derivative of the feedback gain, a simple algorithm can be formulated that will converge to a minimum on the cost function, if started at an initial stabilising controller $\mathbf{G}_0$. The algorithm used here is similar to that in Anderson and Moore (1971):

- For the kth iteration, calculate the cost J_k using equations 3.43 and 3.44. If $k = 0$, use the initial stabilising controller $\mathbf{G}_0$.
- Calculate the derivative of the cost function $\partial J_k / \partial \mathbf{G}_k$, using equation 3.45.

- Update the gain matrix $\mathbf{G}_k$ according to:

$$\mathbf{G}_{k+1} = \mathbf{G}_k - \frac{\epsilon}{\mathbb{F}\left[\partial J_k / \partial \mathbf{G}_k\right]} \frac{\partial J_k}{\partial \mathbf{G}_k} \tag{3.47}$$

  where ϵ is a small value to regulate the stepsize and $\mathbb{F}$ denotes the Frobenius norm. This norm is included to keep the stepsize in $\mathbf{G}_k$ independent of the size of the values in $\partial J_k / \partial \mathbf{G}_k$.

- Check that the system is stable at these new gains and, if that is the case, calculate the cost J_{k+1} using equations 3.43 and 3.44. The controller is stable if all the eigenvalues of the matrix $[\mathbf{A} - \mathbf{B}_c\mathbf{G}\mathbf{C}_c]$ are in the left-half of the complex plane. If the system is no longer stable or $J_{k+1} > J_k$, reduce the stepsize ϵ, because the update has overshot the stability margins or an area where the cost is lower. Repeat the previous step and this step, until the system is stable and $J_{k+1} < J_k$, then repeat from beginning.

- To stop the optimization, a suitable criterion can be chosen, such as a sufficiently small update in the gains, or a sufficiently small improvement in the cost function.

Though it can not be proved that the algorithm converges to a global minimum, it is found in practice that the controller does converge to the same set of gains, independent of the choice of initial controller. The only exception found in the course of this research is in a multichannel situation, when the control locations are located very close together (Engels and Elliott (2005) and in this work, chapter 4). Therefore, for ease of formulation, applying the above algorithm will be referred to as *optimisation.*

For a single-channel case, the feedback matrix $\mathbf{G}$ only consists of a single element, but the theory and the algorithm described above remain valid for a multichannel controller. For the optimisation of the kinetic energy function in figure 3.9(b) with no effort weighting, this algorithm calculates an optimal gain of 30.8 Ns/m.

3.2.2.3 Power minimisation and power absorption maximisation

Solutions for the minimisation of the power input and maximisation of the power absorption can also be calculated using the above algorithms, though the cost matrices and the derivatives change.

For maximum power absorption, the cost function in equation 3.39 can be calculated in a similar fashion as in the previous section:

$$J_{P\,abs} = \text{trace}\,(\mathbf{KP}) \tag{3.48}$$

Now, the matrix $\mathbf{K}$ should be calculated from:

$$\mathbf{K}\mathbf{A}_c + \mathbf{A}_c^T\mathbf{K} + \left[\mathbf{C}_c^T\mathbf{G}^T\mathbf{C}_c - \mathbf{C}_c^T\mathbf{G}^T\mathbf{R}\mathbf{G}\mathbf{C}_c\right] = \mathbf{0} \tag{3.49}$$

instead of equation 3.44. The gradient of equation 3.48 is:

$$\frac{\partial J_{P\,abs}}{\partial \mathbf{G}} = \mathbf{C}_c\mathbf{L}\mathbf{C}_c^T - 2\mathbf{B}_c^T\mathbf{K}\mathbf{L}\mathbf{C}_c^T - 2\mathbf{R}\mathbf{G}\mathbf{C}_c\mathbf{L}\mathbf{C}_c^T \tag{3.50}$$

As the cost function is maximised for this case, instead of equation 3.47, the update should be:

$$\mathbf{G}_{k+1} = \mathbf{G}_k + \frac{\epsilon}{\mathbb{F}\left[\partial J_k/\partial \mathbf{G}_k\right]}\frac{\partial J_k}{\partial \mathbf{G}_k} \tag{3.51}$$

For minimum power input, the matrix $\mathbf{K}$ would be calculated from

$$\mathbf{K}\mathbf{A}_c + \mathbf{A}_c^T\mathbf{K} + \left[\mathbf{Q}_{abs\,struct} - \mathbf{C}_c^T\mathbf{G}^T\mathbf{C}_c + \mathbf{C}_c^T\mathbf{G}^T\mathbf{R}\mathbf{G}\mathbf{C}_c\right] = \mathbf{0} \tag{3.52}$$

in stead of equation 3.44. However, it was found that the power input by the excitation is independent of the control gain and the power absorption by the controller, as was also found by Nelson (1996). This can be seen in figure 3.10, which shows the power input by the excitation and the power absorption by the controller as a function of the direct velocity feedback gain.

That the power input by the excitation does not change means that minimising the total power input and maximising the power output are the same. That the power input does not change can also be seen from the similarity between equation 3.42 and equation 3.34. The expectation of the power input when the structure is excited by a random modal forces, is equal to the energy input of the initial value problem, with uncorrelated impulse (in the case of white noise) or step (in case of red noise) response of the modal amplitude. Similarly, the expectation of the power input by the excitation is equal to the energy in the system at $t = 0$ due to the initial conditions in the time domain analysis. Influencing the matrix $\mathbf{P}$ and thus the total power input is only possible in a feedback situation if there is direct feedthrough from the disturbance to the sensor output and also to the control force. An example of this would be constant gain acceleration feedback. Figure 2.8 indicates that velocity feedback on a red-noise excited system has no direct feedthrough either. The gain that maximises power absorption is higher than the gain that minimises the kinetic energy. In this case the algorithm calculates a gain of 179 Ns/m.

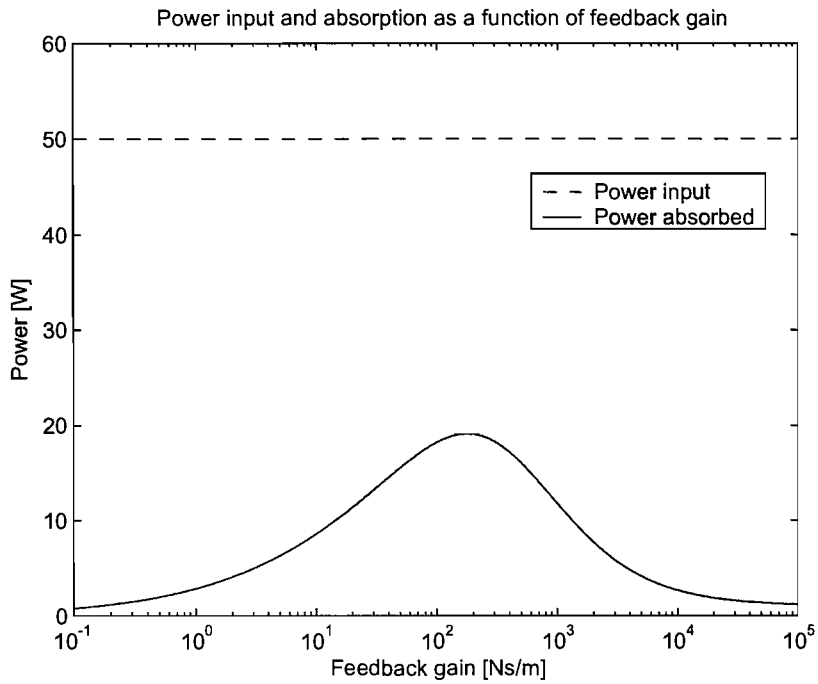

Figure 3.10: Power input by the excitation and power absorption by the controller as a function of the direct velocity feedback gain.

3.2.2.4 Approximation by limiting the number of modes

It would be interesting if one could find the optimum feedback gain for a single channel system analytically on the basis of characteristics of the beam and the mode-shape amplitude at the control location. This would require the analytical solution of equation 3.43. For high numbers of modes this is not practically achievable. However, for low numbers of modes and under special assumptions, this may be achievable. The value for the feedback gain obtained in this manner will not be the optimal value for the complete beam model, but may be a usable approximation of the optimal value.

The simplified model for the first approximation is a beam of which only the first two modes are taken into account and with a single control loop. The modes are assumed undamped and independently excited by white noise. To simplify the problem even further, no cost is put on the control effort. Under these assumptions, equation 3.43 can be solved analytically. More specifically, the required elements of $\mathbf{K}$ can be

solved from the Lyapunov equation:

$$\mathbf{K}\left[\mathbf{A}-\mathbf{B}_c g \mathbf{C}_c\right]+\left[\mathbf{A}-\mathbf{B}_c g \mathbf{C}_c\right]^T \mathbf{K}+\mathbf{Q}=0 \tag{3.53}$$

The matrices can be written out as:

$$\mathbf{K}=\begin{bmatrix} k_{11} & k_{12} & k_{13} & k_{14} \\ k_{12} & k_{22} & k_{23} & k_{24} \\ k_{13} & k_{23} & k_{33} & k_{34} \\ k_{14} & k_{24} & k_{34} & k_{44} \end{bmatrix} \text{ and } \mathbf{A}-\mathbf{B}_c g \mathbf{C}_c=\begin{bmatrix} 0 & 0 & 1 & 0 \\ 0 & 0 & 0 & 1 \\ -\omega_1^2 & 0 & -g\frac{2}{M}\psi_1^2 & -g\frac{2}{M}\psi_1\psi_2 \\ 0 & -\omega_2^2 & -g\frac{2}{M}\psi_1\psi_2 & -g\frac{2}{M}\psi_2^2 \end{bmatrix}$$

where ψ_1 and ψ_2 are the amplitudes of the first and second mode at the control location and ω_1 and ω_2 are the resonance frequencies of those modes. The cost function is the trace of the multiplication of $\mathbf{P}_w$ and $\mathbf{K}$ in the case of white noise excitation, which amounts to:

$$J=c(k_{33}+k_{44}) \tag{3.54}$$

where c is some constant. Equation 3.53 offers enough independent equations to solve k_{33} and k_{44} as a function of g, ω_1, ω_1, ψ_1 and ψ_2. The solution results in a positive and a negative solution for both values, but as they denote energy, it has to be the positive solution. Thus the cost function can be written as an analytical function dependent on g. The minimum of this function is found by differentiating the equation with respect to g and equating to 0. The optimal gain for the two mode beam can then be calculated as:

$$g=\frac{M}{2}\frac{\omega_2^2-\omega_1^2}{\sqrt{\left(\psi_1^2+\psi_2^2\right)\left(\psi_1^2\omega_2^2+\psi_2^2\omega_1^2\right)}} \tag{3.55}$$

or for a generic, modal structure:

$$g=\frac{\omega_2^2-\omega_1^2}{\sqrt{\left(\frac{N_1}{M}\psi_1^2+\frac{N_2}{M}\psi_2^2\right)\left(\frac{N_1}{M}\psi_1^2\omega_2^2+\frac{N_2}{M}\psi_2^2\omega_1^2\right)}} \tag{3.56}$$

where N_1 and N_2 are the integrals of the squared first and second modeshape, respectively, divided by length or surface of the beam or plate.

This formula can will be referred to as the *two-mode formula.* During the derivation it is assumed that both ψ_1 and ψ_2 are not equal to 0. Logically, if the controller can only affect one mode, and not the other, it should clamp that mode. However, if the controller can only affect one mode, the cost will be infinite, as the other mode is unable dissipate its kinetic energy. Despite this, one can see that if one of the ψ's

is zero, equation 3.56 still results in a finite feedback gain. Therefor, the gain is still used in that case.

The same analysis can be done when three modes are taken into account. The formula for the optimal feedback gain then becomes rather more complex:

$$g = \frac{M}{2} \frac{(\omega_2^2 - \omega_1^2)(\omega_3^2 - \omega_1^2)(\omega_3^2 - \omega_2^2)\sqrt{(\psi_1^2\psi_2^2 + \psi_1^2\psi_3^2 + \psi_3^2\psi_2^2)}}{\sqrt{\begin{array}{l}\psi_3^2(\psi_2^2+\psi_1^2)^2(\psi_2^2\omega_1^2+\psi_1^2\omega_2^2)(\omega_3^2-\omega_1^2)^2(\omega_3^2-\omega_2^2)^2 + \\ \psi_2^2(\psi_3^2+\psi_1^2)^2(\psi_3^2\omega_1^2+\psi_1^2\omega_3^2)(\omega_3^2-\omega_2^2)^2(\omega_2^2-\omega_1^2)^2 + \\ \psi_1^2(\psi_3^2+\psi_2^2)^2(\psi_3^2\omega_2^2+\psi_2^2\omega_3^2)(\omega_2^2-\omega_1^2)^2(\omega_3^2-\omega_1^2)^2 + \\ 2\psi_2^4\psi_3^4\omega_1^2(\omega_2^2-\omega_1^2)(\omega_3^2-\omega_1^2)(\omega_3^2-\omega_2^2)^2 - \\ 2\psi_1^4\psi_3^4\omega_2^2(\omega_3^2-\omega_2^2)(\omega_2^2-\omega_1^2)(\omega_3^2-\omega_1^2)^2 + \\ 2\psi_1^4\psi_2^4\omega_3^2(\omega_3^2-\omega_2^2)(\omega_3^2-\omega_1^2)(\omega_2^2-\omega_1^2)^2\end{array}}} \tag{3.57}$$

This formula will be referred to as the *three-mode formula.* If damping factors are included on the different modes, the equation becomes much more complicated and is no longer practical to use.

Both these equations are similar to results described in Variyart et al. (2002), on the basis of an analysis of spillover to other modes. But where in that paper, the cross-spillover from modes is ignored, it has been included here. That paper did include more modes though.

Another possible approximation is to use a single gain, independent of the amplitude of the modeshapes, $\psi_i(x_c)$, at the point of control. On the basis of equation 3.56 a gain could be tuned solely on the first and resonance frequency:

$$g = cM\frac{\omega_2^2 - \omega_1^2}{\sqrt{\omega_2^2 + \omega_1^2}} \tag{3.58}$$

where c is a constant yet to be determined. This formula will be referred to as the *simplified two-mode formula.*

3.2.2.5 Approximation by matching impedance to an infinite structure

For a plate, a constant gain can be matched to the impedance of an infinite plate. This would correspond to a maximum power absorption strategy if there is no damping and there are no reflections of the bending vibrations in the system, along the

boundaries or, in a MIMO set-up, from other control locations. The impedance of an infinite plate is (Cremer et al. (1988)):

$$Z = 8\sqrt{\rho h E I} \tag{3.59}$$

To match this impedance, the feedback gain of the velocity feedback, should be set equal to this value.

For the beam, the impedance of an infinite structure is given by (Cremer et al. (1988)):

$$Z = 2\omega m k\,(1 + j) \tag{3.60}$$

where $k = \sqrt[4]{\frac{\omega^2 m}{EI}}$. This impedance contains a complex component and increases with frequency. Therefore, matching the (conjugate) impedance of the beam will be impossible with a fixed gain method. Considering that the energy in the beam is located relatively more at lower frequencies, it is expected that an approximation based on the two- or three-mode formula is better suitable for the beam.

3.2.3 Simulations on a beam and plate

This section will examine how optimised direct constant gain feedback compares to the approximations defined above. The relation between control effort and the reduction of the kinetic energy will also be considered for both constant velocity feedback control and LQG control. Last, performance, control effort and the control strategy dependent feedback gains will be looked at in relation to the control location. The control strategies will be applied first to the beam model and then to the simply supported plate model.

3.2.3.1 Beam results

Figure 3.11(a) shows the amount of control effort required to obtain a specific change in kinetic energy, for LQG and absolute velocity feedback control. For a single channel, the control effort for velocity feedback control is only dependent on the gain. To create the curve, the controller is optimised for varying magnitudes of the control effort weighting R. Optimising for varying values of R prevents an overshoot of the optimal control gain. Using a higher than optimal gain can result

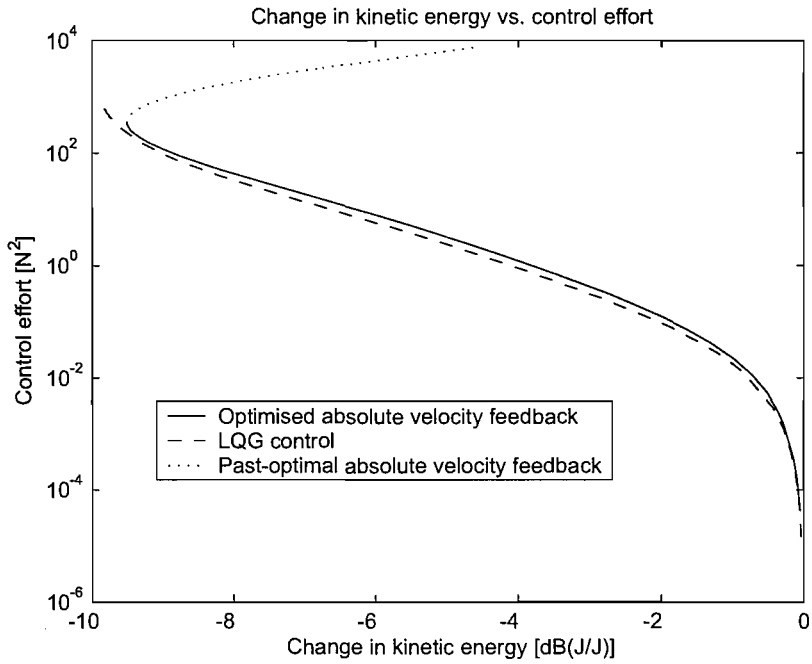

(a) Overall change in kinetic energy vs. control effort

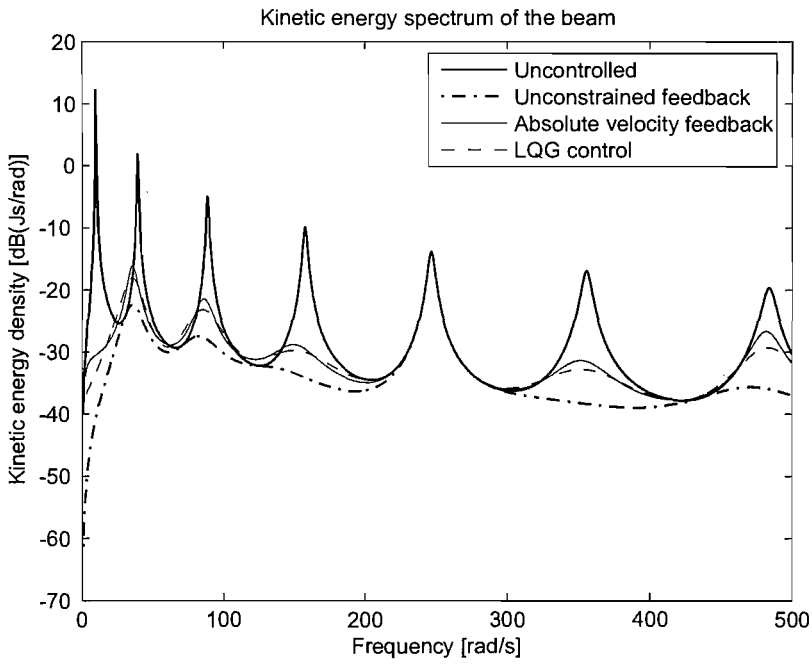

(b) Spectrum for a fixed effort of 200 ± 1 N^2

Figure 3.11: The change in the overall kinetic energy as a function of the control effort and the spectrum of the kinetic energy of the beam at a specific effort, for LQG and velocity feedback control. The control location is at $x = 0.6L$.

in more effort but less performance, this is indicated with the dotted line in figure 3.11(a). The figure shows there is only a small overall performance advantage in using LQG control over absolute velocity feedback control when the same control effort is applied. For these simulations only the first 30 modes of the beam were taken into account.

Figure 3.11(b) shows the spectrum of the kinetic energy of the beam with an LQG controller and a velocity feedback gain tuned to use a fixed control effort of 200 ± 1 N^2. The small overall performance difference seen in figure 3.11(a) results in a few decibels less kinetic energy at some peaks in spectrum. At other points, the performance is similar or sometimes worse than absolute velocity feedback control. The effort can be fixed by varying the weighting of the control effort, until the desired control effort is achieved. The control effort is the expectation of the sum of the squared control forces.

Figure 3.12(a) and 3.12(b) show the velocity feedback gains and control efforts as a function of location for the following strategies:

- a fixed effort weight velocity feedback minimising kinetic energy with the effort weighting, R, set to $1 \cdot 10^{-5}$
- a fixed effort weight velocity feedback maximising power absorption by the controller, with the effort weighting set to $1 \cdot 10^{-4}$
- the two-mode formula (equation 3.56)
- the three-mode formula (equation 3.57)
- the simplified two-mode formula, from equation 3.58, for $c = 1/2, 1, 2$

LQG control is not included in figure 3.12(a) as it does not have a specific 'gain' as it is a frequency dependent function. The gain that maximises power absorption by the controller is much higher than the optimal feedback gain and has a ripple in the gains along the beam with a spatial frequency equal to that of the 30^{th} mode. That indicates that tuning for maximum power absorption is influenced by the higher order modes. Indeed, it was found that when more modes are included, the gains increase as well. For the simplified two-mode formula, $c = 1/2$ seems to correspond best to the level of the two-mode and three-mode formula, while $c = 1$ seems to correspond better with the actual optimisation.

Figure 3.12(c) show the change in kinetic energy for the different control strategies.

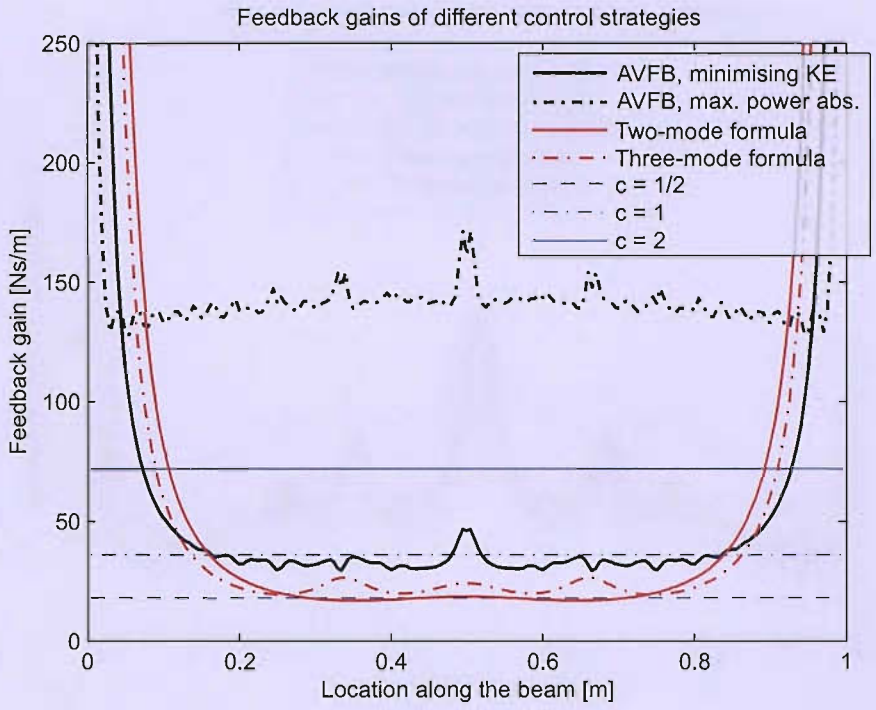

(a) Gain

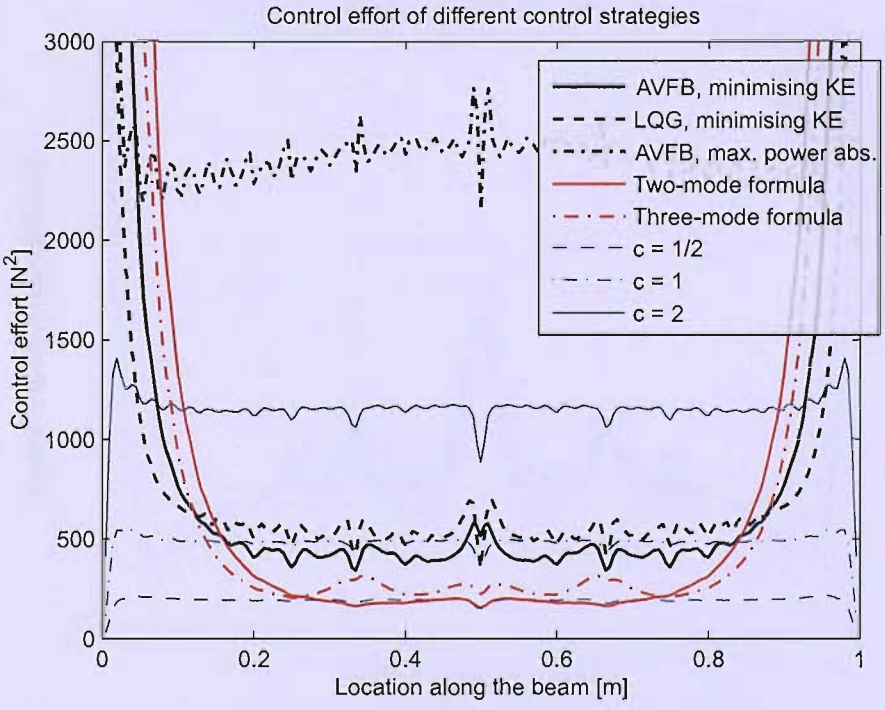

(b) Effort

Figure 3.12: Gains, efforts and change in kinetic energy for different control strategies. For the simplified two-mode formula, several possible constants c are examined. Gains for LQG control are not depicted as that controller is complex and frequency dependent.

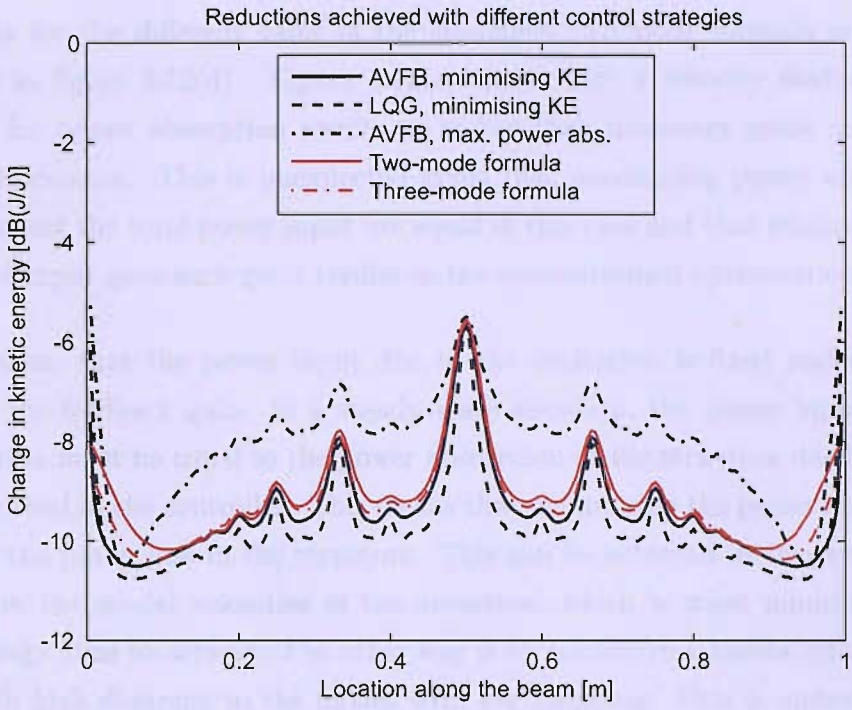

(c) Change in kinetic energy

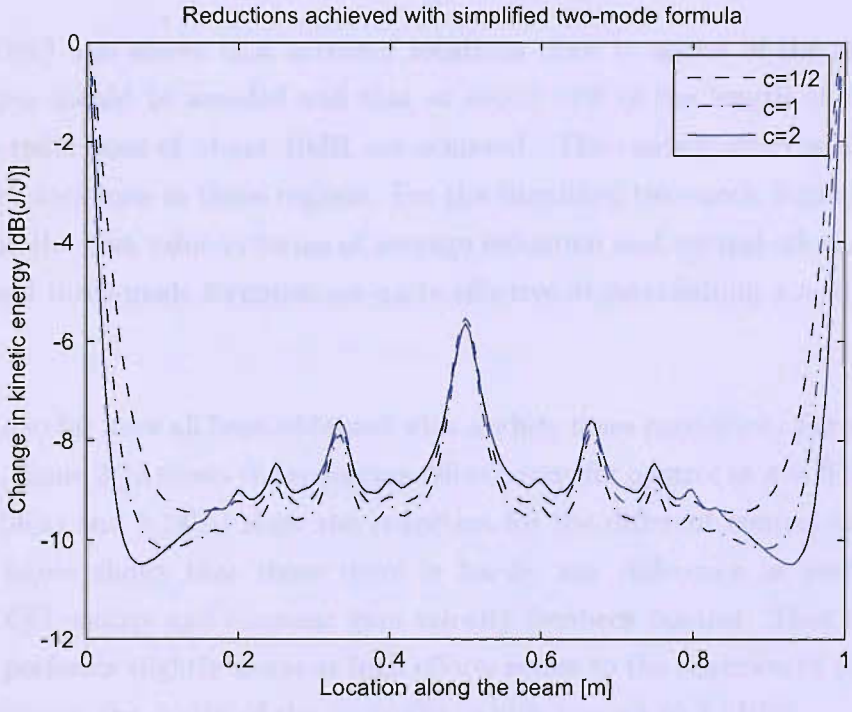

(d) Simplified two-mode formula, change in kinetic energy

Figure 3.12: Gains, efforts and change in kinetic energyfor different control strategies. For the simplified two-mode formula, several possible constants c are examined. Gains for LQG control are not depicted as that controller is complex and frequency dependent. [continued]

The results for the different gains of the simplified two-mode formula are shown separately in figure 3.12(d). Figure 3.12(c) shows that a velocity feedback gain optimised for power absorption results in higher than necessary gains and worse overall performance. This is unexpected given that maximising power absorption and minimising the total power input are equal in this case and that minimising the total power input gave such good results in the unconstrained optimisation.

Consider then, that the power input due to the excitation is fixed and does not vary with the feedback gain. In a steady state situation, the power input due to the excitation must be equal to the power absorption in the structure itself and the power absorbed in the controller. This means that maximising the power absorption minimises the power loss in the structure. This can be achieved in two ways. One is to reduce the modal velocities in the structure, which is what minimising the kinetic energy aims to achieve. The other way is by transferring kinetic energy from modes with high damping to the modes with low damping. This is undesirable as it increases the average kinetic energy in the structure.

Figure 3.12(c) also shows that actuator locations close to nodes of the first three mode shapes should be avoided and that at about 10% of the length of the beam maximum reductions of about 10dB are achieved. The control effort is also large for actuator locations in these regions. For the simplified two-mode formula, $c = 1$ seems to be the best value in terms of average reduction and control effort. Finally, the two- and three-mode formulas are quite effective at establishing a near optimal gain.

The results so far have all been obtained with a white noise excitation. For red noise excitation, figure 3.13 shows the reduction-effort curve, for control at $x = 0.6L$, while gigures 3.14(a) and 3.14(b) show the reduction for the different control strategies. The first figure shows that there there is hardly any difference in performance between LQG control and constant gain velocity feedback control. That the LQG controller performs slightly worse at high efforts is due to the selection of the sensor noise variance in the design of the controller, which was set to $1 \cdot 10^{-8}$.

Since the gains set with the appromixation formulas from section 3.2.2.4 are the same as in the white noise case, no figure was included here to show the gains in the red noise case. It was found that the optimised gains to minimise kinetic energy

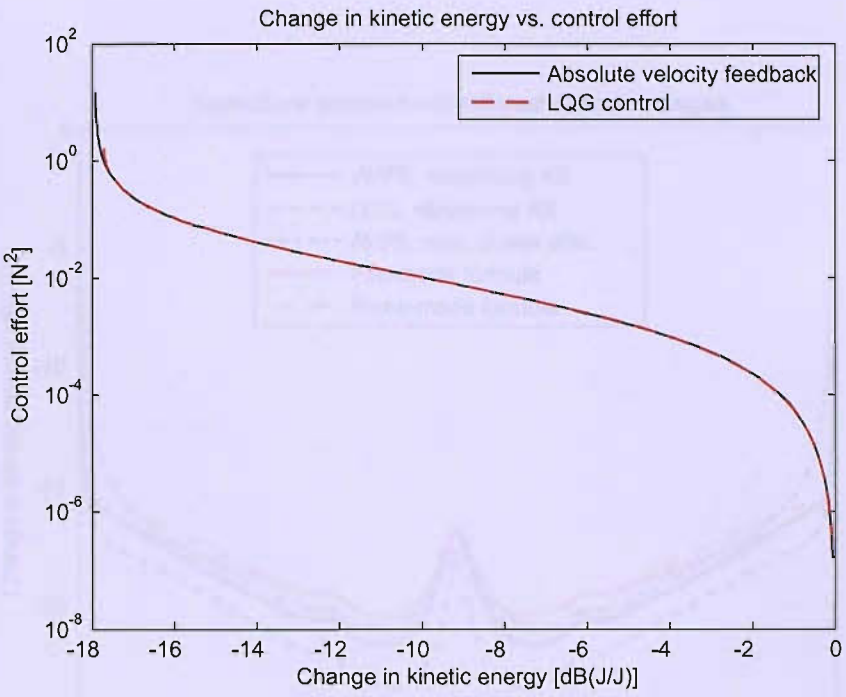

Figure 3.13: Overall change in kinetic energy vs. control effort at the control location $x = 0.6$L, for red noise excitation of the beam.

are slightly higher than they were in the white noise case. Gains for the optimal absorption of power were found to drop considerably, to about 2/3 of the gains for minimising the kinetic energy. Considering the mechanism explained above, this low gain is aimed at minimising kinetic energy transfer from the low frequency, lowly damped modes to modes that are damped more.

The approximations of the optimal kinetic energy through the use of two- and three-mode formulas resulted again in reasonable approximations to the optimal gain, though the gap in maximum performance has increased. Figure 3.14(a) seems to contradict figure 3.13 in that there does seem to be a difference between LQG and the absolute velocity feedback controller. This is due to the fact that both controllers were calculated using equal control effort weightings. This allows the LQG controller to use a higher control effort than the absolute velocity feedback controller and improve its performance. For the gains set with the simplified two-mode formula, the constant $c = 1$ still gives the best overall results.

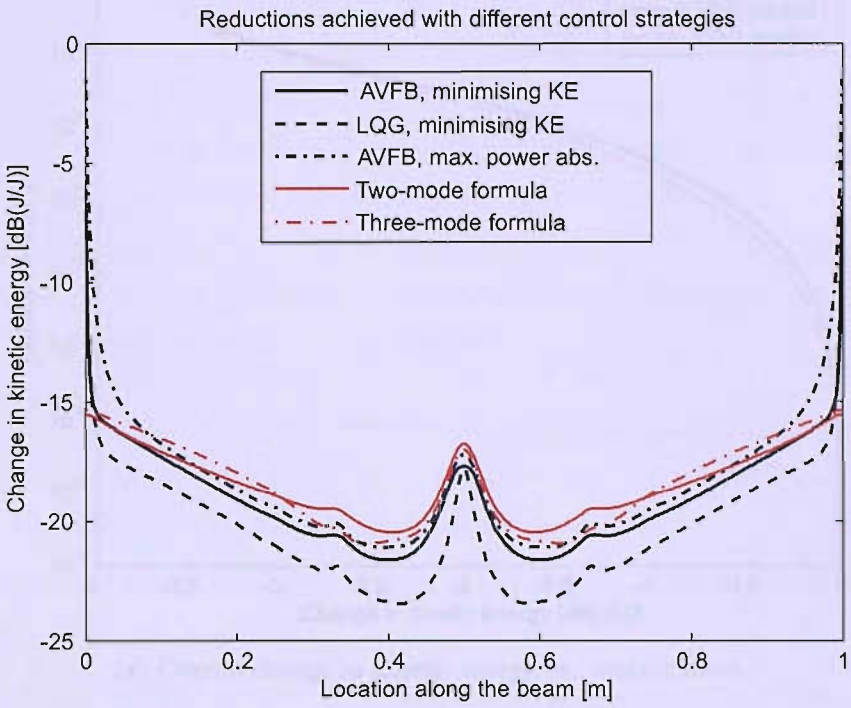

(a) Change in kinetic energy

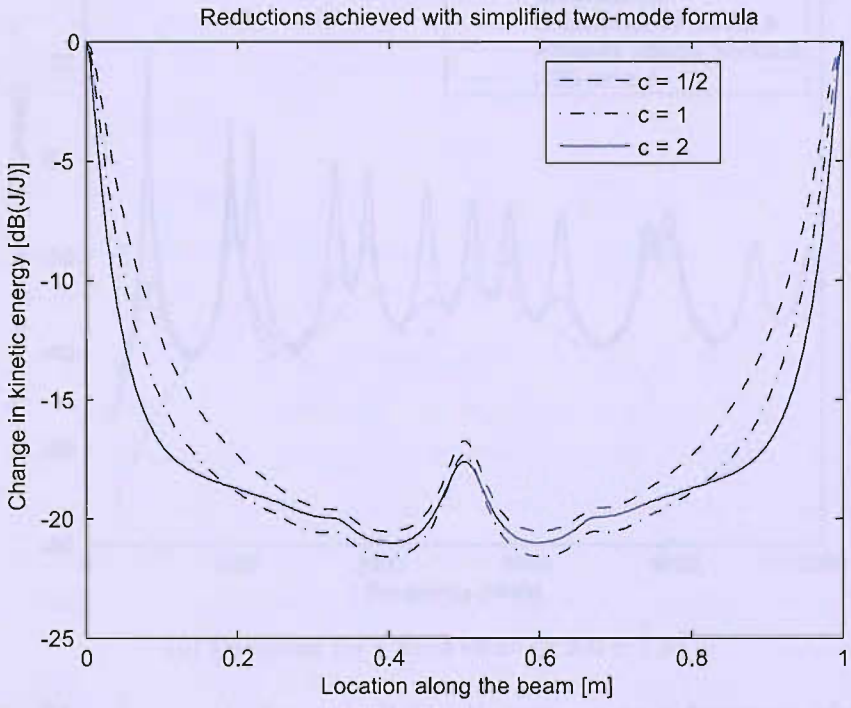

(b) Simplified two-mode formula, change in kinetic energy

Figure 3.14: Change in kinetic energy of the beam, in the case of red noise excitation.

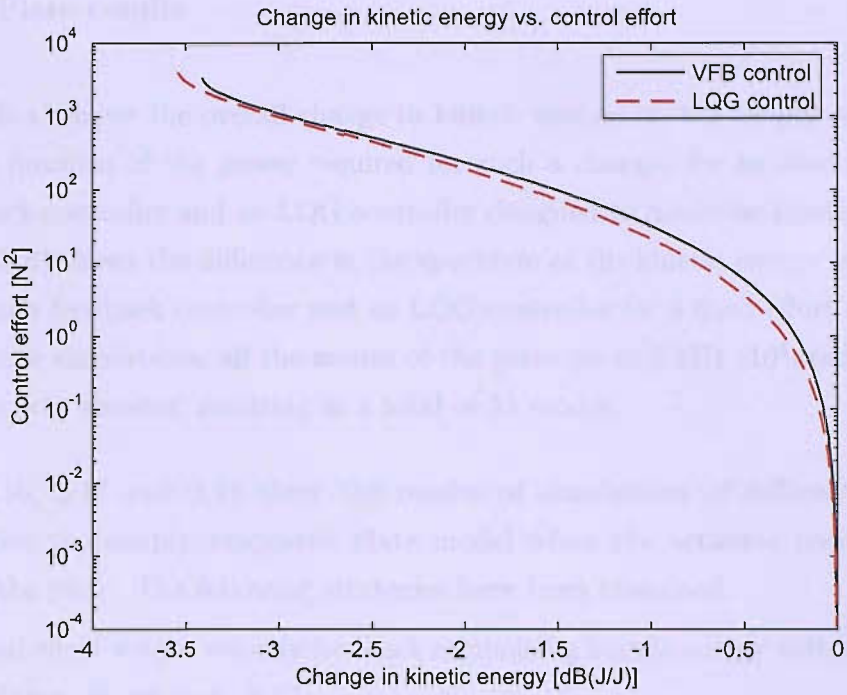

(a) Overall change in kinetic energy vs. control effort

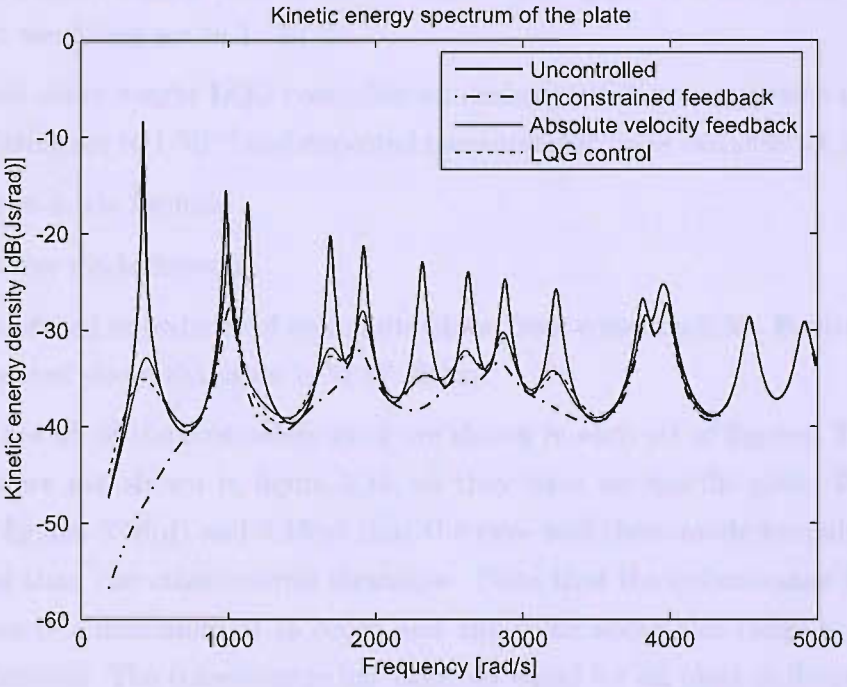

(b) Spectrum for a fixed effort of 200 ± 1 N^2

Figure 3.15: The change in the overall kinetic energy as a function of the control effort and the spectrum of the kinetic energy of the simply supported plate at a specific effort, for LQG and velocity feedback control. The control location is at $(x, y) = (0.24l_x, 0.6l_y)$.

3.2.3.2 Plate results

Figure 3.15(a) shows the overall change in kinetic energy, on the simply supported plate as a function of the power required for such a change, for an absolute velocity feedback controller and an LQG controller designed to minimise kinetic energy. Figure 3.15(b) shows the difference in the spectrum of the kinetic energy between a constant gain feedback controller and an LQG controller for a fixed effort of $2 \cdot 10^3$ N^2. For these simulations, all the modes of the plate up to 5 kHz ($10^4\pi$rad/s) have been taken into account, resulting in a total of 53 modes.

Figures 3.16, 3.17 and 3.18 show the results of simulations of different control strategies on the simply supported plate model when the actuator position was varied on the plate. The following strategies have been examined:

- a fixed effort weight velocity feedback minimising kinetic energy with the effort weighting, R, set to $1 \cdot 10^{-5}$
- a fixed effort weight velocity feedback maximising power absorption, with the effort weighting set to $1 \cdot 10^{-4}$
- a fixed effort weight LQG controller minimising kinetic energy, with the effort weighting set to $1 \cdot 10^{-4}$ and expected measurement noise variance set to $1 \cdot 10^{-5}$
- the two-mode formula
- the three-mode formula
- the matched impedance of an infinite plate, from equation 3.59. For the simply supported plate, that gain is 31.87 Ns/m.

Note that not all of the controllers show are shown in each set of figures. The LQG controllers are not shown in figure 3.16, as they have no specific gain. It can be seen from figures 3.16(d) and 3.16(e) that the two- and three-mode formula set the gain higher than the other control strategies. Note that the colour-range has been limited here to a maximum of 75 Ns/m and any value above this range is coloured as the maximum. The colour-range has been set equal for all plots in figure 3.16.

The higher gains of the two- and three-mode formulas also cause in high control efforts, as can be seen in figures 3.17(d) and 3.17(e).

Finally, figure 3.17 shows the changes in kinetic energy achieved by the different

control strategies. In general one can see that the nodal lines of the modeshapes corresponding to lower resonance frequencies should be avoided if good control is desired. The higher gains set for optimal power absorption result in a smaller reduction of the kinetic energy in some areas compared to gains optimised for kinetic energy, but the differences are small. LQG control with a fixed effort weighting obtains the best performance, but uses a higher effort. Maximising power absorption in this case, gives good results as well. Of the approximations examined, matched infinite plate impedance obtains the best performance, while having limited control effort as well.

Appendix B shows the results for a red noise excitation, overall higher reductions where obtained and the differences between the different strategies are less noticeable.

3.3 Conclusion

In this chapter different control strategies were examined for a single-channel set-up. The goal was to examine if optimal tuning of the controller can be achieved based on only locally measured variables. Unconstrained feedforward and feedback control were examined to see if a relation can be found between the optimal value and structural values. Minimising the total power input and maximising the total power absorption were examined as alternatives to mininising the kinetic energy. None of these strategies resulted in a controller applicable for broadband feedback control. Minimising the total power input was a good approximation, but is not just dependent on variables that can be measured at the control point, nor is miniming the kinetic energy itself. Maximising the total power absorption in a feedback situation is achieved by applying a conjugate impedance of the local mobility. This is obviously a very strong link to the local variables, but it resulted overall in a significant increase, rather than decrease in the kinetic energy.

Tuning constant gain velocity feedback control to optimally reduce the kinetic energy, requireds complete knowlegde of the dynamics of the system. It can not even be proven that only a single, global minimum or maximum exists for the optimisation of the absolute velocity feedback gain, only one minimum was found using a

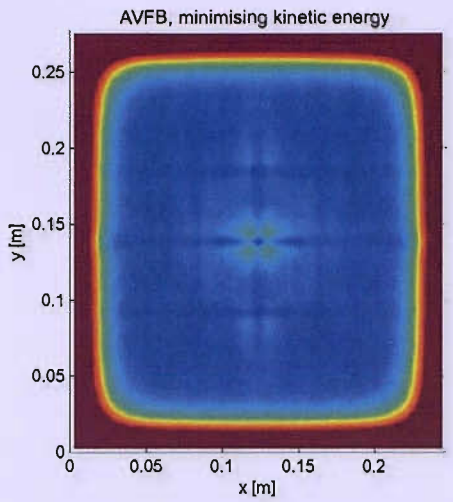

(a) AVFB, minimising kinetic energy

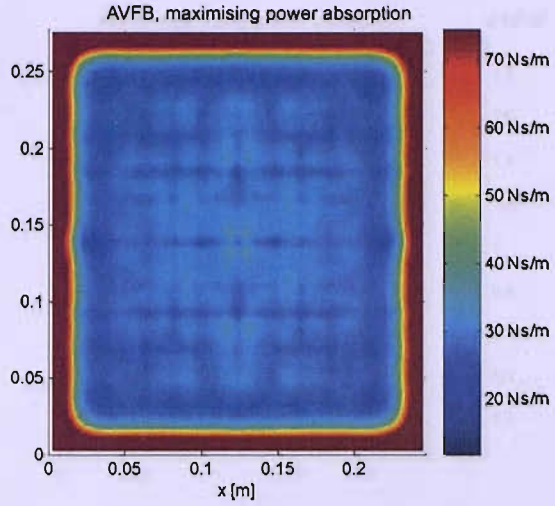

(b) AVFB, maximising power absorption

LQG control has a complex, frequency dependent gain

(c) LQG, minimising kinetic energy

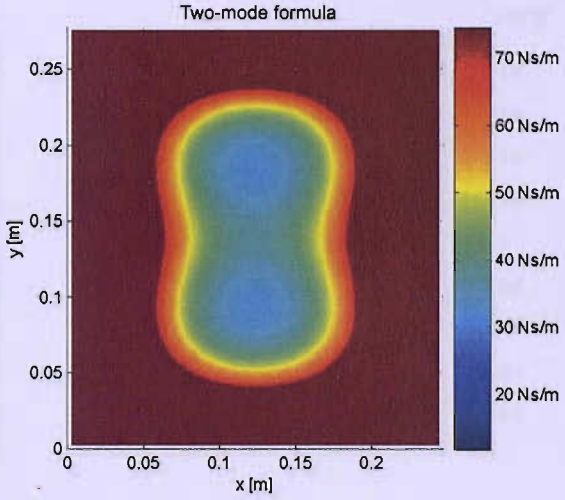

(d) Two-mode formula

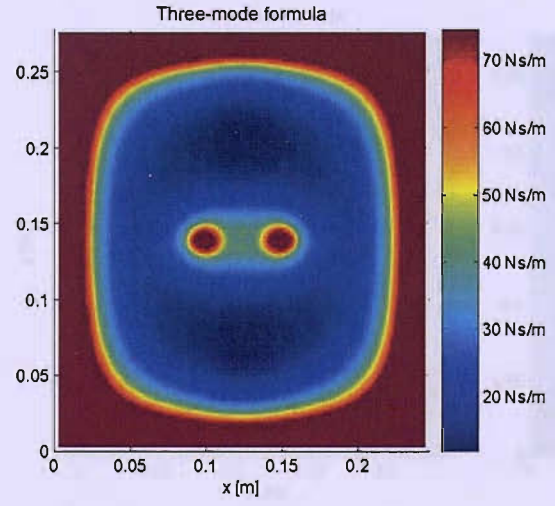

(e) Three-mode formula

Matched infinite plate impedance is a constant gain of 31.87 Ns/m

(f) Matched infinite plate impedance

Figure 3.16: Feedback gains as a function of controller location in x and y directions on the simply supporte plate, for different control strategies on a plate.

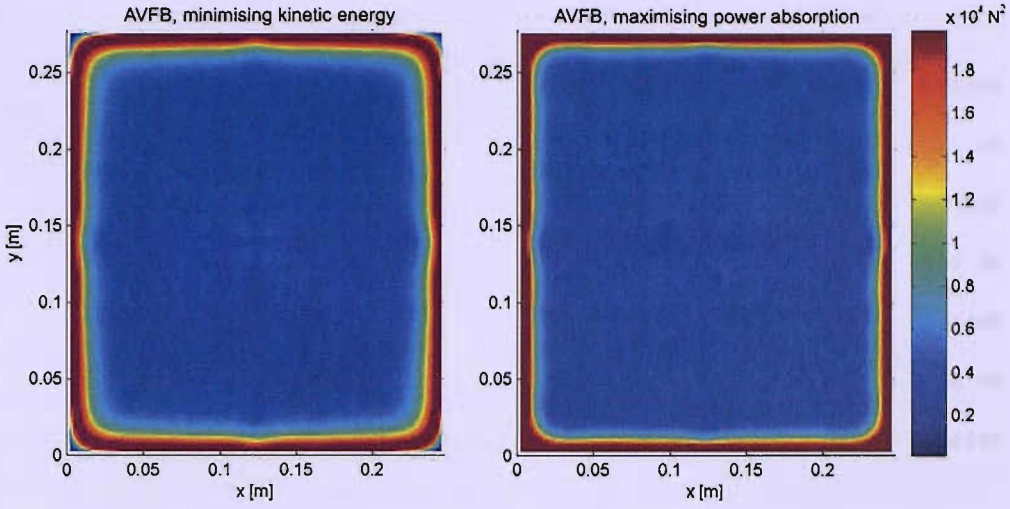

(a) AVFB, minimising kinetic energy (b) AVFB, maximising power aborption

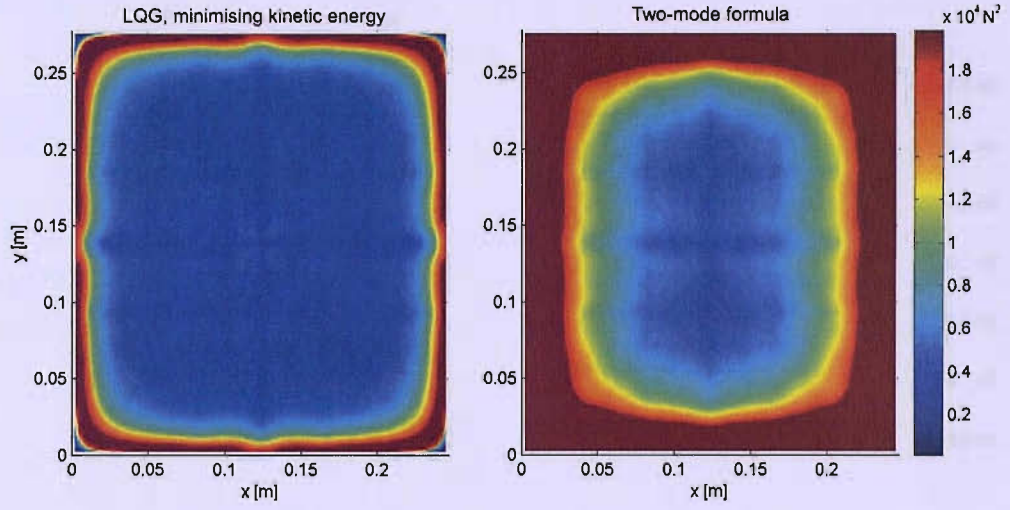

(c) LQG, minimising kinetic energy (d) Two-mode formula

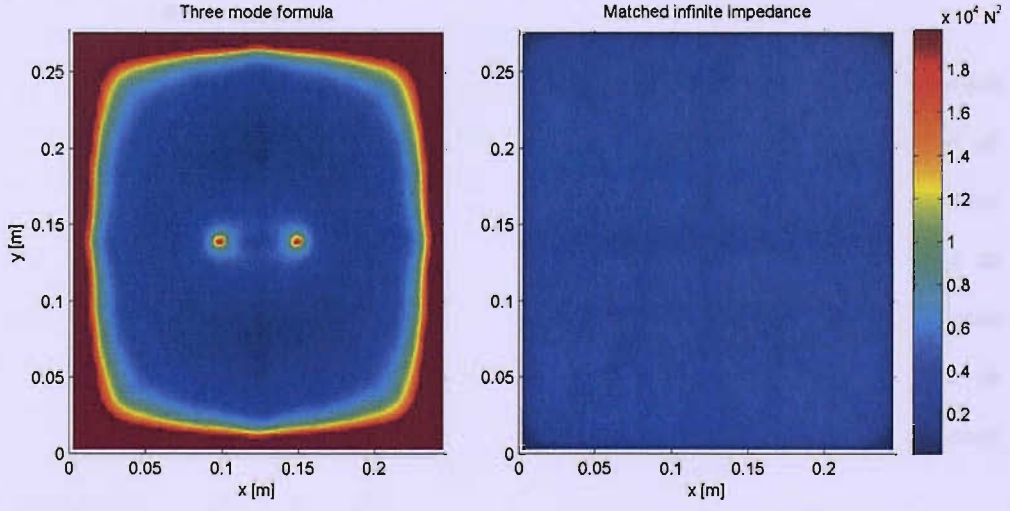

(e) Three-mode formula (f) Matched infinite plate impedance

Figure 3.17: Control effort for different control strategies on a plate

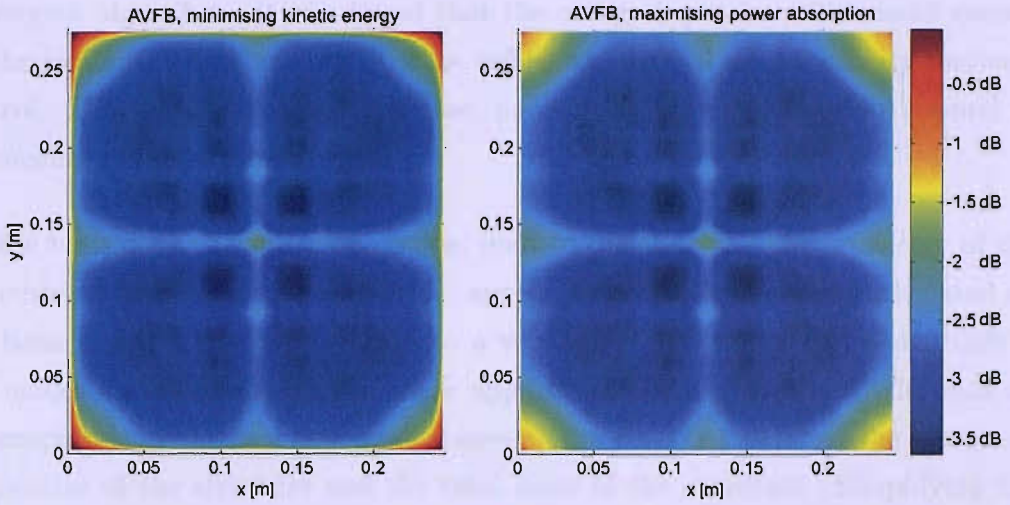

(a) AVFB, minimising kinetic energy (b) AVFB, maximising power absorption

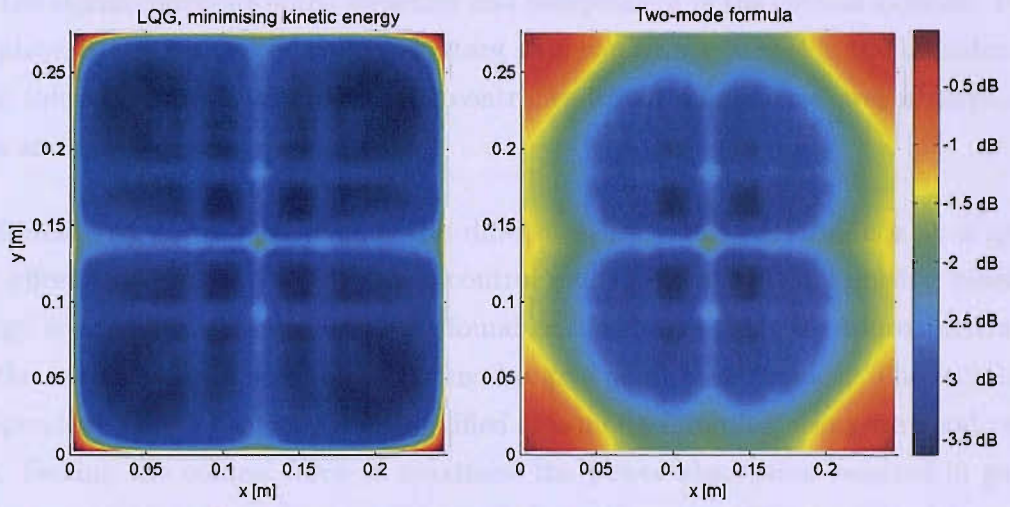

(c) LQG, minimising kinetic energy (d) Two-mode formula

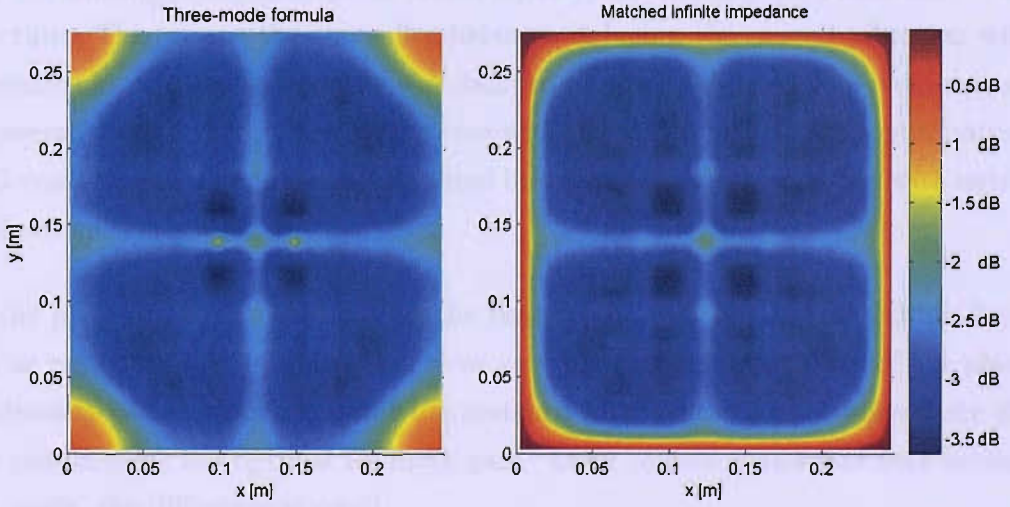

(e) Three-mode formula (f) Matched infinite plate impedance

Figure 3.18: Change in kinetic energy for different control strategies on a plate

convergent algorithm. It was found that the energy input into the model caused by the random excitation could not be influenced with absolute velocity feedback control. That means that, for this case, maximising power absorption is equal to minimising the total power input.

On the basis of the Lyapunov equation, used to calculate the kinetic energy of the structure under white noise excitation, approximation formulas were calculated on the basis of the analytical solution to a very simplified model containing only a few modes and no damping. In these approximations, the gain only depends on the amplitude of the first few modeshapes at the control locations, the resonance frequencies of the structure and the total mass of the structure. Simplifying the formula even further resulted in an approximation that is only dependent on the mass and the eigenfrequencies of the structure and independent of the control location. For the plate, it was recognised that a constant gain can be set to match the impedance of an infinite plate, in which case the controller would maximise power absorption from an infinite plate.

In simulations, it was found that the difference in overall performance at a specific effort between velocity feedback control and LQG control minimising kinetic energy is small. Furthermore, it was found on the beam that the approximations for the feedback gain based on a few modes give good performance. The location independent approximation (the simplified two-mode formula) also gave good results. Setting the control force to maximise the power absorption resulted in gain that were significantly unlike minimising the kinetic energy. This is due to the fact that maximising power absorption is also equal to minimising the power loss in the structure. This means the controller balances reducing the overall vibration with preventing kinetic energy entering well damped modes. It did not, however, increase the overall kinetic energy, as was the case with unconstrained control optimisation. LQG control with a fixed weight obtained best overall performance but with only a small overall difference.

On the plate the approximations on the basis of the first few modes did not function as well, resulting in gains that were very high for large portions of the plate. Maximising power absorption and the matched impedance of an infinite plate did give results close the optimal feedback gain. LQG control performed best overall, but, again, the difference is small.

Chapter 4

Multi-channel control

The previous chapter showed that in the single-channel case, the differences between LQG control and constant gain velocity feedback control are relatively small with collocated and dual sensor-actuator pairs and using equal effort. Setting the feedback gain to maximise the power absorption results in reasonable performance, but on the beam the gains were often higher than the values required to optimally reduce the kinetic energy, resulting in a higher control effort.

This chapter will examine multi-channel control. In particular, we investigate how the performance of the decentralised control strategy compares to a centralised controller. The analysis in a multi-channel (MIMO) system of the control strategies suggested in chapter 3, is performed in two parts.

First, in section 4.2 optimised decentralised control is compared with centralised and LQG control. Second, section 4.3 compares optimised decentralised velocity feedback control and control using the gains calculated with the approximations suggested in chapter 3.

To start with, however, section 4.1 will describe how the optimised centralised and decentralised constant feedback gains can be calculated.

The results in this chapter have been presented in several papers; Engels and Elliott (2004), Baumann et al. (2004), Engels et al. (2004), Engels and Elliott (2005) and Engels et al. (2006).

4.1 Optimisation of constant gain control

Chapter 3 described how a single-channel constant gain feedback controller can be tuned to form a minimum in the cost-surface. In a multi-channel set-up, that algorithm has to be adapted to impose constraints for the controller to be decentralised or to remain stable when it is centralised. This section shows how this can be achieved.

4.1.1 Centralised control

In section 3.2.2.2, an algorithm was described to calculated a single-channel controller to find a minimum of the cost function. The algorithm described there can also be used for calculating a multi-channel controller. Specifically, it can be used to calculate a centralised multi-channel controller since equations 3.45 and 3.50 are written as full matrices. The only difference with the calculation of a single-channel controller is that stability becomes an issue for the centralised controller.

The off-diagonal terms in a centralised velocity feedback controller cause a force at a different location to where the sensor is, as is illustrated in figure 4.1, and are essentially non-collocated control loops. As such they can cause instability, as illustrated in figure 4.1(c). The gain of the off-diagonal terms must be limited in magnitude if the system is to remain stable (Preumont et al. (2002)). The algorithm discussed in section 3.2.2.2 prevents the controller becoming unstable by demanding at each optimisation step that the controller remains stable.

It is interesting to note that the additional damping in the system introduced by the on-diagonal terms stabilises the effect of off-diagonal values of the controller which would otherwise make the system unstable if the on-diagonal terms were absent. Thus, a failure of equipment at one control location can destabilise the system if an optimised, centralised controller is used.

4.1.2 Decentralised control

Geromel and Bernussou (1979) discussed the optimization of a constant gain de-

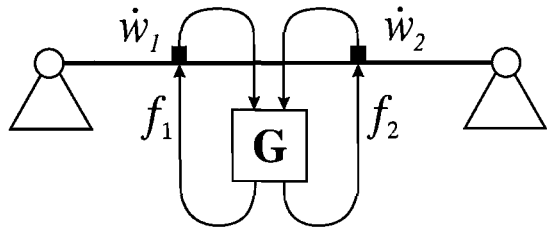

(a) MIMO control diagram

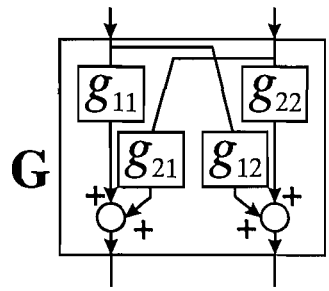

(b) Centralised controller expanded

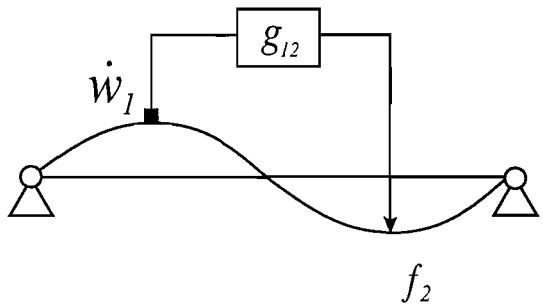

(c) Off-diagonal elements of **G** can cause instability

Figure 4.1: MIMO centralised feedback control.

centralised controller, for the same system and cost functions as Levine and Athans (1970). The same algorithms can be used as for centralised control, except that the initial stabilising control matrix should be diagonal (off-diagonal terms set to 0) and that the gains are adjusted using the derivative with respect to the on-diagonal elements of the gain matrix:

$$\frac{\partial J}{\partial \mathbf{G}} = \mathtt{diag}\left[2\mathbf{R}\mathbf{G}\mathbf{C}_c\mathbf{L}\mathbf{C}_c^T - 2\mathbf{B}_c^T\mathbf{K}\mathbf{L}\mathbf{C}_c^T\right] \tag{4.1}$$

where `diag` denotes a function that sets all off-diagonal terms of the matrix to 0. For maximising the power absorption with a diagonal controller, the same procedure can be used, i.e. the off-diagonal terms of the gradient matrix (equation 3.50) and the initial matrix should be zero.

For decentralised control, stability is guaranteed as long as all the gains remain positive.

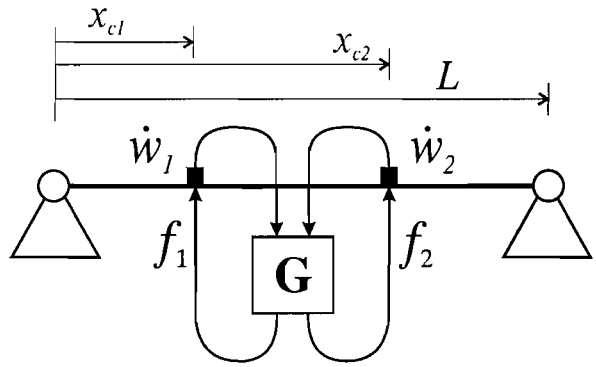

Figure 4.2: Control locations of two channel controller on a beam.

4.2 Comparison of centralised and decentralised control

This section will investigate whether there is a significant difference in performance between centralised and decentralised constant gain feedback control and LQG control, for collocated force actuators and velocity sensors. Therefore, centralised and decentralised control are compared when the control location are varied across the structure and when the control effort is varied. If a small difference is found, that means that decentralised constant gain velocity feedback control can be a good approximation of the centralised, dynamic LQG controller.

4.2.1 Varying control locations on the beam

A two channel controller is considered in which the control locations x_{c1} and x_{c2} are at different points on the simply supported beam, as shown in figure 4.2.

Figures 4.3(a) and 4.3(b) show, for the optimised centralised and decentralised constant gain feedback controllers, the reduction in kinetic energy in comparison to the uncontrolled case as a function of the positions of the two control locations. The control effort weighting was fixed for all control locations to $1.0 \cdot 10^{-5}$. Along the line $x_{c1} = x_{c2}$, a SISO velocity feedback controller is obtained.

It can be seen that best performance is achieved by avoiding the nodal lines of

the first few modes, symmetric placement around the mid-point of the beam and placing both controllers at the same end of the beam. Because the figures are very similar when the control locations are widely spaced, the difference between these two figures has also been plotted in figure 4.4.

Figure 4.4 shows that the differences in performance between the centralised and decentralised controllers are small when the control locations are *widely* spaced. The difference in performance if the control locations are *closely* spaced can be linked to the ability of the centralised controller to estimate the angular velocity of the beam in between the control locations and apply a corresponding negative moment. This is further examined in section 4.2.2.

4.2.2 Analysis of the difference between centralised and decentralised control

There is only a significant difference between optimal centralised and decentralised controllers if the control locations are closely spaced. Here, the performance difference is analysed by examining the structure of the controllers.

4.2.2.1 Centralised controller

When the control locations are closely spaced, the difference in velocity at the two locations may be a good measure of the angular velocity of the beam, around a point in between the two control locations, as shown in figure 4.5.

$$\dot{\alpha}_x \approx \frac{\dot{w}_1 - \dot{w}_2}{2\Delta x} \tag{4.2}$$

The average of the two velocities would be a measure of the linear velocity at that point:

$$\dot{w}_x \approx \frac{\dot{w}_1 + \dot{w}_2}{2} \tag{4.3}$$

Similarly, the difference between the forces applied at the points would be a good approximation to a point moment input, whereas the sum of the forces would be an approximation to a single point force:

$$m_x \approx (f_2 - f_1)\,\Delta x \tag{4.4}$$

$$f_x \approx f_1 + f_2 \tag{4.5}$$

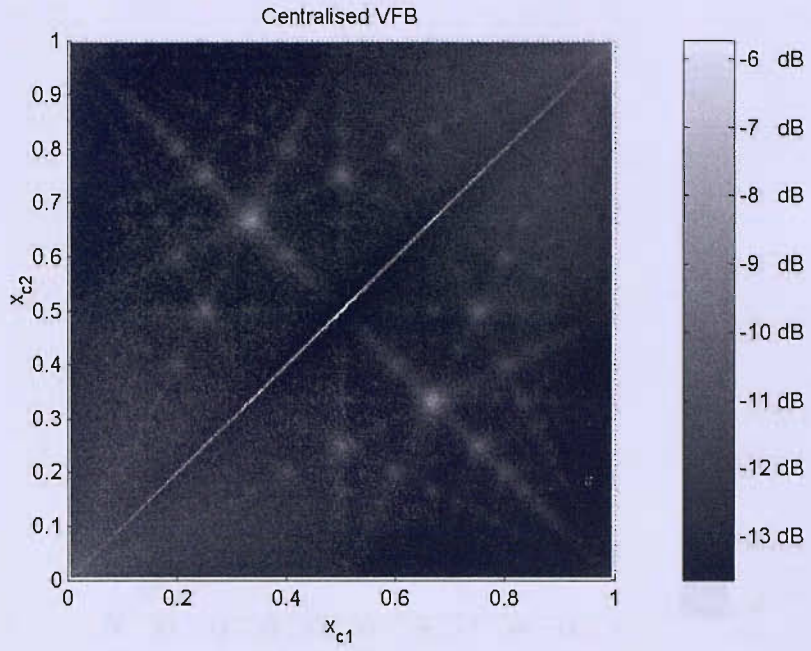

(a) Centralised control

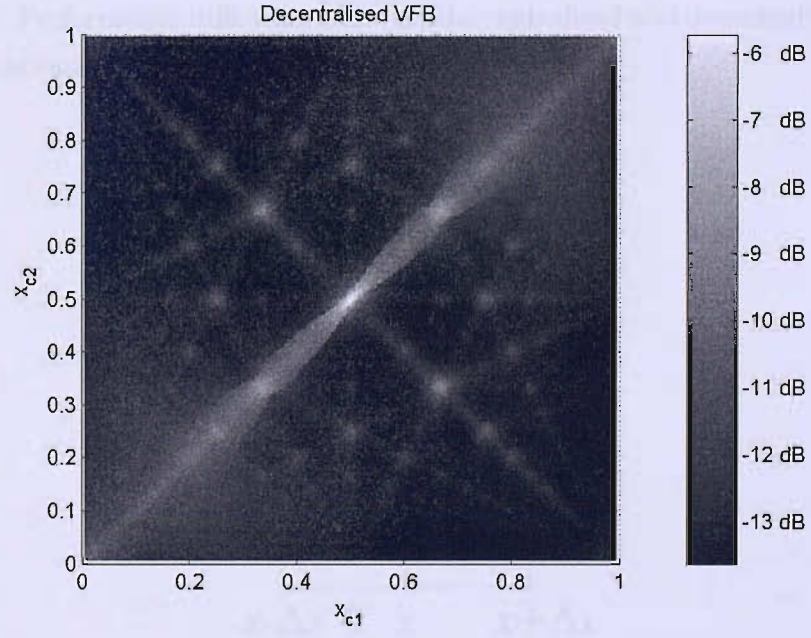

(b) Decentralised control

Figure 4.3: Performance, measured as change in kinetic energy relative to the uncontrolled beam, of the centralised and decentralised control for velocity feedback control using two force actuators on the beam. Control locations at (x_{c1}, x_{c2}).

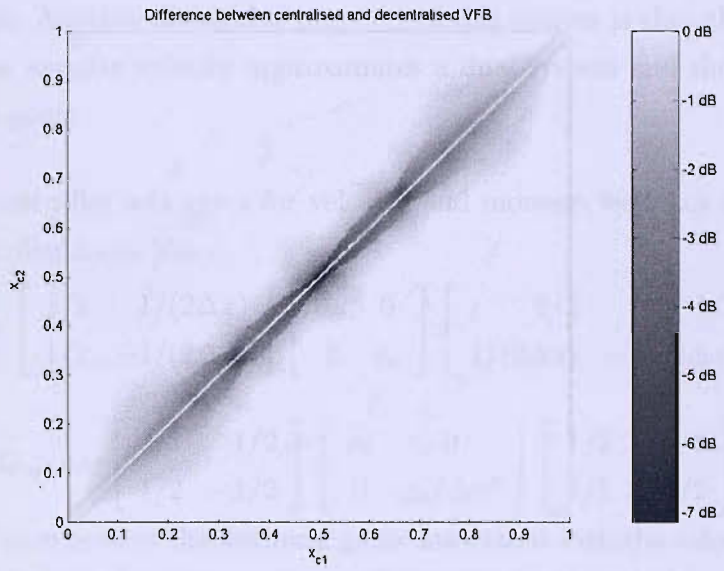

Figure 4.4: Performance difference between the centralised and decentralised control, control locations are at (x_{c1}, x_{c2}).

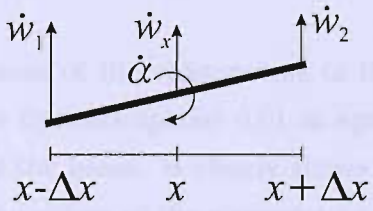

Figure 4.5: If the control locations are closely spaced, the difference in the measured velocity may be due to the angular velocity of the beam.

If these approximations hold for small spacings between the controllers, the centralised controller can calculate the linear and angular velocity and apply an independent force and moment in opposition to these motions, thus extracting power from the beam. Another favourable property of this system is that the control loop controlling the angular velocity approximates a dual system and should be stable, even for large gains.

Thus, if the controller sets gains for velocity and moment feedback independently, then the controller looks like:

$$\mathbf{G}_{split} = \begin{bmatrix} 1/2 & 1/(2\Delta x) \\ 1/2 & -1/(2\Delta x) \end{bmatrix} \begin{bmatrix} g_{\dot{w}} & 0 \\ 0 & g_{\dot{\alpha}} \end{bmatrix} \begin{bmatrix} 1/2 & 1/2 \\ 1/(2\Delta x) & -1/(2\Delta x) \end{bmatrix} \tag{4.6}$$

or:

$$\mathbf{G}_{split} = \begin{bmatrix} 1/2 & 1/2 \\ 1/2 & -1/2 \end{bmatrix} \begin{bmatrix} g_{\dot{w}} & 0 \\ 0 & g_{\dot{\alpha}}/\Delta x^2 \end{bmatrix} \begin{bmatrix} 1/2 & 1/2 \\ 1/2 & -1/2 \end{bmatrix} \tag{4.7}$$

where $g_{\dot{w}}$ and $g_{\dot{\alpha}}$ represent the feedback gains associated with the velocity and angular velocity feedback, at x. The matrices in equation 4.7 can be rescaled according to:

$$\mathbf{G}_{split} = \begin{bmatrix} \frac{1}{\sqrt{2}} & \frac{1}{\sqrt{2}} \\ \frac{1}{\sqrt{2}} & -\frac{1}{\sqrt{2}} \end{bmatrix} \begin{bmatrix} g_{\dot{w}}/2 & 0 \\ 0 & g_{\dot{\alpha}}/\left(2\Delta x^2\right) \end{bmatrix} \begin{bmatrix} \frac{1}{\sqrt{2}} & \frac{1}{\sqrt{2}} \\ \frac{1}{\sqrt{2}} & -\frac{1}{\sqrt{2}} \end{bmatrix} \tag{4.8}$$

or:

$$\mathbf{G}_{split} = \mathbf{T}\mathbf{G}_{eq}\mathbf{T} \tag{4.9}$$

This rescaling has the advantage that $\mathbf{T} = [\mathbf{T}]^{-1}$, such that if $\mathbf{G}_{opt}$ equals $\mathbf{G}_{split}$, $\mathbf{G}_{opt}$ is a similar matrix to $\mathbf{G}_{eq}$. Hence they must share the same eigenvalues, which would be $g_{\dot{w}}/2$ and $g_{\dot{\alpha}}/\left(2\Delta x^2\right)$. Additionally, the columns of $\mathbf{T}$ should be the corresponding eigenvectors.

Figure 4.6(a) shows the values of the eigenvectors of the optimal centralised controller, for control locations that are spaced 0.01 m apart and are placed at equal distances from a point x on the beam. It clearly shows that, when the control locations are closely spaced, the values of the eigenvectors are indeed equal to $\pm 1/\sqrt{2}$ for most of the length of the beam. The exception being when x is close to the ends of the beam, in which case the controller apparently does not approximate equation 4.9. This is due to the cost placed on the control effort.

The distance 0.01 m, chosen for figure 4.6(a) is below the shortest wavelength, of 0.04 m, for the 50 modes included in the model. Hence the values of the eigenvectors

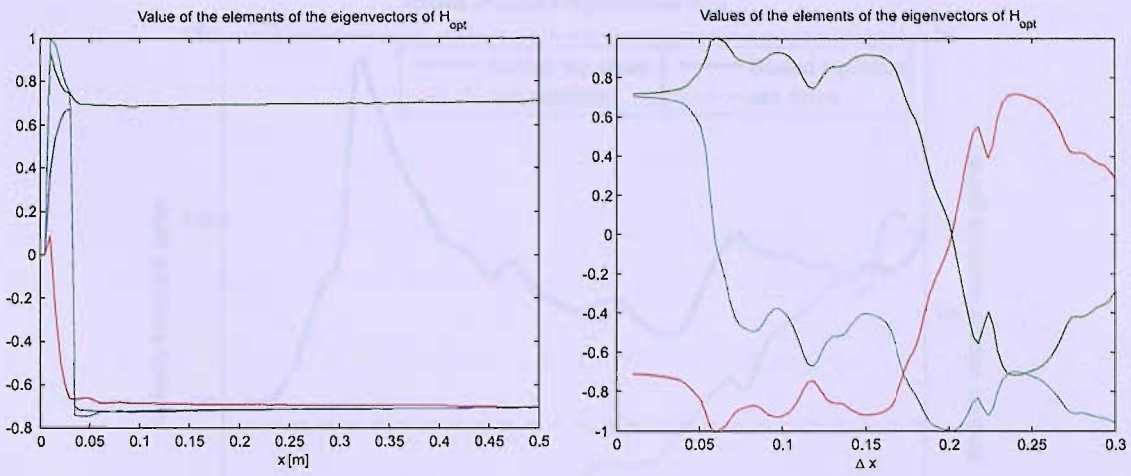

(a) $\Delta x = 0.01$ m, x varies

(b) $x = 0.45$ m, Δx varies

Figure 4.6: Values of the elements of the eigenvectors of the optimal centralised controller $\mathbf{G}_{opt}$, in the case in which a) Δx is small and constant and the position of the controller along the beam is varied, and b) the position is fixed and Δx is varied.

should also be examined for different values of Δx. Figure 4.6(b) shows the values of the eigenvectors as the distance of the control locations to a point 0.45 m along the beam is decreased. This figure shows that the values of the eigenvectors converge to $\pm 1/\sqrt{2}$ as Δx tends to zero. It also shows that this effect is noticeable beyond the width of the smallest wavelength, as the values diverge at about $\Delta x = 0.05$ m. At this point the distance between two control locations is 0.10 m, which is significantly more than the shortest wavelength. The distance between the control locations for which the decompostion seems to hold is apparently not related to the wavelength of highest order mode. Indeed, simulations with different numbers of modes taken into account also place the transition of the values of the eigenvectors at $\Delta x = 0.05$ m.

The distance of 0.10 m between the controllers, for which the decomposition holds, matches the distance for $x = 0.45$ m in figure 4.4 at which the difference between centralised and decentralised control becomes noticeable.

As indicated in figure 4.7, the eigenvalues also seem to converge to fixed values as Δx is reduced. These values can be compared to optimum gains calculated for decentralised angular and transverse velocity feedback control at the specified

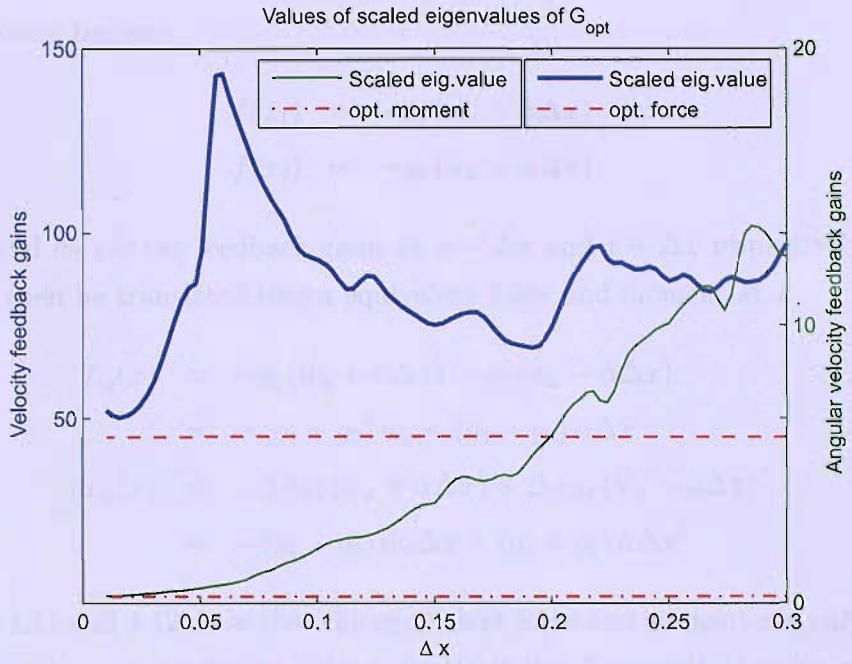

Figure 4.7: Eigenvalues of the controller if controllers are spaced symmetrically with respect to the point $x = 0.45L$, for different distances Δx.

location. However, the gains deviate slightly at very small spacings. This may be due to coupling that can occur between the angular and velocity feedback gains. Though the controller can control rotation and translation velocities separately, it can also implement some coupling.

If this mechanism is valid on the beam, it should work on the plate too. Simulations with 3 randomly placed control locations on the simply supported plate also showed hardly any difference between centralised and decentralised control unless the minimum distance between control locations was smaller than 0.04 m. This corresponds to a 1/10th of the maximum dimension of the examined plate, which is similar to what it was on the beam.

4.2.2.2 Decentralised controller

The decentralised controller can only give a local velocity feedback gain. Assuming that control locations are so closely spaced that equations 4.2 and 4.3 apply, the

feedback forces become:

$$\begin{aligned} f(x_1) &= -g_1\left(\dot{w}_x + \dot{\alpha}\Delta x\right) \\ f(x_2) &= -g_2\left(\dot{w}_x - \dot{\alpha}\Delta x\right) \end{aligned} \tag{4.10}$$

where h_1 and h_2 are the feedback gains at $x - \Delta x$ and $x + \Delta x$ respectively. These forces can then be translated into a equivalent force and moment at x:

$$\begin{aligned} f_{eq}(x) &= -g_1\left(\dot{w}_x + \dot{\alpha}\Delta x\right) - g_2\left(\dot{w}_x - \dot{\alpha}\Delta x\right) \\ &= -\left(g_1 + g_2\right)\dot{w}_x - \left(g_1 - g_2\right)\dot{\alpha}\Delta x \end{aligned} \tag{4.11}$$

$$\begin{aligned} m_{eq}(x) &= -\Delta x g_1\left(\dot{w}_x + \dot{\alpha}\Delta x\right) + \Delta x g_2\left(\dot{w}_x - \dot{\alpha}\Delta x\right) \\ &= -\left(g_1 - g_2\right)\dot{w}_x\Delta x - \left(g_1 + g_2\right)\dot{\alpha}\Delta x^2 \end{aligned} \tag{4.12}$$

Equations 4.11 and 4.12 show that the equivalent force and moment can only control the linear and angular velocity independently if the decentralised gains g_1 and g_2 are equal, in which case the feedback gains associated with the linear and angular velocity are also equal. The tuning of the gains g_1 and g_2 must then be a balance between obtaining control with linear velocity or angular velocity feedback. This is in contrast with centralised control. Centralised control can not only control linear and angular velocity independently, but can also set the corresponding values of the gains independently.

Figure 4.8 shows the gains of the optimal decentralised controller as a function of Δx. The increase of the gains to 200 Ns/m for small values of Δx shows that the decentralised controller is then controlling the angular velocity, rather than the velocity. This results in a controller that effectively pins the structure at x, and then absorbs power from the rotation of the beam around that point. If Δx becomes very small, this mechanism is no longer optimal because of control effort weighting.

4.2.2.3 Not a single minimum

The fact that for the decentralised case, the controller balances two mechanisms of power extraction suggest that there may be two local minima in the cost function. One of these can then be a global minimum. Figure 4.9 shows the relative kinetic energy of the beam for different combinations of feedback gains for x_c =[0.480 0.485] m. This figure clearly shows that, in this case, there are two local minima. The

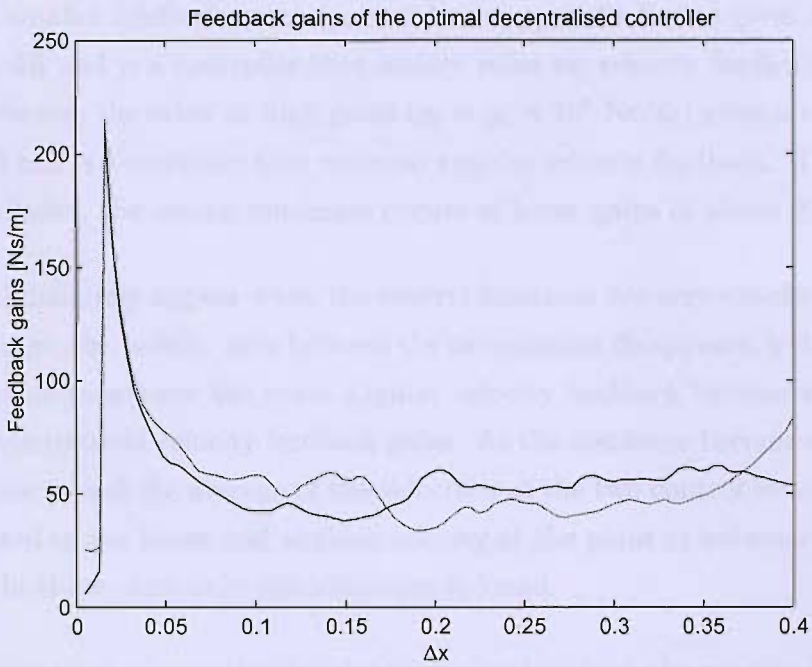

Figure 4.8: The optimised feedback gains of the decentralised controller for varying Δx, $x = 0.45$ m.

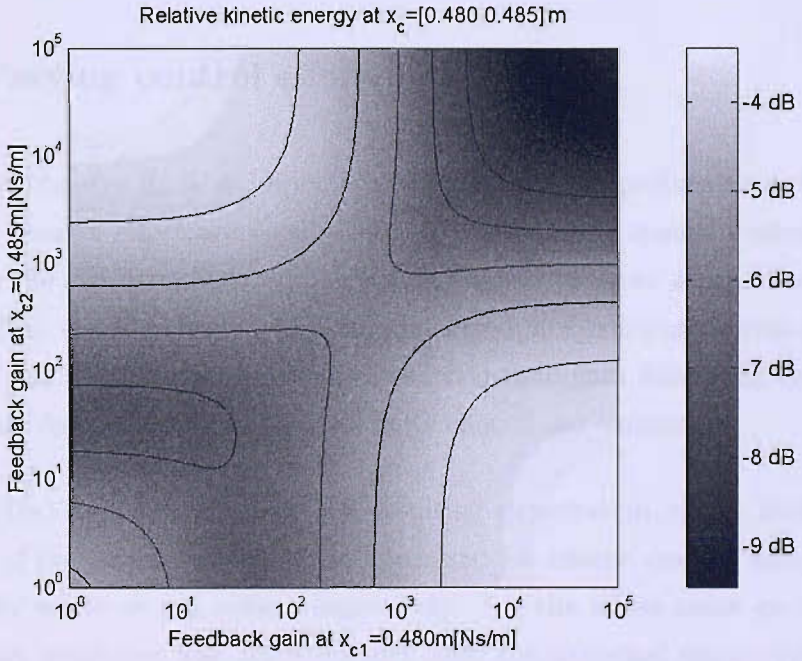

Figure 4.9: The kinetic energy as a function of feedback gains with two velocity feedback loops at x_c =[0.480 0.485] m has 2 local minima.

one at the smaller feedback gains ($g_1 \approx 0$ Ns/m, $g_2 \approx 20$ Ns/m) gives a reduction of about 6 dB and is a controller that mainly relies on velocity feedback to reduce the cost, whereas the other at high gains ($g_1 \approx g_2 \approx 10^5$ Ns/m) gives a reduction of about 9 dB and is a controller that relies on angular velocity feedback. If the control effort is included, the second minimum occurs at lower gains of about 200 Ns/m.

The two minima only appear when the control locations are very closely spaced, for larger spacings, the 'saddle' area between the two-minima disappears, as the required feedback gains to achieve the same angular velocity feedback become smaller and similar to the optimal velocity feedback gains. As the distances become even larger, the difference in and the average of the velocities at the two control locations are no longer related to the linear and angular velocity at the point in between the control locations. In these cases only one minimum is found.

For the comparison of centralised and decentralised control, the existence of the two minima makes little difference, as the difference in performance between the two minima is small compared to the difference between the centralised and decentralised controller.

4.2.3 Varying control effort on a plate

As noted in chapter 3, it is important to compare the performance when equal amounts of control effort are used. Here, sixteen equally spaced control locations are used on the simply supported plate, as indicated in figure 4.10. At each control location, ideal velocity sensors are assumed that are collocated with ideal force actuators. For the comparison, centralised constant gain feedback, decentralised constant gain feedback and centralised LQG control are examined.

Figures 4.11(a) and 4.11(b) show the resulting expectation of the kinetic energy when each of the three controllers are optimised for kinetic energy, when the plate is excited by white or red noise, respectively. For the white noise excitation, the control effort weighting was adjusted such that the expected controller effort was equal to 300 N^2 for each controller. For the red noise, the level of excitation is far less and so the control effort was now limited to $3 \cdot 10^{-3}$ N^2 for each controller. Note that in section 4.2.1 the control effort weighting was fixed and not the control effort

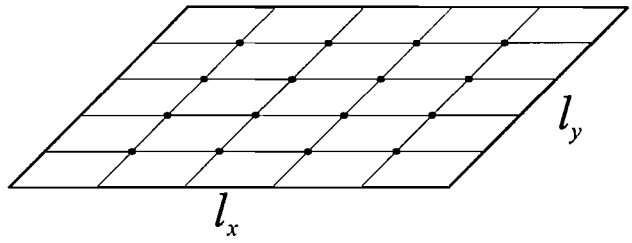

Figure 4.10: Equally spaced sensors and actuators on a simply supported plate. Each dot represents a collocated velocity sensors and point force actuator pair.

itself.

It can be seen from the figures that over all frequencies there is little difference between decentralised and centralised constant gain control. LQG control gives a slight improvement for control of kinetic energy in the white noise case. For red noise, LQG control seems to perform less well than the constant gain controllers. This is due to the extent of the reductions that are achieved, which cause the sensor signals to be in the range of the sensor noise that was assumed in the design of the LQG controller. It is interesting to note that each of the gains in the optimised constant gain decentralised controller were of similar magnitude, but that the optimised centralised constant gain controller also had significant off-diagonal gains, even though these did not contribute significantly to the reduction in the cost function.

The overall difference in the cost function is difficult to see from these plots and it is not clear whether this level of effort is most appropriate. Therefore, the overall reduction in the expected kinetic energy reduction should be examined as a function of control effort. Figure 4.12(a) and 4.12(b) show the change in kinetic energy as a function of the control effort for white and red noise excitation respectively, which has been computed by optimizing the three controllers with varying control effort weightings. It can be seen for white noise, that there is some advantage in using LQG control rather then constant gain feedback since for a given performance, the control effort is slightly lower. This difference is small though.

For red noise there are nearly no differences between the controllers for low control efforts, but the LQG controller performs worse at higher control efforts, which is again due to the fact that the LQG controller takes sensor noise into account in the design, but that no noise was taken into account in the calculation of the cost

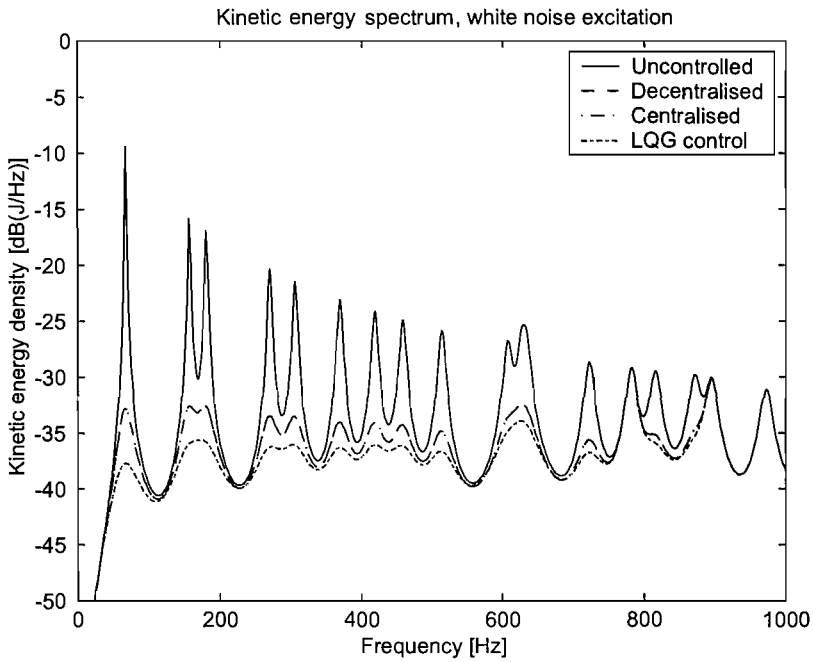

(a) KE vs. frequency, white noise

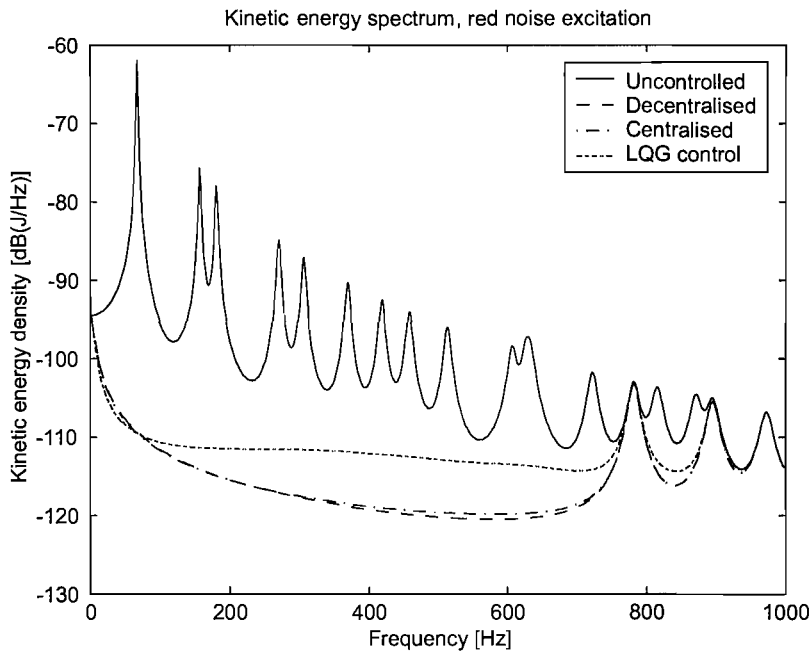

(b) KE vs. frequency, red noise

Figure 4.11: Spectrum of expected kinetic energy (KE), assuming white or red noise excitation, before and after control, using different controllers optimised to control kinetic energy. The expected average control effort for each controller was limited to 300 N^2 for white noise excitation and $3 \cdot 10^{-3}$ N^2 for red noise.

function. The sensor noise was set to have a variance of $1 \cdot 10^{-9}$ for the red noise excitation. For white noise, the variance was set to $1 \cdot 10^{-5}$. In the design of the LQG controller, red noise was taken into account, by using the matrix $\mathbf{P}_r$ defined by equation 2.47. The graphs comparing control effort and change in cost function could also provide an important design tool in determining the correct trade off between performance and control effort for a given application.

From the figures it can be seen that there is little difference between the effectiveness of the different controllers. However, these results were obtained with the controller at particular points on the plate, where certain modes cannot be controlled, as can be seen in figure 4.11(a). It is not clear how this affects the results obtained and whether the same conclusions can be drawn for a different placement of the actuators. Therefore, the difference between the controllers for a give control effort has also been examined for randomly placed control locations. The number of control locations was limited to 5. It was found that the differences between centralised, decentralised constant gain and LQG control remain small, though LQG control did show slightly better performance in the case of white noise. LQG control did not improve the performance in the case of red noise excitation, because of the amount of sensor noise considered in the design of the controller.

4.3 Comparison of optimised and approximated decentralised velocity feedback control

The comparison in section 4.2 found that a difference in performance between decentralised and centralised LQG control only occurs when controllers are closely spaced. As the close spacing of controllers was not found to contribute to the performance and required high control forces to generate the required moment, close spacing is excluded from further comparisons.

If it can now be shown that the difference in performance between the approximations, discussed in chapter 3 and optimal *decentralised* control is also small, then the difference between the approximations and the *centralised* controller must also small. This would satisfy the goal discussed in section 1.3, that the decentralised control strategy should have comparable performance to an optimal centralised controller.

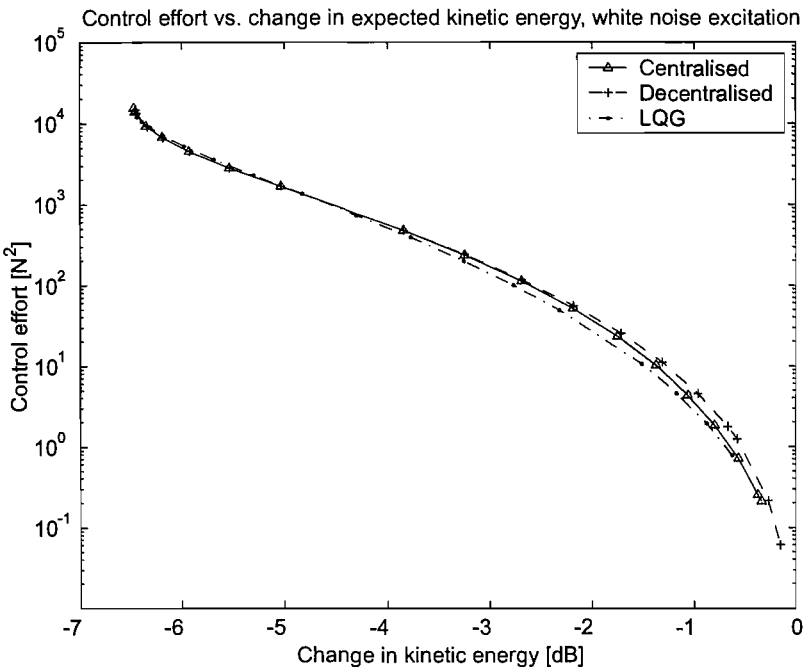

(a) KE vs. effort, white noise

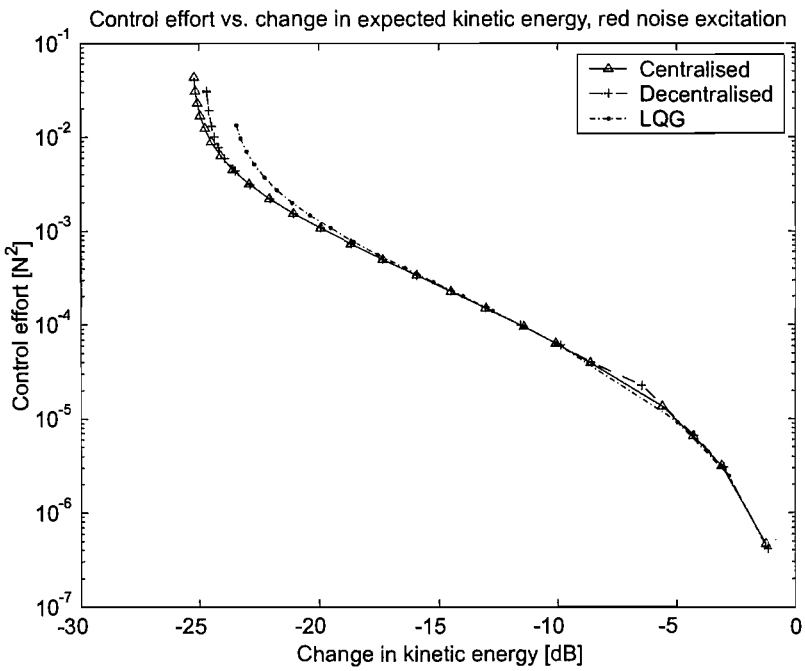

(b) KE vs. effort, red noise

Figure 4.12: Change in expected kinetic energy (KE) as a function of effort, assuming white or red noise excitation, using different controllers optimised to control kinetic energy.

The comparison of the performance in the multi-channel set-up of the optimised decentralised control and the approximations is carried out separately for the plate and the beam structure.

4.3.1 Comparison on the beam

In this section optimised decentralised control is compared to the three-mode and simplified two-mode approximations and to decentralised maximum power absorption. Like the analysis in chapter 3, three aspects are examined: the obtained feedback gains, the control effort and the actual reductions in kinetic energy. They are compared by placing 3 control locations randomly along the beam, but not allowing them to be within 0.1 m of each other or within 0.1 m of the ends of the beam. However, because setting the gains with the simplified two-mode and three-mode formula is not limited with respect to control effort, the effort weighting has been chosen small so it does not influence the optimisation of the gains significantly.

Figure 4.13 shows a histogram of the gains for 3 control locations, placed randomly 500 times, but constrained to match the criteria mentioned above. The gain set with the simplified two-mode formula is not plotted as it is not location dependent, its value for this beam is 35.9 Ns/m. The means of gains set with the different feedback strategies have been listed in table 4.1. The table shows that the gains set with maximum power absorption were on average 3 times as high as the ideal gain for the white noise exicitation. This also has consequences for the control effort, as can be seen in figure 4.14. This figure also shows that the simplified two-mode approximation has a remarkably constant control effort, over the 500 random locations it did not deviate more than 5% from the mean.

Figure 4.15 shows the distribution of the performance of the different approximations. The mean overall reduction achieved with the optimised feedback gains was 14.3 dB. The figure suggests that the simplified two-mode approximation is the best approximation, when using a white noise excitation. Though maximising the power absorption led to significantly higher gains and control effort, the differences in terms of performance are not as big. This is due to the nature of the cost surface. Figure 3.9 showed that, for the single-channel case, the range of the gains performing close to optimal is quite wide, these results indicate that the same may is true in the

multi-channel case. The data from the above figures has been summarised in table 4.1. The reductions for maximum power absorption and with the simplified two-mode approximation are close to the optimum reduction obtained by minimising the kinetic energy.

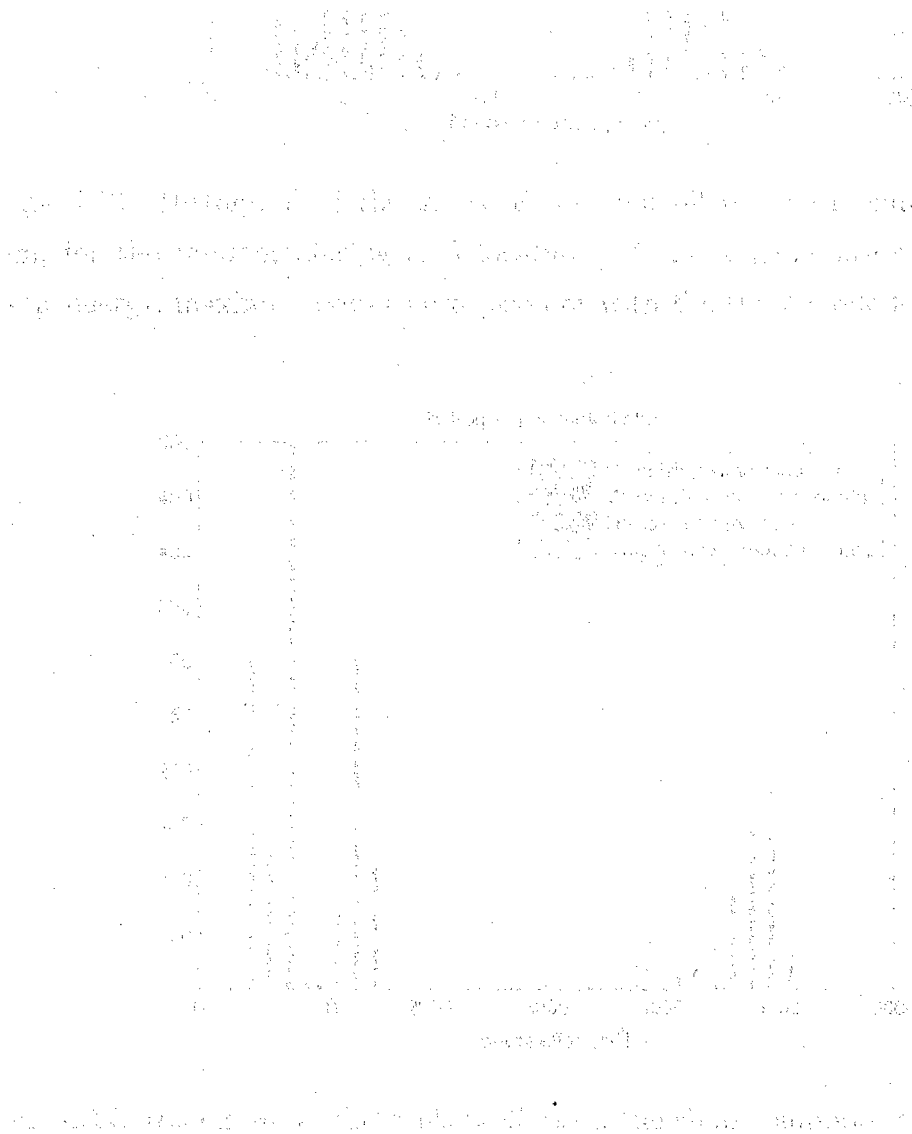

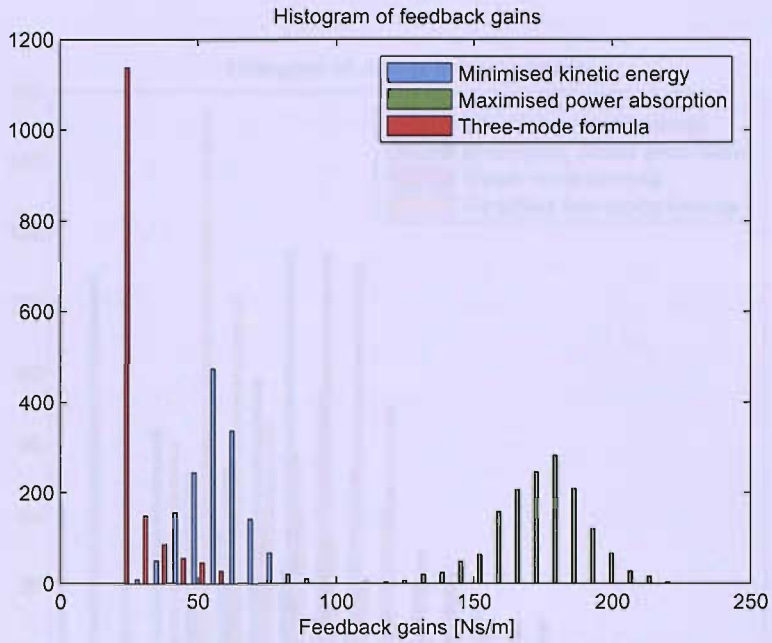

Figure 4.13: Histogram of the gains of the controllers on the simply supported beam, for the random placing of 3 locations. Control gains are set to minimise kinetic energy, maximise power absorption or with the three-mode formula.

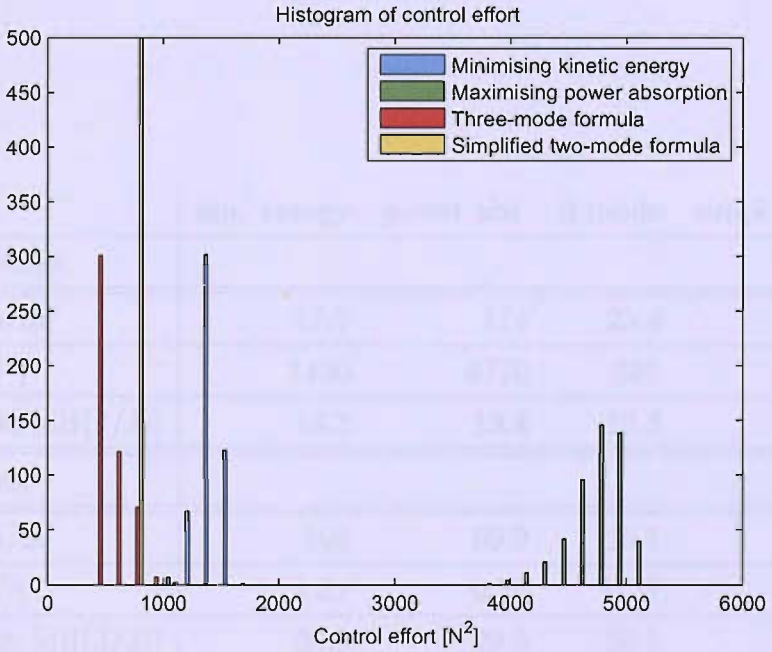

Figure 4.14: Histogram of the control effort on the simply supported beam, for the random placing of 3 locations. Control gains are set to minimise kinetic energy, to maximise power absorption or with the three-mode or simplified two-mode formulas.

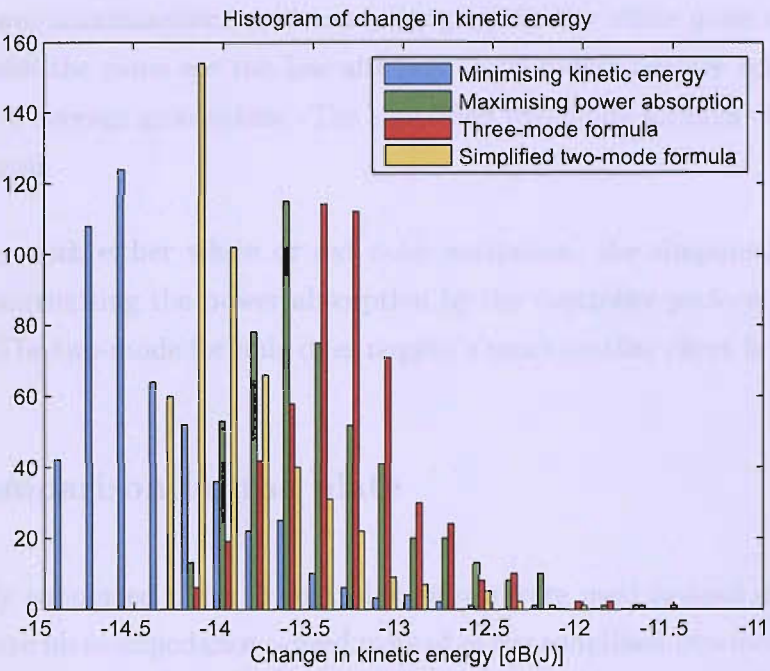

Figure 4.15: Histogram of the changes in kinetic energy on the simply supported beam. Control gains are set to minimise kinetic energy, maximise power absorption or with the three-mode or simplified two-mode formulas.

Strategy	kin. energy	power abs.	3 mode	simpl. 2 mode
WHITE NOISE				
Gain [Ns/m]	57.7	174	25.4	35.9
Effort [N^2]	1430	4770	527	797
Reduction [dB(J/J)]	14.3	13.4	13.3	13.9
RED NOISE				
Gain [Ns/m]	108	69.9	25.7	35.9
Effort [N^2]	1.21	0.77	0.27	0.40
Reduction [dB(J/J)]	30.9	29.5	25.5	27.2

Table 4.1: Mean results for different control strategies on the simply supported beam, for white and red, randomly distributed excitation.

The table also lists the results obtained for the red noise case. It can be seen that where the power maximisation used too large gains in the white noise case, in the case of red noise the gains are too low although good reductions are achieved with a wide range of average gain values. The simplified two-mode formula obtained the best results again.

For the beam, with either white or red noise excitation, the simplified two-mode formula and maximising the power absorption by the controller perform well in the MIMO case. The two-mode formula does require a much smaller effort in both cases.

4.3.2 Comparison on the plate

On the simply supported plate, 5 control locations were used instead of 3 and the matched infinite plate impedance is used instead of the simplified two-mode formula. Again, the controllers are not allowed to be within a distance of 10% of largest dimension to the edges of the plate or each other and have been otherwise placed randomly. Figures 4.16 and 4.17 show the distribution of the gains and the control effort after optimisation. The results for the three-mode formula have not been shown in these figures as the variance in the gains set with this formula is quite large. Figure 4.18 shows the relative performance of the approximations to the optimised kinetic energy.

The results have been listed in table 4.2. The first result that is obvious from both the figure and the table, is that the gains set to maximise power absorption remain much closer to those set to minimise the kinetic energy. Also, the variation in the control effort of the matched infinite plate impedance is very small, i.e. it is nearly independent on the placement of the controllers itself or the other controllers. For the white noise excitation, maximum power absorption and matched infinite plate impedance perform almost as well as the controller that minimises the kinetic energy.

Table 4.2 also lists the results for red noise. Unlike for the beam, the mean of the gains that maximise power absorption hardly changes. However, the difference with the optimal performance increases. For a red noise excitation, maximising power absorption is still the best approximation, followed by matching the impedance of an infinite plate.

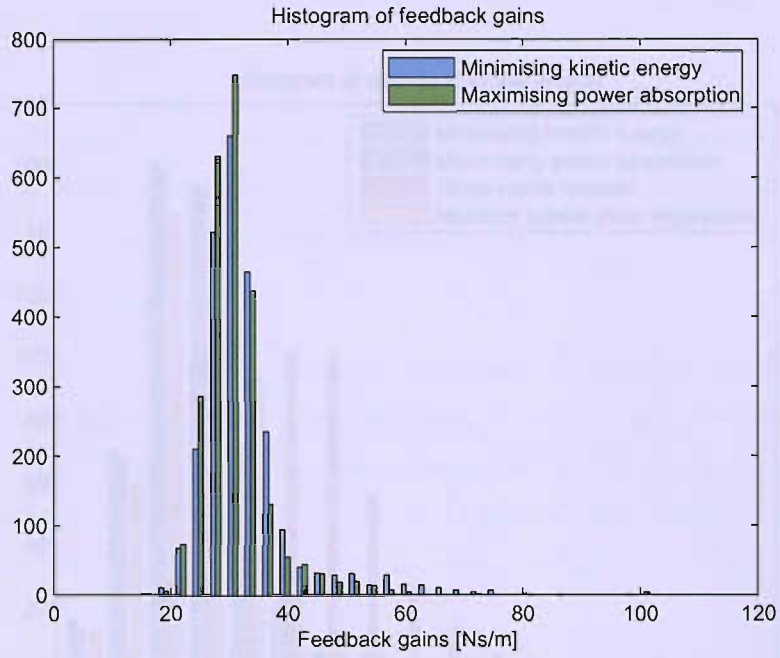

Figure 4.16: Histogram of the gains of the controllers on the simply supported plate, for the random placing of 5 control locations. Gains are set to minimise the kinetic energy or to maximise the power absorbed.

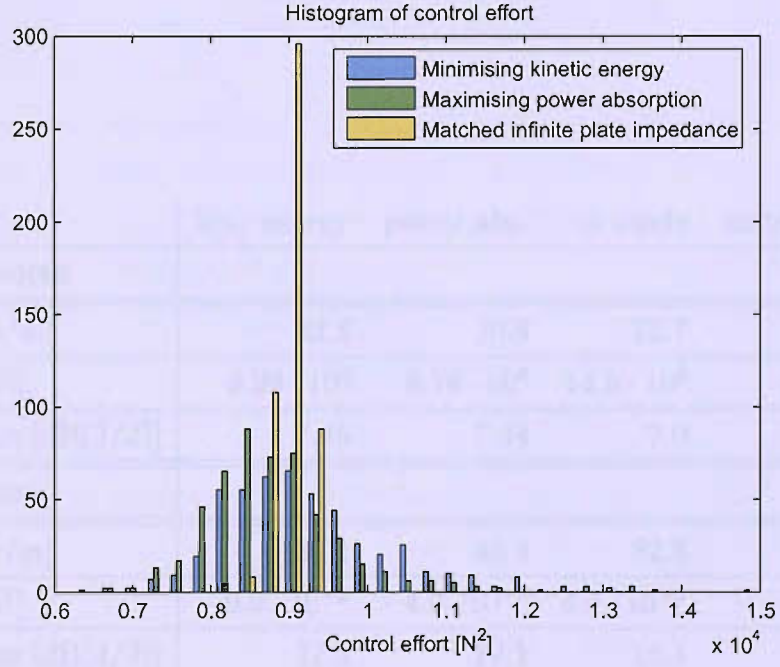

Figure 4.17: Histogram of the control effort on the simply supported plate, for the random placing of 5 control locations. Gains are set to minimise kinetic energy, maximise power absorption or with the matched infinite plate impedance formula.

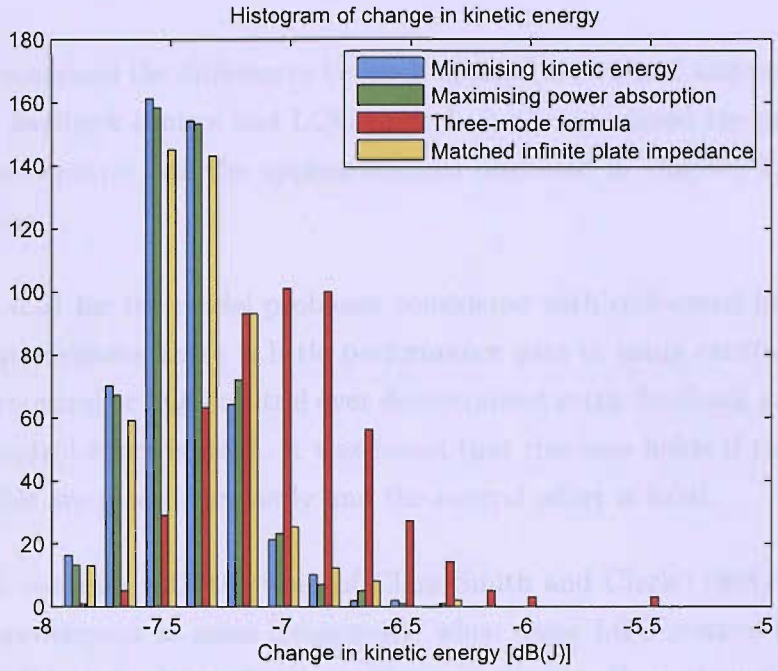

Figure 4.18: Histogram of changes in kinetic energy on the simply supported plate. Gains are set to minimise kinetic energy, maximise power absorption or with the three-mode or matched infinite plate impedance formulas.

Strategy	kin. energy	power abs.	3 mode	matched imp.
WHITE NOISE				
Gain [Ns/m]	32.8	30.8	75.7	31.9
Effort [N^2]	$9.28 \cdot 10^3$	$8.76 \cdot 10^3$	$14.5 \cdot 10^3$	$9.03 \cdot 10^3$
Reduction [dB(J/J)]	7.45	7.44	7.0	7.42
RED NOISE				
Gain [Ns/m]	89.1	44.4	82.5	31.9
Effort [N^2]	$9.9 \cdot 10^{-3}$	$4.2 \cdot 10^{-3}$	$4.6 \cdot 10^{-3}$	$3.0 \cdot 10^{-3}$
Reduction [dB(J/J)]	17.5	17.1	16.1	16.6

Table 4.2: Mean results for different control strategies on the plate, for white and red, randomly distributed excitation.

4.4 Conclusions

This chapter examined the differences between optimal centralised and decentralised constant gain feedback control and LQG control. It also examined the performance of decentralised control and the approximations discussed in chapter 3, for multi-channel systems.

It was shown that for the model problems considered with collocated force actuators and velocity sensors, there is little performance gain in using centralised static feedback gain control or LQG control over decentralised static feedback gain control, when equal control effort is used. It was found that this also holds if the locations of the controller are placed randomly and the control effort is fixed.

This seems to contrast with the work of Clark Smith and Clark (1998) who saw a significant improvement as some frequencies, when using LQG control in a single-channel controller and a large distributed sensoriactuator. Even though significant differences were seen over some frequency ranges, the frequency ranges over which the improvement occurs is limited and may be offset by other frequency ranges were performance is worse. On average, this resulted in only a small difference in the actual, overall cost function. Elliott (2004) has noted that if the number of control loops is equal to the number of controlled modes, then under idealised circumstances the effect of a decentralised constant gain controller would be equal to that of a fully coupled modal controller. This may explain why, in the case of red noise excitation, when there are only very few modes contributing significantly to the cost function, there is hardly any difference between centralised, decentralised and LQG control. Further research into the relation between the number of excited modes and the number of control locations for which the difference in performance between dynamic controllers and static controllers becomes small, may prove interesting.

A comparison of centralised and decentralised constant gain feedback control on the beam, as a function of the spacing of the two controllers found that there is only a significant difference in performance if the controllers are closely spaced. In that case, the centralised controller is able to control both the rotation and the displacement of the structure at a point in between the two control locations. The decentralised controller can, for close spacings, control either the displacement and not the rotation, or pin the structure and only control the rotation. This results in

two minima in the cost surface of the decentralised controller.

The optimised decentralised feedback gain controller was compared to different approximations to the optimum gain on the beam and the plate. Random placement of the controllers was considered, but close spacing of the controllers to each other or the edges of the structure was not allowed, in light of the results of section 4.2.1 and the analysis in section 4.2.2.

On the beam, it was found that the simplified two-mode approximation of the optimum gain and the maximimum power absorbing controller tended to get a performance that in most cases was within 1 dB of the optimal controller. Considering that the differences between LQG and the decentralised controller were also small, these decentralised control strategies are thus seen to give a performance that is close to that of a fully coupled, dynamic controller.

For the plate, maximising the power absorption performed well for both white and red noise excitation, as did matching the infinite plate impedance. The choice as to which of these two should be preferred for approximating the optimal gain on the plate can not be decided on these results. Chapter 6 will compare how such control strategies would tune themselves on an actual plate when other controllers are present.

Considering that the power absorption strategy minimises the power loss in the structure itself, as was discussed in chapter 3, it seems that the power loss in the structure can be influenced in the case of the beam and, especially in the case of red noise, this has a detrimental effect on the kinetic energy in the structure. On the plate, this does not seem to be the case.

Chapter 5

Sound radiation from a plate

Active Structural Acoustic Control (ASAC) is concerned with controlling the sound radiation from a structure, by controlling the velocity of the surface of the structure itself. For single frequency disturbances, the sound radiation from a plate into the farfield can be calculated accurately using either a farfield approximation, as described by Wallace (1972a) and Wallace (1972b) or a nearfield approximation, as used by Elliott and Johnson (1993). To calculate an optimised controller to control broadband noise radiation, a frequency dependent filter is required to estimate the radiation from the structure. This section describes the development of state-space filters for the purpose of calculating the sound radiation from a simply supported plate. Also, it compares the performance of various controllers designed for ASAC with each other and with controllers designed to minimise the kinetic energy of the structure.

First, the two methods of calculating the farfield radiation are presented. Secondly, two methods of creating the required filters are examined and compared. These methods are the direct spectral factorisation of the modal radiation matrix, as used by Baumann et al. (1991) and Thomas and Nelson (1995) and the radiation mode approach based on work by Borgiotti (1990) and Elliott and Johnson (1993). This latter approach is used in various recent papers, e.g. Cox et al. (1998), Clark and Bernstein (1998) and Elliott et al. (2002). The most suitable model is then used to create optimised controllers for ASAC. These controllers are compared with each other to examine the benefits of dynamic and/or centralised control over decentral-

ised controllers and with controllers designed to minimise kinetic energy to examine the benefits of designing for ASAC.

5.1 Far- and nearfield approximation

The radiated sound power of a plate can be calculated either by examining the farfield or the nearfield of sound pressure levels. As the sound propagation models used here do not include any power loss in air itself, these two models should produce the same result as the power going into the system in the nearfield should be equal to the power going 'out' of the system in farfield. Both methods are based on the assumption that the sound pressure levels do not influence the structure itself.

5.1.1 Farfield approximation

This approximation follows the work of Wallace (1972a) and Wallace (1972b), which describes that the radiated sound power from one side of the structure can be found by integrating the farfield acoustic intensity over a half sphere. The acoustic intensity is the time average of rate of flow of energy through a unit area perpendicular to the direction of propagation (Kinsler et al. (1982)) and is given for harmonic waves by:

$$I(\phi,\theta,r,j\omega) = \frac{|p_{acoust}(\phi,\theta,r,j\omega)|^2}{2\rho_0 c_0} \tag{5.1}$$

ρ_0 and c_0 are, respectively, the density and the speed of sound in the medium where sound is radiated into, in this case air. The acoustic pressure at a point in the farfield is calculated as:

$$p(\phi,\theta,r,j\omega) = -jk\rho_0 c_0 \frac{e^{jkr}}{2\pi r} \int_0^{l_y}\int_0^{l_x} \dot{w}(x,y) e^{-j(\alpha x/l_x + \beta y/l_y)} dxdy \tag{5.2}$$

with r the distance between the center of the plate and the point in the farfield and k is the wavenumber ω/c_0. α and β are given by:

$$\begin{aligned} \alpha &= kl_x \sin\theta\cos\phi \\ \beta &= kl_y \sin\theta\sin\phi \end{aligned} \tag{5.3}$$

These factors are based on the approximation that the point at which the pressure is observed is sufficiently in the farfield ($r >> \sqrt{l_x^2 + l_y^2}$, $r >> 2\pi c_0/\omega_n$).

The pressure depends on the transverse surface velocities of the plate. The velocity at a point (x, y) on the plate is given by:

$$\dot{w}(x,y) = \mathbf{\Psi}^T(x,y)\dot{\mathbf{a}} \tag{5.4}$$

where $\mathbf{\Psi}(x,y)$ is a vector of the amplitude of the modeshapes at (x,y) and $\dot{\mathbf{a}}$ is a vector of the modal velocities. This means that the pressure in the farfield is a linear combination of the modal velocities.

The modeshape i for a simply supported plate is sinusoidal:

$$\psi_i(x,y) = \sin\left(\frac{m\pi x}{l_x}\right)\sin\left(\frac{n\pi y}{l_y}\right) \tag{5.5}$$

Because of the sinusoidal shape, the factor for each modeshape can be calculated analytically:

$$\begin{aligned}
p_i(\phi,\theta,r,j\omega) &= -jk\rho_0 c_0 \frac{e^{jkr}}{2\pi r}\int_0^{l_y}\int_0^{l_x} \dot{a}_i\psi_i(x,y)e^{-j(\alpha x/l_x+\beta y/l_y)}dxdy \\
&= -jk\rho_0 c_0 \frac{e^{jkr}}{2\pi r}\int_0^{l_y}\int_0^{l_x} \sin\left(\frac{m\pi x}{l_x}\right)\sin\left(\frac{n\pi y}{l_y}\right)e^{-j(\alpha x/l_x+\beta y/l_y)}dxdy\dot{a}_i \\
&= -jk\rho_0 c_0 \frac{e^{jkr}}{2\pi r} l_x l_y mn\pi^2\left[\frac{(-1)^m e^{-j\alpha}-1}{\alpha^2-m^2\pi^2}\right]\left[\frac{(-1)^n e^{-j\beta}-1}{\beta^2-n^2\pi^2}\right]\dot{a}_i \\
&= \frac{e^{jkr}}{r} z_i \dot{a}_i
\end{aligned} \tag{5.6}$$

The factor z_i has been used here for compact notation. The integral of the farfield intensity, given by equation 5.1, over a half sphere can then be written as:

$$\begin{aligned}
P(j\omega) &= \int_0^{2\pi}\int_0^{\pi/2} \frac{|p_{acoust}(\phi,\theta,r,j\omega)|^2}{2\rho_0 c_0} r^2\sin\theta d\theta d\phi \\
&= \int_0^{2\pi}\int_0^{\pi/2} \dot{\mathbf{a}}^H\mathbf{z}\mathbf{z}^H\dot{\mathbf{a}}\sin\theta d\theta d\phi \\
&= \dot{\mathbf{a}}^H\left[\int_0^{2\pi}\int_0^{\pi/2}\mathbf{z}\mathbf{z}^H\sin\theta d\theta d\phi\right]\dot{\mathbf{a}} \\
&= \dot{\mathbf{a}}^H\mathbf{M}\dot{\mathbf{a}}
\end{aligned} \tag{5.7}$$

where $\mathbf{M}$ is called the modal radiation matrix. It should be noted that the scaling of $\mathbf{M}$ depends on the scaling of the modeshapes. Unfortunately, the integral in equation 5.7 can not be solved analytically and has to be evaluated over a number of points in the farfield to give an accurate approximation. The radiation efficiency for the modes is defined as:

$$\mathbf{S} = 8\mathbf{M}/\rho_0 c_0 l_x l_y \tag{5.8}$$

The on-diagonal elements of **S** are self-radiation efficiencies, the off-diagonal elements are mutual- or cross-radiation efficiencies.

The elements of **S** describing the self- and cross-radiation efficiencies of the first 10 structural modes of the simply supported plate have been plotted in figure 5.1. The self-radiation of volumetric modes (modes for which n and m are both uneven) is more efficient than that of other modes, as is indicated in figure 5.2. The radiation effiency of cross-combinations of modes drops off at higher frequencies, whereas the self-radiation of the modes approaches 1. Figure 5.1 also shows that at about 5 kHz a sort of spatial aliasing starts to occur due to the numerical integration in the farfield. It is interesting to see that it occurs at different frequencies for different modes. The radiation efficiency has been calculated on a grid of 40 points for θ and 160 points for ϕ.

The farfield approach for calculating the sound power is accurate, but requires knowledge of the modeshapes. Furthermore, for the method to work efficiently, the modeshapes of the structure must allow the integral in equation 5.2 to be solved analytically. This limits the applicability of this approach in terms of structural dynamics.

5.1.2 Nearfield approximation

This method is based on the acoustic power calculated at the source and is also described in Elliott and Johnson (1993). The power radiated is equal to the product of the acoustic pressure levels on the plate and the velocity of the plate:

$$P(t) = \int_0^{l_y} \int_0^{l_x} p_{acoust}(x, y, t)\dot{w}(x, y, t)dxdy \tag{5.9}$$

Or in a complex, frequency domain formulation:

$$P(j\omega) = \frac{1}{2}\mathbb{R}\left[\int_0^{l_y} \int_0^{l_x} p_{acoust}(x, y, j\omega)\dot{w}(x, y, j\omega)dxdy\right] \tag{5.10}$$

The acoustic pressure at any point of the plate is itself a function of the velocity of the plate:

$$p_{acoust}(x_1, y_1, j\omega) = \int_0^{l_y} \int_0^{l_x} \frac{j\omega\rho_0}{2\pi r} e^{-jkr}\dot{w}(x_2, y_2)dx_2dy_2 \tag{5.11}$$

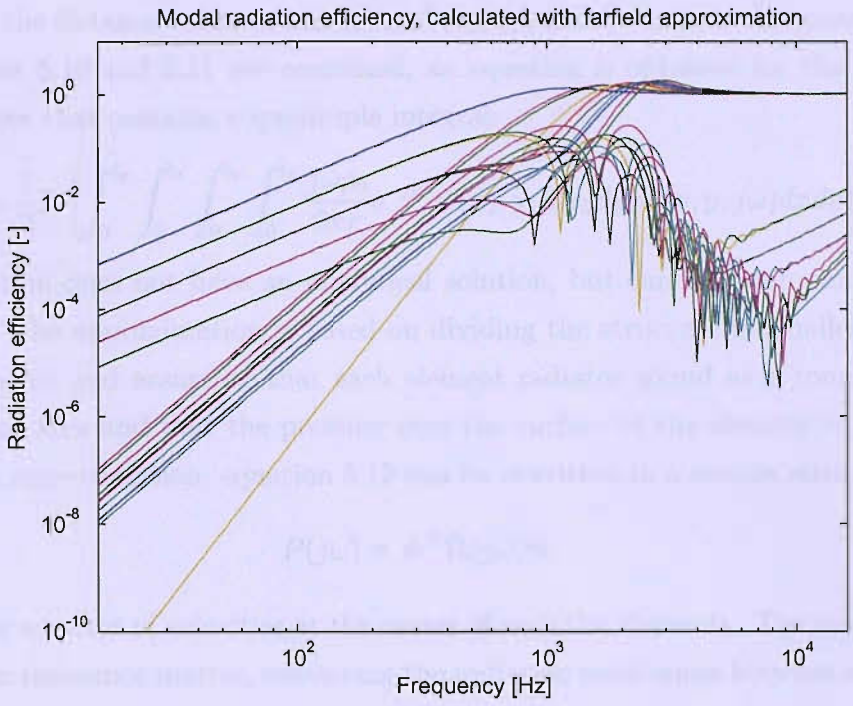

Figure 5.1: The self- and cross-radiation efficiencies of the first 10 structural modes of the simply supported plate as calculated with the *farfield* approximation.

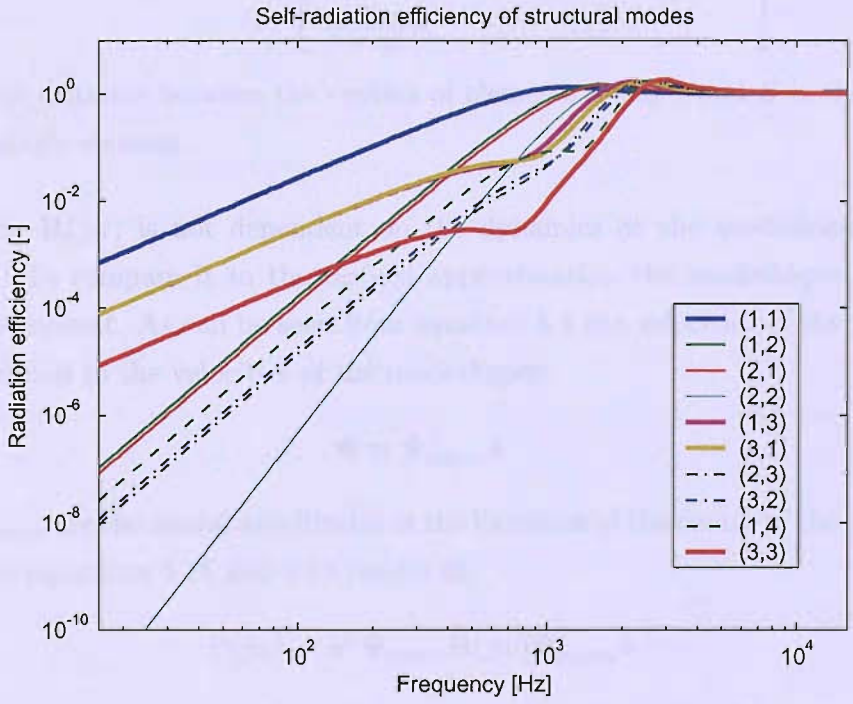

Figure 5.2: The self-radiation efficiencies of the first 10 structural modes of the simply supported plate as calculated with the farfield approximation.

where r is the distance between (x_1, y_1) and (x_2, y_2) and $k = \omega/c$ is the wavenumber. If equations 5.10 and 5.11 are combined, an equation is obtained for the radiated sound power that contains a quadruple integral:

$$P(j\omega) = \frac{1}{2}\mathbb{R}\left[\int_0^{l_y}\int_0^{l_x}\int_0^{l_y}\int_0^{l_x}\frac{j\omega\rho_0}{2\pi r}\mathrm{e}^{-jkr}\dot{w}(x_2,y_2)dx_2dy_2\dot{w}(x,y,j\omega)dxdy\right] \quad (5.12)$$

This equation does not have an analytical solution, but can be approximated numerically. The approximation is based on dividing the structure in smaller equally sized elements and assuming that each element radiates sound as a round piston of the same area and that the pressure over the surface of the element is uniform. Using this approximation, equation 5.12 can be rewritten in a matrix structure as:

$$P(j\omega) = \dot{\mathbf{w}}^T\mathbf{R}(j\omega)\dot{\mathbf{w}} \quad (5.13)$$

where $\dot{\mathbf{w}}$ is a vector of velocities at the center of each the elements. The matrix $\mathbf{R}$ is a radiation resistance matrix, containing the radiation resistances between elements. For a total of N_e elements, $\mathbf{R}$ can be calculated as:

$$\mathbf{R}(j\omega) = \frac{\omega^2\rho_0 S^2}{4\pi c_0}\begin{bmatrix} 1 & \frac{\sin(kr_{12})}{kr_{12}} & \dots & \frac{\sin(kr_{1N_e})}{kr_{1N_e}} \\ \frac{\sin(kr_{21})}{kr_{21}} & 1 & \dots & \dots \\ \dots & \dots & \ddots & \dots \\ \frac{\sin(kr_{N_e1})}{kr_{N_e1}} & \dots & \dots & 1 \end{bmatrix} \quad (5.14)$$

with r_{ij} the distance between the centers of elements i and j and S is the surface area of a single element.

The matrix $\mathbf{R}(j\omega)$ is not dependent on the dynamics or the modeshapes of the structure. To compare it to the farfield approximation the modeshapes must be taken into account. As can be seen from equation 5.4 the velocities of the plate are directly related to the velocities of the modeshapes:

$$\dot{\mathbf{w}} = \mathbf{\Psi}_{points}^T\dot{\mathbf{a}} \quad (5.15)$$

where $\mathbf{\Psi}_{points}$ are the modal amplitudes at the locations of the center of the elements. Combining equations 5.15 and 5.13 results in:

$$P(j\omega) = \dot{\mathbf{a}}^T\mathbf{\Psi}_{points}\mathbf{R}(j\omega)\mathbf{\Psi}_{points}^T\dot{\mathbf{a}} \quad (5.16)$$

and analogous to section 5.1.1 a modal radiation matrix can be obtained:

$$\mathbf{M} = \mathbf{\Psi}_{points}\mathbf{R}(j\omega)\mathbf{\Psi}_{points}^T \quad (5.17)$$

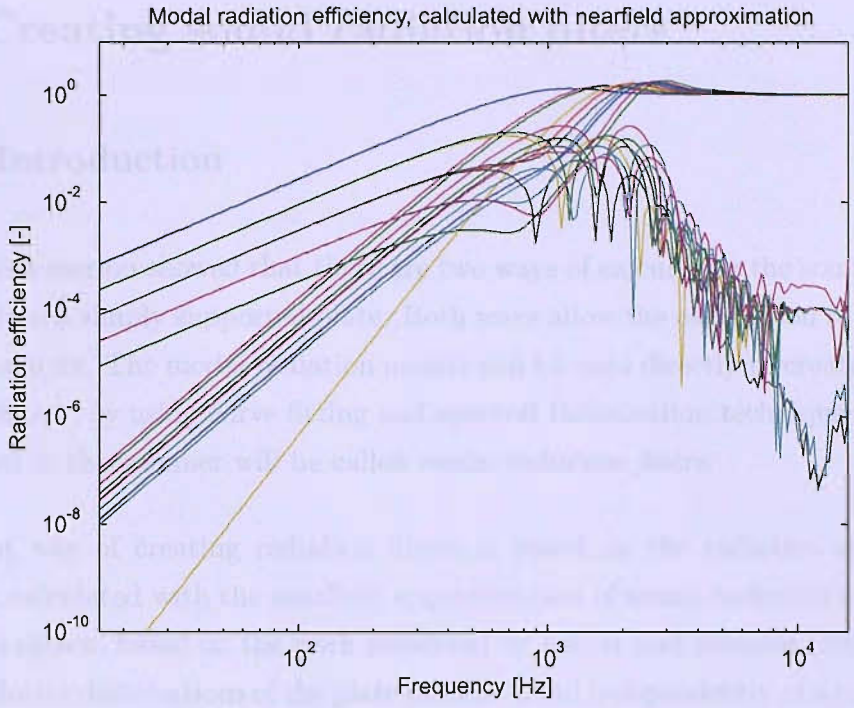

Figure 5.3: The self- and cross-radiation efficiencies of the first 10 structural modes of the simply supported plate as calculated with the *nearfield* approximation.

The accuracy of this approach depends on the number of elements taken into account. The frequency at which spatial aliasing starts to occur is roughly the frequency at which half the wavelength in air corresponds to the largest dimension of the elements. Increasing the number of elements does increase accuracy, but the number of elements in the matrix $\mathbf{R}(j\omega)$ also increases quadratically with the number of elements.

Some elements of the modal radiation efficiency $\mathbf{S}$ (see equation 5.8) of the modal radiation matrix calculated on the basis of the nearfield approximation have been plotted in figure 5.3. The figure shows that spatial aliasing starts to occur from 10 kHz. Note that the model of the sound radiation in this approach splits the dynamics concerning the sound radiation and the dynamics of the structure. That means that the model can be used equally well for plates with different boundary conditions or shapes and thus modeshapes.

5.2 Creating sound radiation filters

5.2.1 Introduction

The previous section showed that there are two ways of calculating the sound power radiated from a simply supported plate. Both ways allow the calculation of a modal radiation matrix. The modal radiation matrix can be used directly to create a set of radiation filters, by using curve fitting and spectral factorisation techniques. Filters constructed in this manner will be called *modal radiation filters*.

A different way of creating radiation filters is based on the radiation resistance matrix $\mathbf{R}$, calculated with the nearfield approximation of sound radiation (equation 5.14). It is shown, based on the work presented by Elliott and Johnson (1993), that specific velocity distributions of the plate radiate sound independently at a particular frequency. These independently radiating velocity distributions are called *radiation modes*. By assuming that the radiation modes remain the same for all frequencies of interest, an approximation to the sound radiation can be achieved. Clark and Cox (1997), as well as subsequent papers (e.g. Cox et al. (1998), Gibbs et al. (2000)), referred to this technique as *Radiation Modal Expansion*. The filters constructed in this manner will be called *radiation mode filters*.

Both these techniques are explained here. First, the techniques are explained in more detail, starting with radiation mode technique. The actual filters are constructed in a separate section. The terminology is prone to confusion, as the terms *radiation modes* and *modal radiation* are much alike. Here, the terms have been applied to refer to each technique separately.

5.2.1.1 Radiation mode filters

Creating radiation filters can be based on the decomposition of the radiation resistance matrix $\mathbf{R}$. This matrix is positive definite at frequencies larger than 0. Therefore, at frequencies larger than 0, this matrix has an eigenvector-eigenvalue decomposition, $\mathbf{R} = \mathbf{Q}\mathbf{\Lambda}\mathbf{Q}^T$, where $\mathbf{\Lambda}$ is a diagonal matrix of the real and positive eigenvalues and $\mathbf{Q}$ the matrix of eigenvectors. The eigenvectors are columns of $\mathbf{Q}$

and define the velocity distributions of $\dot{\mathbf{w}}$ that radiate sound independently at that particular frequency (Elliott and Johnson (1993)). Hence, these distributions are called *radiation modes*.

Borgiotti and Jones (1994) stated that such radiation modes are nested: the space spanned by the radiation modes at a frequency $\omega < \omega_{max}$ is a subspace of the space spanned by the radiation modes at ω_{max}. This means that the modes at ω are a linear combination of the modes at ω_{max}. In the same paper and in work by Gibbs et al. (2000), it was noted that these radiation modes change shape slowly over large frequency ranges and it was assumed that the radiation modes remain constant for all frequencies. Though this is not strictly true, it is a workable approximation for frequencies that are 'close' to the frequency at which the radiation modes are calculated. For each frequency, the contribution of each radiation mode to the sound radiation can be calculated. By curve-fitting the frequency response of these contributions, a frequency dependent filter can be associated with each radiation mode. The squared output of these filters is an approximation for the acoustic power radiated by each radiation mode. The sum of the squared outputs is the approximation of the total radiated sound power.

A slightly more general approach than the one taken by Gibbs et al. (2000) is the following:

- Calculate the radiation modes $\mathbf{Q}$ at a frequency ω_{base}.
- Select a set of the most significant radiation modes $\mathbf{\Phi}_{base}$ at this frequency ω_{base}
- Calculate an amplitude weighting coefficient γ_i for the ith radiation mode at a set of frequencies, ω, as:

$$\gamma_i(\omega) = \mathbf{q}_i^T \mathbf{R}(j\omega)\mathbf{q}_i \tag{5.18}$$

  where $\mathbf{q}_i$ is the velocity distribution associated with the ith radiation mode, i.e. a column of $\mathbf{\Phi}_{base}$.
- Fit a Laplace function through γ_i for that radiation mode. As γ_i is entirely real, the function should have mirrored poles and zeros in the s-plane.
- Split these filters into an entirely stable-causal and anti-stable/causal filter. If the original filter is written as a zero-pole-gain function, this is can be done

reasonably easily. The conversion of the fitted filters to a state-space filter is discussed in greater detail in section 5.2.2.2.

- The estimated sound radiation can now be calculated as the squared output of these filters. The input of the filters is the actual velocity distribution of the plate, multiplied by the velocity distributions of the radiation modes.

In this approach, the choice base frequency ω_{base} is not fixed and can be iterated upon. Gibbs et al. (2000) fixed the frequency ω_{base} at the highest frequency of interest. This is done because there are several important assumptions and approximations that affect the applicability of these filters.

First of all, the assumption that the radiation modes do not change shape is only a reasonable approximation over a limited frequency range. Figures 5.4 and 5.5 show the six most significant radiation modes at 100 Hz and 1.5 kHz respectively. It can be seen that the radiation modes do change shape gradually as a function of frequency. Borgiotti and Jones (1994) observed that the radiation modes at a frequency $\omega < \omega_{max}$ are a linear combination of the radiation modes at a frequency ω_{max}. This implies that there are possibly significant cross-terms in the radiation modes that are ignored in the above approach. *Here* it is assumed that, as long as the radiation modes do not change much at frequencies above or below the base frequency of the chosen set of radiation modes, the calculated sound radiation should not change much in comparison to the actual sound radiation and the radiation modes can be used effectively to design a controller. This does mean that the choice of the base frequency for the radiation modes limits the frequency range for which the model is accurate both below and above the base frequency.

The number of radiation modes taken into account and the accuracy of the fit influence the accuracy also, as does the number of elements on the plate. Elliott and Johnson (1993) shows that number of radiation modes has to increase dramatically with frequency to calculate the sound radiation accurately. Also, the number of structural modes also influences accuracy and should also be sufficient for the frequency range of interest.

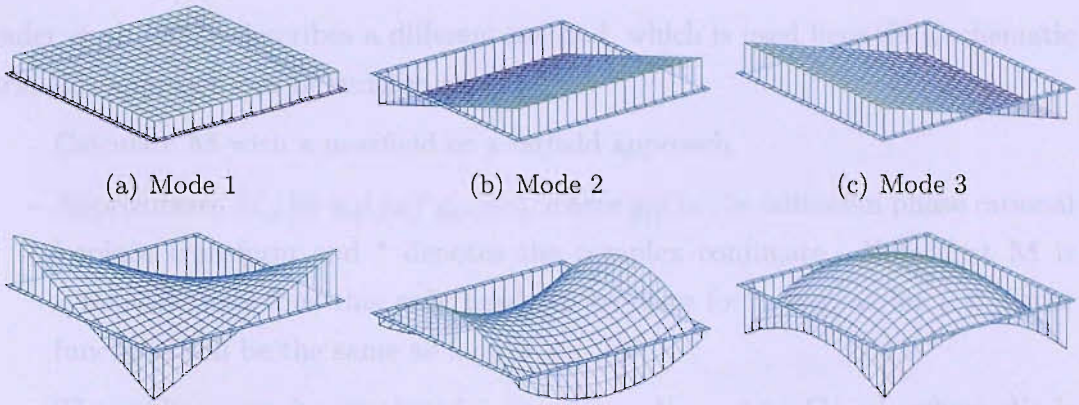

(a) Mode 1 (b) Mode 2 (c) Mode 3

(d) Mode 4 (e) Mode 5 (f) Mode 6

Figure 5.4: Six most significant radiation modes at 100 Hz, sorted by significance.

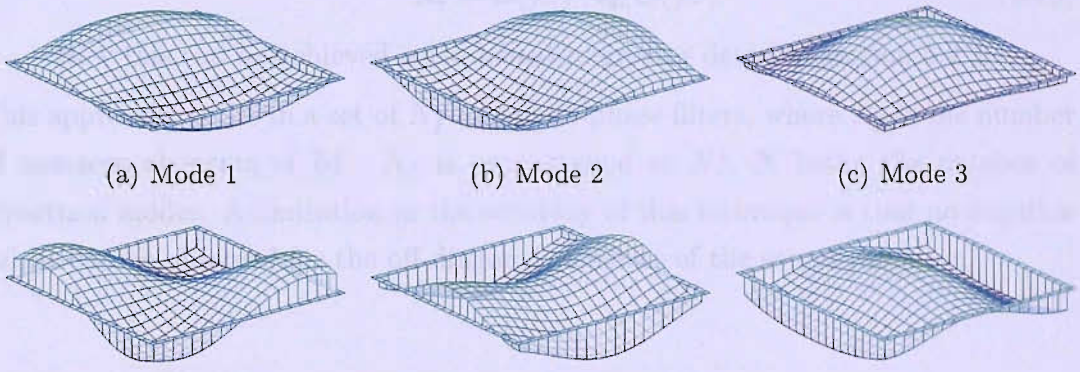

(a) Mode 1 (b) Mode 2 (c) Mode 3

(d) Mode 4 (e) Mode 5 (f) Mode 6

Figure 5.5: Six most significant radiation modes at 1.5 kHz, sorted by significance.

5.2.1.2 Modal radiation filters

The method of creating filters on the basis of the modal radiation matrix is used by Baumann et al. (1991). In that paper, it is described, how the real but frequency dependent matrix $\mathbf{M}$ can be transformed into a set of N^2 filters, where N is the number of structural modes. Each of the elements in $\mathbf{M}$ can be approximated by a sum of a stable and an antistable rational Laplace transform. Using this formulation, the matrix can then be spectrally factorised using the state-space algorithms found in Francis (1987). However, this method requires the solution of a Riccati equation, which can create numerical difficulties.

Kader et al. (2000) describes a different method, which is used here. In a schematic form this approach can be written as:

- Calculate $\mathbf{M}$ with a nearfield or a farfield approach.
- Approximate M_{ij} by $g_{ij}(j\omega)^* g_{ij}(j\omega)$, where $g_{ij}(j\omega)$ is mininum phase rational Laplace transform and * denotes the complex conjugate. Note that $\mathbf{M}$ is symmetric and thus this only needs to be done for $i \geq j$, as for $i < j$, the functions will be the same as for $i > j$.
- These filters can be combined into a N x N_f matrix $\mathbf{G}(j\omega)$, where N_f is the number of non-zero elements of $\mathbf{M}$. An additional, frequency invariant, symmetric matrix $\mathbf{Q}_h$ is used to correctly combine the outputs of the filters such that:

$$\mathbf{M} = \mathbf{G}(j\omega)^H \mathbf{Q}_h \mathbf{G}(j\omega) \tag{5.19}$$

  How this can be achieved is explained in greater detail in section 5.2.3.

This approach results in a set of N_f minimum-phase filters, where N_f is the number of non-zero elements of $\mathbf{M}$. N_f is proportional to N^2, N being the number of structural modes. A limitation in the accuracy of this technique is that no negative values can be obtained for the off-diagonal elements of the sound radiation.

5.2.2 Radiation mode filter construction

As mentioned in the section 5.2.1.1, the frequency at which the set of radiation modes is selected influences the accuracy of the approximation. To see which set is better, a number of different base frequencies, f_{base} have been used to calculate the fixed radiation modes. Each set of fixed modes results in different amplitude coefficients γ_i. If the radiation modeshapes are normalised and do not change with frequency then the amplitude coefficients should be equal to the eigenvalues of the matrix $\mathbf{R}(j\omega)$, calculated with equation 5.14. Figures 5.6-5.8 show the amplitude coefficients calculated for the modes (solid lines) in comparison to the most significant eigenvalues of $\mathbf{R}(j\omega)$ (dotted lines). From the fixed radiation modes at 20 Hz, 10 radiation modes have been selected, whereas for 1 and 2 kHz 20 modes have been selected. This is because there were not 20 significantly efficient radiating modes available at 20 Hz.

The figures show that the eigenvalues and the calculated amplitude coefficients di-

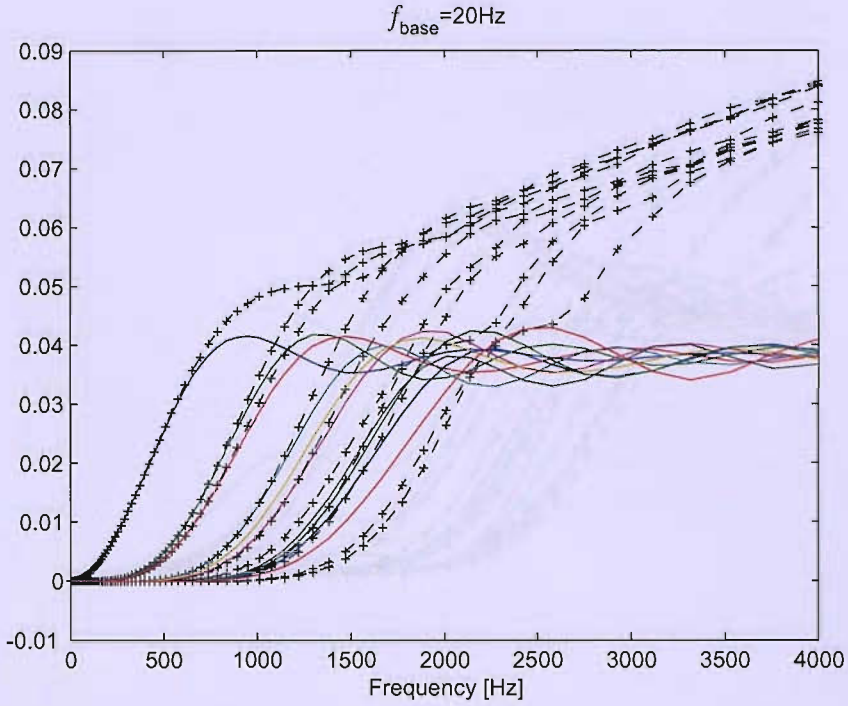

Figure 5.6: Calculated amplitude coefficients (-) for radiation modes calculated at 20 Hz and the eigenvalues of $\mathbf{R}(j\omega)$ (..+..).

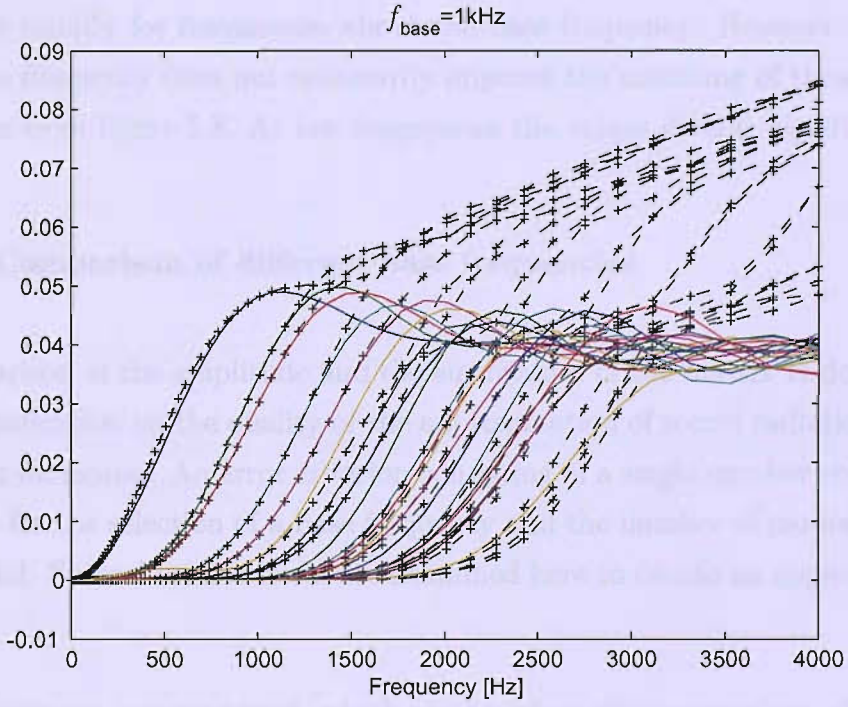

Figure 5.7: Calculated amplitude coefficients (-) for radiation modes calculated at 1 kHz and the eigenvalues of $\mathbf{R}(j\omega)$ (..+..).

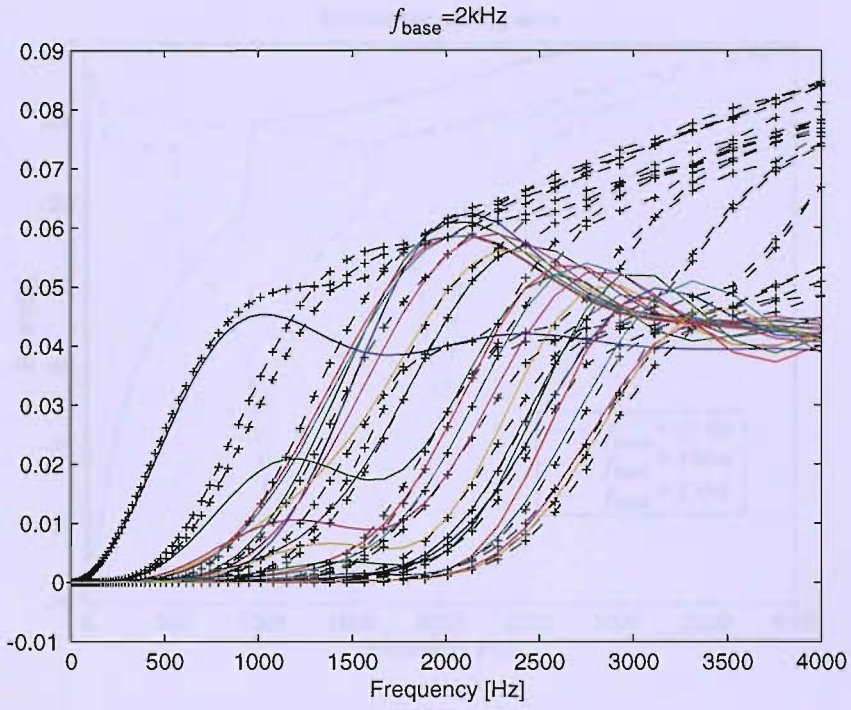

Figure 5.8: Calculated amplitude coefficients (-) for radiation modes calculated at 2 kHz and the eigenvalues of $\mathbf{R}(j\omega)$ (..+..).

verge quite rapidly for frequencies above the base frequency. However, selecting a higher base frequency does not necessarily improve the matching of these values, as can be seen from figure 5.8. At low frequencies the values diverge significantly.

5.2.2.1 Comparison of different base frequencies

The comparison of the amplitude and the eigenvalues of the matrix $\mathbf{R}$ does not give any clear indication on the quality of the approximation of sound radiation by using fixed radiation modes. An error criterion consisting of a single number could prove a useful tool for the selection of a base frequency and the number of modes to include in the model. Several error criteria are examined here to decide an appropriate base frequency.

Two error criteria are examined, which are based on the comparison of the values of $\mathbf{R}(j\omega)$ and $\mathbf{R}_{approx}(j\omega) = \Phi_{base}^T \mathbf{\Gamma}(j\omega)\Phi_{base}$, where $\mathbf{\Gamma}(j\omega)$ is the diagonal matrix of amplitude coefficients for the different radiation modes. Another criterion examined here tries to compare how the modes of the structure interact with these

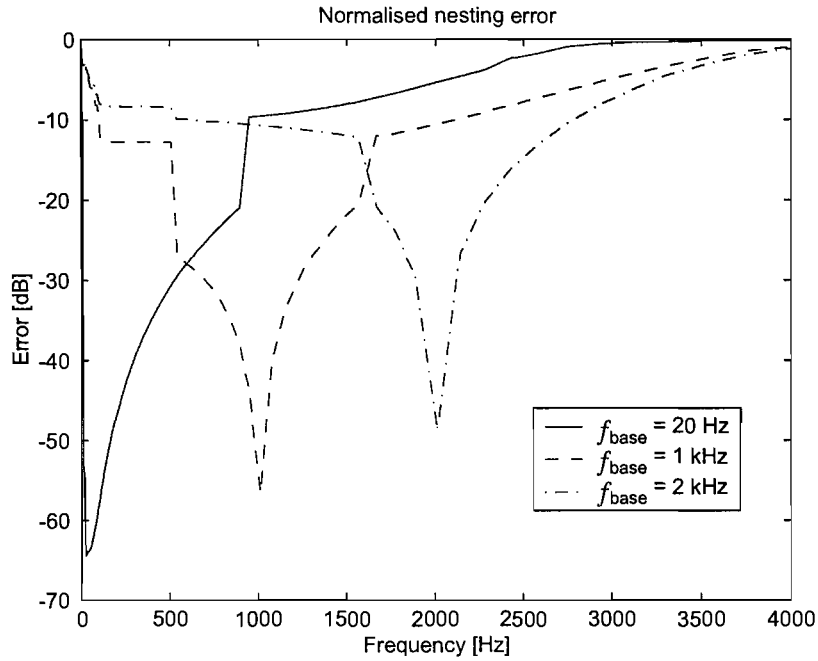

Figure 5.9: Normalised nesting error for different sets of radiation modes

matrices, by examining the difference of the *modal radiation matrices* $\mathbf{\Psi R}(j\omega)\mathbf{\Psi}^T$ and $\mathbf{\Psi R}_{approx}(j\omega)\mathbf{\Psi}^T$, where $\mathbf{\Psi}$ are the structural modal amplitudes at the midpoint of the elements used to calculated $\mathbf{R}(j\omega)$. The final criterion examined here is the calculated sound radiation of the structure, taking the structural dynamics and the excitation into account.

Borgiotti and Jones (1994) suggests a *normalised nesting error* to compare $\mathbf{R}(j\omega)$ and $\mathbf{R}_{approx}(j\omega)$:

$$\epsilon(\omega) = 10\log\left(1 - \sum_i \sum_j \left|\mathbf{\Phi}_i(j\omega)^T \left(\mathbf{\Phi}_{base}\right)_j\right|^2 / N_{rad}\right) \tag{5.20}$$

where N_{rad} is the number of radiation modes examined. Figure 5.9 shows the normalised nesting error for the 3 different sets of radiation modes.

Another criteria to compare the two matrices might be the sum of the squared errors in each of the elements of $\mathbf{R}(j\omega)$, compared to the sum of the squared elements of $\mathbf{R}(j\omega)$:

$$\sum_i \sum_j \left(\mathbf{R}_{ij} - \left(\mathbf{R}_{approx}\right)_{ij}\right)^2 \quad \text{vs.} \quad \sum_i \sum_j \left(\mathbf{R}_{ij}\right)^2 \tag{5.21}$$

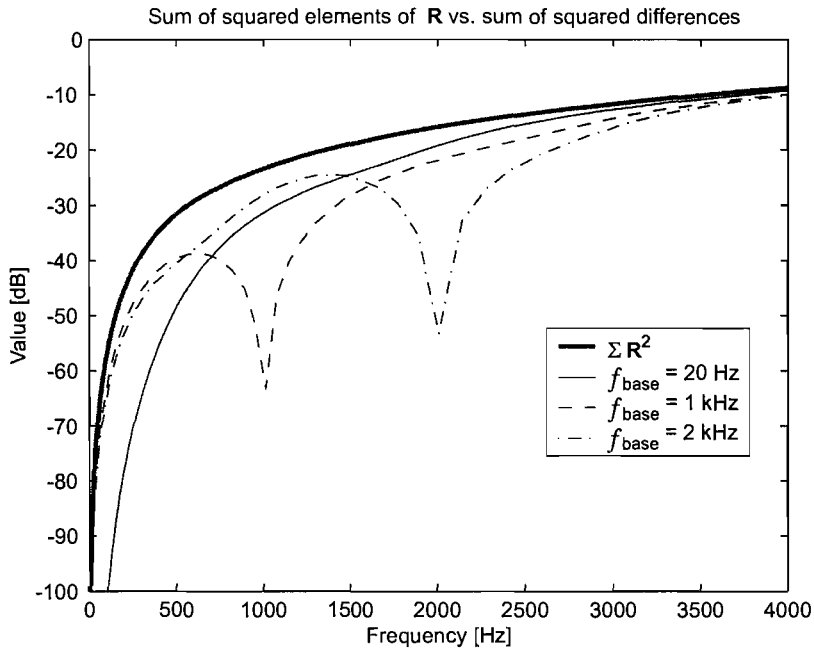

Figure 5.10: Sum of squared error in the elements of the elemental radiation matrix vs the sum of the squared elements of **R** for different sets of radiation modes

Figure 5.10 shows the comparison of these two values for the different sets of radiation modes.

The error in the modal radiation matrices has also been calculated in this way and is shown in figure 5.11. Finally, the error in the calculated sound radiation from an uncontrolled plate, excited by randomly distributed white noise, is shown in figures 5.12(a) and 5.12(b). Two figures have been used to emphasise the difference between low-frequency and high-frequency approximations. The figures show that the radiation calculated with the set of radiation modes at 20 Hz starts to diverge at about 750 Hz and significantly underestimates the radiated sound power above 2500 Hz. The set of radiation modes chosen at 2 kHz gives poor approximations at low frequencies, especially between 400 and 900 Hz. At frequencies between 3 and 4 kHz, the match, though not good, is at least better than that of the 20 Hz set. The set of radiation modes chosen at 1 kHz seems to give a reasonable match up to 2 kHz and performs similar to the 2 kHz set at frequencies between 3 and 4 kHz.

Though it would have been useful to compare the sound radiation models without including the structural model, calculating the sound radiation is the most clear

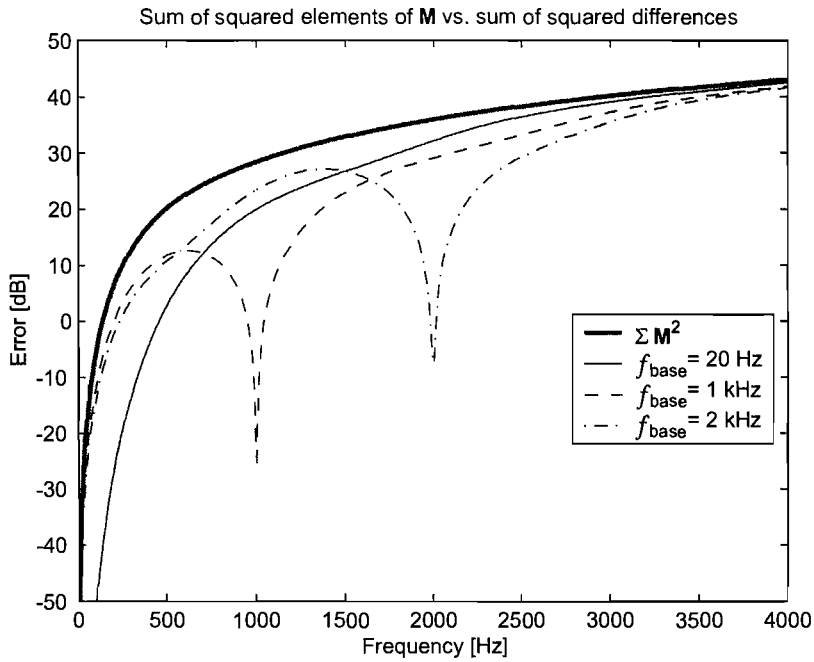

Figure 5.11: Sum of squared error in the elements of the modal radiation matrix vs the sum of the squared elements of $\mathbf{M} = \mathbf{\Psi R \Psi}^T$

criterion of the ones examined here and will be used to select the model.

The different sets of radiation modes perform well if the frequency range of interest is close to the base frequency. The best model thus depends on the frequency range of interest. If the frequency range of interest is chosen to be between 0 and 2 kHz, the set of radiation modes at 1 kHz is the best option, based on the modelling of the sound radiation and this is what is used below.

5.2.2.2 Constructing the state-space models

The amplitude coefficients, γ_i, of the 20 selected radiation modes can be fitted using a zero-pole gain model. As the amplitude coefficients are positive real numbers for different frequencies, a transfer function model must have poles and zeros that are mirrored in, or located on the imaginary axis.

The fitting of the functions has been performed using the Matlab function `invfreqs`. This function fits a zeros-pole-gain model to the response of the model at a finite

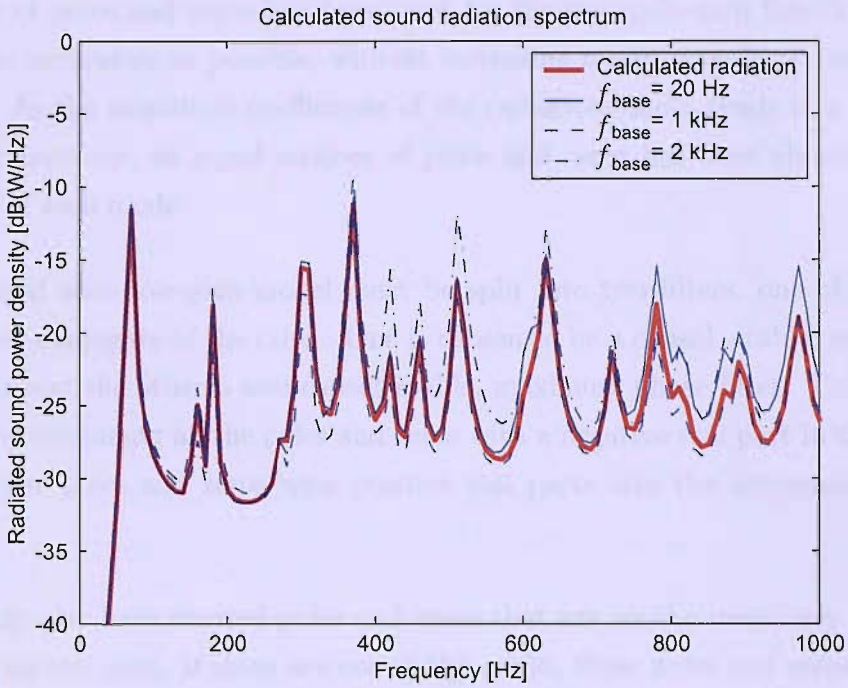

(a) Up to 1 kHz

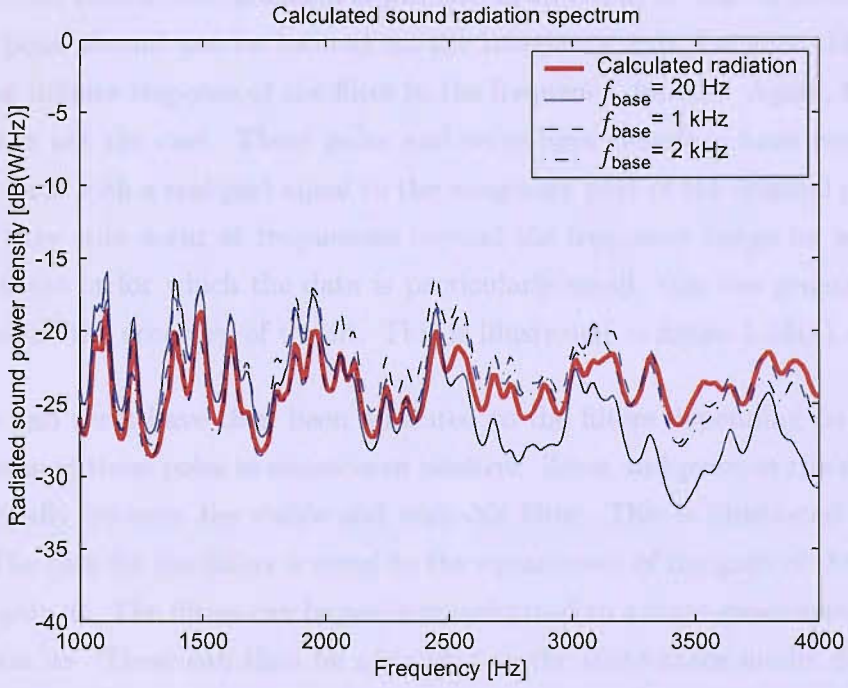

(b) From 1 to 4 kHz

Figure 5.12: Calculated sound radiation spectrum with the nearfield calculation and radiation mode approximation using different base frequencies.

number of frequencies, minimising the difference between the model and the data. A number of poles and zeros has been used for the zero-pole-gain functions to fit the data as accurately as possible, without increasing model complexity more than necessary. As the amplitude coefficients of the radiation modes tends to a constant for high frequencies, an equal number of poles and zeros has been chosen for the modelling of each mode.

The obtained zero-pole-gain model must be split into two filters, one of which is the complex-conjugate of the other. One is chosen to be a causal, stable, minimum-phase filter and the other a anti-causal/stable, maximum phase filter. This can be achieved by combining all the poles and zeros with a negative real part in the stable filter and the poles and zeros with positive real parts into the anti-causal/stable filter.

The fit may also have created poles and zeros that are on the imaginary axis and thus have no real part. If these are not at the origin, these poles and zeros have no physical basis. There should be no zeros on the imaginary axis apart from the origin, due to the fact that sound radiation is positive in all cases, as can be seen in figure 5.7. The poles should not be located on the imaginary axis, because they would result in an infinite response of the filter in the frequency domain. Again, figure 5.7 shows this is not the case. These poles and zeros have therefore been replaced by poles and zeros with a real part equal to the imaginary part of the original poles and zeros. As they only occur at frequencies beyond the frequency range for which the data was fitted or for which the data is particularly small, this has generally little or no effect on the accuracy of the fit. This is illustrated in figure 5.13(a).

The poles and zeros have then been allocated to the filters depending on whether the real value of these poles in negative or positive. Zeros and poles at the origin are divided equally between the stable and unstable filter. This is illustrated in figure 5.13(b). The gain for the filters is equal to the square-root of the gain of the original zero-pole-gain fit. The filters can be easily transformed to a state-space system using the function **ss**. These can then be appended to the state-space model describing the plate dynamics.

Suppose the original plate dynamics to calculate the velocities $\dot{\mathbf{w}}$ at the grid points

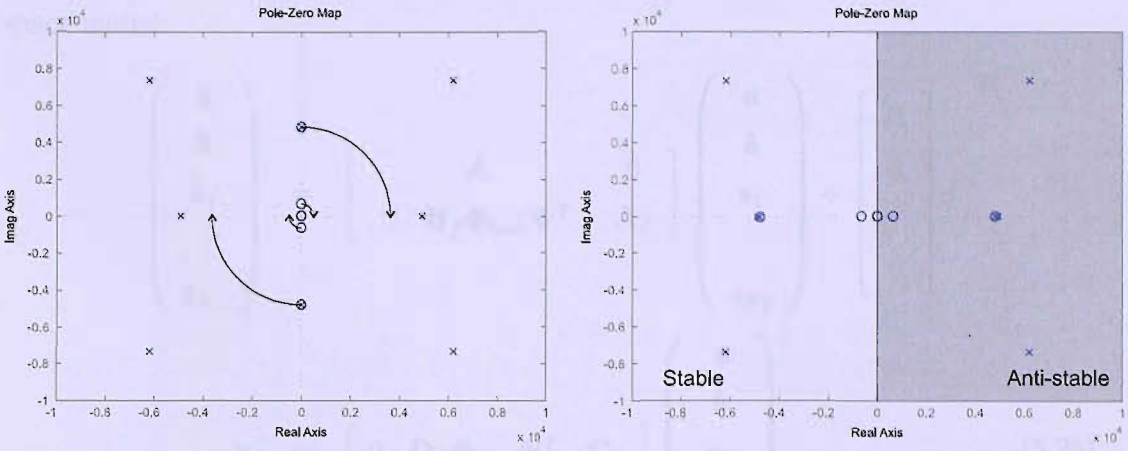

(a) Moving purely imaginary poles and zeros (b) Assigning poles and zeros to filters

Figure 5.13: Changing the fitted filter to comply with physical demands and dividing the poles (x) and zeros (o) into a stable and anti-stable filter.

can be described with:

$$\begin{pmatrix} \dot{\mathbf{a}} \\ \ddot{\mathbf{a}} \end{pmatrix} = \mathbf{A} \begin{pmatrix} \mathbf{a} \\ \dot{\mathbf{a}} \end{pmatrix} + \mathbf{B}\mathbf{f}$$
$$\dot{\mathbf{w}} = \begin{bmatrix} 0 & \mathbf{\Psi}^T \end{bmatrix} \begin{pmatrix} \mathbf{a} \\ \dot{\mathbf{a}} \end{pmatrix} \tag{5.22}$$

and the radiation modes $i = 1 \ldots N_f$ have to be added to the model. Each radiation mode and its associated filter have a number of states described by a vector $\mathbf{s}_i$. Each filter is described by a state space model:

$$\begin{aligned} \dot{\mathbf{s}}_i &= \mathbf{A}_{fi}\mathbf{s}_i + \mathbf{B}_{fi}u_i \\ y_{fi} &= \mathbf{C}_{fi}\mathbf{s} + \mathbf{D}_{fi}u_i \end{aligned} \tag{5.23}$$

where u_i is the input to the filter which can be calculated with:

$$u_i = \left[\mathbf{\Phi}_{base}\right]_i \dot{\mathbf{w}} \tag{5.24}$$

Then the filters and the original state-space model can be combined to one state-

space model:

$$\begin{pmatrix} \dot{\mathbf{a}} \\ \ddot{\mathbf{a}} \\ \dot{\mathbf{s}}_1 \\ \vdots \\ \dot{\mathbf{s}}_{N_f} \end{pmatrix} = \begin{bmatrix} \mathbf{A} & 0 \\ 0 \quad \mathbf{B}_f\boldsymbol{\Phi}_{base}\boldsymbol{\Psi}^T & \mathbf{A}_f \end{bmatrix} \begin{pmatrix} \mathbf{a} \\ \dot{\mathbf{a}} \\ \mathbf{s}_1 \\ \vdots \\ \mathbf{s}_{N_f} \end{pmatrix} + \begin{bmatrix} \mathbf{B} \\ 0 \\ \vdots \\ 0 \end{bmatrix} \mathbf{f}$$

$$\mathbf{y}_f = \begin{bmatrix} 0 \quad \mathbf{D}_f\boldsymbol{\Phi}_{base}\boldsymbol{\Psi}^T & \mathbf{C}_f \end{bmatrix} \begin{pmatrix} \mathbf{a} \\ \dot{\mathbf{a}} \\ \mathbf{s}_1 \\ \vdots \\ \mathbf{s}_{N_f} \end{pmatrix} \tag{5.25}$$

where:

$$\mathbf{A}_f = \begin{bmatrix} \mathbf{A}_{f1} & 0 & \dots & 0 \\ 0 & \mathbf{A}_{f2} & \dots & \dots \\ \dots & \dots & \ddots & \dots \\ 0 & \dots & \dots & \mathbf{A}_{N_f} \end{bmatrix} \tag{5.26}$$

and $\mathbf{B}_f$, $\mathbf{C}_f$ and $\mathbf{D}_f$ are constructed along similar lines from $\mathbf{B}_{fi}$, $\mathbf{C}_{fi}$ and $\mathbf{D}_{fi}$. The sound radiation can then be calculated as the sum of the squared values of $\mathbf{y}_f$:

$$J_{acoust} = \mathbf{y}_f^T\mathbf{y}_f \tag{5.27}$$

Figure 5.14 shows the sound radiation calculated using the original radiation resistance matrix $\mathbf{R}$ (solid line), using the radiation modes and amplitude coefficients calculated for those modes (dashed line) and the sound radiation calculated using the state-space filters (dash-dot line). The figure shows that fitting the sound radiation with a state-space filter results in only a small additional inaccuracy on top of fixing the radiation modes. For a large part of the frequency domain, the lines are actually on top of each other.

5.2.3 Modal radiation filter construction

As stated in section 5.2.1.2, the modelling of modal radiation can be achieved in by the spectral factorisation of $\mathbf{M}$. This is done by factorising each element of

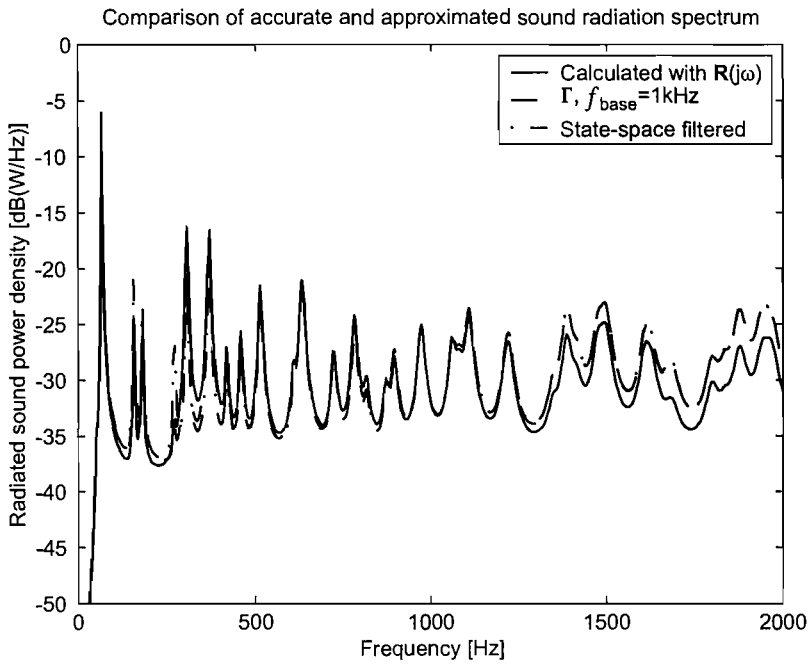

Figure 5.14: Comparison of uncontrolled sound radiation spectrum, calculated with the radiation mode approximation and the nearfield model

the matrix $\mathbf{M}$ and combining the resulting state-space models. Here a step-by-step approach is used to show how the required matrices can be constructed.

- Begin by approximating M_{ij} with a function $g_n^*(j\omega)g_n(j\omega)$ in the same way as in section 5.2.2.2, except that now the number of poles and zeros does not always need to be equal. Note also that, though the radiation function M_{ij} can become negative, $g_n^*(j\omega)g_n(j\omega)$ can not. This limits the accuracy of the fit. For very small elements of $\mathbf{M}$, the function can be fitted by setting $g_n = 0$. The functions g_n corresponding to element M_{ij} can then be written in a state space form:

$$\begin{aligned} \dot{\mathbf{s}}_{f\,ij} &= \mathbf{A}_{f\,ij}\dot{\mathbf{s}}_{f\,ij} + \mathbf{B}_{f\,ij}\dot{a}_i \\ y_{f\,ij} &= \mathbf{C}_{f\,ij}\dot{\mathbf{s}}_{f\,ij} + D_{f\,ij}\dot{a}_i \end{aligned}$$

Due to the symmetry of $\mathbf{M}$, the filters for element M_{ji} are the same.

The index i (or j) indicates the modal velocity of the mode that appears on the ith place in the modal velocity vector. The index does not show which particular mode it is. For instance: the velocity of the mode of the plate of which the modeshape is described by equation 2.10, with $m = 1$ and $n = 3$,

might be located at the 4th position in the vector $\dot{\mathbf{a}}$, while the mode defined by $m = 2$ and $n = 2$ could be located at the 8th position. The element MI_{ij} with $i = 4, j = 8$ would then indicate the cross radiation of the $1,3$ and the $2,2$ modes.

- Combine the state space matrices of each filter. Here, the matrices have been ordered such that:

$$\mathbf{A}_f = \begin{bmatrix} \mathbf{A}_{f\,11} & 0 & 0 & \dots & \dots & \dots & 0 \\ 0 & \mathbf{A}_{f\,12} & 0 & \dots & \dots & \dots & \dots \\ 0 & 0 & \mathbf{A}_{f\,21} & 0 & \dots & \dots & \dots \\ \dots & \dots & 0 & \mathbf{A}_{f\,13} & 0 & \dots & \dots \\ \dots & \dots & \dots & 0 & \mathbf{A}_{f\,31} & \dots & \dots \\ \dots & \dots & \dots & \dots & \dots & \ddots & \dots \\ 0 & \dots & \dots & \dots & \dots & \dots & \mathbf{A}_{f\,NN} \end{bmatrix} \tag{5.28}$$

$\mathbf{B}_f$ should then be:

$$\mathbf{B}_f = \begin{bmatrix} \mathbf{B}_{f\,11} & 0 & \dots & \dots & 0 \\ \mathbf{B}_{f\,12} & 0 & \dots & \dots & \dots \\ 0 & \mathbf{B}_{f\,21} & 0 & \dots & \dots \\ \mathbf{B}_{f\,13} & 0 & 0 & \dots & \dots \\ 0 & 0 & \mathbf{B}_{f\,31} & \dots & \dots \\ \dots & \dots & \dots & \ddots & \dots \\ 0 & \dots & \dots & \dots & \mathbf{B}_{f\,NN} \end{bmatrix} \tag{5.29}$$

and $\mathbf{C}_f$ is:

$$\mathbf{C}_f = \begin{bmatrix} \mathbf{C}_{f\,11} & 0 & 0 & \dots & \dots & \dots & 0 \\ 0 & \mathbf{C}_{f\,12} & 0 & \dots & \dots & \dots & \dots \\ 0 & 0 & \mathbf{C}_{f\,21} & 0 & \dots & \dots & \dots \\ \dots & \dots & 0 & \mathbf{C}_{f\,13} & 0 & \dots & \dots \\ \dots & \dots & \dots & 0 & \mathbf{C}_{f\,31} & \dots & \dots \\ \dots & \dots & \dots & \dots & \dots & \ddots & \dots \\ 0 & \dots & \dots & \dots & \dots & \dots & \mathbf{C}_{f\,NN} \end{bmatrix} \tag{5.30}$$

And the matrix $\mathbf{D}_f$:

$$\mathbf{D}_f = \begin{bmatrix} D_{f\,11} & 0 & \dots & \dots & 0 \\ D_{f\,12} & 0 & \dots & \dots & \dots \\ 0 & D_{f\,21} & 0 & \dots & \dots \\ D_{f\,13} & 0 & 0 & \dots & \dots \\ 0 & 0 & D_{f\,31} & \dots & \dots \\ \dots & \dots & \dots & \ddots & \dots \\ 0 & \dots & \dots & \dots & D_{f\,NN} \end{bmatrix} \tag{5.31}$$

If this is done, one obtains a matrix of the functions $g_{f\,ij}$:

$$\mathbf{G}_f = \begin{bmatrix} g_{f\,11} & 0 & \dots & \dots & 0 \\ g_{f\,12} & 0 & \dots & \dots & \dots \\ 0 & g_{f\,21} & 0 & \dots & \dots \\ g_{f\,13} & 0 & 0 & \dots & \dots \\ 0 & 0 & g_{f\,31} & \dots & \dots \\ \dots & \dots & \dots & \ddots & \dots \\ 0 & \dots & \dots & \dots & g_{f\,NN} \end{bmatrix} \tag{5.32}$$

Finally, the matrix $\mathbf{Q}_h$ must be constructed according to:

$$\mathbf{Q}_h = \begin{bmatrix} 1 & 0 & 0 & 0 & \dots & \dots & 0 \\ 0 & 0 & 1 & 0 & \dots & \dots & \dots \\ 0 & 1 & 0 & 0 & \dots & \dots & \dots \\ 0 & 0 & 0 & 0 & 1 & \dots & \dots \\ \dots & \dots & \dots & 1 & 0 & \dots & \dots \\ \dots & \dots & \dots & \dots & \dots & \dots & \dots \\ 0 & \dots & \dots & \dots & \dots & \dots & 1 \end{bmatrix} \tag{5.33}$$

This way, when calculating $\mathbf{G}(j\omega)^H\mathbf{Q}_h\mathbf{G}(j\omega)$, the i,jth element is:

$$g^*_{f\,ji}g_{f\,ij} \tag{5.34}$$

but as $g_{f\,ji} = g_{f\,ij}$ due to symmetry, this is equal to:

$$g^*_{f\,ij}g_{f\,ij} \tag{5.35}$$

which is the desired function. Note that for quadratic optimisation, this state space model should be combined with the structural model, in a similar way to what was done in section 5.2.2.2 for the radiation modes.

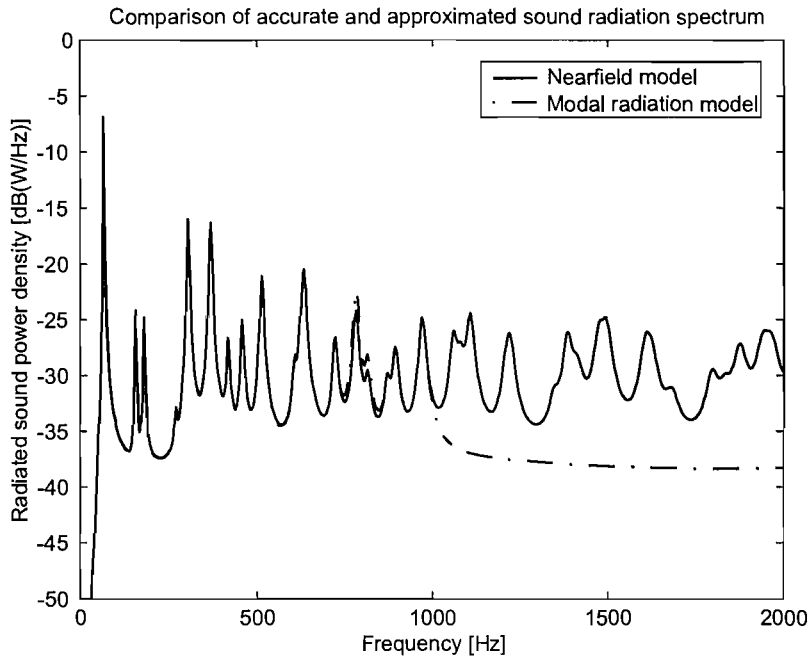

Figure 5.15: Comparison of uncontrolled sound radiation spectrum, calculated with spectral factorisation of the modal radiation and the nearfield model.

The main problem with this technique is the large number of functions that have to be fitted: for the 18 modes of the simply supported plate up to 1 kHz, there are 86 non-zero elements in the matrix $\mathbf{M}$, resulting in 52 functions to be fitted. For the 39 modes up to 2 kHz, 211 functions would have to be fitted. Because of this practical issue, filters have only been constructed only for the first 18 modes. The combined state space model for the matrix $\mathbf{G}$ contained 755 states.

Figure 5.15 shows the sound radiation of an uncontrolled model, excited by a randomly distributed, white noise excitation. The model fits the radiation very well, for the modes that have been taken into account. This is unsurprising, as only the self radiation of the modes is taken into account, because there is no correlation between the excitation of the different modes. Furthermore, the self radiation of modes is most easily fitted with accurate models.

5.3 Comparison of the models

The previous section showed two different ways of modelling the sound radiation into the farfield from a simply supported plate. Here a comparison between the two models is made.

On first inspection of the models, the model complexity is quite different. The radiation mode approach, described in section 5.2.2 results in a model of 20 dynamic filters for 20 radiation modes, with a total of 135 states. The modal radiation approach described in section 5.2.3 modelling only the radiation of the first 18 structural modes, resulted in a model with 86 filters and a total of 755 states. It can also be noted that the radiation mode approach is independent of the dynamics of the structure, i.e. the model does not need to change if the modeshapes of the structure changes. This is not the case of the modal radiation approach.

Figure 5.16 shows different elements of the modal radiation matrix $\mathbf{M}$ calculated with both approximations, compared to the values according the farfield approximation. It can be seen that the modal radiation spectral factorisation technique results in more accurate approximations of the modal radiation efficiency. The radiation mode approach, on the other hand, is capable of creating negative off diagonal elements.

To see how the differences in the models impacts on the actual calculated sound radiation, the models are compared for four characteristics:

- Sound radiation spectrum of the uncontrolled plate, excited by a randomly distributed, white noise pressure field.
- Sound radiation spectrum of the controlled plate, excited by a randomly distributed, white noise pressure field. The controller is a decentralised, constant gain, velocity feedback controller, calculated to minimise the kinetic energy of the plate, as described in chapter 4. The controller uses 16 evenly distributed control locations and was designed with an effort weighting of $1 \cdot 10^{-5}$.
- Sound radiation spectrum of the uncontrolled plate, excited by a single point source at $(x, y) = (0.24l_x, 0.6l_y)$.
- Sound radiation spectrum of the controlled plate, excited by a single point source at $(x, y) = (0.24l_x, 0.6l_y)$. The controller is the same as for the white noise excitation.

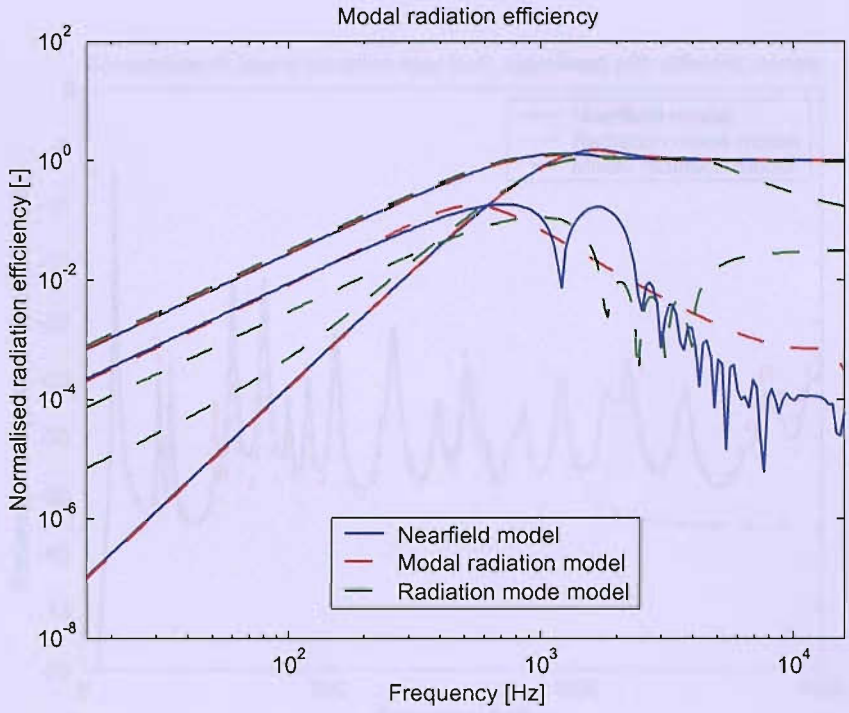

Figure 5.16: Comparison of modal radiation efficiency as calculated with radiation modes, spectral factorisation of modal radiation and the farfield approach. Depicted are the auto radiation of the (1,1) and the (1,2) mode, as well as the cross radiation of the (1,1) mode with the (1,3) mode.

Figures 5.17(a) to 5.18(b) show the sound radiation spectrum of the models up to 1.5 kHz. The modal radiation approach does create a model that is more accurate up to 1 kHz. However, considering the vastly lower number of states and its independence of structural modeshapes, the radiation mode approach is favoured here and will be used to create controllers.

5.4 Control of sound radiation on a plate

This section expands on the control of the plate for ASAC and compares LQG control and centralised and decentralised static velocity feedback control. The LQG and static velocity feedback controller are optimised to control a cost function, J_{ac}, which is a sum of the sound radiation and a weighted control effort term:

$$J_{ac} = \mathrm{E}\left[\mathbf{x}^T\mathbf{Q}_{ac}\mathbf{x} + \mathbf{u}^T\mathbf{R}\mathbf{u}\right] \tag{5.36}$$

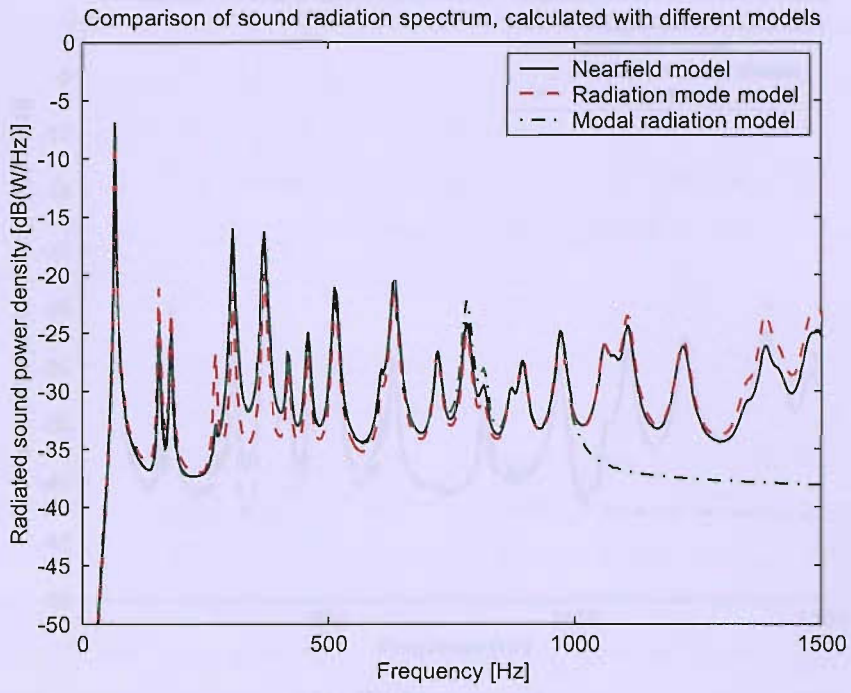

(a) Without control

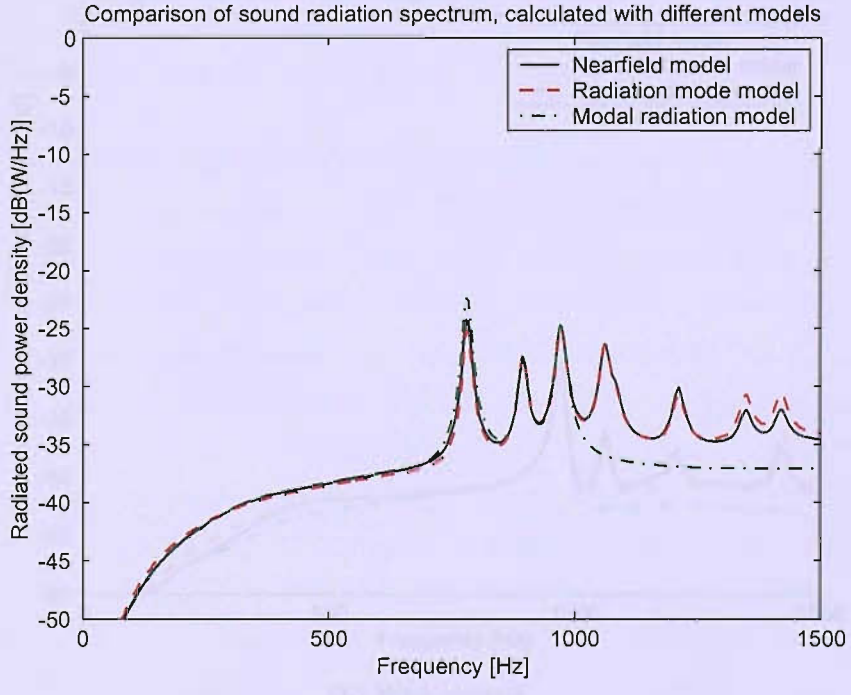

(b) With control

Figure 5.17: Comparison of sound radiation spectrum as calculated with radiation modes, spectral factorisation of the modal radiation and the farfield approach, from a plate, with and without control, excited by randomly distributed white noise.

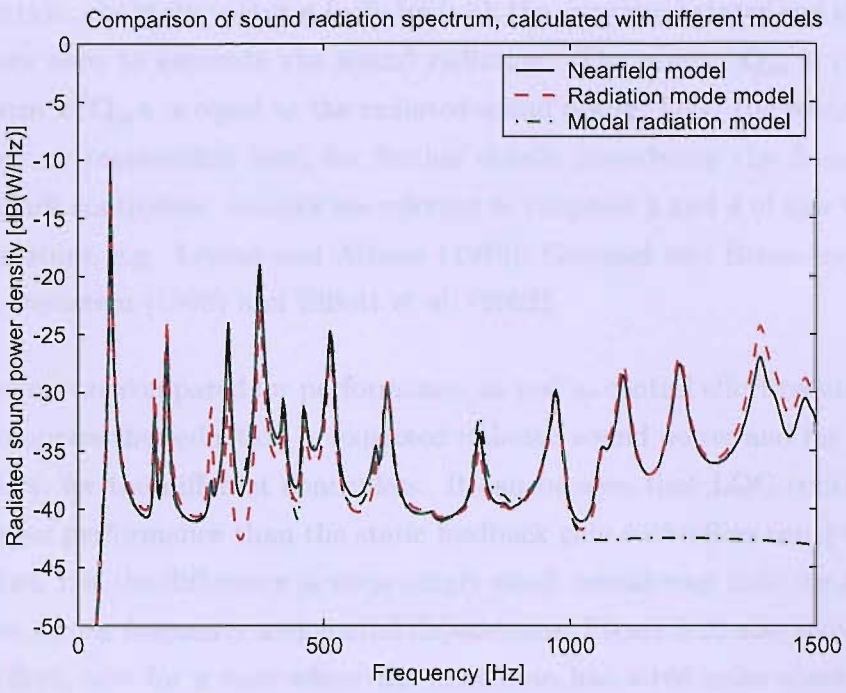

(a) Without control

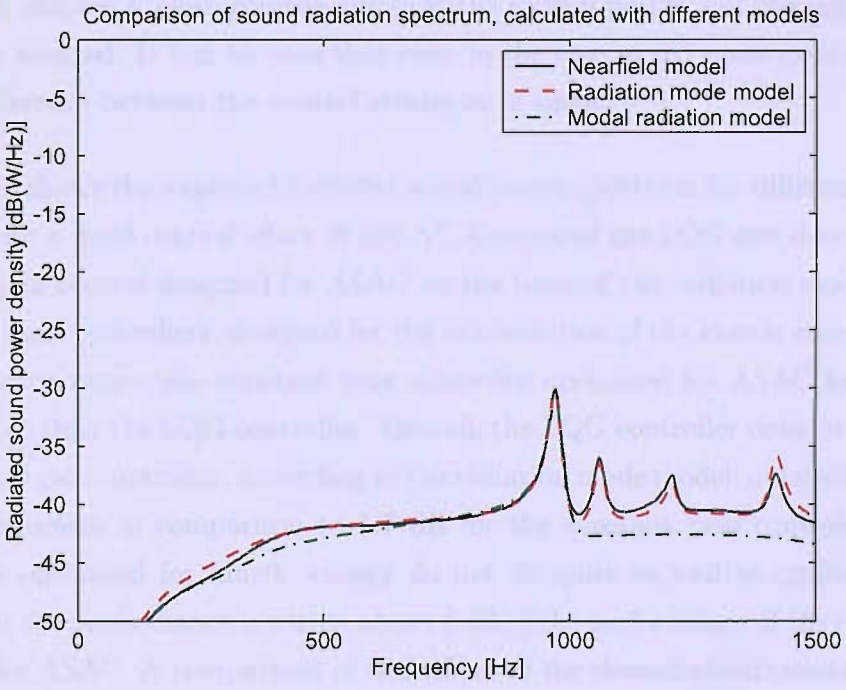

(b) With control

Figure 5.18: Comparison of sound radiation spectrum as calculated with radiation modes, spectral factorisation of the modal radiation and the farfield approach, from a plate, with and without control, excited by a single, white noise, point force at $(x, y) = (0.24l_x, 0.6l_y)$.

In this function, the state-vector $\mathbf{x}$ includes both the structural states and the states of the filters used to estimate the sound radiation. The matrix $\mathbf{Q}_{ac}$ is chosen so that the term $\mathbf{x}^T\mathbf{Q}_{ac}\mathbf{x}$ is equal to the radiated sound power. Only the results of this opimisation are represented here, for further details considering the design of the static feedback controllers, readers are referred to chapters 3 and 4 of this thesis, as well as literature, e.g. Levine and Athans (1970), Geromel and Bernussou (1979), Clark and Bernstein (1998) and Elliott et al. (2002).

The controllers are compared for performance, as well as control effort required. Figure 5.19 compares the reduction in expected radiated sound power and the required control effort, for the different controllers. It can be seen that LQG control has a slightly better performance than the static feedback gain controllers using the same control effort, but the difference is surprisingly small considering that the radiation modes show strong frequency and spatial dependence. Figure 5.20 also shows reduction and effort, now for a case where the excitation has a red-noise spectrum and the structure is controlled at 5 randomly chosen locations. In accordance with the analysis in chapter 4, close spacing amongst the control points and the edges of the plate were avoided. It can be seen that even in the case of red noise excitation the overall difference between the control strategies is small.

Figure 5.21 shows the expected radiated sound power spectrum for different control strategies for a fixed control effort of 300 N^2. Compared are LQG and decentralised constant gain control designed for ASAC on the basis of the radiation mode model and those same controllers, designed for the minimisation of the kinetic energy. Over this frequency range, the constant gain controller optimised for ASAC has better performance than the LQG controller. Overall, the LQG controller does outperform the constant gain controller, according to the radiation mode model, obtaining 2.0 dB average reduction in comparison to 1.7 dB for the constant gain controller. The controllers optimised for kinetic energy do not do quite as well as optimising for ASAC, but the performance is within about 6 dB of the performance of the controller designed for ASAC. A comparison of the values of the decentralised constant gains optimised for ASAC, with the ones optimised for kinetic energy revealed slightly higher gains for the control points closer to the center of the plate.

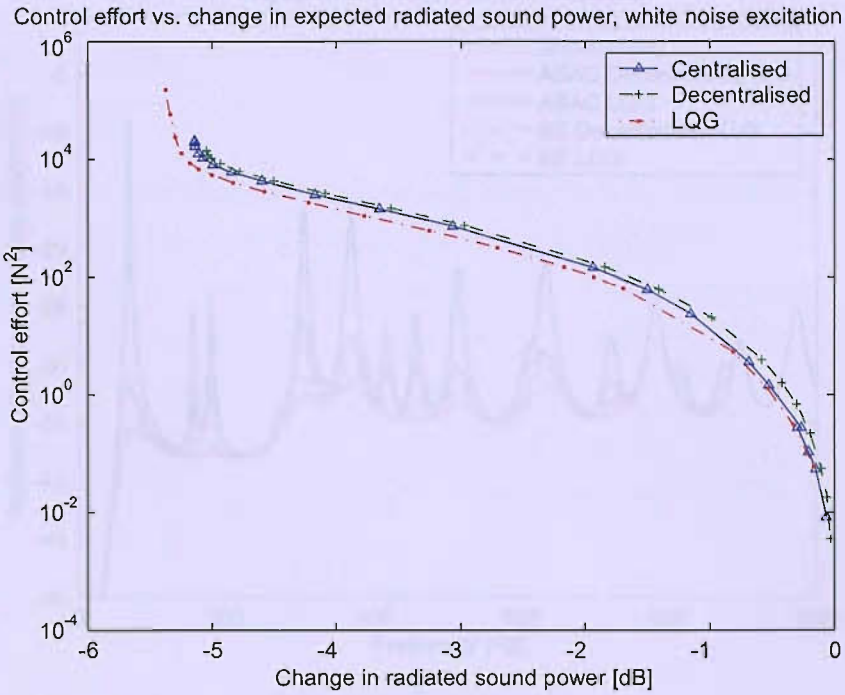

Figure 5.19: Reduction in radiated sound power, calculated with the radiation mode model vs. required control effort, for different controllers, white noise excitation.

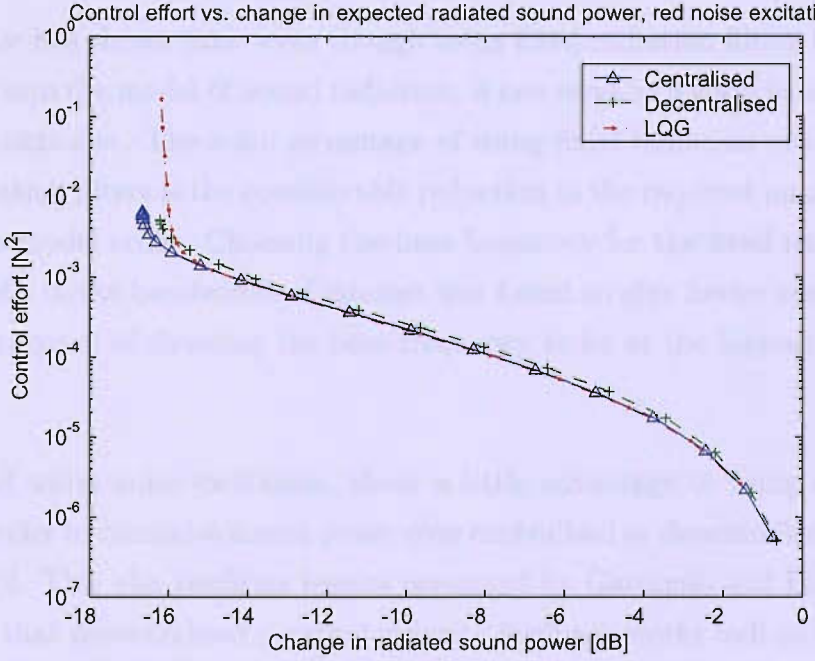

Figure 5.20: Reduction in radiated sound power, calculated with the radiation mode model vs. required control effort, for different controllers, red noise excitation.

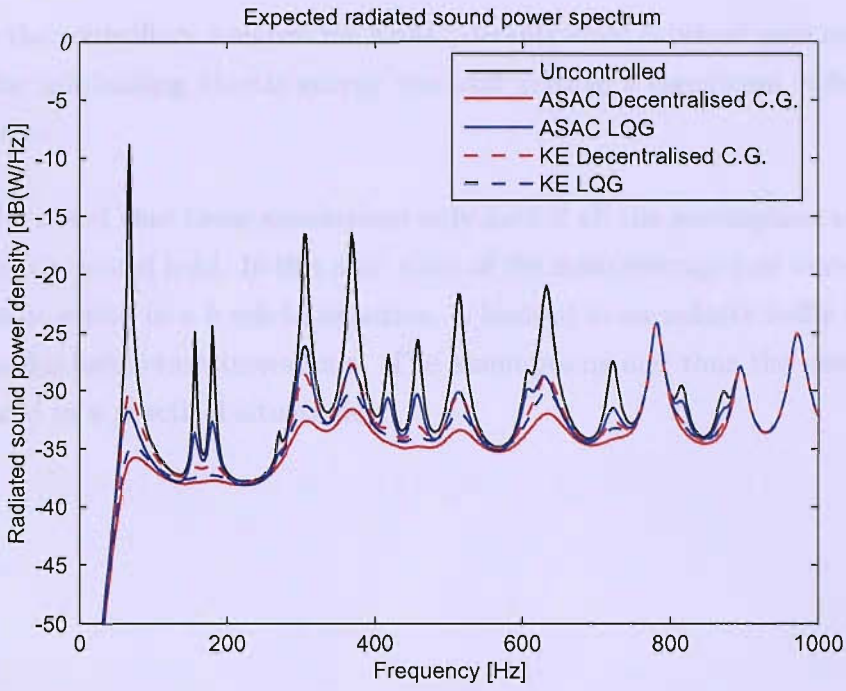

Figure 5.21: Expected radiated sound power spectrum for the different controllers.

5.5 Conclusion

This chapter has shown that, even though using fixed radiation filters introduces an inaccuracy into the model of sound radiation, it can serve as a good basis for creating an ASAC controller. The main advantage of using fixed radiation mode filters over modal radiation filters is the considerable reduction in the required number of filters, and thus in model order. Choosing the base frequency for the fixed radiation filters in the middle of the bandwidth of interest was found to give better results than the previous approach of choosing the base frequency to be at the highest frequency of interest.

For red and white noise excitation, there is little advantage in using a centralised, LQG controller to minimise sound power over centralised or decentralised static feedback control. This also confirms results presented by Gardonio and Elliott (2004a), who found that decentralised constant velocity feedback works well to reduce sound transmission through a panel.

Controllers designed to minimise sound power radiation do obtain better results than controllers designed to minimise kinetic energy in the structure. Although not quite

as good as the controllers designed for ASAC, decentralised constant gain controllers designed for minimising kinetic energy can still achieve a significant reduction in radiated noise.

It should be noted that these conclusions only hold if all the assumption about the sound radiation model hold. In this case, some of the main assumptions were that the plate radiates sound in a freefield situation, is located in an infinite baffle and that there is no fluid-structure interaction. The assumptions and thus the conclusions, may not hold in a practical situations.

Chapter 6

Self-tuning and measurements

This chapter describes how the approximations studied in chapters 3 and 4 could be used to tune a fixed gain feedback controller, based only on information available locally at the control locations.

The tuning of the controller involves two parts. On the one hand, it involves creating estimates of the properties of the structure under control and on the other hand it involves the tuning of the controller, based on those properties. If this can be done online, with both the estimation of the variables and the controller updated continuously or at intervals, this process is known as *adaptive control*. The design of an adaptive feedback controller that uses state estimation for feedback control, requires a reasonable accurate model identification beforehand. The stability and performance robustness of such a system would require an extensive analysis. It was already shown in chapter 4 that, for collocated force actuators and velocity sensors and the assumed excitation, the LQG controller did not improve performance significantly in comparison to decentralised constant gain feedback control if the latter is tuned properly. This chapter will focus on using the locally measured transfer functions to identify the variables required for the tuning of the feedback gain controllers. Optimal power absorption is also examined, but this does not require analysis of the transfer function.

The identification of the required variables might be more difficult when the structure is already being controlled at other control locations. This multi-channel control situation is examined in section 6.2. This is also how 'self-tuning' should be inter-

preted; that in a multi-channel set-up, the controller at each control location is tuned on the basis of the signals measured at that point, without any knowledge of how, if or where controllers at other control locations are set.

Last, it is examined whether the required variables can also be measured in a laboratory set-up and used to experimentally tune a practical feedback controller.

6.1 SISO tuning

In this section, the information that could be gathered locally is reviewed. In particular, it is examined how the information can be used to tune the approximations described in chapter 3.

6.1.1 Data gathering

The open-loop frequency response from the control force to the measured velocity is assumed known for this self-tuning. This is equal to the point mobility of the structure. It could be measured, for example, from the correlation functions between the in- and output (Bendat and Piersol (1986)) when the actuator is driven by a random signal with no feedback. These correlation functions can be influenced by additional noise at the input and the output of the model. From the frequency response, the open-loop impulse response can be calculated. The method of acquisition of the open-loop frequency or impulse response functions is not considered in detail here. Methods of identifying open-loop responses are discussed extensively in Ljung (1999), while in Veres and Wall (2000) the effects and possible benefits of identification in a closed-loop system are discussed.

6.1.2 Maximum power-absorption

The tuning of the controller to maximise power absorption could be done on-line. The maximum power absorption can be calculated from the time-averaged product of the velocity and output force. This quantity could be maximised, by slowly in- or

decreasing the gain (Redman-White et al. (1987) and Nelson (1996)). However, it was already seen in section 3.2.3 of this thesis, that maximising the power absorption can result in gains that are too high in comparison to the optimal feedback gain. Furthermore, the result will be influenced if the excitation changes, because the tuning method is based on the actual power measured at the control point, rather than the local transfer function. However, as long as the feedback gain is constricted to be positive real and the excitation has a narrow auto correlation function, maximising the power absorption is unlikely to increase the overall response of structure, to the degree seen, for instance, in Elliott et al. (1991) for tonal excitation.

Practical single-channel power maximisation was also investigated in two companion papers, Hirami (1997b) and Hirami (1997a). In these papers, the power to be maximised is measured within a so called *sing-around time*. This denotes the time it takes for the wave caused by a switch in feedback gains to reflect of the boundary and get back to the control point. It was argued that, if this method is applied, it is similar to absorbing maximum power from an infinite structure. In simulations on a string this seems to be an effective method. However, string motion is governed by the wave equation (Meirovitch (1986)), with a constant wave-speed for all frequencies. For bending waves, the wave-speed is variable with frequency; as the frequency increases, so does the wave-speed. Thus it is difficult to define a sing-around time for a broadband excitation on a structure dominated by bending waves. The method considered in section 6.1.4, circumvents this problem for the plate structure.

6.1.3 Reduced-number-of-modes approximations

For the two- and three-mode formulas (equations 3.56 and 3.57), the necessary variables for tuning are the resonance frequencies (ω_n), the modal amplitudes (ψ_n), the mass of the structure (M) and the integral of the squared modeshape over the structure (N_n). It can be shown that these last three factors can actually be identified as a single factor for each on the modes. To do that, the measured amplitude of the mobility is compared to the mobility that could be expected on the basis of the measured damping ratio and resonance frequency. It is assumed that at resonance, the structure behaves like a lightly damped mass-spring system.

The damping at a particular resonance can be calculated from the shape of the

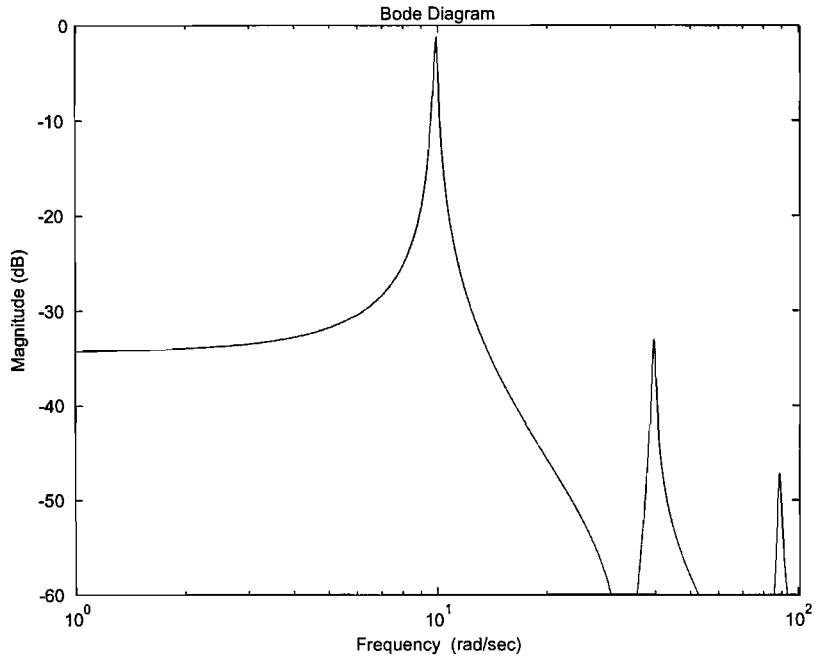

Figure 6.1: Amplitude of displacement response of the beam at $x = 0.6L$

frequency response of the displacement near the resonance frequency (Meirovitch (1986)). Figure 6.1 shows the amplitude of the displacement response of the beam at 0.6 of its length. For light damping, Meirovitch (1986) gives as an estimate of the damping factor:

$$\zeta \approx \frac{\omega_{hp\,2} - \omega_{hp\,1}}{2\omega_n} \tag{6.1}$$

where $\omega_{hp\,1}$ and $\omega_{hp\,2}$ are the *half power points*, which are those points where the amplitude falls to $1/\sqrt{2}$ of the maximum magnitude of the transfer function ($\approx$ -3 dB). For the structure near resonance, the frequency response is dominated by a single mode, whose motion is described by equation 2.4 for the beam, or equations 2.12 and 2.22 for the plate structures. The amplitude of the transfer function of the force to displacement at a point on the structure is then given by:

$$A_{struct}(j\omega_n) = \left| \sum_{i=1}^{\infty} \frac{\psi_i H_i(j\omega_n)\psi_i}{j\omega_n} \right| \approx \left| \frac{\psi_n H_n(j\omega_n)\psi_n}{j\omega_n} \right| = \frac{1}{M}\frac{\psi_n^2}{N_n}\frac{1}{2\zeta\omega_n^2} \tag{6.2}$$

Since ω_n and ζ are known, $A_{struct}(j\omega_n)$ can thus be used to estimate $\frac{1}{M}\frac{\psi_i^2}{N_i}$. The actual mass and squared modeshapes need not be calculated separately.

This method does depend on how accurately the half power points and the maximum response can be measured. For very lightly damped modes, a fine frequency spacing

in the frequency response is required to make an accurate estimate of the damping factor and the required factors. Using such a fine frequency spacing, does allow the accurate calculation of the factor $\frac{1}{M}\frac{\psi_i^2}{N_i}$. Other methods based on curve-fitting might result in better estimates on the basis of a wider frequency spacing. The only exception is if the acuator is located at a nodal line of that particular mode and thus be unable to observe the resonance. In that case, the next resonance is likely to be observable. The method described here is not meant to be a definitive way of calculating the gains, but more a proof-of-principle that the values can be calculated.

The simplified two-mode formula described by equation 3.58 requires the knowledge of the mass of the structure, as well as the first two resonance frequencies. The mass can not be directly derived from the frequency response and would have to be assumed known. Thus, this formula can only be used in an adaptive set-up if the mass of the structure is not going to change. The identification of the first two resonances is not difficult in the single-channel case.

6.1.4 Matched infinite plate impedance

On the plate, it has been shown in chapters 3 and 4 that the matched infinite plate impedance performed well as a control strategy. The measurement of the infinite plate impdeance does not appear straightforward. However, it is shown here to be approximately equal to the frequency average of the real part of the impedance of the plate.

Consider the energy input of a unit impulse force, f_t into an infinite plate:

$$\begin{aligned} E_{in} &= \int_{-\infty}^{\infty} f_t(t)\dot{w}(t)\mathrm{d}t \\ &= \int_{-\infty}^{\infty} f_t(t) \int_{-\infty}^{\infty} \dot{w}_i(\tau) f_t(t-\tau)\mathrm{d}\tau\mathrm{d}t \\ &= \int_{-\infty}^{\infty} \mathbb{R}\left(f_\omega(j\omega) Y_{cc\,\infty}(j\omega) f_\omega(j\omega)\right) d\omega \\ &= \frac{1}{2\pi}\int_{-\infty}^{\infty} \mathbb{R}\left(Y_{cc\,\infty}(j\omega)\right) d\omega \end{aligned} \tag{6.3}$$

where $\dot{w}(t)$ is the velocity of the infinite plate, $Y_{cc\,\infty}(j\omega)$ is the mobility of the infinite plate at the control point and $f_\omega(j\omega)$ is the Fourier transform of the impulse force,

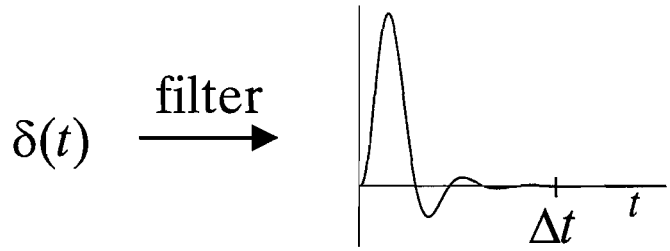

Figure 6.2: Filtering of an impulse function results in a longer time signal.

which is equal to 1 for all frequencies.

The local mobility of an infinite plate is equal to $1/(8\sqrt{EI\rho h})$ (Cremer et al. (1988)) Thus a mathematically ideal impulse with unlimited high frequency content, would result in an infinite energy input into the plate. This is because of the way the flexural motion of the plate has been modelled. By ignoring the rotational inertia, the flexural wave speed approaches infinity as the frequency approaches infinity. The infinite flexural wave speed at high frequencies would seem to imply that, on a finite plate, reflections would immediately interact with the excitation. However, it can be shown that this is not the case if a more complete analysis is performed.

Suppose that the impulse is filtered to create a limited frequency content. Limiting the filter in the frequency domain will cause a lengthening of the signal in the time domain, as illustrated in figure 6.2. If the product of the highest wave speed (the wave speed of the highest significant frequency in the filtered impulse) and the length of the filtered impulse is smaller than twice the distance to the nearest boundary or other control point, the reflection of the input signal can not interact with the signal itself. The wave speed is given by (Cremer et al. (1988)):

$$c(\omega) = \sqrt[4]{\frac{EI}{\rho h}}\sqrt{\omega} \tag{6.4}$$

Figure 6.3 shows the pulse length, measured here as the time it takes for the filtered impulse to decay indefinitely to below 1% of its maximum value, as well as the time required for the highest significant frequency to reflect back. In this case, the filter is taken to be a 4th order low pass Butterworth filter. The highest significant frequency is assumed to be the cut-off frequency at which the Butterworth filter has been set.

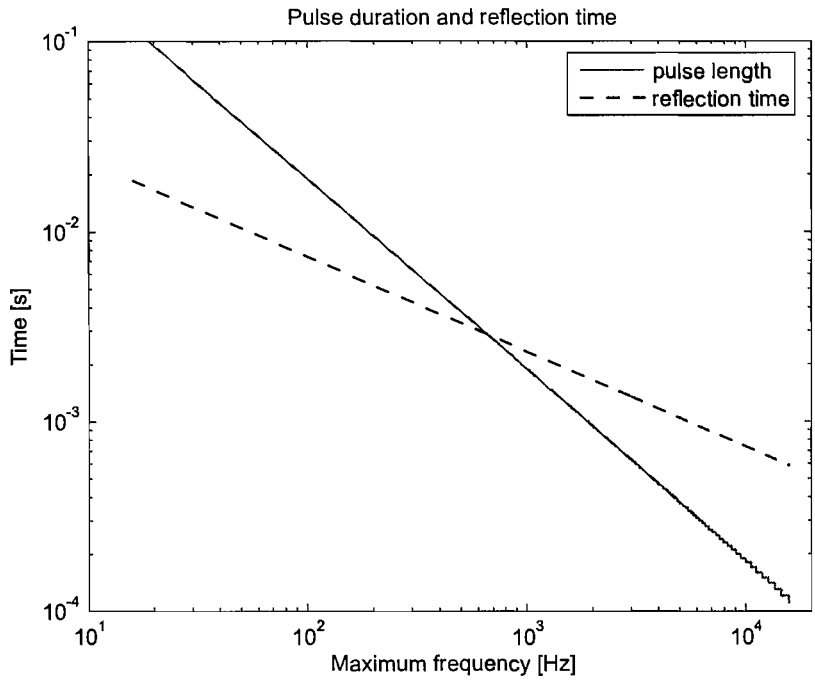

Figure 6.3: Pulse length and minimum reflection time as a function of the cut-off frequency.

Figure 6.3 shows that if the frequency range is high enough, the pulse will be short enough not to interact with its reflections. In addition, higher frequency components should have smaller reflections, because of the damping in the structure. Thus, at the point of excitation, the finite plate must behave as an infinite plate for the duration of the signal. The energy input into the finite plate must therefore also the same as the input into the infinite plate:

$$E_{in} = \frac{1}{\pi}\int_0^{\omega_{max}} \mathbb{R}\left(Y_{cc\,\infty}(j\omega)\right) d\omega = \frac{1}{\pi}\int_0^{\omega_{max}} \mathbb{R}\left(Y_{cc}(j\omega)\right) d\omega \tag{6.5}$$

Here, $Y_{cc}(j\omega)$ is the mobility of the finite plate. One can also conclude then, that over that frequency range the average of the mobility of the finite plate and the infinite plate must be equal.

$$\underset{\omega}{\mathtt{mean}}\left[\mathbb{R}\left(Y_{cc\,\infty}(j\omega)\right)\right] = \underset{\omega}{\mathtt{mean}}\left[\mathbb{R}\left(Y_{cc}(j\omega)\right)\right] \tag{6.6}$$

where $\underset{\omega}{\mathtt{mean}}$ denotes the average over the frequency range.

This last equation allows us to estimate the infinite plate impedance for the matched infinite plate impedance approximation. The impedance of the infinite plate is equal

Frequency range [Hz]	100	200	500	1000	2000	5000
Impedance [Ns/m]	16.65	14.75	23.99	31.71	29.61	30.35

Table 6.1: Average real part of the impedance of the simply supported plate at $(x, y) = (0.24l_x, 0.6l_y)$, calculated over different frequency ranges.

to the inverse of the real part of the average mobility of the finite plate.

Table 6.1 shows the calculated value of the inverse of the average mobility for different frequency ranges on the simply supported plate. The impedance of an infinite plate of the same material and thickness would be 31.87 Ns/m. The table shows that these values from 1 kHz match sufficiently for control purposes. For these simulations all the modes up to 10 kHz have been taken into account. The difference between the theoretical value and calculated value can be due to a number of factors, including the limited accuracy of the numerical integration, the limited number of modes and the cut-off in the frequency domain.

As mentioned before in section 3.2.2.5, an infinite beam does not have a real, frequency invariant impedance and this method is thus not suitable for the beam.

6.1.5 Summary SISO control

In the single-input-single-output situation, the required variables for each of the approximation strategies can be identified on the basis of the mobility or the power absorption. Each strategy should approach the values calculated in chapter 3 at each point of the structure. For matching the impedance of the infinite plate, the frequency range over which the mobility needs to be measured is dependent on the distance to the nearest point to reflect a wave. Placing the control location close to a boundary will require a large frequency range to accurately estimate the impedance of the infinite plate.

6.2 Tuning in MIMO setup

In a multi-input-multi-output (MIMO) situation, the transfer function at the point of control is influenced by the control at other points. This may influence the setting of gains in the multi-channel set-up. This section examines how the presence of other feedback loops influences the measurements and thus the calculation of the variables needed for the calculation of the feedback gains. The tuning of the gains is examined on the beam using 2 and 4 evenly distributed control locations and on the simply supported plate using 4 and 16 evenly distributed control locations.

6.2.1 Use of approximations

In these simulations, it is assumed that the structure is controlled at all locations with a decentralised velocity feedback controller tuned to minimise kinetic energy, as described in chapter 4. At one of the control locations the gain is then set to zero. Using the methods described in section 6.1, the required variables for each approximation of the feedback gain are then estimated. If the gains calculated with the approximations are similar in the controlled and the uncontrolled case, the approximation strategy is considered suitable for multi-channel control.

Figure 6.4(a) shows the open-loop mobility of the beam at $0.33L$. If the beam is controlled at $0.67L$ (dash-dot line), the resonance frequencies seem to have shifted to higher frequencies and are a lot more damped. Figure 6.4(b) shows the open-loop mobility at $0.2L$, with the beam controlled at $0.4L$, $0.6L$ and $0.8L$. Figure 6.5(a) shows the open-loop mobility of the simply supported plate at one of the control locations of a plate with 4 distributed control locations. While figure 6.5(b) shows the open-loop mobility of the plate with 16 evenly distributed control locations. In both cases, the mobility has been examined at one of the corners of the square of control points.

In these cases the number of apparent resonance frequencies drops considerably. In figure 6.4(b) the first resonance in the control case occurs at approximately 75 rad/s and the second at 575 rad/s. Where for the uncontrolled case, they were roughly at 10 and 40 rad/s. Setting the gain on the basis of these results with the simplified two-mode formula results in a gain that is an order of magnitude larger than in the

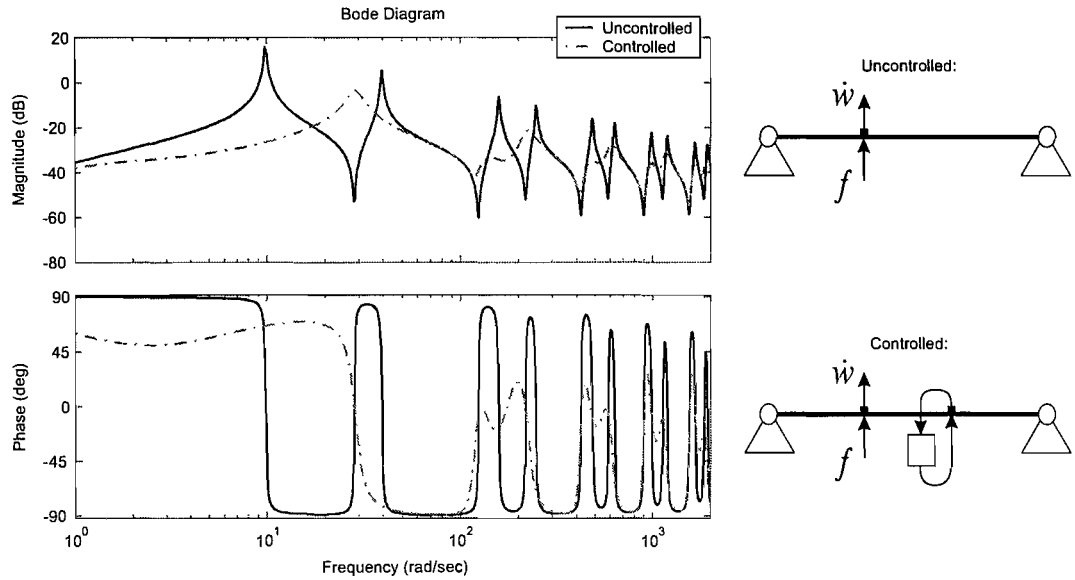

(a) 2 control locations, open-loop mobility at $0.33L$

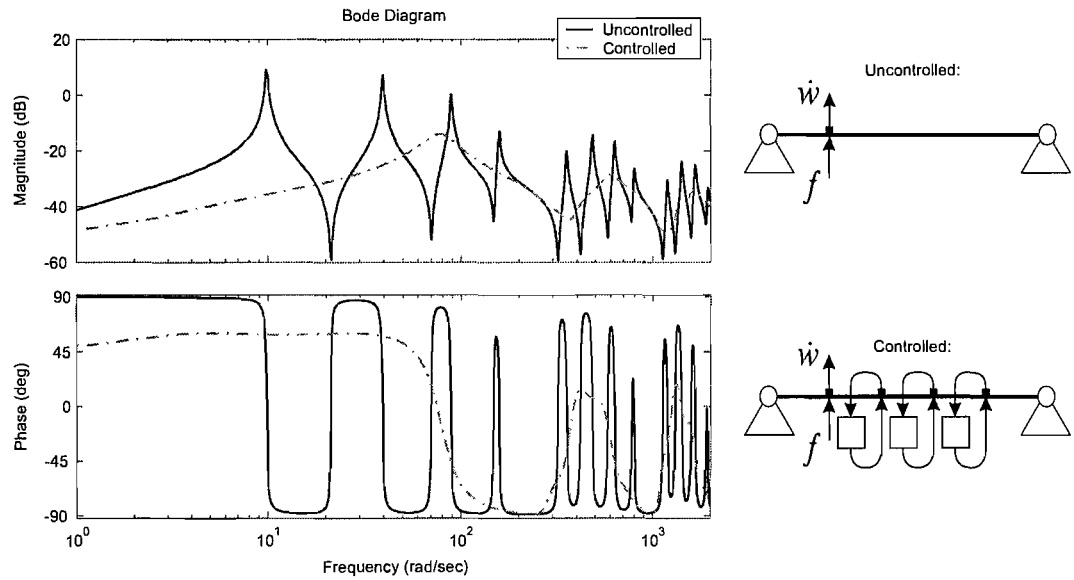

(b) 4 control locations, open-loop mobility at $0.2L$

Figure 6.4: Mobility of the beam with evenly distributed control locations. In the controlled case, control is present at all locations, except the one for which the mobility is depicted.

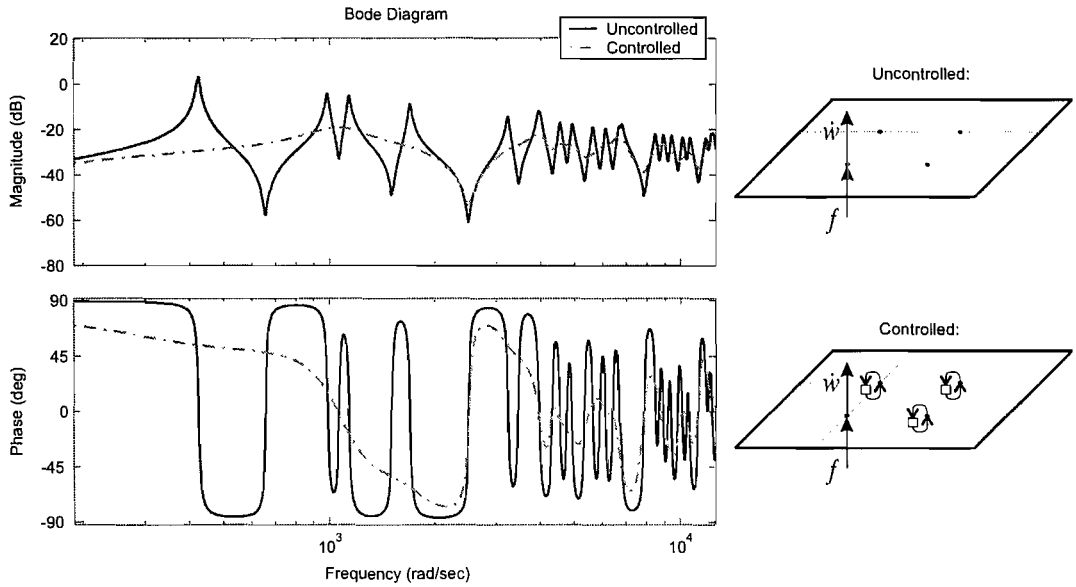

(a) 4 control locations, open-loop mobility at $(0.33l_x, 0.33l_y)$

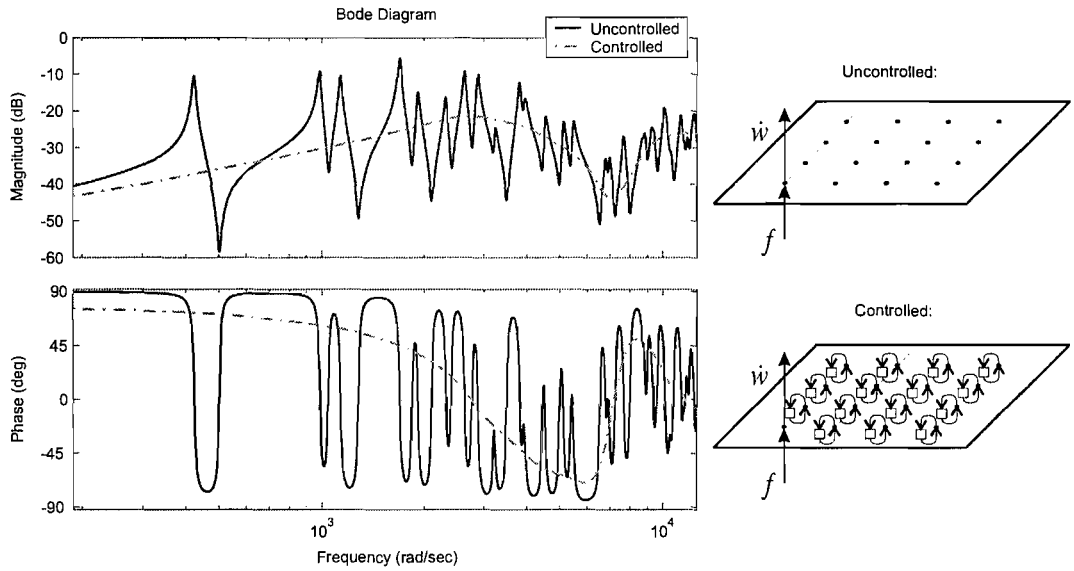

(b) 16 control locations, open-loop mobility at $(0.2l_x, 0.2l_y)$

Figure 6.5: Mobility of the plate with evenly distributed control locations. In the controlled case, control is present at all locations, except the one for which the mobility is depicted.

case where no control is present at other locations on the structure. The simplified two-mode strategy is therefor not suitable as a control strategy. The same seems to hold for the two- and three-mode formulas. However, the calculation of the factor $\frac{1}{M}\frac{\psi_i^2}{N_i}$ will change as well.

Table 6.2 lists the values of the gains calculated using optimisation and approximations. The values for the approximations are calculated on the basis of the measurements presented in figures 6.4(a) to 6.5(b). The results for the uncontrolled situation (unc.) are based on the response that is measured when no control is present at the other locations. These are single channel measurements, discussed in section 6.1. The results in the controlled situation (con.) are calculated using the methods described in section 6.1, but using the response when control is present at the other locations. Thus these gains represent tuning in a multichannel situation. The feedback gains that maximise power absorption in the controlled set-up are also examined and shown in table 6.2.

Despite the large changes in the apparent resonance frequencies, the table shows that the actual calculated feedback gains with the two- and three-mode formulas do not change as much as expected and that in the MIMO controlled case, the gains are of the same order of magnitude as the optimal gains. Maximising power absorption works well on the plate, but overshoots the optimal value by a large margin on the beam.

The infinite plate impedance has also been calculated for the situations shown in figure 6.5(a) and 6.5(b) using the method described in section 6.1.4 over various bandwiths. The results are depicted in table 6.3. The simulations here were done using all the modes up to 10 kHz. The table shows that the presence of control does not influence the calculation of the mean real impedance if a sufficiently large frequency range is examined. The frequency range required to evaluate the gain correctly is the same ($\approx$ 500 Hz). According to the theory in section 6.1.4, this is because the distance to the edge is equal to the distance to the nearest control point. The frequency range needed to evaluate the approximation is then also the same. In the 16 channel case, a larger frequency range is required than in the 4 channel case ($\approx$ 2 kHz). This would be because the distance between the control point and the nearest reflecting point is smaller than in the 4 channel case.

Structure	Beam		Plate	
# control locations	2	4	4	16
optimal feedback gain, unc.	30.49	33.27	23.67	26.53
optimal feedback gain, con.	67.55	103.8	26.64	26.24
2 mode formula, unc.	16.07	24.97	42.74	131.2
2 mode formula, con.	37.95	71.80	37.84	35.18
3 mode formula, unc.	18.78	21.45	14.20	31.94
3 mode formula, con.	42.17	76.65	43.50	36.03
power max, unc.	185.3	173.0	27.07	27.36
power max, con.	199.0	213.1	31.82	33.67

Table 6.2: Calculated feedback gains (Ns/m) for 2 and 3 mode formulas and power maximisation on a structure. The set-ups in the column correspond to the set-ups shown in figures 6.4(a) to 6.5(b). 'unc.' denotes the case where the controller is tuned when no control is present at other locations, whereas for 'con.' there is.

Frequency range [Hz]	100	200	500	1000	2000	5000
Impedance [Ns/m] 4 channel, unc.	1.90	13.0	32.4	28.2	30.9	30.7
Impedance [Ns/m] 4 channel, con.	19.4	14.1	34.3	28.7	31.2	30.6
Impedance [Ns/m] 16 channel, unc.	19.0	13.0	15.2	17.3	30.5	30.2
Impedance [Ns/m] 16 channel, con.	41.7	28.7	17.6	16.0	30.1	30.6

Table 6.3: Average real part of the impedance of the simply supported plate according to the model, calculated over different frequency ranges. The 4 channel case corresponds to the set-up in figure 6.5(a), whereas the 16 channel case corresponds to the set-up in figure 6.5(b).

6.2.2 Concurrent tuning in a MIMO set-up

In the simulation in section 6.2.1, the optimisation of a single control gain is examined, while the other gains are fixed. Ideally, each loop should be able to tune itself while other control loops are also being updated. For the two- and three-mode formulas, concurrent tuning might be difficult, due to the selection of the resonance frequencies as resonances become more and less-pronounced in the frequency response as gains in- and decrease. This possible limit-cycling behaviour is not investigated here.

For matching the impedance of the infinite plate, concurrent tuning should not cause any problems because the value calculated at one location is independent from the gain at a different location if the frequency range examined is sufficiently large.

Concurrent tuning of power absorption may not be trivial. If tuning works correctly, the indepently tuned controller should converge to the optimal decentralised control values. To see if independent tuning of maximised power absorption can converge in a MIMO setup, a simple algorithm was constructed and investigated using simulations of the 16 control locations on the simply supported plate. In this algorithm each control location is adjusted in turn and it follows these steps:

- for a specific control location, examine how much power is absorbed at the current gain.
- increase the current gain by a certain stepsize
- if the power absorption has increased, examine the next control location.
- otherwise, decrease the stepsize and examine the power absorption at the original gain plus the smaller stepsize.
- if the power absorption still has not improved, examine the power absorption at the original gain *minus* the smaller stepsize.
- if the power still has not improved, keep repeating the previous two steps until it does, or the stepsize becomes smaller than a specified minimum.

Figure 6.6 shows the gains of the control locations as they converge together with the the gains that would be optimal to maximise power absorption. As can be seen, the gains become larger than their optimal values. This figure shows that the gains may, through interaction, overshoot their optimal values. The problem is that in

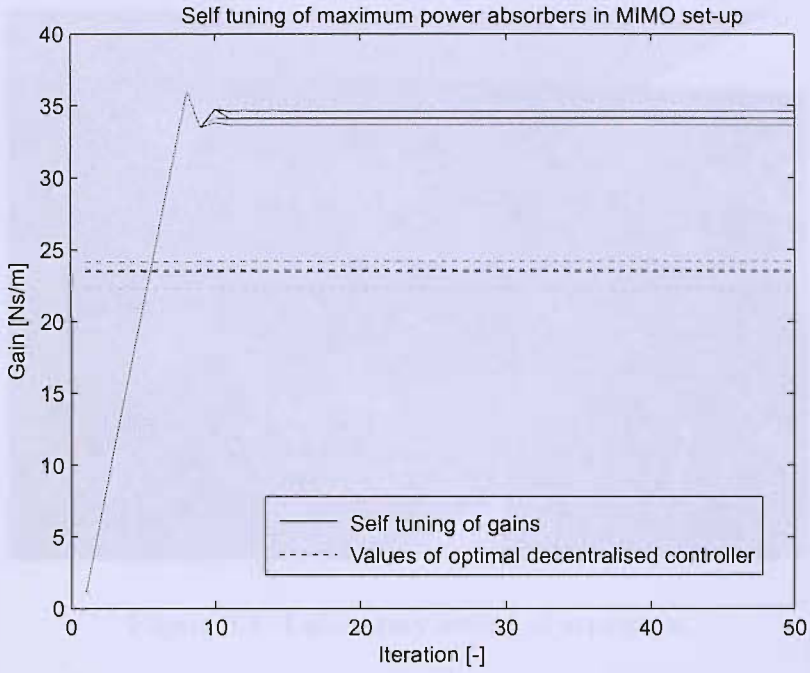

Figure 6.6: Self-tuning of maximum power absorbing controllers, 16 control locations on a plate compared to the values of the optimal decentralised controller maximising power absorption.

the described algorithm, one control location will not 'give up' power absorption in favour of more power absorption at a different control location. It is not clear how to overcome this problem and further study would be required.

6.3 Experiments

The previous sections showed that, theoretically, approximations for the optimal gain can be calculated from the local mobility. This section examines whether these values can be calculated correctly from actual measurements of the open-loop response of an experimental structure and whether stable feedback control is possible using the gains calculated from the approximations. Power measurements were not conducted. The practical measurement of power has been demonstrated by Redman-White et al. (1987) and Hirami (1997a).

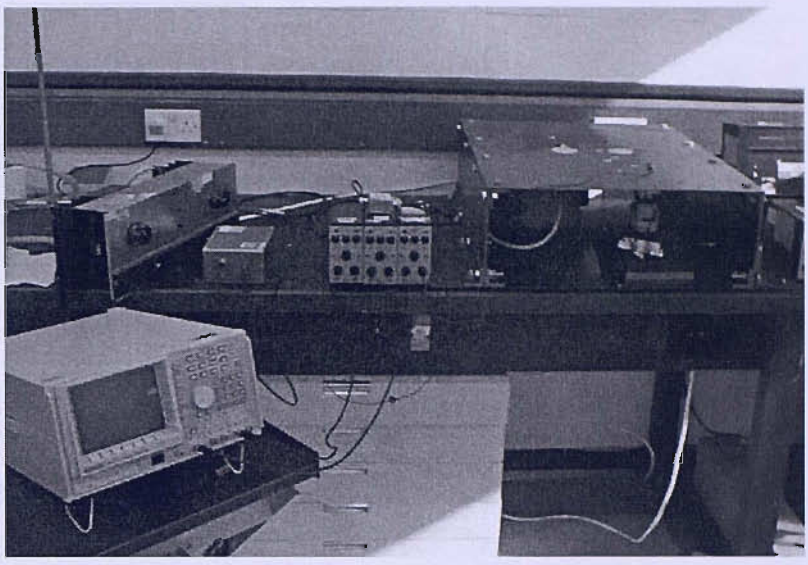

Figure 6.7: Laboratory set-up of structure.

6.3.1 Measuring open-loop response

Figure 6.7 shows the experimental set-up in the laboratory, which was developed by Serrand (1998) and Benassi et al. (2004), though in other configurations. The structure was excited using Ling Dynamic Systems electrodynamic shakers. A LDS type V403 was used as the primary, excitation shaker, while a LDS type V101 was used as the secondary, control shaker. The specifications of these shakers have been listed in tables C.2 and C.3 in appendix C. Accelerometers were used to pick up the signal, which was then amplified and integrated using charge amplifiers. The input signal to the secondary actuator was amplified using a custom made current driver, which gives a specific current output for a particular input voltage. The signal to the primary shaker was amplified using a solid state DC300 amplifier. Appendix C lists all the equipment that was used. The steel plate is 58 cm wide and 70 cm long and its height is 1.85 mm. The outer 4 cm on both ends are used to clamp the edge and have therefor not been taken into account in simulations. The x-axis is taken along the nearest free edge, whereas the y-axis is along the left-hand-side clamped edge.

The open-loop measurement set-up is depicted in figure 6.8. For these measurements the primary, excitation shaker was not attached to the structure.

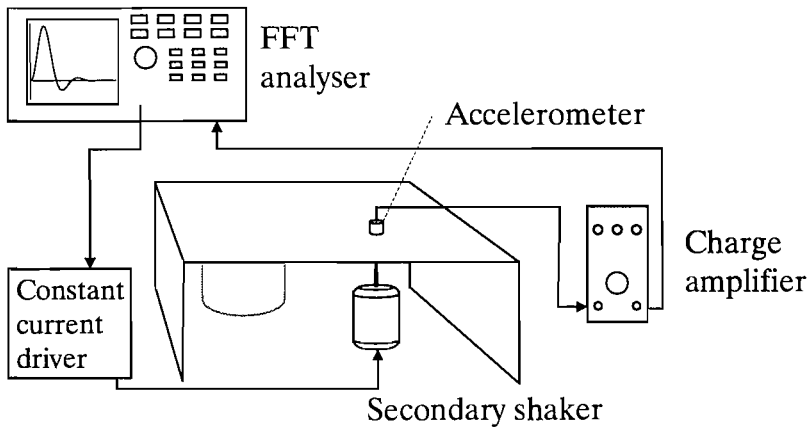

Figure 6.8: Diagram of open-loop measurement set-up of structure.

Figure 6.9(a) shows the response of the structure at $(x, y) = (0.350, .175)$, simulated according to the analysis in section 2.1.3. For the simulation, the 286 modes with a resonance frequency less than 5kHz have been taken into account. Therefor the response drops off at higher frequencies. Figure 6.9(b) shows the measured response, corrected for the gains occurring in the electrical part of the loop. The shaker was assumed to have a flat response and the response was scaled using the low-frequency input-to-force response measured with a force gauge.

The resonances of the structure occur at slightly lower frequencies than expected on the basis of the simulations, but otherwise the model shows reasonable agreement with the measurements at low frequencies. At roughly 6 kHz, a peak occurs in the magnitude of the measured response. The cause of this peak is unclear, as the resonance frequencies of the accelerometer and of the armature of the actuator should occur at higher frequencies. Though this peak limits the range of frequencies for which feedback can effectively be used and requires extra measures to maintain stability, it will be shown in section 6.3.3 that the response is sufficiently close to the model for these experiments.

6.3.2 Deriving variables from experimental data

The variables required for the two-mode and three-mode model can be derived from the measured transfer function by selecting the appropriate resonant peaks. Figure 6.10 shows the resonances and half power points selected for the calculation of the

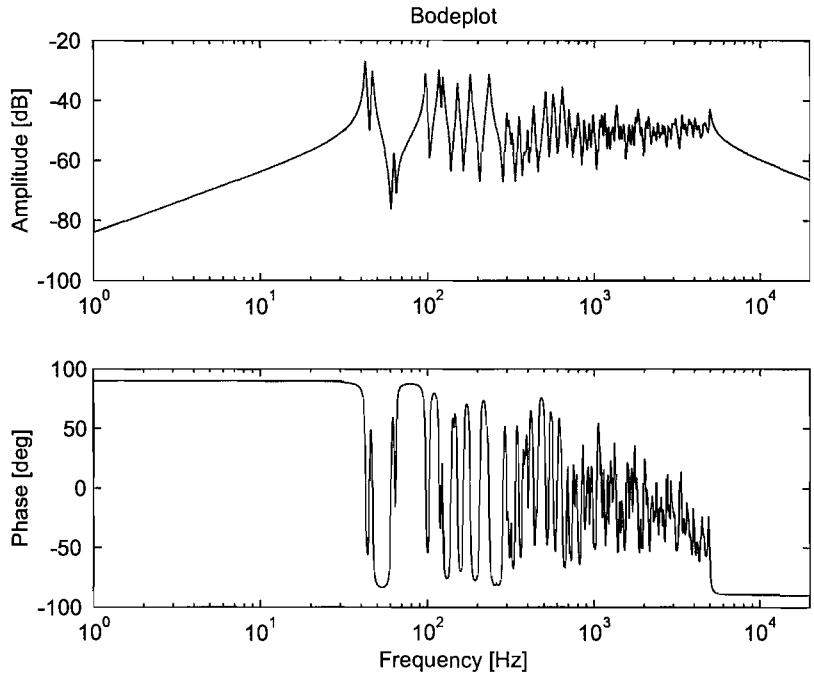

(a) Modelled response

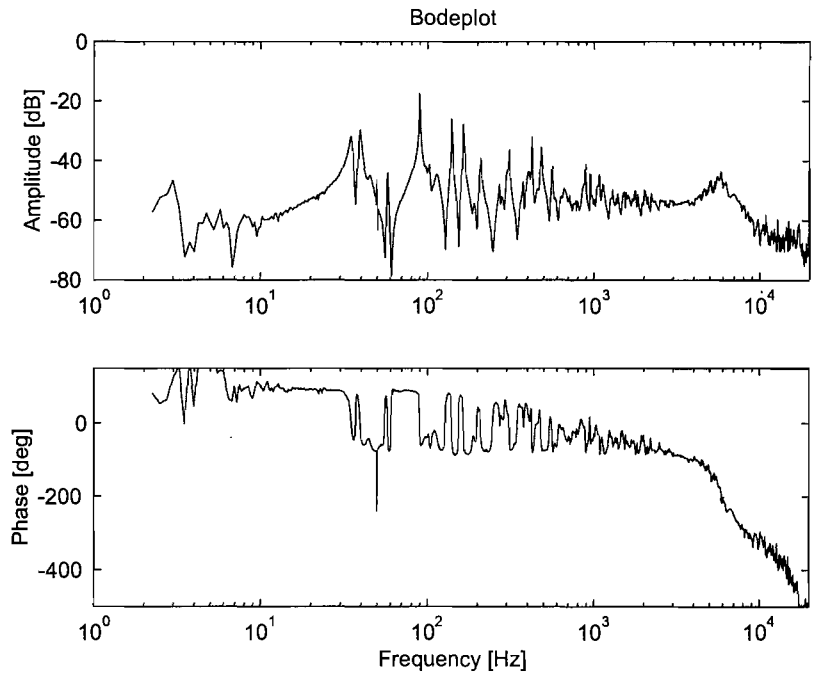

(b) Measured response

Figure 6.9: Mobility of the CFCF plate at $(x, y) = (0.350, .175)$, according to the theoretical model and measured on the structure.

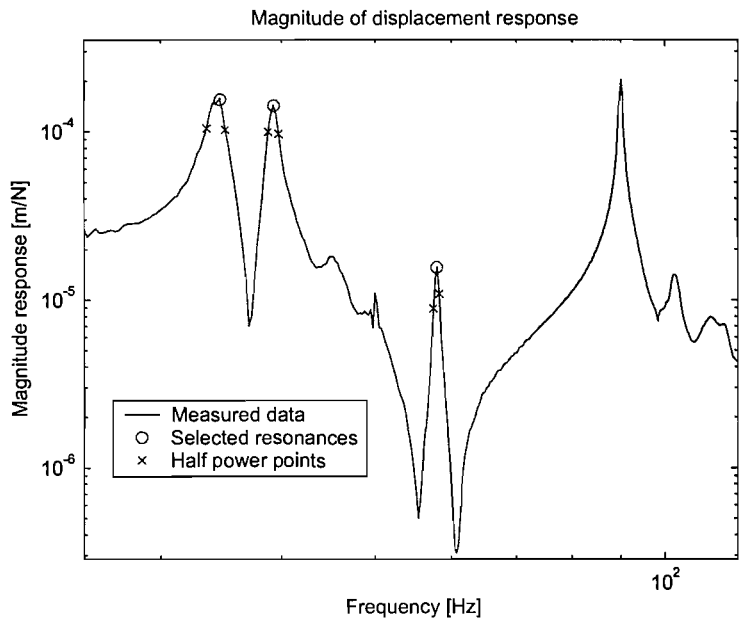

Figure 6.10: Selection of resonances and half power points for two- and three-mode formulas.

two- and three-mode formula in the manner described in section 6.1. The half power points selected are those frequencies where the measured amplitude was below $1/\sqrt{2}$ of amplitude at the resonance frequency. The gain calculated on the basis of the measured data with the two-mode formula was 108 Ns/m and 225 Ns/m for the three-mode formula. On the basis of the modal model of the clamped-free-clamped-free, they were 127 Ns/m and 327 Ns/m.

Table 6.4 shows the frequency average of the real part of the plate impedance according to the theory and as measured on the structure, calculated over different frequency ranges. Again, the mean real impedance comes close to the impedance of the infinite plate, which in this case would theoretically be 327 Ns/m. At 5 kHz, the simulated mean impedance drops off. This is due to the fact that only the modes up to 5 kHz have been taken into account. For the measured data, the impedance also approximates the correct value. From 2 kHz, however, the average impedance drops off. This is due to the phase shift associated with the resonance at 6 kHz, causing the response to have a phase outside the $\pm 90°$.

Frequency range [Hz]	200	300	400	500	1000	2000	3000	5000
Impedance [Ns/m] (simul.)	186	230	314	327	313	328	321	281
Impedance [Ns/m] (meas.)	213	309	334	302	328	303	246	118

Table 6.4: Average real part of the impedance of the CFCF plate at $(x, y) = (.350, .175)$ as calculated using a simulation of the CFCF plate model and as measured on the experimental structure, calculated over different frequency ranges.

6.3.3 Closed-loop measurements

Before closing the loop, the stability of the feedback loop should be examined. Figure 6.11(a) shows the Nyquist plot of the open-loop response at the desired feedback gain. The Nyquist stability criterion demands that the point -1 is not encircled counterclockwise by the open-loop response. The figure, however, shows that it is encircled. The loop that encircles the -1 point is associated with the 6 kHz peak.

The 3 kHz low-pass filter on the charge amplifier is used to reduce the size of the loop that causes the instability. Figure 6.11(b) shows the Nyquist plot of the open-loop response after applying the filter. Now, the response no longer encircles the -1 point and the closed-loop should be stable.

To set the feedback gain in the closed-loop, the amplification factor of the charge amplifier was used. However, this limited the amplification factor to a maximum of 600 Ns/m. Additionally, when both feedback and the disturbance force were presented at the secondary shaker, an additional electronic summing device and a splitter were required, which each have a gain of 1/2. In that case, the feedback gain was limited to a factor 150 Ns/m. It was also found that a low-frequency high-pass filter was necessary to stabilise low-frequency behaviour.

Figure 6.12 shows the set-up of the control when the excitation is presented at the primary location and control is present at the secondary location. The velocity of the structure was measured either at the secondary or at the primary location. Figure 6.13 shows the set-up when the excitation is presented at the secondary location.

Figures 6.14 to 6.16 show the measured transfer functions from, respectively, the primary input to the primary output, the primary input to the secondary output

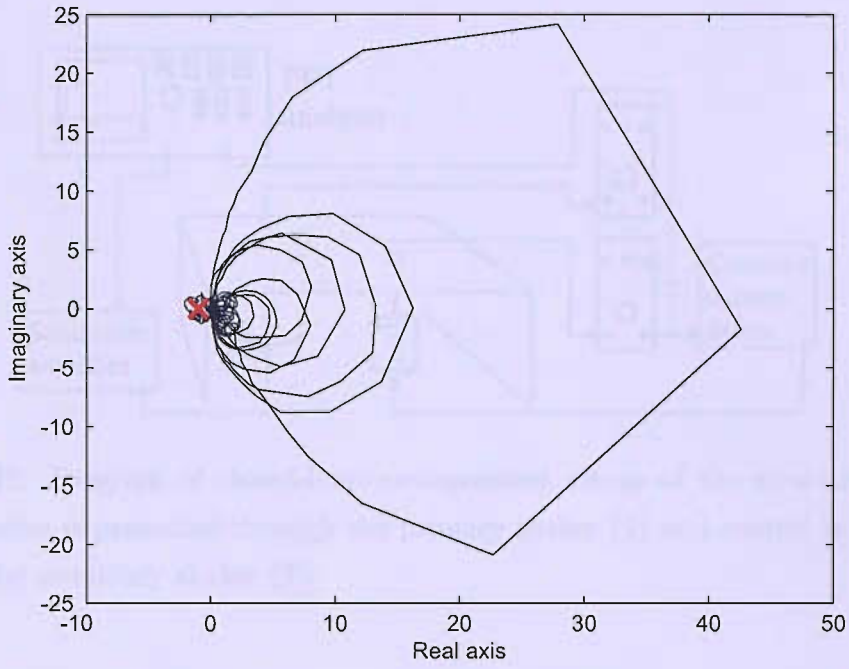

(a) Unfiltered

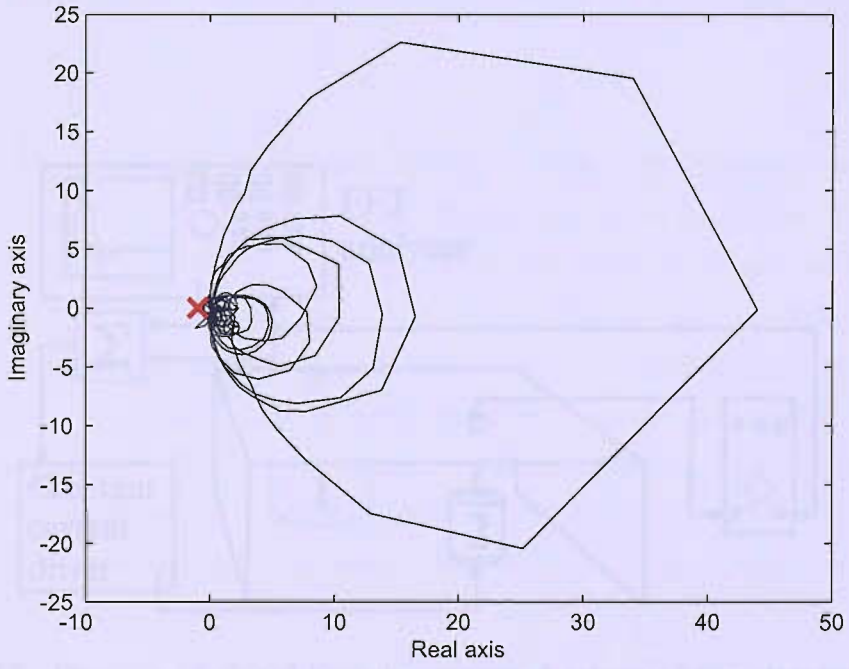

(b) Filtered with 3 kHz low-pass filter

Figure 6.11: Nyquist plot of unfiltered open-loop response at the desired feedback gain.

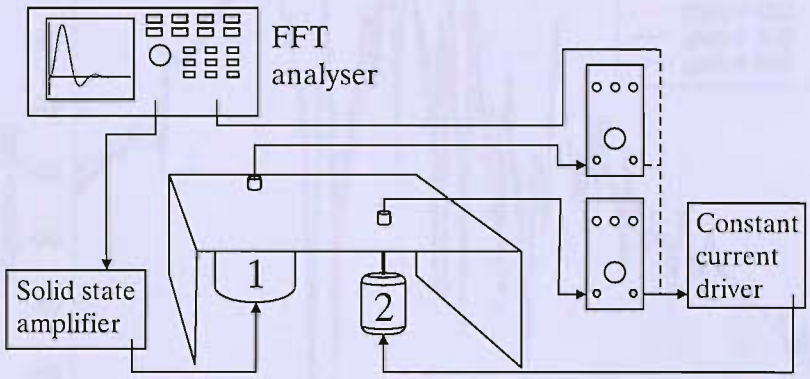

Figure 6.12: Diagram of closed-loop measurement set-up of the structure, when the excitation is presented through the primary shaker (1) and control is achieved through the secondary shaker (2).

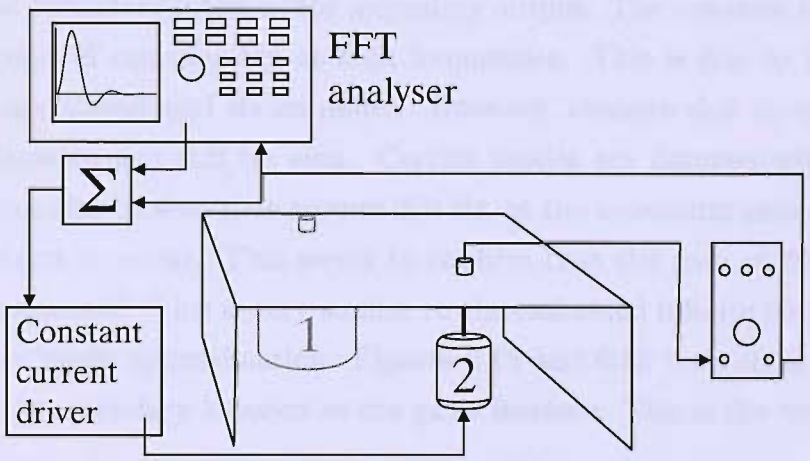

Figure 6.13: Diagram of closed-loop measurement set-up of the structure, when excitation and control are both presented through the secondary shaker.

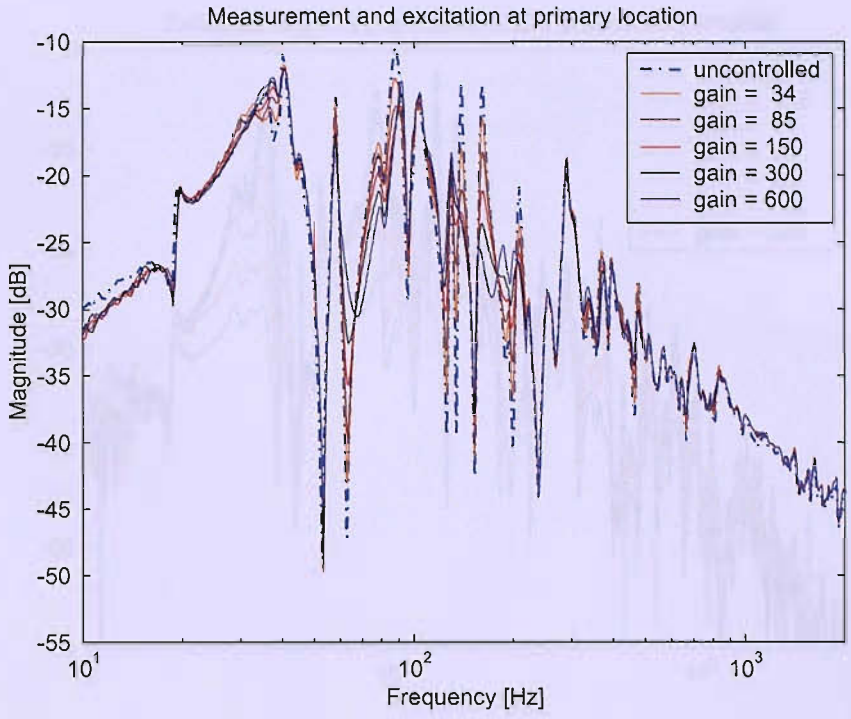

Figure 6.14: Closed-loop measurement of plate response at the primary shaker location with no control and various feedback gains in the control loop at the secondary location.

and from the secondary input to the secondary output. The response in figures 6.14 and 6.15 drops off considerably at high frequencies. This is due to the dynamics of the primary shaker and its amplifier. However, changes due to control at the secondary location can still be seen. Certain modes are damped well due to the control. It can also be seen that around 200 Hz, at the maximum gain of 600, a new resonance starts to occur. This seems to confirm that the gain of 300 is the best from those examined. This is very similar to the estimated infinite plate impedance and the three mode approximation. Figures 6.15 and 6.16 both show a decreasing mobility at the secondary location as the gains increase. This is the 'pinning' of the plate.

6.4 Conclusion

This chapter showed how necessary variables for the tuning of the absolute velocity feedback gain using approximation discussed in chapter 3 can be obtained from

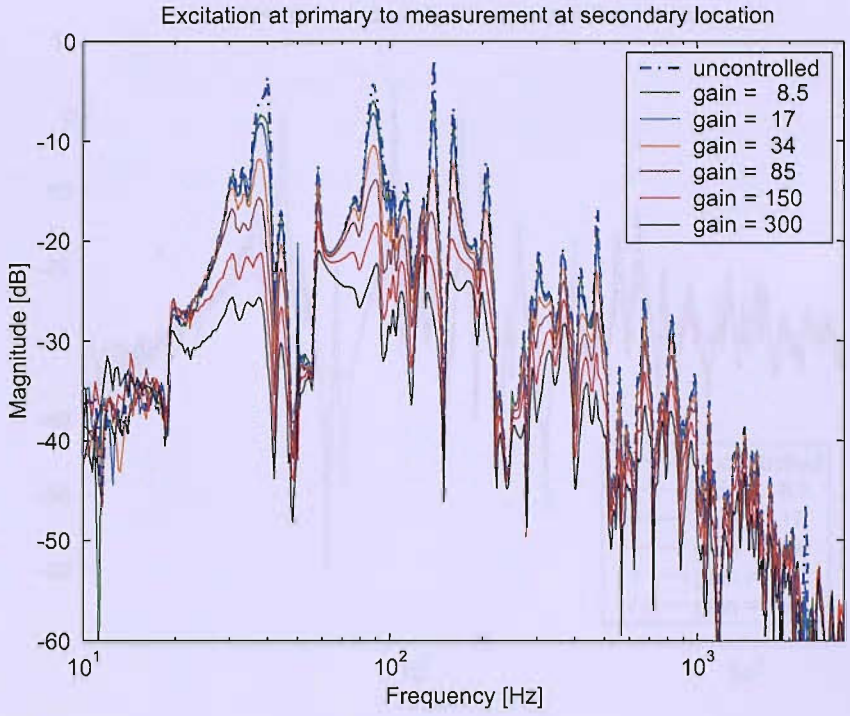

Figure 6.15: Closed-loop measurement of from the primary shaker to the accelerometer at the secondary location with no control and various feedback gains in the control loop at the secondary location.

the mobility at the control point. Section 6.1.3 showed how one can calculate the required values for the two- and three-mode formula from the mobility, in a single-channel control situation. Section 6.1.4 showed that if the mass of the structure is known, the simplified two-mode formula can be tuned on the basis of the first two eigenfrequencies. It also showed that the impedance of the the infinite plate can be derived as the average real impedance in the frequency domain of the finite structure.

Analysis of the tuning of the controllers in a multi-channel situation was done in section 6.2.1. It was shown that for the simplified two-mode formula, the presence of damping in other control loops results in change of an order of magnitude of the feedback gain. It seemed that this would also be the case for the two- and three-mode formulas. However, because of the identification of the factor $\frac{1}{M}\frac{\psi_i^2}{N_i}$, the gains remained in the same order of magnitude of the optimal gain. They can therefore not be ruled out for the purposes of control, but their suitability is difficult to prove.

The impedance of the infinite plate can be derived in the multi-channel set-up,

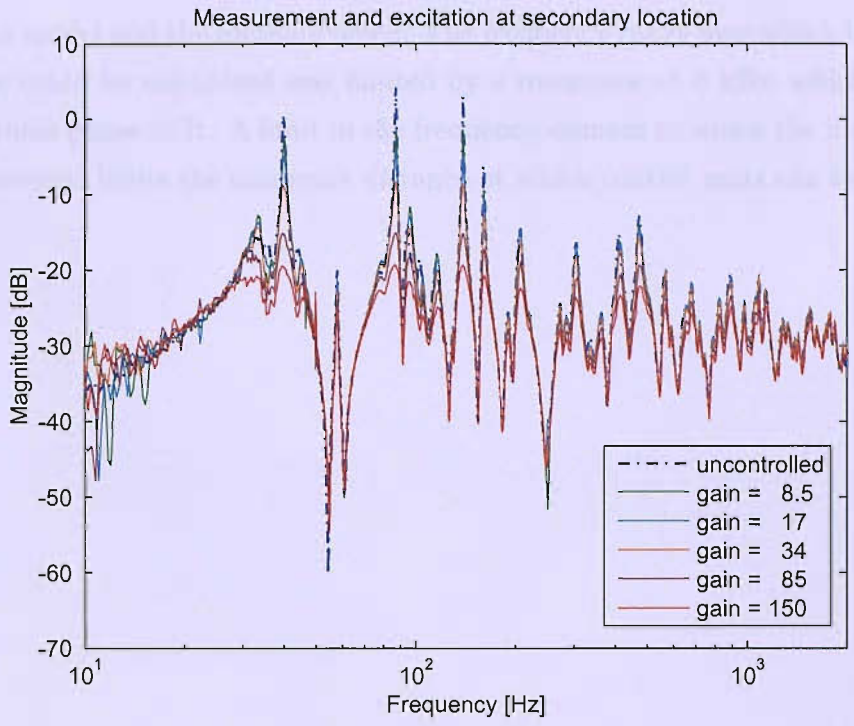

Figure 6.16: Closed-loop measurement of plate response at the secondary shaker location with no control and various feedback gains in the control loop at the secondary location.

using the same method as for the single-channel situation. The limiting factor for identification is the distance to the nearest object that can reflect structural waves. If this distance becomes smaller, a higher frequency range is required to obtain a correct approximation. It was shown that if the frequency range is sufficiently large, the presence of control does not significantly influence the estimation of the impedance. This is therefor a very robust strategy.

For optimal power absorption it was shown that, although it will converge to the optimal value to maximise power absorption for single-channel control, for multi-channel control, this is not guaranteed and the gains can become higher than expected.

Section 6.3 showed that the variables required for the tuning of the approximations can also be measured on an actual structure. The calculation of the two-mode formula resulted in nearly identical gains on the basis of the model and on the basis of the measurements. For the three-mode formula, the values differed by about 50%. Matching the infinite plate impedance also resulted in nearly identical gains on the

basis of the model and the measurements. The frequency range over which the mean impedance could be calculated was limited by a resonance at 6 kHz, which caused an undesirable phase shift. A limit in the frequency domain to which the impedance can be measured limits the minimum distance at which control units can be spaced.

Chapter 7

Conclusions and suggestions for future work

7.1 Conclusion

The goal of the research, as set out in section 1.3, was to examine decentralised control strategies that could be tuned using local variables, but are aimed at reducing a global cost criterion. These strategies have been examined on beam and plate models. The excitation of these structures was assumed to be a randomly distributed, stochastic excitation. This resulted in equal but independent excitation of each mode of the structure. This was done so that the tuning of the controller varied only with the location of the controller and not with the location of the excitation.

Studying the unconstrained optimisation of a single-channel controller, either feedback or feedforward, suggested that minimising the sum of the power inputs of the excitation and the controller is a good approximation for minimising the kinetic energy in the structure. Unconstrained tuning for maximum power absorption resulted in a controller that increased the power input by the excitation and mostly increased, rather than reduced, the overall kinetic energy. It can be shown that in a causal system with an entirely random excitation, a feedback controller can not influence the power input by the excitation. Thus, maximising the power absorption by the controller is equal to minimising the total power input and can be used as a

viable approximation of minimising the kinetic energy. Other approximations that were suggested were based on a model with a reduced number of modes or matching the impedance of the infinite structures. This last approximation is only possible on the plate, as the impedance of an infinite plate is real and constant, whereas the impedance of an infinite beam is frequency variable and complex.

These approximations to the optimal, constant absolute velocity feedback gains feedback gains were simulated using collocated velocity sensors and force actuators and were compared to an optimised absolute velocity feedback gain and a LQG controller. It was found on both the beam and plate, for both white and red noise excitation, that provided the velocity feedback gain and the LQG controller use a similar control effort, then there is hardly any difference in the overall cost function. It was also found that on the beam, for a white noise excitation, the maximisation of the power absorption resulted in far higher gains than optimal. The approximations to the optimal gain based on a small number of modes resulted in good approximations to the optimal performances in these simulations, with a performance within 1 dB of the LQG controller, which obtained an average reduction of about 9 dB. This probably reflects the fact that in this structure the majorty of the kinetic energy is contained in the first few modes. For red noise excitation on the beam, power absorption led to gains that were below optimal. The reductions in red noise case were much larger, between 14 and 25 dB, and depended much more strongly on the location of the colocated sensor and actuator along the beam, with the best performance just off the middle of the beam. On the plate, the reductions were less, respectively 3 and up to 11 dB for white and red noise excitation. The differences between maximum power absorption and minimising the kinetic energy were smaller both in gains and performance. The approximations on the basis of a few modes performed reasonable, as long as the control location is not near the edges of the plate, while the approximation by matching the infinite plate impedance always performed well.

The multichannel case allows the use of cross coupling terms in the controller. It was found that, although the off diagonal terms were significant in the optimised constant gain controller, they only added performance when the controllers were closely spaced. In that case, they allow the controller to separately implement angular velocity feedback and transverse velocity feedback. Again, it was found that there was hardly any difference between LQG and absolute velocity feedback control if the

control effort is similar. On the beam with white noise excitation, it was again found that maximising the power absorption resulted in too high gains and performed less well than other approximations studied, the three mode and two resonance formulas. In the red noise case it performed better than the other approximations. On the plate, maximum power absorption was the best approximation in terms of performance, closely followed by the matched infintie plate impedance, both in the case of red and white noise.

These controllers examined the control of kinetic energy as the sum of the squared modal velocities, which weights the motion of each location of the plate equally. It seemed appropriate therefore to study a cost function which is more selective. It was chosen to study sound radiation. The modelling of sound radiation for the purpose of ASAC was examined first and found that radiation mode filtering is a more effective strategy of modelling sound radiation in terms of calculation time than modal radiation filtering, though the latter was found to be more accurate. The examination of the performance of different controllers showed that a centralised controller again added no real benefit in terms of performance over a decentralised controller. The difference between a decentralised, constant gain velocity feedback controller and LQG control, though bigger than for AVC, was also very small. Although a controller optimised for ASAC does have better acoustic performance than a controller optimised for AVC, in practice an AVC system would do a good job in controlling sound radiation.

Finally, chapter 6 showed that tuning of the feedback gains using the approximations to the optimised controller is possible on the basis of the measured local variables (power and mobility transfer function) in both a single-channel and a multi-channel set-up. Though it is not unexpected for the maximisation of power absorption and it can be proven to be true for the matched infinite plate impedance, it was not expected to be the case for the two- and three-mode formulas. The multi-channel online tuning of the two- and three-mode formulas might be difficult as included modes may become critically damped when control is present at other locations and have to be discarded. This this could result in limit-cycling behaviour. Creating a strategy for self-tuning of units based on maximum power absorption in a multichannel controller may also create some difficulty, as it could be difficult to set up the independent controllers to 'give up' power so that more power can be extracted at other control locations. It was shown that the method of measuring

the infinite plate impedance only depends on the distance to the nearest reflecting object and that this impedance can also be measured in a practical set-up.

In short, the aim of this thesis is satisfied on the plate: matching the infinite plate impedance can be measured locally, in both a single-channel and multi-channel set-up and has AVC performance that is close to that of a centralised, dynamic controller. For the beam, the approximations based on a low number of modes seem to work better, but the convergence of the tuning can not be guaranteed. Power maximisation can also work well, especially on the plate, but implementation might be difficult and tuning could change if the excitation is not white, or not randomly distributed.

7.2 Discussion and suggestions for future work

This work examined the tuning of decentralised control units on the basis of local measurements for a rather idealised control system. First of all, the dynamics of both the sensor and actuator were neglected. For the generation of feedback forces on plates, a combination of an accelerometer and an active mass driver (see also Paulitsch (2005) and Benassi et al. (2004)) seems most logical. Stability analysis of such units in a multi-channel set-up would be useful to show the relevance for further research. Another interesting practical question is whether the use of the matched impedance on a more complicated engineering structures than plates is feasible and would still produce good results.

On the plate, it was observed that setting a velocity feedback gain to match the impedance of an infinite plate worked well and the performance of a dynamic, centralised controller was not much better. This might be explained in terms of physics. One can imagine a point on an *infinite* plate, where waves come in at random intervals and from random directions. To reduce these waves as much as possible, the maximum amount of energy would need to be extracted from them, which can be done by applying a matched impedance. Logically, if that point was on a *finite* plate of the same material and thickness and if the waves are still coming in randomly, i.e. reflections can be neglected, then the same impedance would still result in a maximum reduction of the waves. This may be an explanation for the small difference

in performance between optimised, dynamic, centralised kinetic energy control and decentralised constant gain control; If reflections do not contribute significantly to the velocity signal measured at some point, trying to control them on the basis of the velocity signal would not help much. Thinking about the control of the waves in the plate in this way, leads to an interesting question: can the controllers be placed in such a way that the 'diffuseness' of the waves in the plate is maximised?

If the suggested explanation is correct, the difference in performance between dynamic, centralised control and constant velocity feedback gain set to match the infinite plate impedance, should decrease ever further. Also, it would be interesting to examine how the performance in that case compares to the performance to regularly placed controllers, or controllers placed to minimise AVC. The sound radiation of a structure with such diffuse waves would also be interesting to examine; would the sound radiation increase or decrease? How does a controller that is optimised at those locations compare to the matched impedance?

The two- and three-mode approximations seem to work in a multi-channel set-up, because it is assumed that the observed resonances are independent modes that are excited equally and independently. If it can be established that the modeshapes corresponding to those resonances are orthogonal and that the excitation of each of those modeshapes is indeed equal, then the basis for using these approximations becomes stronger. An algorithm that prevents limit-cycling would then need to be developed.

Finally, it should be noted that matching the impedance of the infinite plate was possible to implement because it is a constant and real variable. If one was to measure a different quantity, such as rotational velocity or bending, and use a corresponding dual acutator, this is likely to change. It would be interesting to study other cases where the input-output transfer function of a collocated and dual actuator-sensor pair is a constant gain when measuring an infinite structure. If the inverse of this 'infinite mobility' is then applied on the finite structure, does it also occur that dynamic, centralised controllers have little performance gain to offer over a constant gain, feedback strategy with matched 'infinite impedance'?

Appendix A

Modal analysis of a beam

A simply supported beam is a beam that is supported at its ends on hinges, allowing free rotation, but no displacement. This is illustrated in figure A.1.

To analyse the motion of the beam, an infinitesimal portion of the beam must be considered. The forces acting on such an portion of the beam are depicted in figure A.2. The moments at the cross-sections are caused by a pressure distribution over the entire cross-section of the beam.

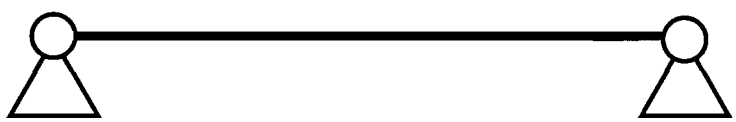

Figure A.1: A simply supported beam.

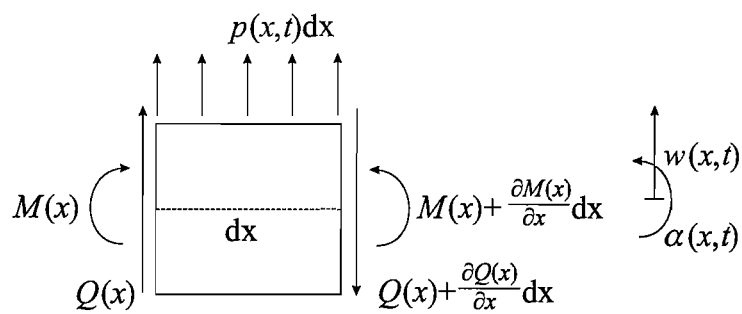

Figure A.2: Forces governing infinitesimal portion of a beam.

The transverse forces acting on the beam are related to the bending of the beam and as such are related to the transverse displacement of the beam. The differential equations that describe the transverse displacement are given by:

$$-\frac{\partial Q(x,t)}{\partial x} + p(x,t) = \rho S \frac{\partial^2 w(x,t)}{\partial t^2} \tag{A.1}$$

$$-Q(x,t) + \frac{\partial M(x,t)}{\partial x} = I \frac{\partial^2 \alpha(x,t)}{\partial t^2} \tag{A.2}$$

In this analysis, it is assumed that rotational motion of the element is insignificant in comparison to the transverse motion of the element and that shear deformation is small compared to bending deformation. These assumptions are valid if the height of the beam or plate is small in comparison to its length (and width), and bending, the second derivative of the transverse deflection, remains limited. Under these assumptions, the combination of equation A.2 and A.1 results in:

$$-\frac{\partial^2 M(x,t)}{\partial x^2} + p(x,t) = \rho S \frac{\partial^2 w(x,t)}{\partial t^2} \tag{A.3}$$

The moments acting on the cross sections of the beam are due to the strains related to bending of the beam. The relation between the strains and bending are described by the following differential equation:

$$M(x,t) = EI \frac{\partial^2 w(x,t)}{\partial x^2} \tag{A.4}$$

Substituting equation A.4 into A.3 leads to what is known as the Euler-Bernouilli thin beam equation of motion:

$$\frac{\partial^2}{\partial x^2} EI \frac{\partial^2 w(x,t)}{\partial x^2} + \rho S \frac{\partial^2 w(x,t)}{\partial t^2} = p(x,t) \tag{A.5}$$

Where EI is the bending stiffness of the beam, $w(x,t)$ the transverse deflection, ρ the density and S the cross-sectional area. $p(x,t)$ is an external pressure acting on the beam. EI is assumed constant along the beam.

To obtain a solution for $w(x,t)$ in the inhomogeneous differential equation A.5, the homogeneous solution should first be considered ($p(x,t) = 0$). In that case, a solution can be found that is separable in space and time:

$$w(x,t) = w_x(x) w_t(t) \tag{A.6}$$

Implementing this into equation A.5 results in:

$$w_t(t) EI \frac{\partial^4 w_x(x)}{\partial x^4} + \rho S w_x(x) \frac{\partial^2 w_t(t)}{\partial t^2} = 0 \tag{A.7}$$

If furthermore the time dependent part is harmonic, then it can be written as: $w_t(t) = w_\omega(j\omega)e^{j\omega t}$. Combining this with equation A.7 results in:

$$EI\frac{\partial^4 w_x(x)}{\partial x^4} - \rho S w_x(x)\omega^2 = 0 \tag{A.8}$$

or:

$$\frac{\partial^4 w_x(x)}{\partial x^4} - k^4 w_x(x) = 0 \tag{A.9}$$

At this point the boundary conditions of the beam must be considered. For a simply supported beam, the boundary conditions are such that there are no deflections or bending moments at the beginning ($x = 0$) and the end of the beam ($x = L$):

$$\begin{aligned} w_x(0) &= 0 \qquad EI\tfrac{\partial^2 w_x(0)}{\partial x^2} = 0 \\ w_x(L) &= 0 \qquad EI\tfrac{\partial^2 w_x(L)}{\partial x^2} = 0 \end{aligned}$$

The solutions to A.8 that comply with the boundary conditions, are sinusoidal modeshape functions:

$$w_x(x) = c_n \sin(k_n x) \tag{A.10}$$

where $k_n = \frac{n\pi}{L}$ and n is an integer. These modeshapes can be scaled arbitrarily. Here they have been chosen to be:

$$w_x(x) = \psi_n(x) = \sin(k_n x) \tag{A.11}$$

These modeshapes have natural frequencies:

$$\omega_n(x) = \left(\frac{n\pi}{L}\right)^2 \sqrt{\frac{EI}{\rho S}} \tag{A.12}$$

Now the solution for the homogeneous equation is obtained, the solution to the inhomogeneous Euler-Bernouilli equation (equation A.5) can be derived. To do this, the *expansion theorem* is used:

Theorem 1. *Expansion theorem: Any function $w(x,t)$, satisfying the boundary conditions of the problem and such that $\frac{\partial^2}{\partial x^2}\left(EI\frac{\partial^2 w(x,t)}{\partial x^2}\right)$ is a continuous function, can be represented by the absolutely and uniformly convergent series of the system eigenfunctions:*

$$w(x,t) = \sum_{n=1}^{\infty} a_n(t)\psi_n(x) \tag{A.13}$$

where $a_n(t)$ can be interpreted as the modal response of that particular mode to the input force. Then, by combining equations A.13 and A.5, this can be written as:

$$\sum_{n=1}^{\infty} \rho S \frac{\partial^2 a_n(t)}{\partial t^2} \psi_n(x) + \sum_{n=1}^{\infty} a_n(t) \left(EI \frac{\partial^4 \psi_n(x)}{\partial x^4} \right) = p(x,t) \tag{A.14}$$

Assuming that the pressure is a point force, $f(t)$, at x_f:

$$\sum_{n=1}^{\infty} \rho S \ddot{a}_n(t) \psi_n(x) + \sum_{n=1}^{\infty} a_n(t) \left(EI \frac{\partial^4 \psi_n(x)}{\partial x^4} \right) = f(t)\delta(x - x_f) \tag{A.15}$$

This equation is not useful in determining the individual $w_n(t)$ for each mode. However, by using the orthogonality of the modeshapes, equations for each $w_n(t)$ can be obtained. Multiplying both sides of equation by $\psi_m(x)$ and integrating over the length of the beam gives:

$$\sum_{n=1}^{\infty} \left(\rho S \ddot{a}_n(t) + EI k_n^4 a_n(t) \right) \int_0^L \psi_n(x)\psi_m(x)dx = \int_0^L \psi_m(x) f(t) \delta(x - x_f) dx \tag{A.16}$$

Due to the orthogonality of the modes, $\int_0^L \psi_n(x)\psi_m(x)dx$ is equal to 0 if $n \neq m$ and the summation is thus eliminated from the equation. If $n = m$, $\int_0^L \psi_n(x)\psi_m(x)dx$ is equal to $1/2L$. Thus differential equation A.16 simplifies to:

$$1/2L \left(\rho S \ddot{a}_m(t) + EI k_m^4 a_m(t) \right) = \psi_m(x_f) f(t) \tag{A.17}$$

A Laplace transform or Fourier transform of this equation, allows the formulation of the transfer function from the force to the modal displacement in terms of the Laplace variables or frequency. In terms of frequency, the transfer function is:

$$\begin{aligned} H_m(j\omega) &= \frac{a_m(j\omega)}{F(j\omega)} \\ &= \frac{2}{L} \frac{\psi_m(x_f)}{(-\rho S\omega^2 + EIk_m^4)} \\ &= \frac{2}{\rho SL} \frac{\psi_m(x_f)}{(\omega_m^2 - \omega^2)} \end{aligned} \tag{A.18}$$

So far, no damping has been included in the model. The damping has been assumed to be small and to act on each mode individually. The differential equation and the transfer function then become:

$$1/2L \left(\rho S \ddot{a}_m(t) + \rho S \zeta \omega_m \dot{a}_m(t) + EI k_m^4 a_m(t) \right) = \psi_m(x_f) f(t) \tag{A.19}$$

$$H_m(j\omega) = \frac{2}{\rho SL} \frac{\psi_m(x_f)}{(\omega_m^2 + 2j\omega\zeta\omega_m - \omega^2)} \tag{A.20}$$

where ζ is a viscous damping factor.

Appendix B

Single channel red-noise results on a plate

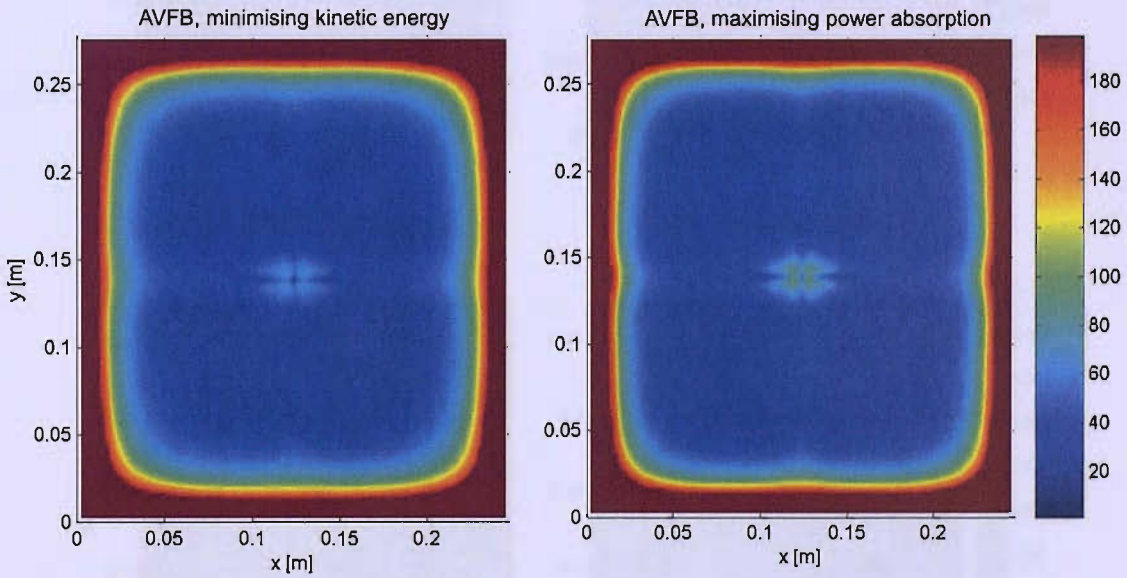

(a) AVFB, minimising kinetic energy

(b) AVFB, maximising power absorption

Figure B.1: Constant gains [Ns/m] for different single channel optimisations on a plate, under red noise excitation. Gains for LQG control, two- and three- mode formulas and matched infinite plate impedance have not been depicted, as they are not-constant (LQG control) or the same as for white-noise excitation.

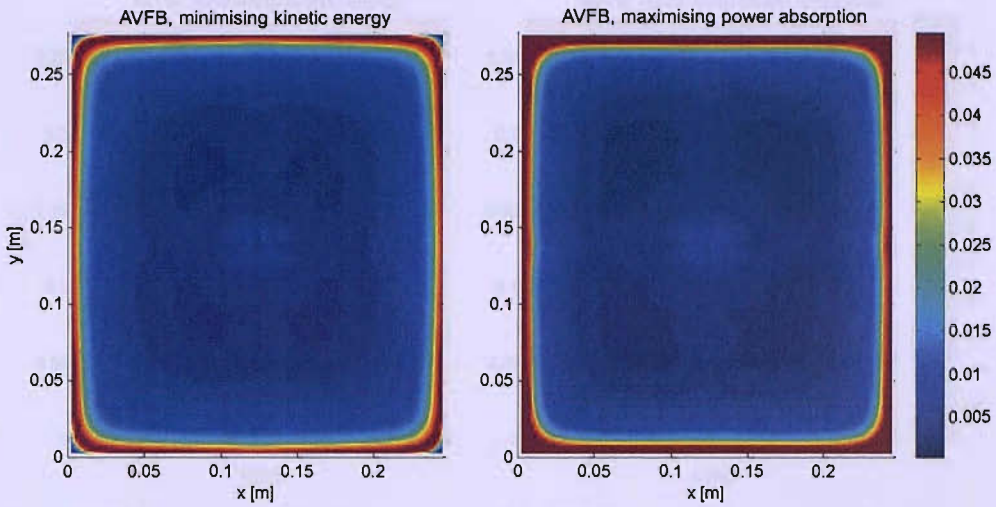

(a) AVFB, minimising kinetic energy (b) AVFB, maximising power absorption

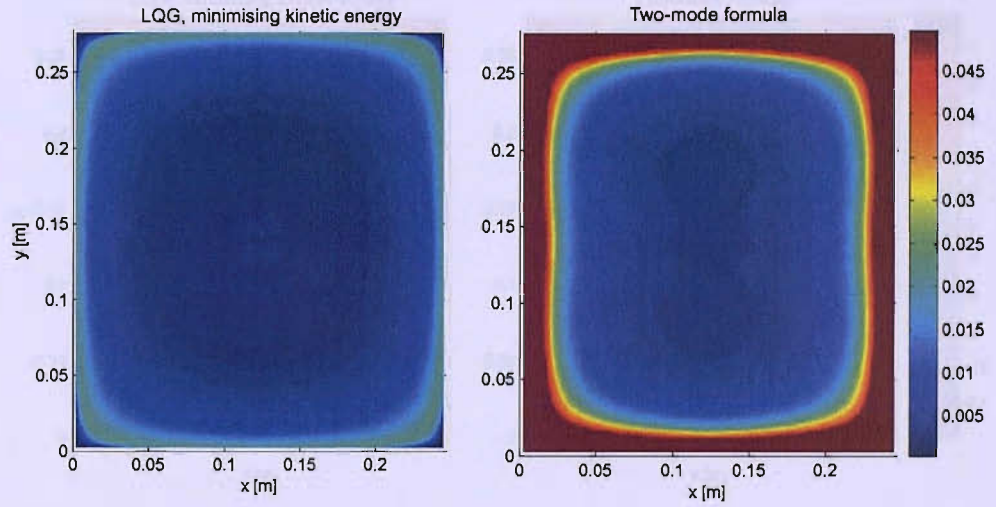

(c) LQG, minimising kinetic energy (d) Two-mode formula

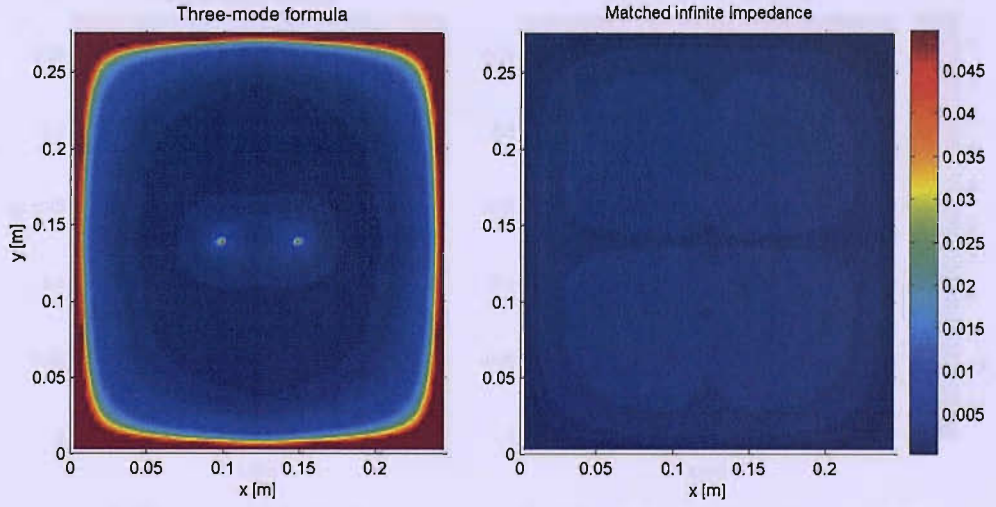

(e) Three-mode formula (f) Matched infinite plate impedance

Figure B.2: Control effort [N^2] for different control strategies on a plate, under red noise excitation.

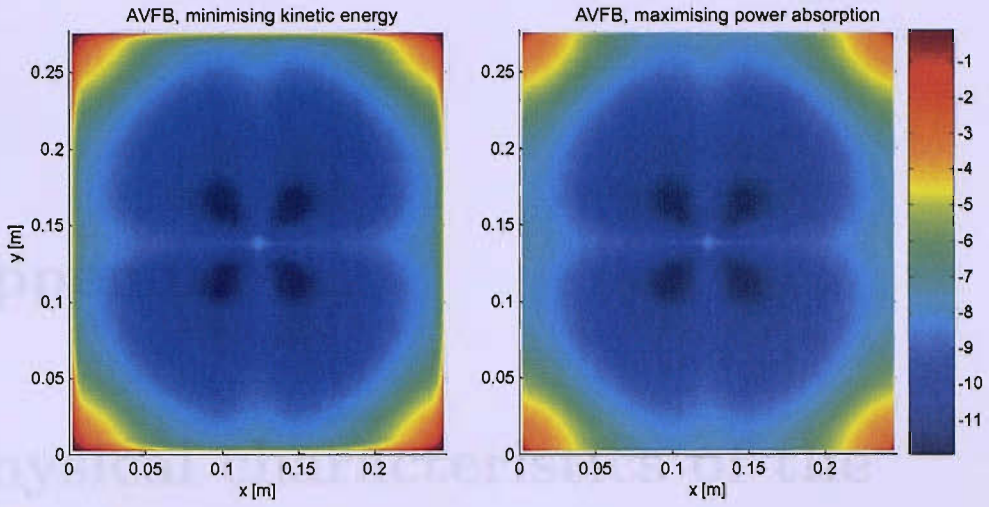

(a) AVFB, minimising kinetic energy (b) AVFB, maximising power absorption

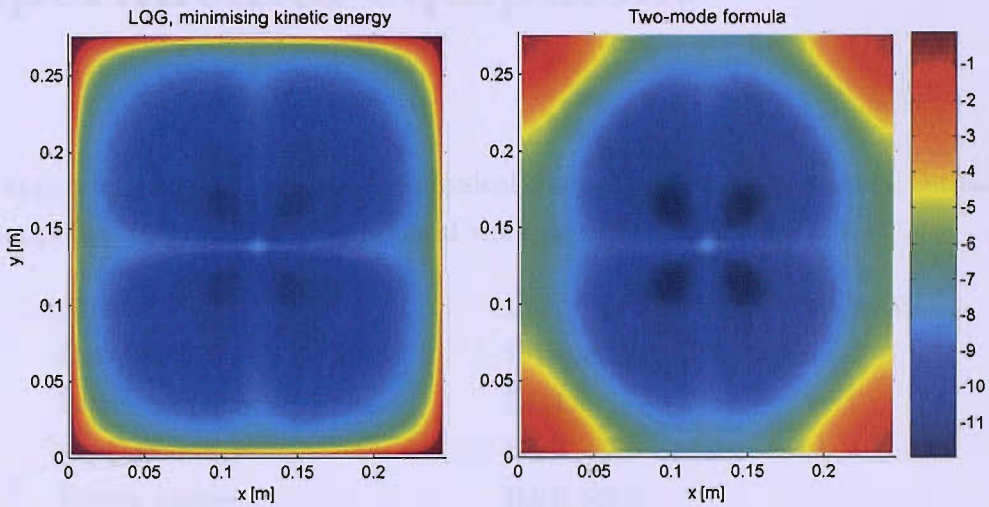

(c) LQG, minimising kinetic energy (d) Two-mode formula

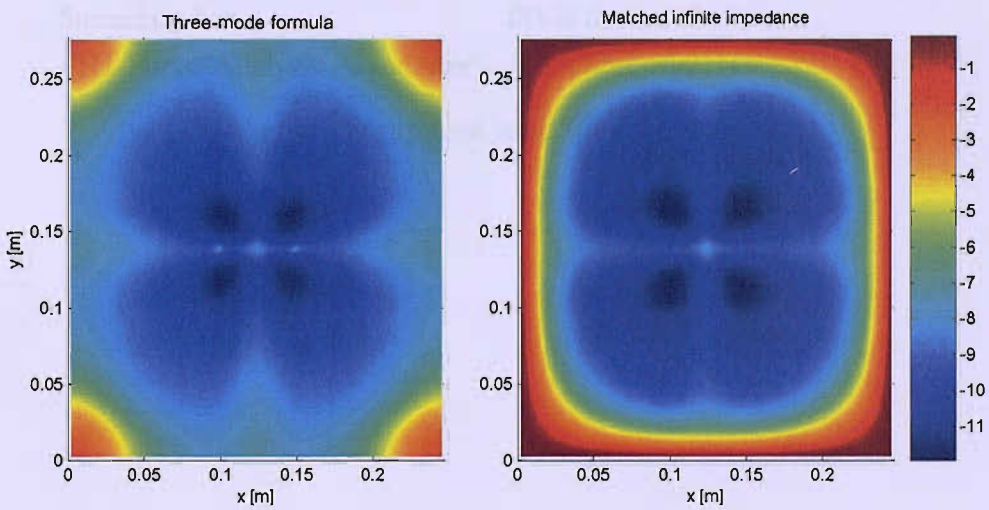

(e) Three-mode formula (f) Matched infinite plate impedance

Figure B.3: Change in kinetic energy in decibels for different control strategies on a plate.

Appendix C

Physical characteristics of the experimental equipment

This appendix contains tables of the physical characteristics of the sensors, actuators and amplifiers used in the experimental work described in section 6.3.

Shakers	LDS type V101 and type V403
Current driver	ISVR designed
Power amplifier	DC300
Accelerometer	B&K 4375
Fource gauge	B&K 8200
Charge amplifier	B&K 2635
Summing box	ISVR designed
FFT Servo Analyzer/Generator	Advantest R9211C

Table C.1: Equipment used for experiments.

Effective moving mass	0.0065 kg
Maximum sine force - peak	8.9 N
Maximum displacement peak - peak (DC)	2.5 mm
Maximum sine velocity - peak	1.31 m/s
Maximum sine acceleration	1373 m/s^2
Suspension axial stiffness	3.15 N/mm
Electrical requirement - Amplifier	0.09 kVA

Table C.2: Specification of the LDS type V101 shaker.

Moving mass	0.200 kg
Maximum sine force - peak	98 N
Maximum displacement peak - peak (DC)	17.6 mm
Maximum sine velocity - peak	1.52 m/s
Maximum sine acceleration	981 m/s^2
Suspension axial stiffness	12.3 N/mm
Electrical requirement - Amplifier	0.27 kVA

Table C.3: Specification of the LDS type V403 shaker.

References

Anderson, B. D. O. and Moore, J. B. (1971). *Linear optimal control.* Prentice-Hall, Inc., Englewood Cliffs, New Jersey.

Balas, M. J. (1979). Direct velocity feedback control of large space structures. *Journal of Guidance and Control*, 2(3):252–253.

Balas, M. J. (1982). Trends in large space structure control theory: Fondest hopes, wildest dreams. *IEEE Transactions on Automatic Control*, 27(3):522–535.

Bamieh, B., Paganini, F., and Dahleh, M. A. (2002). Distributed control of spatially invariant systems. *IEEE Transactions on Automatic Control*, 47(7):1091–1107.

Bardou, O., Gardonio, P., Elliott, S. J., and Pinnington, R. J. (1997). Active power minimization and power absorption in a plate with force and moment excitation. *Journal of Sound and Vibration*, 208(1):111–151.

Baumann, O. N., Engels, W. P., and Elliott, S. J. (2004). A comparison of centralised and decentralised control for the reduction of kinetic energy and radiated sound power. In *Proceedings of ACTIVE04.*

Baumann, W. T., Saunders, W. R., and Robertshaw, H. H. (1991). Active suppression of acoustic radiation from impulsively excited structures. *Journal of the Acoustical Society of America*, 90(6):3202–3206.

Benassi, L. (2004). *Feedback Control of Vibration with Inertial Actuators.* PhD thesis, University of Southampton, Faculty of Engineering and Applied Science.

Benassi, L., Elliott, S. J., and Gardonio, P. (2004). Active vibration isolation using an inertial actuator with local force feedback control. *Journal of Sound and Vibration*, 276:157–179.

Bendat, J. S. and Piersol, A. G. (1986). *Random data, analysis and measurement procedures.* Wiley-Interscience, second edition.

Borgiotti, G. V. (1990). The power radiated by a vibrating body in an acoustic fluid and its determination from boundary measurements. *Journal of the Acoustical Society of America*, 88(4):1884–1893.

Borgiotti, G. V. and Jones, K. E. (1994). Frequency independence property of radiation spatial filters. *Journal of the Acoustical Society of America*, 96(6):3516–3524.

Brennan, M. J. (1997). Vibration control using a tunable vibration neutralizer. *Proceedings of the I MECH E Part C Journal of Mechanical Engineering Science*, 211(2):91–108.

Brennan, M. J., Elliott, S. J., and Pinnington, R. J. (1995). Strategies for the active control of flexural vibration on a beam. *Journal of Sound and Vibration*, 186(4):657–688.

Clark, R. L. and Bernstein, D. S. (1998). Hybrid control: separation in design. *Journal of Sound and Vibration*, 214(4):784–791.

Clark, R. L. and Cole, D. G. (1995). Active damping of enclosed sound fields through direct rate feedback control. *Journal of the Acoustical Society of America*, 97(3):1710–1716.

Clark, R. L. and Cox, D. E. (1997). Multi-variable structural acoustic control with static compensation. *Journal of the Acoustical Society of America*, 102(5):2747–2756.

Clark Smith, G. and Clark, R. L. (1998). The influence of frequency-shaped cost functionals on the structural acoustic control performance of static, output feedback controllers. *Journal of the Acoustical Society of America*, 104(4):2236–2244.

Cox, D. E., Gibbs, G. P., Clark, R. L., and Vipperman, J. S. (1998). Experimental robust control of structural acoustic radiation. In *39th AIAA/ASME/ASCE/AHS/ASC Structures, Structural Dynamics and Materials Conference.* AIAA.

Cremer, L., Heckl, M., and Ungar, E. E. (1988). *Structure-borne Sound.* Springer-Verlag.

Dayou, J. and Brennan, M. J. (2001). Optimum tuning of a vibration neutralizer for global vibration control. *Proceedings of the I MECH E part C Journal of Mechanical Engineering Science*, 215(8):933–942.

Dayou, J. and Brennan, M. J. (2003). Experimental verification of the optimal tuning of a tunable vibration neutralizer for global vibration control. *Applied Acoustics*, 64(3):311–323.

dell'Isola, F., Porfiri, M., and Vidoli, S. (2003). Piezo-electromechanical (PEM) structures: passive vibration control using distributed piezoelectric transducers. *Comptes Rendus Mechanique*, 331(1):69–76.

Doyle, J. C., Glover, K., Khargonekar, P. P., and Francis, B. A. (1989). State-space solutions to standard h_2 and h_∞ control problems. *IEEE Transactions on Automatic Control*, 34(8):831–847.

Dyke, S. J., Spencer Jr., B. F., Sain, M. K., and Carlson, J. D. (1996). Modeling and control of magnetorheological dampers for seismic response reduction. *Smart Materials and Structures*, 5:565–575.

Elliott, S. J. (2004). Distributed control of sound and vibration. In *Proceedings of ACTIVE04*.

Elliott, S. J., Gardonio, P., Sors, T. C., and Brennan, M. J. (2002). Active vibroacoustic control with multiple local feedback loops. *Journal of the Acoustical Society of America*, 111(2):908–915.

Elliott, S. J. and Johnson, M. E. (1993). Radiation modes and the active control of sound power. *Journal of the Acoustical Society of America*, 94(4):2194–2204.

Elliott, S. J., Joseph, P., Nelson, P. A., and Johnson, M. (1991). Power output minimization and power absorption in the active control of sound. *Journal of the Acoustical Society of America*, 90(5):2501–2512.

Engels, W. P., Baumann, O. N., and Elliott, S. J. (2004). Centralised and decentralised feedback control of kinetic energy. In *Proceedings of ACTIVE04*.

Engels, W. P., Baumann, O. N., Fraanje, R., and Elliott, S. J. (2006). Centralized and decentralized control of structural vibration and sound radiation. *Journal of the Acoustical Society of America*, 119(3):1487–1495.

Engels, W. P. and Elliott, S. J. (2004). Optimal velocity feedback control on a beam. In *Proceedings of the IOA Spring Conference*, volume 26. Institute of Acoustics.

Engels, W. P. and Elliott, S. J. (2005). Optimal velocity feedback control on a beam. *Submitted to Smart Materials and Structures.*

Fraanje, R., Verhaegen, M., Doelman, N., and Berkhoff, A. (2004). Optimal and robust feedback controller estimation for a vibrating plate. *Control engineering practice*, 12:1017–1027.

Francis, B. A. (1987). *A course in H_∞ Control Theory.* Springer-Verlag.

Fuller, C. R., Elliott, S. J., and Nelson, P. A. (1996). *Active Control of Vibration.* Academic Press, London.

Fuller, C. R., Kidner, M., Li, X., and Hansen, C. H. (2004). Active-passive heterogeneous blankets for control of vibration and sound radiation. In *Proceedings of ACTIVE04.*

Gardonio, P. and Elliott, S. (2004a). Smart panels for active structural acoustic control. *Smart Materials and Structures*, 13(6):1314–1336.

Gardonio, P. and Elliott, S. J. (2004b). Smart panel with anechoic edges for active structural acoustic control. In *Proceedings of ACTIVE04.*

Geromel, J. C. and Bernussou, J. (1979). An algorithm for optimal decentralized regulation of linear quadratic interconnected systems. *Automatica*, 15(4):489–491.

Gibbs, G. P., Clark, R. L., Cox, D. E., and Vipperman, J. S. (2000). Radiation modal expansion: Application to active structural acoustic control. *Journal of the Acoustical Society of America*, 107(1):332–339.

Guicking, D., Melcher, J., and Wimmel, R. (1989). Active impedance control in mechanical structures. *Acustica*, 69(2):39–52.

Hirami, N. (1997a). An active maximum power absorber for the reduction of noise and vibration. *Journal of Sound and Vibration*, 200(3):261–279.

Hirami, N. (1997b). Optimal energy absorption as an active noise and vibration control strategy. *Journal of Sound and Vibration*, 200(3):243–259.

Hiramoto, K., Doki, H., and Obinata, G. (2000). Optimal sensor/actuator placement for active vibration control using explicit solution of algebraic riccati equation. *Journal of Sound and Vibration*, 229(5):1057–1075.

Jacquot, R. G. (2000). Random vibration of damped modified beam systems. *Journal of Sound and Vibration*, 234(3):441–454.

Jacquot, R. G. (2001). Suppression of random vibration in plates using vibration absorbers. *Journal of Sound and Vibration*, 248(4):585–596.

Jalili, N. and Knowles, D. W. (2004). Structural vibration control using and active resonator absorber: modeling and control implementation. *Smart Materials and Structures*, 13:998–1005.

Johnson, M. E. and Elliott, S. J. (1995). Active control of sound radiation using volume velocity cancellation. *Journal of the Acoustical Society of America*, 98(4):2174–2186.

Kader, M., Lenczner, M., and Mrcarica, Z. (2000). *Linear Estimation*. Information and System Sciences Series. Prentice Hall, Upper Saddle River, new Jersey.

Kalman, R. E. and Bertram, J. E. (1960). Control system analysis and design via the "second method" of lyapunov, i continuous-time systems. *Transactions of the ASME - Journal of Basic Engineering*, 82 series D:371–393.

Kim, S.-H., Choi, S.-B., Hong, S.-R., and Han, M.-S. (2004). Vibration control of a flexible structure using a hybrid mount. *International Journal of Mechanical Sciences*, 46:143–157.

Kim, S. M., Elliott, S. J., and Brennan, M. J. (2001). Decentralized control for multichannel active vibration isolation. *IEEE Transactions on Control Systems Technology*, 9(1):93–100.

Kinsler, L. E., Frey, A. R., Coppens, A. B., and Sanders, J. V. (1982). *Fundamentals of Acoustics*. John Wiley & Sons, third edition.

Knyazev, A. S. and Tartakovskii, B. D. (1965). Application of electromechanical feedback for the damping of flexural vibrations in rods. *Soviet Physics - Acoustics*, 11(2):150–154.

Knyazev, A. S. and Tartakovskii, B. D. (1967). Application of electromechanical feedback for the damping of plate vibrations and radiation. *Soviet Physics - Acoustics*, 12(3):330–331.

Leissa, A. W. (1969). Vibration of plates. Technical Report SP-160, Office of technology utilization National Areonautics and Space Administration Washington, D.C.

Levine, W. S. and Athans, M. (1970). On the determination of the optimal constant output feedback gains for linear multivariable systems. *IEEE Transactions on Automatic Control*, AC-15(1):44–48.

Ljung, L. (1999). *System Identification: Theory for the user.* Information and sciences series. Prentice Hall PTR, Upper Saddle River, New Jersey, second edition.

Meirovitch, L. (1986). *Elements of Vibration Analysis.* McGraw-Hill Book Company, second edition.

Nelson, P. A. (1996). Acoustical prediction. In *Proceedings of Internoise96.*

Niederberger, D., Fleming, A., Moheimani, S. O., and Morari, M. (2004). Adaptive multi-mode resonant piezoelectric shunt damping. *Smart Materials and Structures*, 13(5):1025–1035.

Olson, H. F. (1956). Electronic control of noise, vibration, and reverberation. *Journal of the Acoustical Society of America*, 28(5):966–972.

Paulitsch, C. (2005). *Vibration control with electrodynamic actuators.* PhD thesis, University of Southampton, Faculty of Engineering and Applied Science.

Preumont, A. (2002). *Vibration Control of Active Structures: An Introduction.* Kluwer Academic Publishers, second edition.

Preumont, A., Franois, A., Bossens, F., and Abu-Hanieh, A. (2002). Force feedback versus acceleration feedback in active vibration isolation. *Journal of Sound and Vibration*, 257(4):605–613.

Preumont, A., Franois, A., Man, P. D., and Piefort, V. (2003). Spatial filters in structural control. *Journal of Sound and Vibration*, 265:61–79.

Redman-White, W., Nelson, P., and Curtis, A. R. D. (1987). Experiments on the active control of flexural wave power flow. *Journal of Sound and Vibration*, 112(1):187–191.

Rex, J. and Elliott, S. J. (1992). The QWSIS- a new sensor for structural radiation control. In *Prodeedings of the First international Conference on Motion and Vibration Control, Yokohama, Japan*, pages 339–343.

Rizet, N., Brissaud, M., Gonnard, P., Béra, J.-C., and Sunyach, M. (2000). Modal control of beam flexural vibration. *Journal of the Acoustical Society of America*, 107(4):2061–2067.

Rockwell, T. H. and Lawther, J. M. (1964). Theoretical and experimental results on active vibration dampers. *Journal of the Acoustical Society of America*, 36(8):1507–1515.

Sadri, A. M., Wynne, R. J., and Wright, J. R. (1999). Robust strategies for active vibration control of plate-like structures: theory and experiment. *Proceedings of the I MECH E part I Journal of Systems And Control Engineering*, 213(6):489–504.

Serrand, M. J. (1998). Active isolation of base vibration. Master's thesis, Institute of Sound and Vibration Research, Faculty of Engineering and Applied Science, University of Southampton.

Singh, A., Pines, D. J., and Baz, A. (2004). Active/passive reduction of vibration of periodic one-dimensional structures using piezoelectric actuators. *Smart Materials and Structures*, 13(4):698–711.

Singh, S. P., Pruthi, H. S., and Agarwal, V. P. (2003). Efficient modal control strategies for active control of vibrations. *Journal of Sound and Vibration*, 262(3):563–575.

Skogestad, S. and Postlethwaite, I. (1996). *Multivariable Feedback Control - Analysis and Design*. John Wiley & Sons, Chichester, England.

Smyser, C. P. and Chandrashekhara, K. (1997). Robust vibration control of composite beams using piezoelectric devices and neural networks. *Smart Materials and Structures*, 6(2):178–189.

Sors, T. C. and Elliott, S. J. (2002). Volume velocity estimation with accelerometer arrays for active structural acoustic control. *Journal of Sound and Vibration*, 258(5):867–883.

Stein, G. and Athans, M. (1987). The LQG/LTR procedure for multivariable feedback control design. *IEEE Transactions on Automatic Control*, 32(2):105–114.

Sutton, T. J., Elliott, S. J., Brennan, M. J., Heron, K. H., and Jessop, D. A. C. (1997). Active isolation of multiple structural waves on a helicopter gearbox support strutt. *Journal of Sound and Vibration*, 205(1):81–101.

Thomas, D. R. and Nelson, P. A. (1995). Feedback control of sound radiation from a plate excited by a turbulent boundary layer. *Journal of the Acoustical Socicty of America*, 98(5):2561–2662.

Trindade, M. A., Benjeddou, A., and Ohayon, R. (2001). Piezoelectric active vibration control of damped sandwich beams. *Journal of Sound and Vibration*, 246(4):653–677.

Variyart, W., Brennan, M. J., and Elliott, S. J. (2002). Active damping for a beam using feedback control. In Gardonio, P. and Rafaely, B., editors, *Proceedings of Active 2002*, pages 839–850.

Veres, S. M. and Wall, D. S. (2000). *Synergy and Duality of Identification and Control*. Taylor & Francis, New York.

Vipperman, J. S., Burdisso, R. A., and Fuller, C. R. (1993). Active control of broadband structural vibration using the lms adaptive algorithm. *Journal of Sound and Vibration*, 166(2):283–299.

Wallace, C. E. (1972a). Radiation resistance of a baffled beam. *Journal of the Acoustical Society of America*, 51(3):936–945.

Wallace, C. E. (1972b). Radiation resistance of a rectangular panel. *Journal of the Acoustical Society of America*, 51:946–952.

Wang, D.-A. and Huang, Y.-M. (2002). Robust vibration control of a beam using the H_∞-based controller with model error compensator. *Journal of Sound and Vibration*, 254(5):877–895.